UNIVERSITÀ DI PARMA

UNIVERSITÀ DEGLI STUDI DI PARMA

DOTTORATO DI RICERCA IN FISICA

CICLO XXXV

Coherent and incoherent dynamics of molecular nanomagnets investigated by magnetic resonances and inelastic neutron and x-ray scattering

Coordinatore:
Chiar.mo Prof. Stefano Carretta

Tutore:
Chiar.mo Prof. Stefano Carretta

Co-tutore:
Dr.ssa Elena Garlatti
Chiar.mo Prof. Giuseppe Allodi

Dottorando:
Simone Chicco

Anni Accademici 2019/20 - 2022/23

Abstract

The focus of this thesis is the characterization of the coherent and incoherent dynamics of molecular nanomagnets. For this purpose, we will exploit several state-of-the-art experimental techniques, such as magnetic resonances and inelastic scattering of neutrons and X-rays. By means of nuclear magnetic resonances we will characterize the nuclear relaxation times and the parameters of the spin Hamiltonian of two V-based molecular qudits, demonstrating, in addition, the capability to coherently manipulate their nuclear states. This proof-of-concepts experiments represent an important first step towards the implementation of molecular qudits in quantum information processing. Moreover, by X-ray inelastic scattering, we will investigate the phonon dispersions of one benchmark molecular qudit and their role in its relaxation dynamics. We will also focus on the key factors governing the phonon-induced relaxation in Dy-based single molecule magnets by studying, through inelastic neutron scattering, the changes induced in their phonon density of states by chemical substitutions or structural deformations. Finally, a synergistic approach combining electron and nuclear magnetic resonance will give us insights on the electronic relaxation dynamics of a supramolecular assembly linking an isolated nuclear qudit and an electronic spin qubit.

List of Collaborators

University of Parma (IT)

- Supervisor and Co-Supervisors: E. Garlatti, G. Allodi, S. Carretta.
- Collaborators: A. Chiesa, P. Bonfà, I.J. Onuorah, R. De Renzi, P. Santini.

University of Florence (IT)

- F. Santanni, A. Albino, F. Totti, L. Sorace, R. Sessoli.

University of Turin (IT)

- E. Salvadori, M. Chiesa.

Lab.Nat. Champs Magnétiques Intenses, Grenoble (FR)

- M. Atzori.

University of Manchester (UK)

- F. S. J. Lockyer, A. Brookfield, J. Skelton, F. Tuna, D. Mills, N. Chilton, E. McInnes, R. Winpenny.

Trinity College Dublin (IE)

- A. Nguyen, A. Lunghi.

University of Glasgow (UK)

- A. Mavromagoulos, A. B. Canaj, M. Murrie.

University of Camerino, (IT) and ISIS Neutron and Muon source, Didcot, OX (UK)

- T. Guidi.

European Synchrotron Radiation Facility, Grenoble (FR)

- L. Paolasini.

Institue Laue Langevin, Grenoble (FR)

- M. Jimenez Ruiz, A. Piovano, A. Ivanov.

Brookhaven National Laboratory, Upton, NY (USA)

- C. Mazzoli, C. Yong.

Contents

1 Introduction 15

1.1 Molecular nanomagnets 15

1.2 Di Vincenzo criteria for Molecular Magnets 18

1.3 Spin Hamiltonian formalism 23

1.3.1 Electronic and Nuclear Zeeman interactions 24

1.3.2 The Hyperfine interaction 25

1.3.3 The Nuclear quadrupolar coupling 28

1.3.4 Second order effects 28

1.4 Lindblad Master equation 30

2 Experimental techniques 33

2.1 Resonance techniques 33

2.1.1 Nuclear Magnetic Resonance 33

2.1.2 Electron Paramagnetic resonance 37

2.2 Scattering techniques 39

2.2.1 Inelastic scattering 40

2.2.2 Inelastic Neutron Scattering 41

2.2.3 Inelastic Xrays Scattering 46

3 Extensive broadband NMR study of Vanadium-based molecular qudits 50

3.1 Vanadium-based qudits 50

3.2 NMR investigation of the [VO(TPP)] molecular qudit 51

3.3 Comprehensive study of an Organometallic spin Qudit with Radiofrequency and Microwave techniques 61

3.4 Encoding a QEC algorithm on the [VO(TPP)] molecular qudit 75

3.5 Conclusions 77

4 Unveiling phonons in a prototypical molecular qubit by IXS 79

4.1 State of art 79

4.2 Inelastic X-ray scattering experiment 80

4.2.1 Results 83

4.3 The critical role of ultra-low energy vibrations 86

4.4 Conclusions 89

5 Effect of chemical and structural modifications on the phonon induced magnetization dynamics of Dysprosium-based Single-Molecule

Magnets 90
5.1 The effect of chemical composition on the pDOS of new Dy-based SMMS 91
5.1.1 Inelastic neutron scattering experiment 96
5.1.2 Results 98
5.2 Measuring phonon modes of a Dy-based SMM in applied pressure 99
5.2.1 Inelastic neutron scattering experiment 101
5.2.2 Results 103
5.3 Conclusions 105

6 Combined EPR-NMR study of the Supramolecular $\{Cr_7Ni\}$-Cu dynamics 106
6.1 Electronic spin-lattice and spin-coherence times 107
6.2 Spin dynamics probed by ^{1}H-NMR 110
6.3 Electronic spin Manipulations 113
6.4 Conclusions 114

General Conclusion 115

List of Figures

1.1 On the left and on the right side of the figure, the chemical structure of two iconic single molecule magnets. On the left the first SMMs to exhibit magnetic hysteresis at the molecular level and slow relaxation of magnetization, Mn_{12} [1] (formally $\{Mn_{12}O_{12}[O_2CCD_2C(CD_3)_3]_{16}(CD_3OD)_4\}$). On the right, the first rare-earth based SMMs to display magnetic hysteresis up to liquid nitrogen temperature, Dysprosocenium [2] ($[(Cp^{ttt})_2Dy][B(C_6F_5)_4]$. In the middle, a sketch of a double well potential for the reversal of the magnetization for a high-spin S complex, with a high-spin ground state $m_S = \pm S$. 16

1.2 Structure of some of the most representative molecular qubit emerged for each class described in the main text. (a) $\{Cr_7Ni\}$ for d-block cluster molecules. [3] (b) Vanadium and Vanadyl-based molecular qubit [4, 5, 6] (c) Terbium and Ytterbium based single ion qubit for rare-earth based class. [7, 8] (d) Two example of structure linking together more than one molecular qubit: a rare-earth based dimer [CeEr] [9] and a supramolecular chain decorated with two $\{Cr_7Ni\}$ qubit linked with three copper based qudit [10] 18

1.3 Bloch sphere showing the $|0\rangle$ and $|1\rangle$ basis of a qubit and all the possible linear combination $a|0\rangle + b|1\rangle$ filling the sphere surface. . . . 20

1.4 Scheme of two feasible cooling methods: thermal initialization (left), based on the slow cooling of the system to a temperature low enough to isolate the ground state from the excited ones; projection measurements (right), based on resonant e.m. pulses to rapidly project the system to a desired state (when the thermal population is negligible). 21

1.5 In a rotating frame system, precessing spins are represented by static Bloch sphere states. On the left, the system evolution from a perturbed in-plane state toward the thermodynamical equilibrium state $|0\rangle$, timed by T_1 relaxation time. On the right, the spin dephasing process over time (blue and green arrow represents spins with increased or decreased nutating frequency respectively), timed by T_2 dephasing time. 22

1.6 On the left, the S=1/2 electronic ground state degeneracy splitting induced by the electronic Zeeman interaction $\mathcal{H}_Z$, as a function of the field. On the right, the $|-1/2\rangle \rightarrow |1/2\rangle$ electronic transition enabled by this Hamiltonian contribution observed in a canonical spectral analysis 25

1.7 On the left, the nuclear degeneracy splitting induced by nuclear Zeeman interaction $\mathcal{H}_{Zn}$, as a function of the field in a $S = 1/2$, $I = 3/2$ system. On the right, the m_I degenerate $|3/2\rangle \rightarrow |1/2\rangle$, $|1/2\rangle \rightarrow |-1/2\rangle$, $|-1/2\rangle \rightarrow |-3/2\rangle$ nuclear transition enabled within the same electronic multiplet $\Delta m_S = 0$. The spectra is extended to display both electronic and nuclear transitions. 26

1.8 On the left the splitting effect induced by the parallel Hyperfine component $A_{\|}$ when the external field is applied parallel to it; On the right the expected spectra showing the degenerate nuclear and the resolved electronic transitions, arising from the Hyperfine tensor expressed in inset. 27

1.9 On the left the splitting effect induced by an axial Hyperfine tensor (inset) when the external field is applied perpendicular to the strongest component; On the right the expected spectra where all the nuclear and electronic transitions are resolved. 27

1.10 On the left the splitting of the state with different $|m_I|$ induced by a Quadrupolar coupling $\mathbf{P}$ with components only along $\hat{z}$ when the external field is applied parallel to it; on the right the resulting spectral components for the spin Hamiltonian with only Quadrupolar, electronic and nuclear Zeeman couplings. The nuclear transitions are partially resolved, while the interaction leaves the electronic gaps unperturbed. 28

2.1 Sketch of the "HyReSpect" spectrometer hardware and of the LC-Resonant probe. Transmitter and Receiver stages hardware are better detailed in [11]. 37

2.2 Scattering process with incoming and scattered beam energies E_i, E_f and wavevectors $\vec{k}_i, \vec{k}_f$, and geometrical representation of the transfer momentum $\vec{Q}$ and the scattering angle θ. 40

2.3 The layout of the IN8 spectrometer at ILL. The picture is reproduced from the facility webpage. 44

2.4 Top (left) and side (right) views of the IN1 spectrometer layout. The picture is reproduced from the ILL webpage. 45

2.5 Schematic representation of the ID28 spectrometer layout. The picture is reproduced from the ESRF website 48

3.1 [VO(TPP)] molecular structure. The principal orthogonal symmetry directions of the molecular crystal are shown independently: the porphyrin lying in the ab plane and the oxidovanadium bond direction along the c axis 51

3.2 Spectra collected at different applied field B_0 along the molecule symmetry directions: the ab plane (a), and the c axis (b). In inset, a spurious peak is identified from the absence of any time-domain spin-echo signals. Indeed black line shows the echo signal in quadrature for a real nuclear excitation in correspondence of τ (dashed line), whereas a spurious appears as the persistent gray oscillations. Reproduced from Ref. [4] with permission from the Royal Society of Chemistry. . 52

3.3 Red dots correspond to the measured transition frequencies in the broadband NMR spectra of ^{51}V. Black lines represent the calculated evolution of the transition frequencies as a function of the field B_0 applied (a) in the *ab*-plane, and (b) along *c*-axis. With capital letters **AB#** and **C#** we label the $\Delta m_I = \pm 1$ transitions for each direction. Shaded areas were not experimentally explored. Reproduced from Ref. [4] with permission from the Royal Society of Chemistry. 53
3.4 Energy levels as a function of the applied field from the diagonalization of the spin Hamiltonian with static field B_0 applied (a) in plane *ab* and (b) along *c*-axis. The red and blue shades highlight the $m_S = \pm 1/2$ multiplets, respectively. On the left of each plot, two insets show a zoom into the nuclear level splitting of the lower and upper multiplets, with the levels marked by the nuclear spin components m_I along the field. Vertical marks highlight the nuclear transitions identified in the spectra of figure 3.2. Reproduced from Ref. [4] with permission from the Royal Society of Chemistry. 54
3.5 Difference in subsequent nuclear transitions energies $\delta(m_I) = (E_{m_I+1} - E_{m_I}) - (E_{m_I} - E_{m_I-1})$ in the $m_S = 1/2$ multiplet (crosses), as a function of the applied field $B\hat{\mathbf{x}}$. These values are in sound agreement with what expected from the diagonalization of the pseudo-quadrupolar Hamiltonian (black line). Reproduced from Ref. [4] with permission from the Royal Society of Chemistry. 55
3.6 Echo intensity decay as a function of the delay between the Hahn echo exciting and refocusing pulses. The experimental data for a selected nuclear transition ((a) **AB**2, (b) **C**1) are plotted together with the relaxation rate T_2 single exponential fit for different applied fields. Reproduced from Ref. [4] with permission from the Royal Society of Chemistry. 56
3.7 Nuclear phase memory time for different nuclear transitions, measured with a refocusing Hahn-echo sequence, as a function of the applied field B_0 (a) in the *ab*-plane and (b) along *c*-axis. Reproduced from Ref. [4] with permission from the Royal Society of Chemistry. . 56
3.8 Nuclear Rabi oscillations over a wide time interval, for transitions **AB**1 and **AB**7, corresponding to the transition $m_I = -3/2 \rightarrow -1/2$ for both the lower and higher-energy electronic multiplets $m_S = \pm 1/2$, respectively. Reproduced from Ref. [4] with permission from the Royal Society of Chemistry. 57
3.9 Rabi oscillations as a function of pulse B_1 attenuation, on the transition labeled **AB**1 between the states $m_I = -3/2 \rightarrow -1/2$ of the lowest electronic multiplet $m_S = 1/2$. The rf power is defined with an increasing attenuation from a reference value (0 dB). Reproduced from Ref. [4] with permission from the Royal Society of Chemistry. . 58

3.10 Simulated effect of a rf pulse resonant with a nuclear transition that increase the m_I value by $\Delta m_I = +1$, when the system is initialized in $m_I = 1/2, -1/2, -3/2$ (a,d; b,e; c,f respectively). On the left (a-c) the difference between target level population as a function of time. On the right (d-f) the colormap represents the population evolution with time for all the nuclear states. The pulse is applied along the molecule $\hat{x}$ axis with intensity $B_1 = 5$ G. The targeted transitions are: (a,d) $m_I = 1/2 \rightarrow 3/2$, (b,e) $m_I = -1/2 \rightarrow 1/2$, (c,f) $m_I = -3/2 \rightarrow -1/2$, with $\Delta m_S = 0$. The focus here is on the $m_S = 1/2$ spin multiplet, which is the only one populated because of the states initialization. Reproduced from Ref. [4] with permission from the Royal Society of Chemistry. 60

3.11 Simulated effect of a rf pulse resonant with a nuclear transition $\Delta m_I = +1$, on the thermally populated system. On the left (a-c) the difference between the target levels populations as a function of time. On the right (d-i) the colormap represents the population evolution over time for all the nuclear states of both the electronic spin multiplets $m_S = \pm 1/2$. The pulse is applied along the molecule $\hat{x}$ axis with intensity $B_1 = 5$ G. The targeted transitions are: (a-d) $m_I = 1/2 \rightarrow 3/2$, (b-e) $m_I = -1/2 \rightarrow 1/2$, (c-f) $m_I = -3/2 \rightarrow -1/2$, with $\Delta m_S = 0$. Reproduced from Ref. [4] with permission from the Royal Society of Chemistry. 61

3.12 On the left, the $[V(Cp)_2Cl_2]$ bent-metallocene structure. The molecular reference frame is shown, with the y-axis bisecting the Cl-V-Cl angle, the z-axis perpendicular to the Cl-V-Cl plane (axial direction) and the x-axis unequivocally defined. On the right the crystallographic unit cell with the two inequivalent molecules labeled as V1 and V2. Reprinted with permission from Ref. [12]. Copyright 2021 American Chemical Society. 62

3.13 Picture of the crystal collected from microscopy (left) and a sketch of the crystal shape (right). The two are compared to show the edge length hierarchy and the relative indexing of crystal faces with the corresponding crystallographic planes. Reprinted with permission from Ref. [12]. Copyright 2021 American Chemical Society. 63

3.14 The crystallographic planes (111), (010) and (10-1), that correspond to the crystal faces, are highlighted in the unit cell. This sketch assist in the visualization of the applied field directions with respect to the molecular reference frame. Reprinted with permission from Ref. [12]. Copyright 2021 American Chemical Society. 63

3.15 (a) Continuous Wave ($\nu = 9.405$ GHz, black) and Echo Detected Field Sweep ($\nu = 9.70$ GHz, blue) X-band EPR powder spectra of sample **3c** measured at $T = 20$ K. The spectra are both simulated (red) using the Hamiltonian parameter of table 3.2. EDFS is translated in B for better comparison. (b) CW-EPR Q band spectrum ($\nu = 33.7$ GHz, black). (c,d) 2D colormap (blue negative, red positive) of **3c** single crystal X-band EPR spectra as a function of θ_A and θ_B rotations. Black lines correspond to the simulated spectra for the two inequivalent molecules. It is evident the overlap of the two spectra along the reference frame axis ($\theta_{A,B} = 0°, 90°$) within the EPR resolution. Reprinted with permission from Ref. [12]. Copyright 2021 American Chemical Society. 64

3.16 Broadband NMR spectra measured at $T = 4$ K at fixed applied static field $B_0 = 0.2$ T, for the field directions $\mathbf{B}_S$, $\mathbf{B}_M$, $\mathbf{B}_L$ schematized in inset with respect to the crystal faces. In black, the Gaussian spectral lines fitting. Reprinted with permission from Ref. [12]. Copyright 2021 American Chemical Society. 65

3.17 The measured NMR frequencies for a single crystal of **3b** (yellow and cyan dots) are compared with the spin Hamiltonian fitting model (black and red dots for each molecule, respectively). The applied field directions $\mathbf{B}_S$, $\mathbf{B}_M$, $\mathbf{B}_L$ are schematized in inset. Cyan experimental points label the transitions whose ${}^nT_2$ was measured. Shaded areas were not explored experimentally. Reprinted with permission from Ref. [12]. Copyright 2021 American Chemical Society. 67

3.18 Calculated energy levels for the experimental field configurations $\mathbf{B}_S$, $\mathbf{B}_M$, $\mathbf{B}_L$ with respect to the crystal faces. Black and red lines relates to the two inequivalent molecules. For the nuclear transitions labeled by vertical colored lines it was also measured the nuclear phase memory time ${}^nT_2$ (fig. 3.19). Reprinted with permission from Ref. [12]. Copyright 2021 American Chemical Society. 68

3.19 (a) Temperature evolution of the electronic spin-lattice ${}^eT_1$ and spin coherence ${}^eT_m$ relaxation times, for each dilution percentage of [V(Cp)$_2$ Cl$_2$]. Solid and dashed lines represent respectively the models 3.4 and 3.5 fitting results. (b,c,d) Nuclear phase memory time ${}^nT_2$ measured on dilution **3b** for the transitions labeled in figure 3.18 at $T = 4$ K as a function of the applied field, for $\mathbf{B}_S$, $\mathbf{B}_M$, $\mathbf{B}_L$ configuration, respectively (sketch in inset). Reprinted with permission from Ref. [12]. Copyright 2021 American Chemical Society. 70

3.20 Transverse magnetization decay from NMR echo relaxation experiments, as a function of the delay τ between exciting and refocusing pulses, at $T = 4$ K and fixed static field B_0, along $\mathbf{B}_S$ (a), $\mathbf{B}_L$ (b), $\mathbf{B}_M$ (c) for transitions **S1**, **L2**, **M2**. Lines shows the single exponential decay fitting. Reprinted with permission from Ref. [12]. Copyright 2021 American Chemical Society. 71

3.21 (a) Electronic Rabi nutation experiments (EPR X-band) on **3c** at $T = 20$ K at different excitation powers. (b) Frequency domain picture to highlight the monochromaticity of the oscillations. (c) Linear dependence of Rabi frequency ($\Omega_R = \omega_R/2\pi$) on the exciting microwave pulse amplitude B_1. Reprinted with permission from Ref. [12]. Copyright 2021 American Chemical Society. 72
3.22 (a,b) Nuclear Rabi nutation experiments on transitions **S1** and **L1**, respectively, at $T = 4$ K and fixed field $B_S = B_L = 0.1$ T, on a single crystal of **3b**. Differences in the oscillations damping rates λ_S, λ_L are attributed to the inhomogeneities of the applied field with respect to crystal rather than to ${}^nT_2$, which is comparable for the two transitions. (c,d) Nuclear states population changes induced by the Rabi sequence for transitions **S1** and **L1** simulated by numerically solving the Lindblad master equation for a single π rotation of the nuclear spin system. All the states are labeled by the nuclear spin component m_I (accurate at more than 99 % because of state factorization at this field). The only levels that undergoes significant population changes are the targeted ones. Reprinted with permission from Ref. [12]. Copyright 2021 American Chemical Society. 73
3.23 (a) Calculated spectral frequency of three subsequent transitions A, B and C, belonging to the same electronic multiplet. The static field is applied along $\mathbf{B}_S$. (b,c,d) Simulated coherent Rabi oscillations, corresponding to the transitions A: $m_I = 7/2 \rightarrow 5/2$ (b), B: $m_I = 5/2 \rightarrow 3/2$ (c) and C: $m_I = 3/2 \rightarrow 1/2$ (d). The leakage to the other nuclear states is negligible. The optimal excitation conditions for monochromatic oscillations are found to be: $B_0 = 0.22$ T and $B_1 = 2$ G. The resulting inversion (π-pulse) is still much shorter than the phase memory time ${}^nT_2$ corresponding to this transitions. Reprinted with permission from Ref. [12]. Copyright 2021 American Chemical Society. 74
3.24 (a) Encoding sequence sketch for the four labeled nuclear spin states $m_I = -3/2, -1/2, 1/2, 3/2$ (colored horizontal lines), ordered by energy. Each rf-pulse in the sequence is labeled by the angular rotation induced on the nuclear system. (b) Step by step time evolution of the diagonal elements of the system density matrix ρ (colored lines) when targeted by the pulse sequence in (a) with a pulse amplitude of $B_1 = 1$ mT. The system is initialized in the generic $0.83|-1/2\rangle + 0.55i|1/2\rangle$ state superposition and brought into the encoded state 3.6 in an overall manipulation time of 4 μs. The final state is in sound agreement with the squared expectation values (crosses), with the secondary oscillations induced by the rf manipulations that do not affect significantly the encoding. Reproduced from Ref. [4] with permission from the Royal Society of Chemistry. 76
3.25 Rabi nutation experiment at the fixed static field $B_0 = 0.3$ mT along the system $\hat{\mathbf{x}}$-axis induced by 7.7 dB attenuated linearly polarized rf-pulses B_1 along $\hat{\mathbf{z}}$. The targeted nuclear states are the one involved in the encoding sequence 3.6. Reproduced from Ref. [4] with permission from the Royal Society of Chemistry. 77

4.1 (a-b) view of the [VO(TPP)] crystal structure along the a and c axis respectively. (c) Brillouin zone picture, in which the symmetry direction probed in our experiment are highlighted (red arrows). 81
4.2 Longitudinal (**a**, **b**, **c**) and transverse (**d**, **e**, **f**) IXS scans along the directions $\Gamma - N$, $\Gamma - K_x$ and $\Gamma - K_z$, collected in low-resolution configuration. 82
4.3 Longitudinal (**a**) and transverse (**c**) IXS scans along the directions $\Gamma - K_x$, $\Gamma - N$, and $\Gamma - K_z$, collected in high-resolution configuration, to resolve the low energy phonons contribution close to the elastic line. 83
4.4 The 2D colormap shows the inelastic cross-section calculated starting from phonon energies and polarisazion vectors extracted from ab initio calculations, along the three sampled symmetry directions in the recirpocal space in both longitudinal and transverse configuration: (a,e) $\Gamma - N$, (b,f) $\Gamma - K_x$, (c,d) $\Gamma - K_z$. The line-width associated to each phonon modes is chosen small enough to enable the distinction of the contribution arising from any branch. Cyan dots and squares ($\delta E = 3$ / 1.5 meV respectively) represent the excitation energies extracted from the spectra in figures 4.2 and 4.3. White dots/squares represent the energies extracted from the inspection of secondary analyzers. Shaded areas highlight the regions non accessible experimentally due to the dominant elastic contribution. . . 84
4.5 Experimental IXS spectra (black dots) are compared with the simulated cross-sections (red line). The latter are convoluted with the experimental resolution ((a-e,g): $\delta E = 3$ meV; (f,h,i): $\delta E = 1.5$ meV). A representative spectra is shown for each probed symmetry direction. Blue lines represent the inelastic cross-section, calculated with a line-width that enables to discriminate the contribution of each phonon mode. The elastic line is omitted for clarity. 85
4.6 Phonon density of state (black line) and modulus $|\mathbf{V}_\alpha|$ of the spin-phonon coupling coefficient (red line, negative axis) computed *ab initio*, as a function of energy. In inset the comparison between the low energy pDOS of [VO(TPP)] (black) and the parent molecular qubit [VO(acac)$_2$] (green). [13] 86
4.7 Calculated spin relaxation time T$_1$ for [VO(TPP)] (red squares) compared to the T$_1$ measured in [14] with pulsed X-band EPR (black dots). These data are then compared to the simulated T$_1$ after the removal of phonons with energy lower then 6 meV (blue triangles). . 87
4.8 Sketch of the distortion of the molecular structure, from the equilibrium structure (yellow) to an extensively distorted one (red). These distortions consist in a bending of the porphirin planar ring and a twist of the phenyl groups, and are associated with the lowest energy optical mode at Γ-point. 88

5.1 (a) Dysprosocenium **a** molecule and its counterion [15]. The arrow sketches the substitution made on the counterion for the synthesis of sample **3**. (b) Sample **3** structure [Dy(Cp^{ttt})$_2$][B(C$_6$H$_5$)$_4$] with ^{1}H substituted with F in the counterion. 92

5.2 (a) Dysprosocenium **a** molecule and its counterion [15]. The arrow sketches the counterion substitution made for the synthesis of sample **2**. (b) Structure of sample **2** [Dy(Cp^{ttt})$_2$][Al{OC(CF$_3$)$_3$}$_4$] with the Al-based counterion that substitute the Boron-based one of sample **a** 92

5.3 (a) Dysprosocenium **a** molecule and its counterion [15]. The arrow sketches the counterion and Cp-group substitution made for the synthesis of sample **1**. (b) Sample **1** structure [Dy(Dtp)$_2$][Al{OC(CF$_3$)$_3$}$_4$] with counterion and Dysprosium ligands substitution. 93

5.4 Magnetization relaxation rates for **1** (from [16]), **2** and **3** in the range T=2-110 K, from ac susceptibility (high-T) and dc decay experiments (low-T). These measurements were performed by Prof. Mills group at the University of Manchester (see List of Collaborators). 94

5.5 Magnetization relaxation rates for **1** (orange dots) and **a** (light purple dots) respectively (from [16] and [15]), extracted at high temperature from ac susceptibility measurements and at low temperature from dc decay experiments. Solid red lines represents a fit of the Orbach and Raman contributions. The fitting results of the two curves are respectively: $U_{eff}^{\mathbf{1}} = 1760$ K, $\tau_0^{\mathbf{1}} = 10^{-11.7}$ s, $C^{\mathbf{1}} = 10^{-3.5}$ $s^{-1}K^{-n}$, $n^{\mathbf{1}} = 1.1$; $U_{eff}^{\mathbf{a}} = 1760$ K, $\tau_0^{\mathbf{a}} = 1.98 \times 10^{-11}$ s, $C^{\mathbf{a}} = 1.66 \times 10^{-6}$ $s^{-1}K^{-n}$, $n^{\mathbf{a}} = 2.15$ 94

5.6 Comparison of the calculated pDOS for samples **a**, **2**, **3**. Panel (a) exhibits the whole calculated energy range, while panel (b) shows the restricted low-energy regime, highlighting the significant differences in the low energy spectra, compared to the less pronounced ones in the intermediate-energy spectra. 95

5.7 pDOS measured on IN1 for sample **1** (green line), **2** (light blue line) and **3** (magenta line), compared with the same measurement collected for the benchmark Dysprosocenium on the MERLIN spectrometer at ISIS (dotted black line).[17] The two panels (a) and (b) show the whole collected energy range and a close up of the low energy pDOS, respectively. 97

5.8 Comparison of the experimental phonon density of state (5 K) with the neutron weighted pDOS calculated *ab initio* for (a) sample **a**, (b) sample **2** and (c) sample **3**. The *ab initio* calculations were performed by our collaborators at the University of Manchester (see the List of Collaborators). 98

5.9 (a) Molecular structure of [Dy(H$_2$O)$_5$(HMPA)$_2$] and its counterion I$_3$·2HMPA at ambient pressure. The Dy ion (seagreen) and the O (red) environment are highlighted for clarity. (b) Magnetization data from Ref.[18] as a function of the applied field showing hysteresis loops at different temperature in ambient pressure (Y-diluted sample). (c) Magnetization relaxation rates from Ref.[18] as a function of temperature (black dots), extracted from ac susceptibility measurements. The Orbach regime is highlighted by the Arrhenius fit (red line) for an energy barrier $U_{eff} = 600$ K and $\tau_0 = 1.2 \times 10^{-11}$ s, as reported in [18] 99

5.10 (a) Molecular structure of [Dy(H_2O)$_5$(HMPA)$_2$] and its counterions I_3·2HMPA under an applied pressure of 1.1 GPa. Dysprosium ion (seagreen) and the Oxygen (red) environment are highlighted. (b) Magnetization data as a function of the applied field showing hysteresis loops at different temperature in an applied hydrostatic pressure of 1.1 GPa. These measurements were performed by our collaborators at the University of Glasgow (see the List of Collaborators) 100
5.11 INS cross section measured at 77 K for two different applied pressure on a [Dy(H_2O)$_5$(HMPA)$_2$] single crystal (dots), at the Γ-point for $\vec{Q}_1 = (0\,3\,-12)$. Here, the pressure cell+gasket blank signal is already subtracted from the scattered intensity. The solid line represent the INS cross section calculated starting from DFT-calculated eigenvalues and eigenvectors and convoluted with experimental resolution of 3 meV (low resolution configuration). The low-energy differences in the INS cross section induced by the applied pressure are evident and emerge considerably from the error bars. 102
5.12 Temperature dependence of the high-resolution INS cross section measured at $\vec{Q}_1 = (0\ 3\ -12)$ in a [Dy(H_2O)$_5$(HMPA)$_2$] single crystal, for a constant applied pressure of 1 GPa. 102
5.13 Phonon density of states from normalized inelastic neutron scattering experiment on [Dy(H_2O)$_5$(HMPA)$_2$] powders. The spectra was collected at 77 K for two $|\vec{Q}|$ values. The high and low resolution scans are merged in order to maximize the extent of the high resolution region. 103
5.14 (a) Simulated pDOS at two different applied pressures (atmospheric and 1 GPa). The pDOS is convoluted with a sharp resolution σ in order to better evaluate the contribution of different phonon branches that would overlap with the experimental one. (b) Zoom to the lower energy regime, where the larger pressure-induced differences are observed. 104
5.15 Comparison of the experimental nw-pDOS (dots) with the one obtained with periodic DFT (gray lines). The calculated pDOS is convoluted with the experimental resolution in the corresponding energy ranges. 105

6.1 Q-band pulsed EPR EDFS at 3K on a 0.2 mM frozen solution of {Cr_7Ni}[Cu(hfac)$_2$]. The Hahn-echo refocusing sequence $\pi/2-\tau-\pi$ used for the echo detection features a π-pulse of 120 ns. Light blue and green ticks mark the {Cr_7Ni} and [Cu(hfac)$_2$] in plane $g_{x,y}$ signals, respectively. 107
6.2 Electronic spin-lattice saturation recovery paths for a 0.2 mM frozen solution of {Cr_7Ni}[Cu(hfac)$_2$] measured at 3K with Q-band EPR (dots). The three static fields shown correspond to: (a) the $g_{x,y}$ component of the ring $B_0 = 13.755$ kG, (b) the $g_{x,y}$ component of the Cu $B_0 = 11.745$ kG, and (c) one of the hyperfine lines along the g_z component of the Cu, at $B_0 = 10.862$ kG. The double or triple exponentials recovery rates are reported in the inset for each panel (red line). 108

6.3 Electronic spin echo decays measured for a 0.2 mM frozen solution of $\{Cr_7Ni\}[Cu(hfac)_2]$, measured at 3K with Q-band EPR (dots). The three static fields shown correspond to: (a) the $g_{x,y}$ component of the ring $B_0 = 13.755$ kG, (b) the $g_{x,y}$ component of the Cu $B_0 = 11.745$ kG, and (c) one of the hyperfine lines along the g_z component of the Cu, at $B_0 = 10.862$ kG. The decays are fitted with a slightly stretched single exponential decay (parameters are shown in inset). 108
6.4 X-band pulsed EPR Echo Detected Field Sweep at 5.4K on a 0.2 mM frozen solution of $\{Ti_7Ga\}[Cu(hfac)_2]$. The π-pulse used for the detection, at fixed mw-power, was 32 ns long, calibrated on the highest spectral feature. Light blue and orange ticks mark the field at which the spin lattice and spin coherence times in figure 6.5 are measured and correspond to the in plane $g_{x,y}$ and one axial g_z $[Cu(hfac)_2]$ spectral components. 109
6.5 (a,b) X-band electronic saturation recovery data (dots) measured at 5.4 K on a 0.2 mM frozen solution of $\{Ti_7Ga\}[Cu(hfac)_2]$ with an inversion sequence for the two field (a) $B_0 = 3334$ G and (b) $B_0 = 3061$ G marked in figure 6.4. In inset the resulting triple exponential fit (red line) for spin-lattice rates. (c,d) X-band echo decay experiments for the same conditions above and at the same static fields. The spin coherence time extrapolated from the single exponential stretched fit (red line) are shown in inset. 110
6.6 (a) Fastest ^{1}H-NMR normalized saturation recovery at 10 K for different applied static field B_0. (b) Normalized single exponential ^{1}H-NMR echo decay measured at 10 K for two applied fields. 111
6.7 Proton nuclear spin-lattice relaxation rates $1/^nT_1$ extracted from fitting the saturation recovery curves in figure 6.6 as a function of the system temperature, at three different applied static field B_0. 112
6.8 (a) Proton nuclear spin-spin relaxation rates $1/^nT_2$ at two static applied fields, extracted from fitting the echo amplitude decay with a stretched single exponential function at fixed stretching parameter β. (b) Transverse magnetization $M^H_{x,y}(0)T$ from the echo amplitude extrapolated at zero delay in the echo decays. Multiplied by the temperature, it gives a hint on the number of nuclei with a still measurable decoherence. 112
6.9 Q-band EPR-EDFS at 3K on a 5% diluted fine powder of $\{Cr_7Ni\}[Cu(hfac)_2]$. Red and black ticks mark the in plane $g_{x,y}$ and axial g_z ring and copper signal respectively. 113
6.10 Rabi nutation experiments at 3 K on fine powder of $\{Cr_7Ni\}$-$[Cu(hfac)_2]$. The field was fixed to match respectively the two higher spectral components (a) $B_{ring} = 13.597$ kG and (b) $B_{Cu} = 11.704$ kG (as sketched in inset) corresponding to the $g_{x,y}$ plane. The pulse power-attenuation is varied to highlight the Rabi frequency $^e\omega_R$ and damping λ_R dependencies. For each pulse-power, the pulse length in the Rabi-sequence was modified in order to maintain the effectiveness of the $\pi/2-\pi$ refocusing. 114

Chapter 1

Introduction

Molecular magnetism has represented a very active research topic over the last few decades. The fruitful collaboration of scientists belonging to different backgrounds, such as Physics and Chemistry, has contributed in paving the way for the implementation of these systems in quantum information processing. This thesis focuses on several aspects of the experimental characterization of molecular magnets spin dynamics. By exploiting different techniques we deepen the understanding of relaxation dynamics mechanisms in various molecular magnets, we fully characterize the model spin Hamiltonian of some prototypical systems, we detect the effect of physical and chemical stimuli on their phonon-induced relaxation and finally we implement targeted manipulation of the system spin states by radiofrequency and microwave pulses, demonstrating the possibility of exploiting these complexes for quantum information processes.

1.1 Molecular nanomagnets

The discovery, at the beginning of the 1990s, of magnetic hysteresis originating at the single molecule level by R. Sessoli and coworkers [1] triggered the development of a brand new research field [19] which nowadays permeates into several branches of science, from quantum information theory to super-dense information storage, from nanoscopic sensing and nanoscopic probing to electric transport etc: Molecular magnetism.

The progenitor of this compounds class, displaying magnetic hysteresis and slow relaxation of the magnetization, was the so-called Mn_{12} (aka $[Mn_{12}O_{12}(CH_3COO)_{16}(H_2O)_4]$). [1, 20] This system, and the class of compounds that emerged in the following years (as Fe_8 or Ni_{10}), are clusters of exchange-coupled d-block metals, whose magnetic behavior can be approximated to a single gigantic total spin S slowly relaxing because of an effective double well potential arising from the large ground state spin and a strong magnetic anisotropy. [21, 22] The presence of an energy barrier to the reorientation of the magnetic moment leads to the bistability of the ground state total spin $\mathbf{S}$ (fig. 1.1). This effect made these molecules interesting candidates for the ultimate miniaturization of the memories, where each molecule can encode a single "bit" of memory (from here the name Single-Molecule-Magnets). However, the magnetic bistability of the giant spin ground states with $m_S = \pm S$ in undermined by different relaxation processes: some are temperature independent, such as the quantum tunneling of the magnetization (QTM) below the energy barrier, others are instead thermally activated, due to the coupling of the spin with molecular vibrations, generating other relaxation paths such as the Orbach multistep mechanisms over the energy barrier and non-resonant Raman. Consequently, the magnetic hysteresis in these first SMMs can be observed only when QTM is not activated/ineffective and at extremely low temperatures, where thermal fluctuations are suppressed. [19, 23, 24, 25]

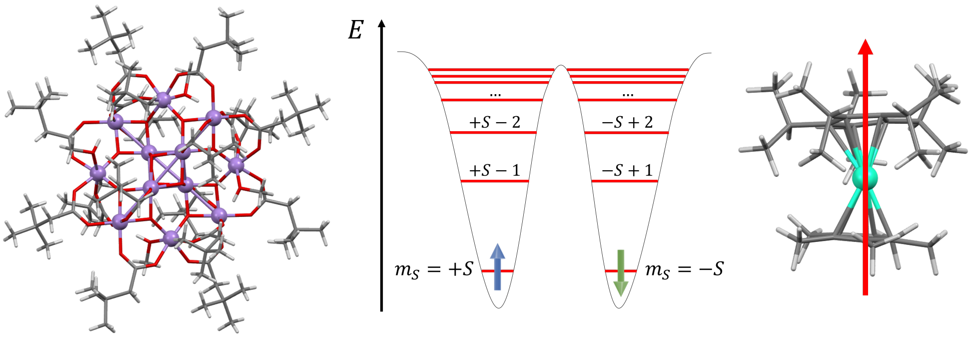

Figure 1.1: On the left and on the right side of the figure, the chemical structure of two iconic single molecule magnets. On the left the first SMMs to exhibit magnetic hysteresis at the molecular level and slow relaxation of magnetization, Mn_{12} [1] (formally $\{Mn_{12}O_{12}[O_2CCD_2C(CD_3)_3]_{16}\ (CD_3OD)_4\}$). On the right, the first rare-earth based SMMs to display magnetic hysteresis up to liquid nitrogen temperature, Dysprosocenium [2] ($[(Cp^{ttt})_2Dy][B(C_6F_5)_4]$. In the middle, a sketch of a double well potential for the reversal of the magnetization for a high-spin S complex, with a high-spin ground state $m_S = \pm S$.

A remarkable step in the magnetization blocking temperature of SMMs have been achieved in the following years with a second generation of molecular nanomagnets, based on a single f-block magnetic ion. [26] Here indeed, the strong spin-orbit coupling of the rare-earth elements (e.g. Lanthanides) combined with a prominent axial ligands crystal field, produces a large anisotropy barrier, that stabilize the ground state spin even at high temperature (fig. 1.1). The energy barriers of several hundreds of Kelvin degrees high of most of these single molecule magnets is however not the only factor that governs the persistence of the hysteresis at high temperatures. Indeed, the complex interplay of several relaxation processes interferes with the magnetic stability and an extensive knowledge on these mechanisms is fundamental for the improvement of the performances. At very low temperature, the most effective relaxation mechanism is the quantum tunneling of the magnetization (QTM), [19] which is temperature independent but can be made inefficient in pronounced axial ligands field environment. [27] Moreover, at higher temperature, where lattice and molecular vibrations are activated, the coupling of phonons with the magnetic moments induce an incoherent relaxation dynamics in these systems. As a consequence, the engineering of these vibrations and the study of their coupling with the spin is a key step for the improvement of the performances of molecular systems. [28, 29, 30] Taking into consideration all these factors, a record breaking magnetic blocking temperatures of 80 K have been recently reported in Dysprosium-based molecules ($[(Cp^{ttt})_2Dy][B(C_6F_5)_4]$, with Cp^{ttt}= 1,2,4-tri-tert-butylcyclopentadienyl) with double-decker axial ligands environment (see fig. 1.1). [2, 15] Here, the prominent axiality of the ligands field, besides inducing a great isolation of the ground state Kramer doublets from the excited crystal field states, contribute significantly to the suppression of the quantum tunneling of the magnetization under the barrier. Moreover, the strong bonds in the ligands environment of the rare-earth ion prevents efficient spin coupling with molecular vibrations, thus enhancing the persistence of the magnetic bistability at higher temperature.[15]

Very recently a cost-effective semi-*ab initio* approach have been developed to understand the relaxation dynamics of these systems. Physical insights on the origin of these relaxation mechanism can indeed give fundamental information in order to develop the next class of record breaking molecular complexes, with blocking temperatures above the liquid nitrogen limit. [17, 31] In particular non-resonant two phonon Raman processes were discovered to play the key role in triggering the magnetization relaxation for these SMM class in the range of temperatures crucial for the determination of T_B (see also sect. 5).

Because of the long spin lifetime and the remarkable coherence intrinsic to several molecular magnets, these systems offers also an attractive option for the realization of quantum bits. Indeed, the two quantum basis state $|0\rangle$ and $|1\rangle$ can be easily encoded into the two states of a single spin $S = 1/2$ molecule. The major obstacle for the exploitation of these systems in quantum information processing is the persistence of the coherence of a given superposition of states in each qubit unit, defined by the decoherence time T_2 (see sect. 1.2). Therefore, since lattice vibrations, together with electric and magnetic interactions with the environment, make quantum superpositions of states very fragile, lot of effort have been oriented in the last decades to the synthesis of molecular complexes with long coherence times and to the investigation of the decoherence mechanisms.[5, 28, 30, 32, 33, 34, 35, 36, 37]

The first proposed molecular qubit in the 2000s with a coherence time $T_2 > 1$ μs was again a cluster with an even number of d-block atoms antiferromagnetically (AF) coupled: a [$Cr_7NiF_6Piv_{16}$] ring. Indeed, the substitution of a Cr magnetic center in an Homometallic $S = 0$ ring [38] with a divalent Ni cation causes the unbalance of the AF coupling and the emergence of a $S = 1/2$ doublet ground state. [3, 39]

As well as long coherence time (T_2), these clustered systems were also capable to implement the first one-qubit operations, with clear Rabi oscillations of spin populations demonstrated in the benchmark Cr_7Ni ring and in Vanadium-based molecular clusters.[40, 41]

Recently, complexes with a single transition-metal ion are in fact emerging as highly coherent spin qubits (see fig. 1.2). In particular, several Vanadium-based systems display coherent oscillations of spin state populations also approaching room temperature, [35] as well as temperature-resilient coherence times, of the order of the milliseconds in the optimal conditions.[5] Vanadium complexes have also been recently studied as promising coupled qubit-qudit systems. Indeed, the coupling of the electronic S and nuclear I spin degrees of freedom provides a $2I + 1$ multilevel structure called qudit (i.e., quantum digits featuring more than two levels $d > 2$) that can be exploited to expand the computational space or to implement quantum error correction algorithms on single molecular objects. [4, 12, 42]

Rare-earth ions play a role also in the development of molecular qubits. Indeed, the ones featuring a ground state Kramer doublet, well separated from the excited states by a significant crystal field splitting, can be described as systems with an effective spin $S^{eff} = 1/2$ [8, 33, 43] for qubit encoding (see fig. 1.2). In other cases, owing

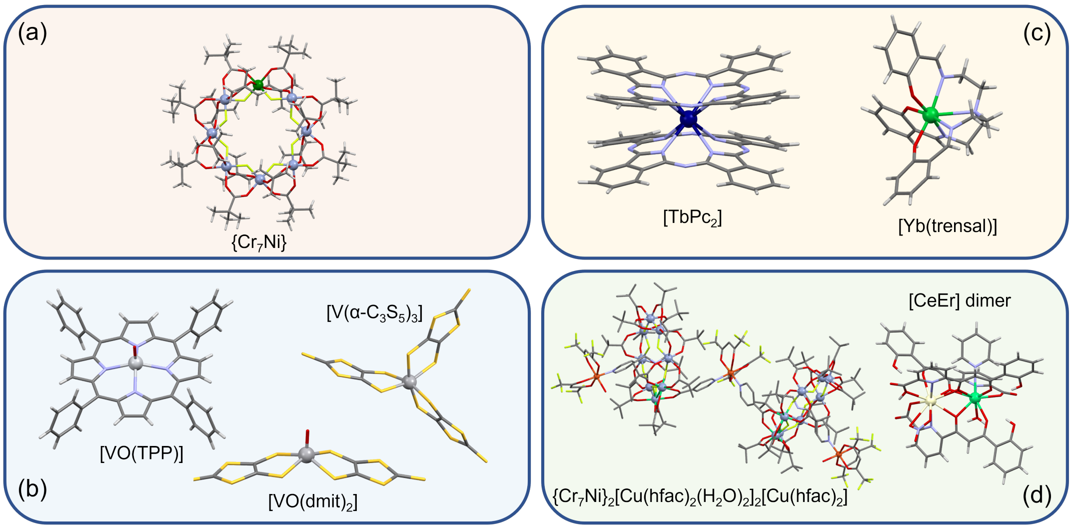

Figure 1.2: Structure of some of the most representative molecular qubit emerged for each class described in the main text. (a) {Cr$_7$Ni} for d-block cluster molecules. [3] (b) Vanadium and Vanadyl-based molecular qubit [4, 5, 6] (c) Terbium and Ytterbium based single ion qubit for rare-earth based class. [7, 8] (d) Two example of structure linking together more than one molecular qubit: a rare-earth based dimer [CeEr] [9] and a supramolecular chain decorated with two {Cr$_7$Ni} qubit linked with three copper based qudit [10]

an electronic spin $S > 1/2$, rare-earth based molecular qubits can open new possibilities for the expansion of the available computational space. This can be done by exploiting all the electronic spin states to encode more than a single qubit in each molecule [44] or a single qudit with several d states. [7, 45] In addition, rare-earth based systems embedding more than one asymmetric magnetic unit, as dimers [46] or trimers [47] have been proposed as single-molecule quantum hardwares with chemically coupled qubits. A similar approach has been pursued for chemically-linking together several transition metal clusters (i.e. rings) in supramolecular assembly (see examples in fig. 1.2). [10, 48, 49]
The final step for the actual implementation of molecular systems for quantum computation is the deposition of single objects and their wire-up in ”processor-like” structures. [42, 50, 51] Consequently, several studies have recently focused on the deposition of magnetic molecules on surfaces,[52, 53, 54] and on the coupling with systems that enable the manipulation and read-out of these single quantum objects,[55] e.g. with superconducting resonators or nanostructured junctions.[7]

1.2 Di Vincenzo criteria for Molecular Magnets

Molecular spin systems have been identified as a promising evolution of Noisy Intermediate-Size Quantum devices (NISQs) in order to push forward the capabilities of modern quantum technologies. [56, 57, 58]
Indeed, among a variety of possible systems studied in the past decades, as ultracold atoms,[59] photons,[60] superconducting circuits, [61, 62] Nitrogen and other

vacancies in solid crystals [63, 64, 65, 66] etc., molecular systems appear to be particularly suitable for the realization of quantum computation, [50, 51, 67, 68, 69]. This because they potentially fulfill the requirements set by Di Vincenzo and coworkers at the beginning of the millenium for the realization of a quantum computing platform. [70] Indeed, despite shorter with respect to other platforms (e.g. see [71]), the coherence times of many molecular qubits have been demonstrated to be long enough for the spin state manipulation without significant losses in coherence. [39] In the following, we will deepen each of these basic criteria for the actual realization of quantum information processing with physical platforms, highlighting how molecular spin systems satisfy these requirements and which aspects are currently the most critical. [42]

Scalable defined Qubit

Any system, to being exploited as a quantum bit, must be well characterized. This means that the parameter of its Hamiltonian, together with the coupling with other nearby qubits and with physical (photons, phonons, external fields, etc.) stimuli exploited for state manipulation, must be known with accuracy. Here, magnetic molecules have the advantages to be perfectly reproducible quantum objects, chemically synthetized and ”engineerable”, and easily characterized by bulk spectroscopic resonant techniques as Nuclear Magnetic Resonance and Electron Spin Resonance for single molecular-crystals (as detailed in sect. 2.1.1 and 2.1.2). [45, 72] Indeed, even for a large ensamble of individual molecules, such as a single crystal arrangement, the strain of the single molecule parameters (g-strain and D-strain as defined in [73]) is generally limited and results in a moderate broadening of spectral linewidth (centered around the resonant frequency for the mean parameter values). Thus, despite strain effects, for the purpose of electromagnetic field manipulations, molecules in a crystal can be considered practically identical. In addition, some of these molecules naturally posses a real (or effective) $S = 1/2$ ground state that outline a very simple realization of a qubit, since the two $m_S = \pm 1/2$ spin states naturally represent the $|0\rangle$ and $|1\rangle$ state that define the qubit state. [3, 5, 8]

Moreover, besides being well defined, a physical system for being applied as a qubit in a quantum hardware must be scalable. The scaling up, to expand the computational space, can be done in several ways. [50] By chemical design, for example, it is possible to create molecular structure that hosts more that one magnetic center, as dimers or trimers of qubits. [9, 47] Similarly, AF rings, such as [Cr_7Ni], are well known and thoroughly studied systems that feature the possibility to be bonded together in supramolecular structures, combined with other spin 1/2 complexes, [10, 48, 49, 74, 75, 76] and to be deposited on surfaces, retaining their magnetic properties. [53, 77, 78]
Another option, more recently developed, is to exploit the internal degrees of freedom of the system, to expand the computational space. The resulting quantum system can be seen as a qubit that feature more than two discrete states (*qudit*) or as a collection of effective two-level qubit embedded within the same molecular unit. This happen for example in $S > 1/2$ complexes, as the $S = 7/2$ of Gd^{3+} ions where $d = 8$ electronic spin levels are available. [43, 44] Rather than the electronic spins, the nuclear spin degrees of freedom of the molecule metal ion can be exploited as

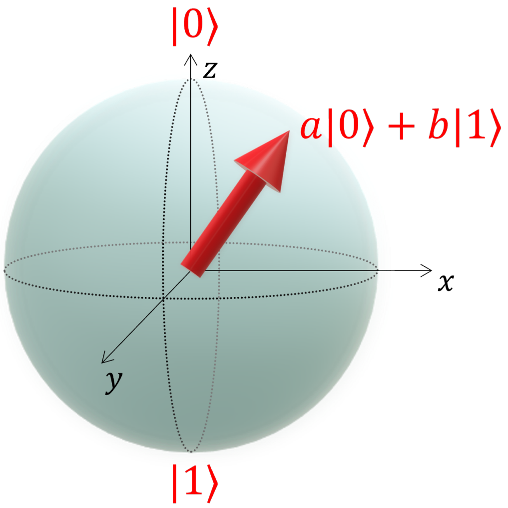

Figure 1.3: Bloch sphere showing the $|0\rangle$ and $|1\rangle$ basis of a qubit and all the possible linear combination $a|0\rangle + b|1\rangle$ filling the sphere surface.

another powerful resource for quantum computation, because of their isolation from the environment. The nuclear spin is indeed efficiently coupled to the electrons by Hyperfine interaction, resulting in a split of the level degeneracy and in a considerable speed up of the required manipulation time, regardless of its isolation from the environment. [4, 12, 45]
However, the advantages gained by increasing the number of electronic and nuclear states of the qudit is not sufficient to cover complex algorithm at single molecule level. Therefore, it is necessary to design multi-qubit platforms that enables the realization of two- or many-qubits gates. As proposed in this review [50] by S. Carretta *et al.*, a possibility provided by molecular qubits, thanks to their stability (even isolated) and chemical tunability, is to link the molecules chemically, by introducing switchable molecular linkers [76, 79] with ultra-fast switching-time (well below the hundred of ns, depending on the system) [76, 80], or physically by periodic deposition on active substrates, as superconducting on-chip resonator. [51, 81] Both these approaches allows to control coherently and individually the spin states. [50]

Qubit Initialization

From a computational point of view it is fundamental to have a clear picture of the qubits state at the beginning of the quantum information processing. This requirement is fulfilled if the physical system chosen for the computation can be easily initialized to a well known state. [70] For the case study of molecular magnets, initialization of the state can be easily achieved by cooling strategies. Given a molecular system with an effective spin $S = 1/2$ ground state, by naturally cooling at the mK temperature (rutinely achieved in NISQ platforms) we initialize the system by populating only the lowest energy spin state (fig. 1.4). [82] Fast initialization during computation processes can also be implemented by artificial cooling with projecting measurements into the desired state (e.g. with electromagnetic pulses). Another strategy suitable for molecular systems is the exploitation of cooling algorithms, [83] that allows to reach initialized states with pulse sequences, even at temperature in which all the states are thermally populated.

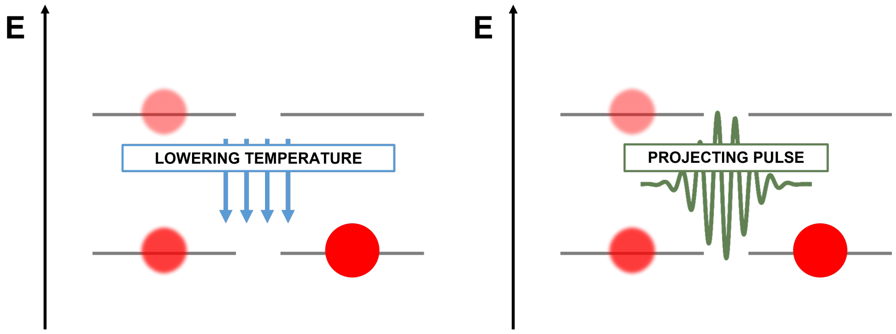

Figure 1.4: Scheme of two feasible cooling methods: thermal initialization (left), based on the slow cooling of the system to a temperature low enough to isolate the ground state from the excited ones; projection measurements (right), based on resonant e.m. pulses to rapidly project the system to a desired state (when the thermal population is negligible).

Qubit Coherence times

When the physical quantum system is placed in contact with the environment, the generic qubit state $|\psi\rangle = a|0\rangle + b|1\rangle$ degenerates, in a time we define as *decoherence time*, into the classical mixture described by the system density matrix $\rho = |a|^2|0\rangle\langle 0| + |b|^2|1\rangle\langle 1|$. Therefore, this decoherence time represents the lifetime of the quantum superposition state in which the qubit is placed for computational purposes.
For a proficient implementation of a quantum algorithm, the decoherence time of the physical platform on which it is implemented is not supposed to last longer than the entire computation itself. Indeed, the error induced on quantum states by decoherence can be corrected by error correction protocols, as proposed by Shor and Steane in 1995 and 1996 respectively. [84, 85] As a consequence, a good compromise for the decoherence of a system is set by the gate time ("Clock time" in [70]) if Quantum Error Correction (QEC) is applied. In order to implement proficiently any quantum gate, with negligible coherence losses due to relaxation, the system decoherence time must be longer than the time needed to implement a single gate (at least 10^4 times the "clock" for complete fault-tollerant computation [70]).
In this regards, magnetic molecules display unique advantages in tuning the relaxation mechanisms. The principal sources of decoherence come from the interaction of molecular spins with molecular vibrations (phonons), ligands nuclear spins and nearby electronic spins. [51] In the last decades, after the identification of these relaxation mechanisms, several strategies have been proposed to remarkably improve the decoherence times of molecular spins. The identification of the specific vibrational modes most strongly coupled with the spin (detrimental for quantum coherence) enables the suppression of those relaxation path by chemical optimization of the structure, e.g. by stiffening of ligands or groups removal (see sect. 4). [29, 30, 86] Moreover, decoherence effects induced by magnetic dipolar interaction have been remarkably reduced by exploiting strong magnetic dilution of molecular magnets in diamagnetic host structures. Finally, the interaction of electronic spins with the nuclei hosted into the molecule ligands structure cannot be easily suppressed, since

Hydrogen is the one that interfere the most and also the most abundant element in this class of molecules. However, the molecular structure can be optimized in order to reduce this contribution to relaxation by separate as much as possible the sources of decoherence and reducing their abundance (e.g. by deuteration or fluorination). [87]

Two different characteristic times are used to quantify the decoherence of a molecular qubit: T_1 and T_2. The first describe the interaction of the spin with the crystal structure (phonons) and it is then called spin-lattice relaxation time, while the second is called spin-spin relaxation time (or phase memory time) and accounts for the interaction with nearby spins, denoting the coherence time of the qubit. If we represent the spin motion of the system in the rotating frame (that allows us to get rid of nutation motion) as a Bloch sphere, the two relaxation mechanisms can be distinguished in two different motions as shown in figure 1.5.

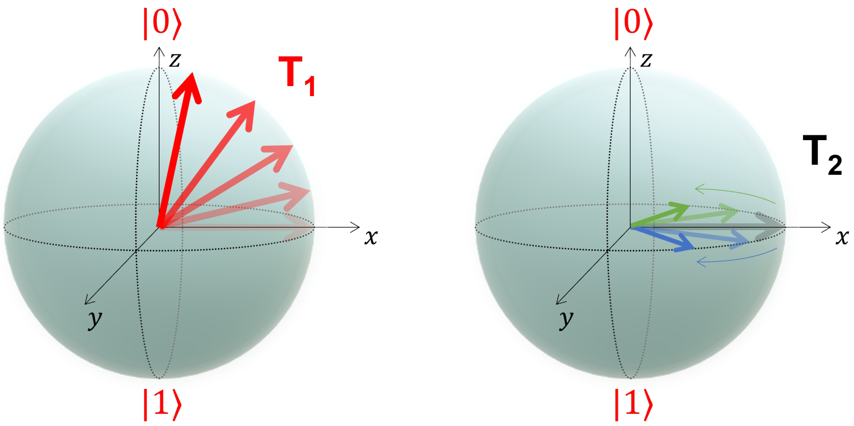

Figure 1.5: In a rotating frame system, precessing spins are represented by static Bloch sphere states. On the left, the system evolution from a perturbed in-plane state toward the thermodynamical equilibrium state $|0\rangle$, timed by T_1 relaxation time. On the right, the spin dephasing process over time (blue and green arrow represents spins with increased or decreased nutating frequency respectively), timed by T_2 dephasing time.

T_1 indicate the time needed for the system to re-establish the thermodynamical equilibrium after a perturbing stimulus, thus probing its coupling with the environment with which it exchanges energy. T_2 instead, indicates the decay rate of spin phase coherence within the system.

The possibility of implementing QEC, to protect the intrinsic fragility of quantum information, on a single multilevel quantum object represents another fundamental advantage of exploiting magnetic molecules as building blocks for quantum computation platforms. Indeed the *qudit* architecture, featuring multiple electronic or nuclear levels in a single molecule, enables the encoding of error protected ”logical” qubits into a single quantum object. [88] The aptitude to the implementation of QEC permits to release the strict requirements of extremely long relaxation time for molecular qubits, since the errors arising from dephasing can be mitigated by artificial corrections.

Universality

The fourth requirement set by Di Vincenzo for a prototypical quantum platform is the capability of implementing a Universal set of single and multi-qubit quantum gates. Since any quantum algorithm can be decomposed as a sequence of unitary transformations U_i,[89] the requirement is translated in identifying system in which is possible to implement any unitary transformation. When referring to a physical system, this condition is fulfilled if all the manipulation of the system can be identified by a set of Hamiltonians, that generate all the required unitary transformations $U_i = e^{iH_it/\hbar}$. Implementing the universal set of unitary transformation enable the simulation of any quantum time evolution of a system.

In this regard, molecular magnets are easily manipulable systems, where the molecule spin is pushed in interaction with an external electromagnetic (e.m.) stimulus to manipulate the electronic and nuclear states, without any significant constraint. Therefore, we can easily assume that given a magnetic molecule, its spin state can be manipulated in order to cover uniformly the whole Bloch sphere (fig. 1.3). The expansion of the computational space to multi-qubit gates, must go through the coupling of several molecular units. Therefore, as discussed for the scalability, to realize functional two and multi-qubit entangling gates, various molecular units must be wired up by coupling with external superconducting on-chip resonators [81] or by introducing switchable molecular couplers or linkers, sensible to external stimuli. [76, 79]

Qubit measurements

The final step of a quantum computation process is the readout of the result. The ideal physical platform must allow the measurement of the state of each specific qubit, without altering the state of the others.

This aspect is currently the most critical, since it potentially require the realization of a single molecule read out mechanism. Regarding the two possible architecture proposed above, having single-molecule qubits spatially separated and selectively coupled by planar resonators can allow the individual readout of a desired processor region with e.m. stimuli, without causing the collapse of the full system wavefunction. [50, 55] However, up to date this approach poses strict experimental limitation, due to the very weak spin-photon coupling (see [90]). Moreover, other platforms permits single qubit readout by electric transport measurements [42] or light irradiation. [91] Electric and magnetic field are also exploited for the readout of single molecule qudit, when the population of a single couple of levels can be extracted by resonant excitations, without affecting nearby states.

1.3 Spin Hamiltonian formalism

The Spin Hamiltonian approach enables the description of the static properties and coherent dynamics of magnetic molecules and it represents the most effective formalism for the interpretation of experimental data from spectroscopic techniques. Given a molecular system it permits to describe accurately the energy levels of the system and the hierarchy of magnetic interactions. [19, 92, 93]

This approach permits to describe all the contribution to the system Hamiltonian

in terms of spin-only operators, starting from the assumption that each ion in the molecule can be described as an effective spin $\hat{\mathbf{s}}_i$. The latest assumption is accurate for systems with quenched orbital angular momentum (as in almost all 3d systems), or when the orbital angular momentum is not quenched (as in 4f systems), but the crystal field splitting of the J quantum number yields a well isolated ground state multiplet.
The most general spin Hamiltonian describing molecular nanomagnets can be written adding several contributions: [19, 92]

$$\mathcal{H} = \mathcal{H}_{ex} + \mathcal{H}_{CF} + \mathcal{H}_{dip} + \mathcal{H}_{Z} + \mathcal{H}_{n}. \tag{1.1}$$

Here, $\mathcal{H}_{ex}$ represents the exchange interaction between mangnetic ions in the molecule, $\mathcal{H}_{CF}$ the effect of the local crystal field, and $\mathcal{H}_{dip}$ the through-space and through-bond dipolar coupling. Finally, $\mathcal{H}_Z$ models the Zeeman interaction with an external magnetic field and $\mathcal{H}_n$ defined as "fine structure" Hamiltonian, accounts for the interaction with the nuclear degrees of freedom. In this thesis we will mainly focus on single ion molecules with effective or intrinsic spin $S = 1/2$, in which the exchange interaction $\mathcal{H}_{ex}$ between ions in the molecule is absent and the crystal field excited states are ignored because of the considerable isolation from the ground state Kramer doublet. Moreover, by drastic dilution (up to 2%) of the MNM in its crystal structure with its diamagnetic analogue, the inter-molecular dipolar contribution to the spin Hamiltonian in 1.1 is also strongly suppressed. Therefore, for these systems, the spin Hamiltonian in 1.1 can be universally expressed in its reduced form:

$$\mathcal{H} = \mathcal{H}_Z + \mathcal{H}_n = \mathcal{H}_Z + \mathcal{H}_{Hyp} + \mathcal{H}_q + \mathcal{H}_{Zn}, \tag{1.2}$$

where in the fine structure Hamiltonian we made explicit all the contribution due to the interaction with the nuclear momentum: the Hyperfine coupling $\mathcal{H}_{Hyp}$, the nuclear quadrupolar interaction $\mathcal{H}_q$ and the nuclear Zeeman terms $\mathcal{H}_{Zn}$. These terms are expressed in terms of product of spin operators, as detailed in the following sections.

1.3.1 Electronic and Nuclear Zeeman interactions

The ground state Kramer degeneracy (for both systems characterized by real or effective spin 1/2 ground states) is removed by applying an external magnetic field $\mathbf{B}$, as a results of its Zeeman coupling with the electronic spin S. The Hamiltonian for the electronic Zeeman effect is thus given by the scalar product:

$$\mathcal{H}_Z = \mu_B \hat{\mathbf{S}} \cdot \mathbf{g}_S \cdot \mathbf{B}, \tag{1.3}$$

where $\mu_B = 1.3996 \times 10^4$ MHz/T is the Bohr magneton and $\mathbf{g}_S$ the spectroscopic splitting tensor, that varies for different ions and structures. If we focus on the coordinate reference frame of the molecule, the tensorial product is reduced as:

$$\mathcal{H}_Z = \mu_B (g_x S_x B_x + g_y S_y B_y + g_z S_z B_z), \tag{1.4}$$

with the field components $B_{x,y,z}$ defined in polar coordinates with respect to the molecule frame ($B_x = B \sin\theta \cos\phi$, $B_y = B \sin\theta \sin\phi$, $B_z = B \cos\theta$). When the field is instead applied along a specific molecular axis ($B_z\hat{\mathbf{z}}$), the electronic Zeeman term can be defined as a simple scalar contribution to the spin Hamiltonian $\mathcal{H}_Z = \mu_B g_z S_z B_z$. The Zeeman splitting induced with the applied field enables $|m_S = -1/2\rangle \rightarrow |m_S = 1/2\rangle$ electronic transitions at an energy that increase linearly with B and can be schematically depicted as in figure 1.6. For these electronic excitations, the typical energies involved are in the microwave range (mw).

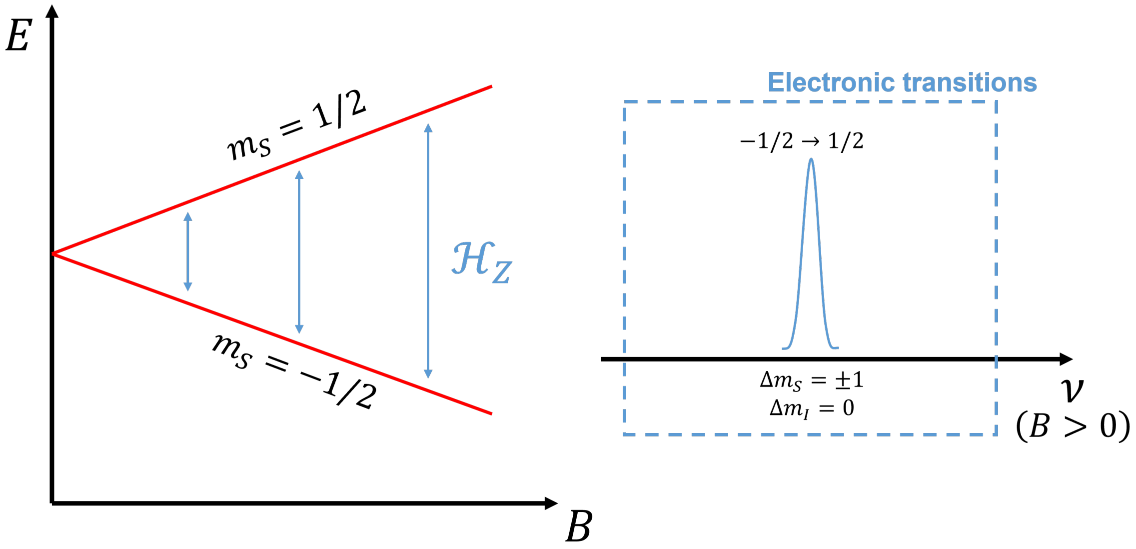

Figure 1.6: On the left, the S=1/2 electronic ground state degeneracy splitting induced by the electronic Zeeman interaction $\mathcal{H}_Z$, as a function of the field. On the right, the $|-1/2\rangle \rightarrow |1/2\rangle$ electronic transition enabled by this Hamiltonian contribution observed in a canonical spectral analysis

Regarding instead the fine structure Hamiltonian, we have to consider that also the nuclear magnetic moment couples with the external magnetic field B. This interaction is usually small compared to the other contribution to 1.2 and it can be easily written as the scalar product between B and the nuclear spin $\hat{\mathbf{I}}$:

$$\mathcal{H}_{Zn} = \mu_N g_N \hat{\mathbf{I}} \cdot \mathbf{B}. \tag{1.5}$$

Here the proportionality constants are the scalar nuclear magneton μ_N ($\mu_N = 7.6226$ MHz/T) and the ion dependent isotropic spectroscopic splitting g_N . This terms introduces a small isotropic splitting of the nuclear states within the same electronic multiplets ($\Delta m_S = 0$), enabling $\Delta m_I = \pm 1$ transitions as shown in figure 1.7. Differently from what outlined for the electronic Zeeman splittings, nuclear state excitation energies falls typically in the radiofrequency range (rf).

1.3.2 The Hyperfine interaction

Finally, for a single ion magnetic molecule, the most relevant contribution to the fine structure Hamiltonian is constituted by the interaction between the nuclear and electronic magnetic moments, mediated by the local steady electronic magnetic field generated at the nucleus site. This interaction can be expressed in terms of spin

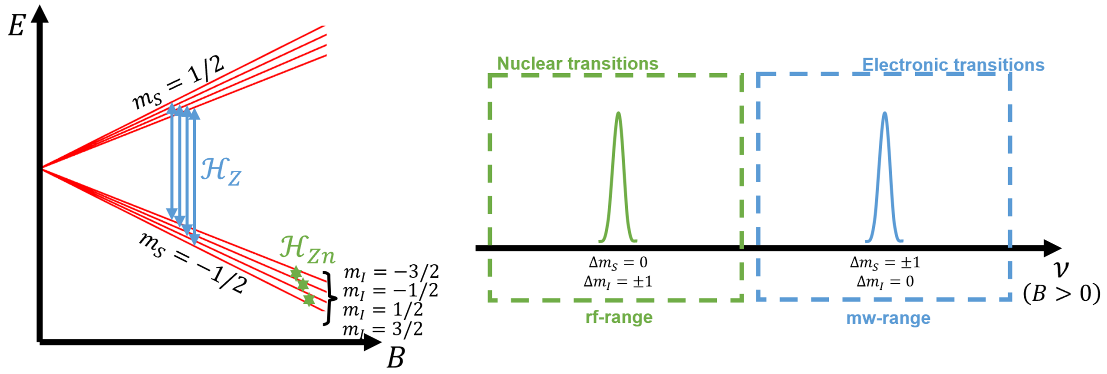

Figure 1.7: On the left, the nuclear degeneracy splitting induced by nuclear Zeeman interaction $\mathcal{H}_{Zn}$, as a function of the field in a $S = 1/2$, $I = 3/2$ system. On the right, the m_I degenerate $|3/2\rangle \rightarrow |1/2\rangle$, $|1/2\rangle \rightarrow |-1/2\rangle$, $|-1/2\rangle \rightarrow |-3/2\rangle$ nuclear transition enabled within the same electronic multiplet $\Delta m_S = 0$. The spectra is extended to display both electronic and nuclear transitions.

operators as the quadratic form between the electronic $\hat{\mathbf{S}}$ and the nuclear $\hat{\mathbf{I}}$ spin.

$$\mathcal{H}_{Hyp} = \hat{\mathbf{I}} \cdot \mathbf{A} \cdot \hat{\mathbf{S}}. \tag{1.6}$$

The tensor $\mathbf{A}$ is called Hyperfine tensor and it describes the electron-nucleus interaction. For spin $S = 1/2$ systems it arises from two different mechanism: the dipolar magnetic interaction between S and I and the contact interaction of the electron spin density effect on I. [19] By assuming that the principal axis of the molecule reference frame are coincident with the one of the Hyperfine tensor, the Hamiltonian can be rewritten as:

$$\mathcal{H}_{Hyp} = A_x S_x I_x + A_y S_y I_y + A_z S_z I_z. \tag{1.7}$$

For systems with axial symmetry this expression is usually further simplified by defining a transversal $A_\perp$ and longitudinal $A_\parallel$ components of the Hyperfine tensor:

$$\mathcal{H}_{Hyp} = A_\perp (S_x I_x + S_y I_y) + A_\parallel (S_z I_z). \tag{1.8}$$

The energy involved in the Hyperfine splittings is typically smaller than the electronic Zeeman effect. Therefore, for sufficiently high magnetic fields we observe a splitting of the nuclear multiplet m_I confined within each electronic $m_s = \pm 1/2$ lines. The transverse and longitudinal components of the Hyperfine tensor with respect to the applied field contributes differently to the m_I splitting, as detailed in figures 1.8 and 1.9. For intermediate magnetic field applied along the system z axis $B_z\hat{\mathbf{z}}$, the component $A_\parallel$ induces an equivalent field-independent splitting of all the m_I levels, thus without altering the degeneracy of the $\Delta m_I = \pm 1$ transitions. However, at zero field $A_\parallel$ splits the states with concordant sign for m_S and m_I from the states in which m_S and m_I have discordant signs, e.g. $|\pm 1/2, \pm 3/2\rangle$ from $|\pm 1/2, \mp 3/2\rangle$. As a consequence, the degeneracy of the electronic transitions $\Delta m_S = \pm 1$ for different m_I values is broken and all the Hyperfine lines are split in the ESR regime (see fig. 1.8).
If we now consider an Hyperfine tensor with axial symmetry, also a transverse $A_\perp$

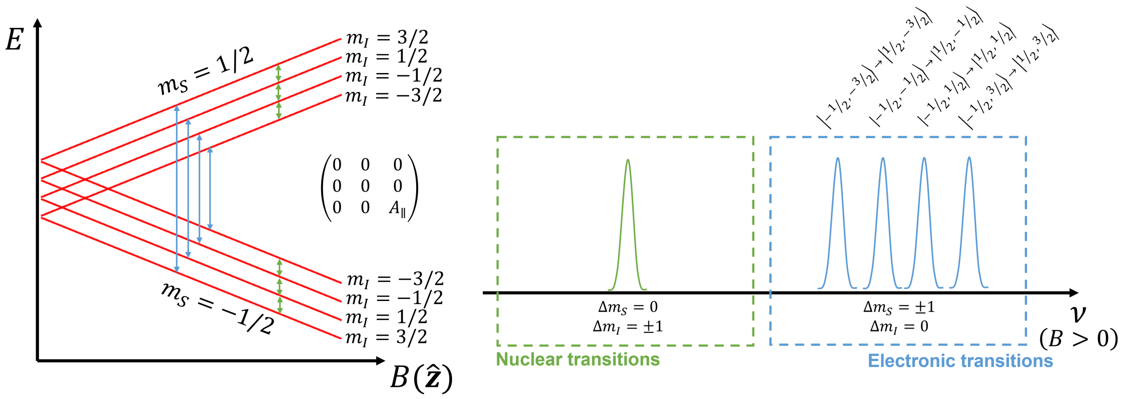

Figure 1.8: On the left the splitting effect induced by the parallel Hyperfine component $A_\parallel$ when the external field is applied parallel to it; On the right the expected spectra showing the degenerate nuclear and the resolved electronic transitions, arising from the Hyperfine tensor expressed in inset.

contribution will appear. This contribute at low field to a mixing of the electronic and nuclear wave functions and at intermediate field introduces anisotropy in the splitting of the m_I states, acting as a pseudo-quadrupolar contribution. Both the two aspect will be developed in the following subsections. The effect of an axial hyperfine tensor is shown in figure 1.9, where all the nuclear transitions of both electronic multiplets are also resolved.

The dominant contribution in the matrix element of the NMR transitions can vary

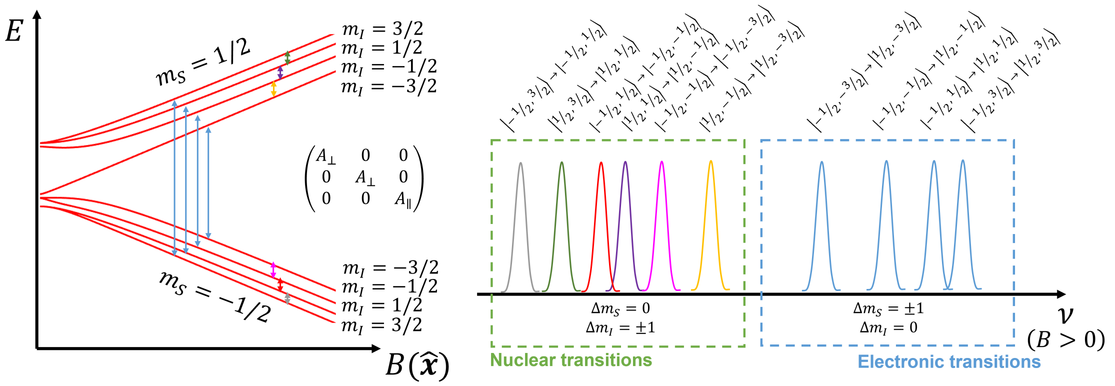

Figure 1.9: On the left the splitting effect induced by an axial Hyperfine tensor (inset) when the external field is applied perpendicular to the strongest component; On the right the expected spectra where all the nuclear and electronic transitions are resolved.

as a function of the increasing applied field, e.g., when the Zeeman $g_I \mu_N$ overcome the $A_\perp$ contribution. The Hamiltonian hierarchy change can results in crossings of the levels and of transitions energies within a nuclear multiplet m_I or even from different electronic m_S multiplets.

1.3.3 The Nuclear quadrupolar coupling

When the nuclear spin of the magnetic ion is $I \geq 1$, the nuclear quadrupole moment interacts with the electric field gradient arising at the nucleus. The gradient, responsible for this term, is generated by the anisotropy in the electric charge distribution on the paramagnetic ion. This interaction, can be expressed in terms of spin operators as the quadratic form:

$$\mathcal{H}_q = \hat{\mathbf{I}} \cdot \mathbf{P} \cdot \hat{\mathbf{I}}, \tag{1.9}$$

where $\mathbf{P}$ is the quadrupolar tensor, generally oriented along the principal axis of the other Hamiltonian terms ($\mathbf{A}$, $\mathbf{g}$). When referring to the principal axis the quadrupolar Hamiltonian $\mathcal{H}_q$ can be rewritten in the simpler form:

$$\mathcal{H}_q = P_x I_x^2 + P_y I_y^2 + P_z I_z^2, \tag{1.10}$$

When considering the simple case of a quadrupolar tensor with component only along $\hat{z}$ axis, in zero field (ineffective Zeeman interaction) the nuclear states with different absolute value of $|m_I|$ are splitted by the quadrupolar interaction, while the states that differ only for the m_I sign are kept degenerate, as shown in figure 1.10.

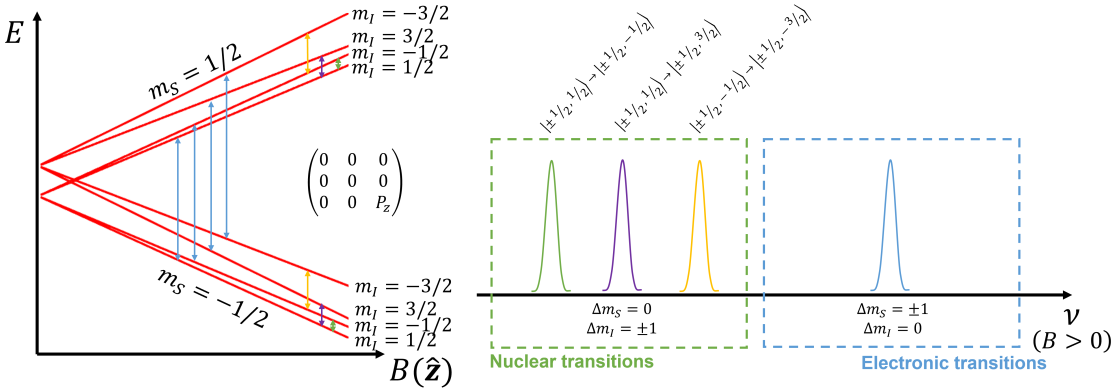

Figure 1.10: On the left the splitting of the state with different $|m_I|$ induced by a Quadrupolar coupling $\mathbf{P}$ with components only along $\hat{z}$ when the external field is applied parallel to it; on the right the resulting spectral components for the spin Hamiltonian with only Quadrupolar, electronic and nuclear Zeeman couplings. The nuclear transitions are partially resolved, while the interaction leaves the electronic gaps unperturbed.

This contribution to the spin Hamiltonian is thus fundamental, together with the pseudo-quadrupolar of section 1.3.4, to distinguish the excitation energy of each nuclear transition, enabling the possibility to selectively address each nuclear and electronic state of the system. [4]

1.3.4 Second order effects

Electro-nuclear mixing

In the low field region, the level diagram for an axial Hyperfine coupling in figure 1.9 shows a wide anticrossing that induce a strong curvature of the levels, sympthomatic of a mixing between the electronic and nuclear degrees of freedom of the system wavefunction. This electro-nuclear mixing [45] derives directly from the component of the Hyperfine field perpendicular to the applied field. Indeed, assuming that the magnetic field is applied along the $\hat{z}$ axis, the system eigenstates $|\Psi_{m_S,m_I}\rangle$ can be easily calculated analytically to the first order of perturbation theory in the limit of $g_z\mu_B B \gg |A_\perp|$. Neglecting the nuclear Zeeman and quadrupolar coupling, the system wave function results:

$$|\Psi_{m_S,m_I}\rangle = |m_S, m_I\rangle \pm \frac{\alpha A_\perp}{g_z\mu_B B + (m_I + 1/2)A_\parallel}|m_S \mp 1, m_I \pm 1\rangle, \tag{1.11}$$

where the first ket is the unperturbed wave-function while the second one takes into account the effect of the transverse $A_\perp$ to the mixing ($\alpha = \langle m_S \mp 1, m_I \pm 1|S_x I_x + S_y I_y|m_S m_I\rangle$). Consequently, the matrix element of the allowed NMR transitions $|\Psi_{m_S,m_I}\rangle \rightarrow |\Psi_{m_S,m_I\pm1}\rangle$, for an applied field along $\hat{z}$ are composed by a pure nuclear excitation $\mu_N g_I$ summed to a second component dependent on $A_\perp$ and arising from the electro-nuclear mixing of the wavefunction described above:

$$\begin{aligned}
&\langle\Psi_{m_S,m_I}|g_I\mu_N I_x + g_x\mu_B S_x|\Psi_{m_S,m_I\pm1}\rangle = \qquad (1.12)\\
&= g_I\mu_N\langle m_I|I_x|m_I \pm 1\rangle \pm \frac{\alpha A_\perp}{g_z\mu_B B + (m_I + 1/2)A_\parallel} g_x\mu_B\langle m_S \mp 1|S_x|m_S\rangle\\
&\underset{\substack{(B\gg 0\\ g_x\approx g_z)}}{\approx} \alpha(g_N\mu_N \pm \frac{A_\perp}{2B}).
\end{aligned}$$

The mixing of the electronic and nuclear degrees of freedom in the system wavefunction is fundamental for the purpose of studying the NMR response of molecular qubits, because of the strong enhancement of the NMR transition matrix elements caused by the $A_\perp$ contribution: $\frac{A_\perp}{2B} \gg g_I\mu_N$, even at field where the mixing is small ($B \sim 0.2$ T). As a consequence, also the manipulation time of the nucleus becomes very short.

Pseudo-quadrupolar contribution

As already mentioned above, the transverse component of the Hyperfine interaction with respect to the applied field acts as a pseudo-quadrupolar contribution to the energy spectra, thus contributing to the degeneracy-breaking of the nuclear transition energies.

This effect is a fundamental resource for the manipulation of spin states in this class of systems. Indeed, by retaining only the secular terms in the spin Hamiltonian (i.e. large B_0 or small transverse Hyperfine), the difference between the gaps of m_I nuclear transitions, fundamental for their selective addressability, is due to the nuclear quadrupolar interaction, which however is small for 3d-ion based molecular magnets (see sect. 3.2 and 3.3). Nevertheless, when the Hyperfine component transverse to the applied field B_0 is significant, up to the second order perturbation theory with respect to the Zeeman term, it induces a non negligible splitting of the m_I multiplets, analogous to the one induced by the quadrupolar coupling. [4]

If we restrict to the lowest electronic m_S multiplet, the low-energy effective Hamiltonian can be expressed as the sum of a pseudo-Zeeman contribution $\mathcal{H}_{Pseudo-Z}$ and an effective quadrupolar coupling $\mathcal{H}_{Pseudo-q}$:

$$\mathcal{H}^{eff} = \mathcal{H}_{Pseudo-Z} + \mathcal{H}_{Pseudo-q}, \tag{1.13}$$

where, if B_0 is applied along $\hat{x}$ and perpendicular to A_z, the pseudo-Zeeman contribution has the form:

$$\mathcal{H}_{Pseudo-Z} = B^{eff} I_x = \left[\frac{A_x}{2} + \frac{\left(A_z^2 + A_y^2\right) g_N \mu_N + 2A_y A_z g_S \mu_B}{8B_0(g_S^2\mu_B^2 - g_N^2\mu_N^2)} \right] I_x, \tag{1.14}$$

while the effective quadrupole interaction can be written as

$$\mathcal{H}_{Pseudo-q} = P_x^{eff} \left[I_x^2 - \frac{I(I+1)}{3} \right] + P_r^{eff} \left(I_z^2 - I_y^2 \right), \tag{1.15}$$

with

$$P_x^{eff} = \frac{\left(A_z^2 + A_y^2\right) g_S \mu_B + 2A_y A_z g_N \mu_N}{8B_0(g_S^2\mu_B^2 - g_N^2\mu_N^2)}, \tag{1.16}$$

$$P_r^{eff} = \frac{\left(A_y^2 - A_z^2\right) g_S \mu_B}{8B_0(g_S^2\mu_B^2 - g_N^2\mu_N^2)}. \tag{1.17}$$

These two effective quadrupolar couplings results to be larger than the intrinsic quadrupole interaction **P** for some 3d-ions, as for the largely studied Vanadium complexes.[4, 5, 6, 35] The advantage of a secondary mechanism inducing the splitting of the m_I states, acting analogously to the zero-field splitting for the electronic states, is to expand significantly the class of complexes suitable for quantum computing applications. Indeed, it removes the strict requirement of a strong intrinsic quadrupole to realize systems displaying selective addressability of states, since it can be achieved also by properly designed hyperfine tensors and applied magnetic fields.

1.4 Lindblad Master equation

To understand and reproduce the incoherent spin dynamics of molecular qubits it is fundamental to consider their interaction with the environment, which plays a key role in triggering the relaxation and decoherence processes. Therefore the spin system S must be treated as an open quantum system, since its evolution depends on both the internal dynamics and the coupling with the environment.
Given a Spin quantum system S coupled via an interaction $\hat{V}$ with the environment B, the total Hamiltonian describing the closed Spin+environment system have the form:

$$\hat{H}_{tot}(t) = \hat{H}_s \otimes \hat{I}_B + \hat{I}_S \otimes \hat{H}_B + \hat{V}(t), \tag{1.18}$$

where the open Spin system Hamiltonian $\hat{H}_S$ and the environment $\hat{H}_B$ act respectively on their subspaces. For a closed quantum system the time evolution can be accounted by an appropriate equation of motion of the system density matrix $\hat{\rho}$: the *Liouville-von Neumann* equation.

$$\frac{d}{dt}\hat{\rho}(t) = -\frac{i}{\hbar} \left[\hat{H}, \hat{\rho}(t) \right], \tag{1.19}$$

with $\hat{\rho}(t_0) = \sum_i w_i \left|\psi_i(t_0)\right\rangle \left\langle\psi_i(t_0)\right|$, where w_i are the weigth of the state vectors $\left|\psi_i(t_0)\right\rangle$. However, treating the whole environment system is typically unaffordable, since it hosts infinite and non-easily definable degrees of freedom. Therefore, it is convenient to describe the system by focusing on the reduced Hilbert space of the spin S system, which contains all the spin dynamics information. The operators $\hat{X}$ acting on this reduced Hilbert space are defined by means of the partial trace formalism:

$$\langle \hat{X} \rangle = tr_S \left\{ \hat{X} \hat{\rho}_S \right\}, \tag{1.20}$$

where the reduced density matrix $\hat{\rho}_S = tr_B(\hat{\rho})$ is obtained from the partial trace of the total density matrix, over the environment degrees of freedom. The equation of motion for the open system becomes then:

$$\frac{d}{dt}\hat{\rho}_S(t) = -\frac{i}{\hbar} tr_B \left[\hat{H}_{tot}, \hat{\rho}(t) \right]. \tag{1.21}$$

If we assume that the correlation time of the environment dynamics are negligibly shorter then the time scale of the system correlation (Markov approximation), and that the time dependent coupling $\hat{V}$ is a small perturbation of the system (weak-coupling approximation), we can then formulate the quantum master equation in interaction picture as the *Lindblad* equation:

$$\frac{d}{dt}\hat{\rho}_S(t) = -\frac{i}{\hbar} \left[\hat{H}_{tot}, \hat{\rho}_S(t) \right] + \mathcal{D}(\hat{\rho}_S(t)), \tag{1.22}$$

where the first term of the equation represents the unitary coherent dynamics generated by the system Hamiltonian $\hat{H}$ unperturbed by B, while the second term $\mathcal{D}(\hat{\rho}_S(t))$ (*Dissipator*) accounts for the non-unitary effect of the interaction with the environment and is written as: [94]

$$\mathcal{D}(\hat{\rho}_S(t)) = \sum_{m,n} \left[L_{m,n}\hat{\rho}_S(t)L^{\dagger}_{m,n} - \frac{1}{2}(L^{\dagger}_{m,n}L_{m,n}\hat{\rho}_S(t) + \hat{\rho}_S(t)L^{\dagger}_{m,n}L_{m,n}) \right], \tag{1.23}$$

with L_m, n defined as Lindblad operators.
Spin systems are subject to the pure dephasing mechanism, due to the coupling with the environment. For taking into account the non-unitary effect of dephasing, the Lindblad operators L_m, n must be written as: [94, 95]

$$L_{m,n} = \delta_{m,n}\sqrt{\frac{\gamma_m}{2}}|m\rangle\langle m|, \tag{1.24}$$

and the Lindblad equation becomes: [94]

$$\begin{aligned} \frac{d}{dt}\hat{\rho}_S(t) = & -i \left[\hat{H}_{tot}, \hat{\rho}_S(t) \right] + \\ & \sum_{m,n} \gamma_m \delta_{m,n} \left[|m\rangle\langle m|\hat{\rho}_S(t)|m\rangle\langle m| - \frac{1}{2}(|m\rangle\langle m|\hat{\rho}_S(t) + \hat{\rho}_S(t)|m\rangle\langle m|) \right], \end{aligned} \tag{1.25}$$

where $|m\rangle$ are the eigenstate of the system. This dissipator causes the decoherence of the off-diagonal elements of the density matrix $\rho_{m,n}(t)$ with a rate $\tau^{m,n} = (\gamma_m + \gamma_n)/2)$, whilst the diagonal nature of the Lindblad operator keeps unchanged the diagonal population $\rho_{m,m}(t)$ (no energy exhange between system and environment).

For the nuclear spin system that will be discussed in section 3, the eigenstates are labelled by the corresponding component of the nuclear spin $|m_I\rangle$ and the dephasing rate corresponds to the nuclear phase memory time $\tau^{m,n} = 1/T_2^{m_I,m'_I}$. [4] Moreover, for the case-study of molecular qubits it could be useful to simulate the effect of an external stimulus on a spin system already coupled with the environment. This can be simply achieved by adding a time dependent term $\hat{H}_1(t)$ to the Hamiltonian of the master equation that rules the unitary evolution of the system density matrix. The Lindblad master equation becomes:

$$\begin{aligned} \frac{d}{dt}\hat{\rho}_S(t) = &- i\left[\hat{H}_0 + \hat{H}_1(t), \hat{\rho}_S(t)\right] + \\ &\sum_{m,n} \gamma_m \delta_{m,n} \left[|m\rangle\langle m|\hat{\rho}_S(t)|m\rangle\langle m| - \frac{1}{2}(|m\rangle\langle m|\hat{\rho}_S(t) + \hat{\rho}_S(t)|m\rangle\langle m|)\right]. \end{aligned} \tag{1.26}$$

By numerically solving this master equation by using realistic parameters of the spin Hamiltonian, the time dependent perturbation and the dephasing rates gives fundamental insight into the dynamics of prototypical molecular qubits.

Chapter 2

Experimental techniques

The experimental study of molecular nanomagnets in this thesis has been done by exploiting several techniques: resonant techniques, such as broadband Nuclear Magnetic Resonance, Electron Paramagnetic Resonance, and scattering techniques, such as neutron and X-rays inelastic scattering. In the following sections we will give a brief introduction to all of them.

2.1 Resonance techniques

In this section we will focus on two resonance techniques which have several similarities, from the poin of view of the theoretical background, and one important difference, the physical target. Both Nuclear Magnetic Resonance (NMR) and Electron Paramagnetic Resonance (EPR) are in fact resonant experimental techniques exploiting the interaction of magnetic moments with an external electromagnetic irradiation, perturbing the system. In the first case, the magnetic moments $\boldsymbol{\mu}_I = \mu_N g_N \mathbf{I}$ arise from the nuclear spin I of the system, while, for the second technique, the focus is on the magnetic moments $\boldsymbol{\mu}_e = \mu_s \mathbf{g}_s \cdot \mathbf{S}$ arising from the unpaired electrons spin S. Since we are dealing with resonant techniques, this implies that the electromagnetic irradiation must be tuned to a natural frequency of the system in order to be effective, which is, depending on the different physical target, the frequency of the magnetic moments gyroscopic precession under an external static magnetic field. These magnetic resonance frequencies falls typically in the radio-frequency (rf) region for the nuclei, while for the electrons in the microwave (mw) one, thus, we will refer to rf and mw irradiation depending if we are describing an NMR or an EPR experiment. In the following chapter we will discuss in details the Broadband NMR (sect. 2.1.1) and EPR (sect. 2.1.2) techniques.

2.1.1 Nuclear Magnetic Resonance

In the nuclear magnetic resonance technique we are dealing with nuclear magnetic moments μ_I, arising from the atomic ground states of several nuclei featuring $I \neq 0$. Because of the small magnetic moment μ_N (compared to the electronic one $\mu_e/\mu_I \approx 10^{3\div4}$), and the absence of a strong exchange mechanism, nuclear ferromagnetism is limited to the mK temperatures. Thus, in a NMR experiment under applied static field, the target system will be a spin paramagnets featuring several states E_m (depending on the spin I) corresponding to the different values

of the quantum number $m_I = I_z$ of the spin quantized along the applied field. The population of these nuclear states will be governed by the Boltzmann statistic $P_m \propto e^{-E_m/kT}$. Nuclear magnetic resonance is therefore the spectroscopic technique that enables to study these energy levels and the transitions induced among them by a resonant rf radiation. There exist two possible resonant excitation methods: field-sweep and frequency-sweep. Here we focus on the frequency-sweep method, used for the NMR investigations of this thesis. It consists in targeting the system with a rf-field of variable frequency. When this frequency ν_{rf} matches one of the characteristic gaps of the nuclear states structure $\Delta \approx h\nu_{rf}$, the transition probability is enhanced and the process detected. The detection of these energy gaps and the measurement of the spin relaxation processes towards equilibrium after the rf irradiation are the information commonly accessible from an NMR experiment on a magnetic nucleus. The NMR experiment can be interpreted in two different ways: as a forced precession of the nuclear magnetic moment in a rf field (from F. Bloch [96, 97, 98]) or as the result of the competition between the relaxation to the thermal equilibrium (Boltzmann populations) and the excitation induced by the electromagnetic irradiation. [92, 99]
In a quantum mechanical approach, the eigenvalues of the angular momentum $\hat{\mathbf{I}} = \hbar\mathbf{I}$ component I_z along the external field direction $\hat{\mathbf{z}}$, coincide with all the $2I+1$ possible configurations $m = -I, -I+1, ...I-1, I$. Thus, given the relationship between the magnetic moments and the angular momentum components $\langle Im|\mu_z|Im'\rangle = \mu_N g_N \langle Im|I_z|Im'\rangle$, the effect of an applied external static field $H_0\hat{\mathbf{z}}$ is the Zeeman interaction energy:

$$\mathcal{H} = \boldsymbol{\mu} \cdot \mathbf{B} = \gamma\hbar B I_z = \mu_N g_N B I_z, \tag{2.1}$$

that splits the nuclear spin states, characterized by the eigenvalues E_m for each m state:

$$E = -\mu_N g_N B m. \tag{2.2}$$

To induce excitations between these Zeeman levels and thus performing the NMR experiment, the system must be targeted with a perturbation $\hbar\omega$ resonant to one of the gaps within the E_m states.

$$\hbar\omega = E_{m'} - E_m. \tag{2.3}$$

In this case, the perturbation consists in a rf-field $\mathbf{B}_1 \perp \mathbf{B}_0$ that induces an additional interaction term $\mathcal{B}_1 = -\mu_N g_N B_{0,x} I_x cos(\omega t)$ that drives the transition between close nuclear states $m \to m \pm 1$ with $\Delta m = \pm 1$. By considering the case of a spin $I = 1/2$ system, the transition probability between the two m_I nuclear states is defined as $|\langle + |I_x| - \rangle|^2$, where $|+\rangle$ and $|-\rangle$ correspond to the states of component $m_I = \pm 1/2$. For stimulating the transition it is necessary to have a population difference between the two target states. Indeed, by defining the number of spin per level as $N_\pm(t)$ and the transition rate as W, the excited spin per unit time is defined by the product $N_\pm(t)W$ and the states population variation is described by the rate equation:

$$\frac{dN_\pm}{dt} = WN_\mp(t) - WN_\pm(t), \tag{2.4}$$

whose solution in terms of population difference $n(t) = N_+(t) - N_-(t) = n_0 e^{-2Wt}$ gives an exponential decay toward a condition in which there is no population difference. Indeed, the time dependent energy of the system $E(t) = N_- E_- + N_+(E_+ + \hbar\omega)$

saturates with an absorption rate:

$$dE/dt = \hbar\omega W n(t) = n_0\hbar\omega(We^{-2Wt}). \tag{2.5}$$

However, after the rf-stimulus is removed, the nuclear spin system interacts with the thermal bath environment and relaxes towards the initial thermal equilibrium state, following a Boltzmann distribution:

$$\frac{N_-}{N_+} = e^{-\frac{\Delta E_{+,-}}{kT}}. \tag{2.6}$$

Thus, the relaxation of the population difference induced by the rf field, which is governed by the interaction with the environmental thermal bath (lattice), is modeled by a relaxation rate $1/T_1$ called spin-lattice relaxation rate:

$$n(t) = n_0(1 - e^{-t/T_1}). \tag{2.7}$$

This, combined with the rate equation 2.4, gives an energy absorption rate from the nuclear spin system:

$$\frac{dE}{dt} = n_0\hbar\omega\left(\frac{W}{1+2WT_1}\right). \tag{2.8}$$

The nuclear spin time evolution during and after the rf-manipulation can be described by the phenomenological Bloch equations for the nuclear magnetization. [96, 97, 98] This approach enables the definition of the relaxation constants that are usually employed to model spin relaxation. We start from a nuclear spin system in its thermodynamical equilibrium when a static field $\mathbf{B} = B\hat{\mathbf{z}}$ is applied. This condition corresponds to a null transverse magnetization $M_{x,y} = 0$ and a saturated longitudinal magnetization $M_z = M_0 = \chi_n H_0$, with χ_n nuclear susceptibility. The classical precession of the nuclear spins in this field, plus a relaxation term, is described by the Bloch equations:

$$\begin{cases} \frac{dM_z}{dt} = \mu_N g_N(\mathbf{M}\times\mathbf{B})_z + \frac{M_0 - M_z}{T_1} \\ \frac{dM_{x,y}}{dt} = \mu_N g_N(\mathbf{M}\times\mathbf{B})_{x,y} + \frac{M_0 - M_{x,y}}{T_2} \end{cases}, \tag{2.9}$$

where T_1 and T_2 account for the relaxations of the longitudinal and transverse magnetization, respectively.

When a rf exciting field $\mathbf{B}_1 \perp \mathbf{B}$ is added to the spin system, in a reference frame $\hat{x}_r\hat{y}_r\hat{z}$ rotating at the same frequency of $\mathbf{B}_1$, the nuclear spins time evolution is still described by a precession, but in this configuration the precession is around an effective field $B_{eff} = B_1\hat{\mathbf{x}}_r + (B - \omega/\gamma)\hat{\mathbf{z}}$, sum of the two applied fields. The Bloch precession equations become:

$$\begin{cases} \frac{dM_z}{dt} = \mu_N g_N B_1 M_y - \frac{M_z - M_0}{T_1} \\ \frac{dM_x}{dt} = (\mu_N g_N B_0 - \omega)M_y - \frac{M_x}{T_2} \\ \frac{dM_y}{dt} = -(\mu_N g_N B_0 - \omega)M_x + \mu_N g_N B_1 M_z - \frac{M_x}{T_2} \end{cases}. \tag{2.10}$$

As already outlined above, the relaxations times of the longitudinal $\hat{z}$ and transverse $\hat{x}, \hat{y}$ magnetization components are kept distinct. This because these constants represent two different processes. As seen for the definition of the absorption rates

for a thermal-like relaxation process, T_1 is related to the recovery of the thermal equilibrium of the nuclear state population, induced by the coupling with a thermal bath constituted by the electronic and crystal environment of the nuclear spins (spin-lattice relaxation). Conversely, the transverse relaxation consists in a dephasing that occurs during spin precession in the xy-plane (spin-spin relaxation).
If the rf field is a short pulse of duration t_P (short enough to avoid simultaneous decoherence) resonant with the system natural frequency $\omega = \mu_N g_N B$, the effect of the perturbation is a nutation of an angle $\theta = \mu_N g_N B_1 t_P$ around the effective field $B_1\hat{\mathbf{x}}$. Consequently, by tuning t_P, it is possible to realize $\pi/2$ rotations onto the xy plane or π inversion of the nuclear magnetization. In particular, after a $\pi/2$ pulse the nuclear magnetization evolves following Bloch equations:

$$M_{xy}(t) = M_{xy}(0)e^{-t/T_2} \tag{2.11}$$

which is the so-called free induction decay that follows the resonant perturbation. The decoherence induced by static fields once the nuclear magnetization is on the xy plane can be refocused by applying a second π pulse to the spins system that reverse the dephasing, generating an echo-like signal from the refocusing of the spin precession (dynamical contributions are irreversible phenomena that defines the intrinsic T_2). Conversely, the longitudinal relaxation consist in a recovery of the initial state M_0 by the exchange of energy with the thermal bath. From the Bloch equations the recovery follows the trend:

$$M_z(t) = M_0 + (M_z(0) - M_0)e^{-t/T_1} \tag{2.12}$$

T_2 and T_1 can be measured experimentally by proper pulse sequence on well defined spin transitions (at fixed ω). By refocusing the echo with a $\pi/2 - \tau - \pi$ pulse sequence for example, as a function of the delay τ we can measure the decay of the transverse magnetization (T_2 spin relaxation). By "heating" the nuclear spin system with a pulse train to the most disordered state and then refocusing after a delay τ, we measure the recovery of the longitudinal saturation in a "cooling-down"-like process ($P_{train} - t - \pi/2 - \tau - \pi$). Moreover, by collecting the resonance signals over a wide frequency range, from the collected NMR spectra we can link the energy gaps of the excited transitions to the levels structure of the spin Hamiltonian, and fit its parameters, as outlined in section 1.3.

HyReSpect broadband spectrometer

The paramagnetic state of an ordinary magnetic material is characterized by a spin dynamics that features fast Hyperfine field fluctuations. Being these fluctuations faster then the nuclear Larmor ω_L frequency, the resulting nuclear relaxation, correlated to the hyperfine field fluctuations, is ultra-fast and prevent the detection of a resonance signal. Molecular NanoMagnets, however, at low temperatures are characterized by spin-lattice relaxation rates much longer than the rather short time needed for the system manipulation with rf pulses (fastened by strong hyperfine couplings). Thus, during the short time-scales of a spin-echo rf sequence, the target nucleus experiences a quasi-static electronic environment. [100]
In this context, the NMR apparatus must be suitable for the excitation and detection of fast relaxing signals. For the experiments reported in this thesis, we exploited a pulsed broadband NMR spectrometer named "HyReSpect" ("Hyperfine Resonance

Spectrometer"), entirely designed at the University of Parma and optimized for the investigation of magnetic materials, spanning both frequency and field. [11] This

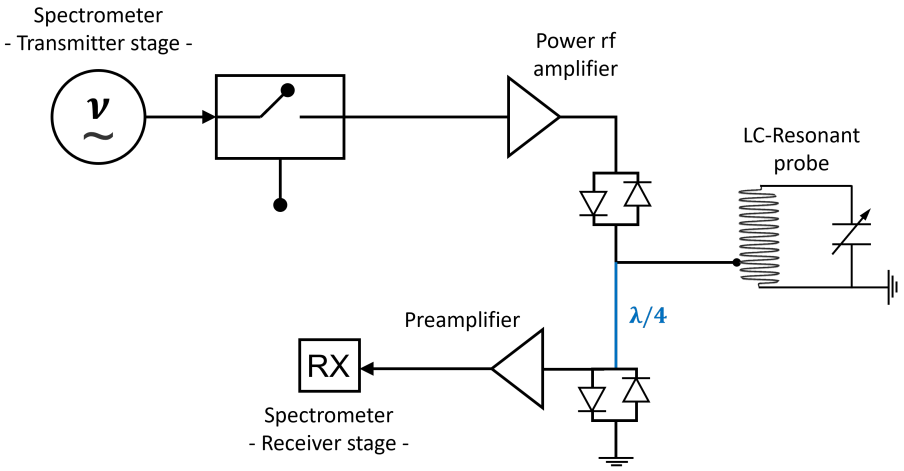

Figure 2.1: Sketch of the "HyReSpect" spectrometer hardware and of the LC-Resonant probe. Transmitter and Receiver stages hardware are better detailed in [11].

experimental apparatus (sketched in fig. 2.1) features a wide frequency span with a flat response in the 8-800 MHz range, covering the natural frequency range of several nuclei, such as transition metals (V, Cu, Mn, etc.). It is also equipped with a fast rf switching, with pulses that are programmable in steps of 12 ns, broadband receiver ±3 MHz and an effective experimental irradiating bandwidth limited to 1-2 MHz due to the LC resonator finite passband. The receiver bandwidth, together with a short instrumental dead time and a high speed digital pulser, enables the generation of pulse sequences characterized by short pulses and delays, necessary for the detection of short living signals with a fine time resolution. Faster signal averaging with respect to commercial NMR spectrometers enables also the collection of optimal signal to noise ratio on shorter experiment timescales. The used probehead is a LC resonant circuit in which the sample is placed within the coil and inserted into a Maglab EXA superconducting cryomagnet.

2.1.2 Electron Paramagnetic resonance

As already highlighted in the introduction, Electron Paramagnetic Resonance (EPR) is complementary to NMR, since it gives fundamental and non redundant information on the coupled electro-nuclear spin system. Electronic resonances indeed investigate the electronic magnetic moments arising in systems with unpaired electrons. [101, 102] The EPR experiment can be described exactly in the same theoretical framework used for the NMR experiment, with the only difference of the magnetic moment $\boldsymbol{\mu}_e = \mu_B \mathbf{g}_S \cdot \mathbf{S}$, which originates from the unpaired electrons of the system. Thus, in the case of an electronic spin multiplet $S = 1/2$, for a static field $B\hat{\mathbf{z}}$ aligned with the $\hat{\mathbf{z}}$ axis of the $\mathbf{g}$ tensor, the Zeeman interaction:

$$\mathcal{H} = \boldsymbol{\mu}_e \cdot \mathbf{B} = \mu_B g_{S_Z} B S_z, \tag{2.13}$$

causes the splitting of the energy levels, labeled by the two electronic spin component along the static field direction $m_S = \pm 1/2$

$$E_{m_S} = -\mu_B g_{S_Z} B m_S. \tag{2.14}$$

Consequently, for this simple model system, the energy of the mw-EPR stimulus inducing the transition for the resonant experiment between the two m_S states must be:

$$\hbar\omega = g_{S_Z} \mu_B B. \tag{2.15}$$

EPR experiments are usually performed at fixed mw-frequency and the transition energies are varied by sweeping the static field B until the Zeeman gaps match the irradiation energy. This because the resonator quality factor strongly depends on the target frequency and thus limits the frequency span range. For this reason, EPR can be performed with different characteristic frequencies reported in table 2.1, each of them particularly suited for specific experiments/samples.

EPR frequency bands	
L-band	0.8-1.2 GHz
S-band	3.4-3.8 GHz
X-band	9-10 GHz
Q-band	34 GHz
W-band	94 GHz

Table 2.1: EPR frequency bands. X and Q bands are the most commonly exploited for the study of molecular magnets spin Hamiltonians and decoherences.

In EPR spectroscopy the spin system can be targeted both by a continuous mw-field (continuous wave EPR) or by a pulsed mw-field (pulsed EPR). In this section we will focus only on the pulsed EPR technique, which is the one used for the measurements of spin relaxation reported in section 6. When the system is targeted by the mw-field B_1 of a pulsed EPR experiment, in analogy with what shown in section 2.1.1 for NMR, the electronic spin magnetic moments precess following the Bloch equations 2.1.1. Thus, it is possible to manipulate, through mw-pulses the electronic spins, inducing tuned nutations of angles $\theta = \mu_B g_x B_1 t_P$. This enables the characterization of the system energy spectra, together with the electronic spin lattice ${}^{e}T_1$ and spin-coherence ${}^{e}T_2$ relaxation times. The former is detected with a slightly difference pulse sequence with respect to NMR. Here the pulse train is substituted by a simple inversion π pulse and the resulting sequence is known as inversion-recovery sequence $\pi - \pi/2 - \pi$. The detection is done by refocusing the electronic spins previously pushed into the "inverted" non equilibrium state $-M_Z$, as a function of the time required to recover the equilibrium condition $M_0 = M_Z$. Pulsed-EPR spectra as a function of the static field B in fixed frequency regime enables the fitting of the spin Hamiltonian model. This analysis is complementary to the fitting of the NMR spectra, since the two techniques feature different sensitivity to the Hamiltonian parameters of electronic or nuclear origin respectively (e.g., the best fit of the spectroscopic splitting tensor $\mathbf{g}$ is achieved with EPR, while NMR features better sensitivity on the hyperfine tensor components).

Elexsys-E580 Pulsed spectrometer

In order to perform the measurements reported in the previous section, the EPR apparatus must feature high sensitivity and high speed manipulations. For this purpose, we exploited a Bruker Elexsys-E580 pulsed-EPR spectrometer from the EPSRC National Service for Electron Paramagnetic Resonance Spectroscopy Laboratory at the University of Manchester. This pulsed-EPR spectrometer is equipped with a SuperQ-FT microwave bridge for pulsed Q-band ($\nu_{EPR} = 34$ GHz) experiments combined with a dedicated Q-band resonator. The spectrometer is supplied with a 1.8 T electromagnet and a cryogen-free cryostat incorporating a closed helium circuit.

The sample is placed into a modular Bruker Flexline resonator, suitable for the multi-resonance Elexsys platform, featuring high cavity filling factor and short deadtimes. The cavity quality Q-factor is variable and enables experiment optimization. It could be critically coupled for continuous wave (CW) investigations, or kept low for short deadtime and large irradiation bandwidth or matched to the sample relaxation time to increase the signal to noise ratio.

The wide detection bandwidth (800 MHz) and the fast averaging signal processing are guaranteed by the combination of the PatternJet-II pulse programmer, which delivers a high time resolution (up to 1 ns), and the fast SpecJet-III digitizer, which enables high speed acquisition with 1 ns resolution, zero dead time between shots and on board signal processing. This two digital units in particular allowed to average FIDs and fast-decaying spin echoes within the sample T_1 limit. The SpinJet-AWG (arbitraty Waveform Generator) additional modulus, enables high speed manipulation and detection of pulses with non-trivial shaping over a multiple channel architecture.

2.2 Scattering techniques

Studying the scattering of a coherent radiation on a sample and the energy exchanged during the process gives unique insights into the atomic structure and coherent dynamics of the system. Indeed, scattering techniques are of fundamental interest in molecular magnetism, since the radiation interaction with the nuclei allows to directly probe the molecular and lattice vibrations triggering their phonon-induced relaxation dynamics. [30, 31] Moreover, for probes featuring a non-zero spin, i.e. neutrons, the magnetic interaction with spin and orbital momenta enables also the characterization of the system spin Hamiltonian and its coherent spin dynamics. [103]

In this thesis, X-ray and neutron scattering experiments are used for probing the phonon spectra and dispersions in Molecular nanomagnets (MNMs). Thus, in the following sections, we will give a brief introduction to the Inelastic Neutron Scattering (INS) and the Inelastic X-ray Scattering (IXS) techniques, highlighting the important information that can be extracted from the experiments. [104, 105, 106, 107]

2.2.1 Inelastic scattering

An inelastic scattering process, as sketched in figure 2.2, is defined by the two conservation laws for momentum and energy:

$$\vec{Q} = \vec{k}_f - \vec{k}_i, \tag{2.16}$$

$$\hbar\omega = E_f - E_i, \tag{2.17}$$

with the squared momentum depending on the scattering angle:

$$Q^2 = k_i^2 + k_f^2 - 2k_i k_f \cos(\theta). \tag{2.18}$$

To describe the scattering process we start defining an incident flux of the incoming beam per unit of perpendicular sample surface and per second I_0. The scattering cross section σ_s is then defined as the number of scattered particle per flux unit:

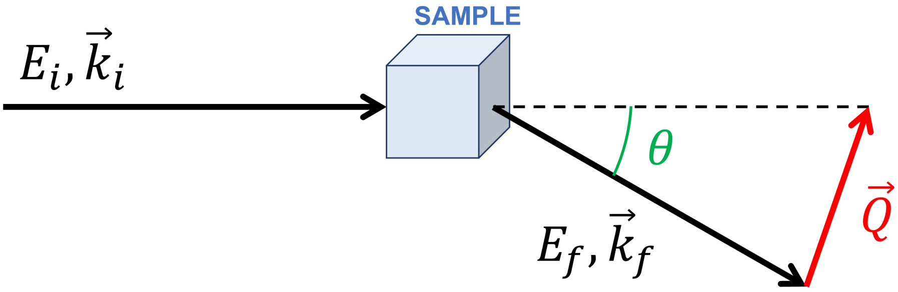

Figure 2.2: Scattering process with incoming and scattered beam energies E_i, E_f and wavevectors $\vec{k}_i, \vec{k}_f$, and geometrical representation of the transfer momentum $\vec{Q}$ and the scattering angle θ.

$$\sigma_s = \frac{\text{number of scattered particles}}{I_0}. \tag{2.19}$$

If we now restrict to a given direction identified by a small solid angle $d\Omega$ and to a final energy of the scattered particles in a narrow range $(E_f, E_f + dE_f)$, the local double differential cross section becomes:

$$\frac{\partial^2\sigma_s}{\partial\Omega\partial E} = \frac{\text{scattered particles into solid angle } d\Omega \text{ with energy } (E_f, E_f + dE_f)}{I_0 d\Omega dE_f}. \tag{2.20}$$

The double differential cross section includes all the physical information that can be extracted from the scattering experiment.
All the scattering processes can be described within the Fermi Golden Rule formalism, defining a transition rate between two identified states, by means of the interaction of the probe with the sample expressed by a potential V. Let's consider a scattering event in a $d\Omega$ solid angle, defining a final wavevector $\vec{k}_f$, in which the energy of the scattering system changes from E_λ to $E_{\lambda'}$. The probe-sample states changes consequently from $|\vec{k}_i, \lambda\rangle$ to $|\vec{k}_f, \lambda'\rangle$. The resulting double-differential cross-section can be written as:

$$\frac{\partial^2\sigma_s}{\partial\Omega\partial E} = \frac{1}{I_0 d\Omega dE_f} \sum_{k_f \text{ in } d\Omega} W_{|\vec{k}_i,\lambda\rangle \to |\vec{k}_f,\lambda'\rangle}. \tag{2.21}$$

Here $W_{|\vec{k}_i,\lambda\rangle\rightarrow|\vec{k}_f,\lambda'\rangle}$ represents the transitions rate between the two states. Given the Fermi Golden Rule, this rate can be written as a function of the squared matrix element of the interaction potential V between the two states and the energy conservation rule for the probe-sample system ($E_i + E_\lambda = E_f + E_{\lambda'}$):

$$\sum_{k_f \text{ in d}\Omega} W_{|\vec{k}_i,\lambda\rangle\rightarrow|\vec{k}_f,\lambda'\rangle} = \frac{2\pi}{\hbar}\rho_{k_f}|\langle\vec{k}_f,\lambda'|V|\vec{k}_i,\lambda\rangle|^2\delta(E_\lambda - E_{\lambda'} + E_i - E_f), \qquad (2.22)$$

where ρ_{k_f} defines, for the scattered particles with momentum $\vec{k}_f$, the number of states, per unit energy, in $d\Omega$. For a further expansion of this expression it is necessary to specify the nature of the interacting potential V and the $d\Omega, dE$ density of states $\rho_{k_f}dE_f$, in order to calculate the matrix element and extrapolate the normalization constants. Thus, it is necessary to separate the treatment depending if the scattering particles are neutrons of X-rays.

2.2.2 Inelastic Neutron Scattering

The interaction between a neutron and a bound nucleus is defined by the Fermi pseudopotential V_{nuc}:

$$V_{nuc}(r,t) = \frac{2\pi\hbar^2}{m_n}\sum_j b_j\delta(\vec{r} - \vec{R}_j(t)) \qquad (2.23)$$

with b_j scattering length of the jth atom in position $\vec{R}_j$ defining the interaction magnitude with the neutron at position $\vec{r}$.
Moreover, by exploiting the quantum mechanics *box normalization* and the relations between the energy and momentum of a neutron, the state density $\rho_{k_f}dE_f$ in the transition rate definition 2.2.1 can be rewritten as the number of wavevectors in the unit volume $8\pi^3/V_0$:

$$\rho_{k_f}dE_f = \frac{V_0}{8\pi^3}d\vec{k}_f \qquad (2.24)$$

Thus we obtain the density of states as a function of the final momentum:

$$\rho_{k_f} = \frac{V_0}{8\pi^3}\frac{m_n k_f}{\hbar^2}d\Omega \qquad (2.25)$$

By combining all these terms, we can write the cross section associated to the scattering event $|\vec{k}_i,\lambda\rangle \rightarrow |\vec{k}_f,\lambda'\rangle$ as:

$$\left(\frac{\partial^2\sigma_s}{\partial\Omega\partial E}\right)_{|\vec{k}_i,\lambda\rangle\rightarrow|\vec{k}_f,\lambda'\rangle} = \left(\frac{1}{N}\right)\frac{k_f}{k_i}\left(\frac{m_n}{2\pi\hbar}\right)^2|\langle\vec{k}_f,\lambda'|V|\vec{k}_i,\lambda\rangle|^2\delta(E_\lambda - E_{\lambda'} + \hbar\omega). \qquad (2.26)$$

However, in a typical scattering experiment we cannot focus only on the processes in which the system undergoes the specific $\lambda \rightarrow \lambda'$ transition. Thus, summing over all the final states λ' and averaging over the initial λ, we obtain:

$$\left(\frac{\partial^2\sigma_s}{\partial\Omega\partial E}\right) = \sum_{\lambda,\lambda'} p_\lambda\left(\frac{\partial^2\sigma_s}{\partial\Omega\partial E}\right)_{|\vec{k}_i,\lambda\rangle\rightarrow|\vec{k}_f,\lambda'\rangle}. \qquad (2.27)$$

Now, we substitute the pseudopotential V definition within the Fermi Golden Rule, and we write the matrix element summation as a thermal average (indicated as $\langle\rangle$)

on the initial states. The double differential cross section thus takes the integral form:

$$\left(\frac{\partial^2\sigma_s}{\partial\Omega\partial E}\right) = \left(\frac{1}{N}\right)\frac{k_f}{k_i}\left(\frac{1}{2\pi\hbar}\right)^2 \sum_{j,j'} \overline{b_j b_{j'}} \int_{-\infty}^{\infty} \langle e^{-i\vec{Q}\cdot\vec{R}_j(0)} e^{i\vec{Q}\cdot\vec{R}_{j'}(t)}\rangle e^{-i\omega t} dt, \qquad (2.28)$$

where the integral thermal average is a correlation function that depends on atom position as a function of time and the scattering function $S_{j,j'}(\vec{Q}, E)$ can be defined as:

$$S_{j,j'}(\vec{Q}, E) = \left(\frac{1}{2\pi\hbar}\right) \sum_{j,j'} \int_{-\infty}^{\infty} \langle e^{-i\vec{Q}\cdot\vec{R}_j(0)} e^{i\vec{Q}\cdot\vec{R}_{j'}(t)}\rangle e^{-i\omega t} dt. \qquad (2.29)$$

It is now possible to disentangle the contributions to the scattering function due to correlations between the same atom at different times or between different atoms. Indeed, if $j = j'$ then $\overline{b_j b_{j'}} = \overline{b^2}$, while if $j \neq j'$ then $\overline{b_j b_{j'}} = \overline{b}^2$. The two scattering lengths can be brought out from the jj' sum and the resulting cross-section is written as the sum of a coherent and incoherent terms:

$$\left(\frac{\partial^2\sigma_s}{\partial\Omega\partial E}\right) = \left(\frac{\partial^2\sigma_s}{\partial\Omega\partial E}\right)_{coh} + \left(\frac{\partial^2\sigma_s}{\partial\Omega\partial E}\right)_{incoh}, \qquad (2.30)$$

where:

$$\left(\frac{\partial^2\sigma_s}{\partial\Omega\partial E}\right)_{coh} = \left(\frac{\overline{b}^2}{N}\right)\frac{k_f}{k_i}\left(\frac{1}{2\pi\hbar}\right)^2 S_{j,j'}(\vec{Q}, E), \qquad (2.31)$$

contains the position correlations between different nuclei at different times (interference effects), while:

$$\left(\frac{\partial^2\sigma_s}{\partial\Omega\partial E}\right)_{incoh} = \left(\frac{\overline{b^2}}{N}\right)\frac{k_f}{k_i}\left(\frac{1}{2\pi\hbar}\right)^2 S_{j,j}(\vec{Q}, E), \qquad (2.32)$$

contains the position correlations at different times for the same nucleus (auto-correlations).

The time dependent displacement $u_j(t)$ of a nucleus from its equilibrium position l_j (induced by thermal vibrations) is defined as $R_j(t) = l_j + u_j(t)$. Substituting this definition into the time integral of the coherent scattering function, with $U = -i\vec{Q} \cdot u_j(0)$ and $V = i\vec{Q} \cdot u_{j'}(t)$ we obtain:

$$S_{j,j'}(\vec{Q}, E) \propto \sum_{j,j'} e^{i\vec{Q}\cdot(\vec{l}_{j'} - \vec{l}_j)} \int_{-\infty}^{\infty} \langle e^U e^V \rangle e^{-i\omega t} dt. \qquad (2.33)$$

After some manipulations, the thermal average can be rewritten as the product $\langle e^U e^V\rangle = e^{\langle U^2\rangle} e^{\langle UV\rangle}$. The first term, corresponding to a thermal average of the displacement auto-correlations function, it is the so-called Debye-Waller effect $e^{\langle U^2\rangle} = e^{-2W(\vec{Q})}$. The second term instead, is the thermal average of the displacement correlation function. For small displacements, in harmonic approximation, the exponential can be expanded in Taylor series, and each order n of the series correspond to a scattering process involving a number n of phonons

$$e^{\langle UV\rangle} \approx 1 + \langle UV\rangle + \frac{1}{2}\langle UV\rangle^2 + \frac{1}{n!}\langle UV\rangle^n. \qquad (2.34)$$

Here the order "zero" of the series $e^{\langle UV\rangle} \approx 1$ correspond to a scattering process that does not involves phonons (i.e. elastic scattering), while the first order $e^{\langle UV\rangle} \approx 1 + \langle UV\rangle$ corresponds to a scattering process that causes the emission or absorption of one single phonon, and so on for the following orders. Thus, assuming the displacements $\vec{u}_j$ as the normal modes of a quantum harmonic oscillator with frequency $\omega_s(\vec{q})$ (eigenvalue) and polarization vector $\vec{\sigma}_s(\vec{q})$ (eigenvector), the one-phonon coherent scattering function can be rewritten in terms of creation and annihilation operators for bosons:

$$S_{coh}(\vec{Q},E) \propto \left(\frac{1}{2m_n}\right)\sum_{\vec{\tau}} e^{-2W(\vec{Q})}\sum_{s\vec{q}}\frac{|\vec{Q}\cdot\vec{\sigma}_s(\vec{q})|^2}{\omega_s(\vec{q})}\times$$
$$[(n_s(\vec{q})+1)\delta(\omega-\omega_s(\vec{q}))\delta(\vec{Q}-(\vec{\tau}+\vec{q}))+n_s(\vec{q})\delta(\omega+\omega_s(\vec{q}))\delta(\vec{Q}-(\vec{\tau}-\vec{q}))] \tag{2.35}$$

with $\vec{\tau}$ vector of the reciprocal space, $\vec{q}$ wavevector of the normal modes and s phonon branch index. The two delta functions ensure the conservation of the energy and momentum within the scattering process and the correlated creation/annihilation of one-phonon. It now is evident from the coherent scattering function that in the scattering experiment of a single crystal we have access to both phonon dispersions and eigenvectors.

When more than one element d is present in the unit cell the scattering function must be weighted for the scattering length and mass of each element. This term took the name of structure factor $F(\vec{Q},\vec{q}) = |\sum_d b_d m_d^{-1/2}\exp(i\vec{Q}\cdot\vec{r}_d)|\vec{Q}\cdot\vec{\sigma}_s(\vec{q})|\exp(-2W(\vec{Q}))|$. The same phonon expansion in 2.2.2 can be applied to the incoherent scattering function $S^{incoh}_{j,j}(\vec{Q},E)$.

$$S_{incoh}(\vec{Q},E) \propto \left(\frac{1}{2m_n}\right) e^{-2W(\vec{Q})}\sum_{s,\vec{q}}\frac{|\vec{Q}\cdot\vec{\sigma}_s(\vec{q})|^2}{\omega_s(\vec{q})}\times$$
$$[(n_s(\vec{q})+1)\delta(\omega-\omega_s(\vec{q}))+n_s(\vec{q})\delta(\omega+\omega_s(\vec{q}))]. \tag{2.36}$$

We observe that in the incoherent scattering function the momentum $\vec{Q}$ selection rule δ is released. Thus, the scattering only depends on the number of phonon modes (3N in total) satisfying $\delta(\omega \pm \omega_s(\vec{q}))$. For this reason the function 2.2.2 can be expressed as a function of the phonon density of states $\rho(\omega)$, averaging over the wavevectors $\vec{q}$ and polarization states s:

$$S_{incoh}(\vec{Q},E) \propto \left(\frac{N}{4m_n}\right) e^{-2W(\vec{Q})}\frac{Q^2}{\omega}\rho_d(\omega)[(n_s(\vec{q})+1)+n_s(\vec{q})]. \tag{2.37}$$

Here $[(n_j(\vec{q})+1)+n_j(\vec{q})]$ correspond to the Bose-Einstein occupancy factor. If the system is composed by more than one element d, the partial density of states $\rho_d(\omega)$ for each d is weighted by its incoherent cross section $\sigma_{incoh} = 4\pi(\overline{b^2}-\overline{b}^2)$ and mass M_d, into the global neutron-weighted density of states:

$$\rho_{n-w}(\omega) = \sum_d \frac{\sigma_s(d)}{2M_d}\rho_d(\omega). \tag{2.38}$$

The latter is directly correlated to the output of the incoherent scattering experiment on powders.

IN8

The INS measurements shown in section 5.2 were collected at the Institute Laue-Langevin (ILL) on the thermal neutron triple-axis spectrometer IN8.[108] IN8 was chosen because it is a high incident flux spectrometer, optimized for the characterization of lattice vibrations and magnetic excitations in the range 0-100 meV, for small samples (as the SMMs we are dealing with).
The instrument layout is shown in figure 2.3. The monochromator, that constitute the first "axis" of the spectrometer, selects only the neutrons within a narrow energy band E_i by Bragg scattering. Then the second "axis", the Analyzer, is moved (exploiting air cushions) in order to select a specific scattering direction corresponding to a final wavevector $\vec{k}_f$, thus selecting one momentum transfer value $\vec{Q}$. Finally, the detector (third "axis") collects the neutrons scattered from the analyzer selecting their final energy E_f, varying the Bragg scattering angle between the detector and the Analyzer. By exploting the different combinations of these three axis, the spectrometer can precisely select a well defined scattering event within the ($\vec{Q}$, $E_f - E_i$) space.

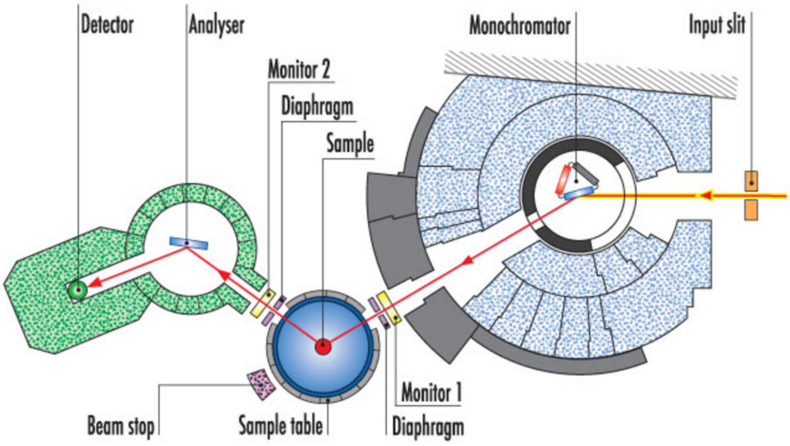

Figure 2.3: The layout of the IN8 spectrometer at ILL. The picture is reproduced from the facility webpage.

For the purpose of our experiment we exploited only two of the three faces of the double focusing monochromator: the Si(111) and the pyrolytic graphite PG(002), featuring an elastic Half Width Half Maximum (HWHM) of 0.88 meV and 3 meV, respectively. Both the monochromators can select two initial wavevectors $k_i = 2.662$ Å^{-1} or $k_i = 4.1$ Å^{-1}. The take-off angle of the monochromator must be in the range $10° < 2\theta_M < 90°$. An horizontal virtual source (horizontal slit) is placed before the monochromator at a distance that matched the monochromator-sample one, to focus the monochromatic beam. Further collimation of the beam is realized by a series of diaphragms in the beam path, in order to exclude as much as possible the background introduced by the sample environment (Paris-Edinburgh pressure cell in our case). The analyzer used is a double focusing PG(002). At the sample position the selected scattering angle is limited in the range $0° < 2\theta_S < 130°$. The detector is a single ^{3}He tube vertically mounted inside a heavy borated polyethylene shielding.

IN1-LAGRANGE

The INS experiment shown in section 5.1 were performed at ILL on the spectrometer IN1-Lagrange (LArge GRaphite ANalyzer for Genuine Excitations).[109] IN1-Lagrange is dedicated to the study of lattice and molecular excitations, providing direct access to the sample phonon Density of States (pDOS). This spectrometer is particularly suited to the study of pDOS in molecular magnets since it provides a unique combination of both high flux and high resolution, the latter dependent on the energy range. The instrument layout is shown in figure 2.4

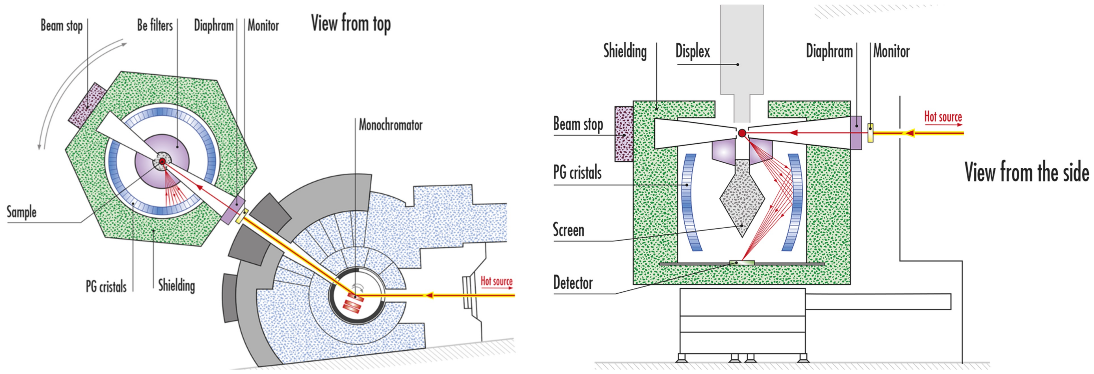

Figure 2.4: Top (left) and side (right) views of the IN1 spectrometer layout. The picture is reproduced from the ILL webpage.

The spectrometer works in indirect geometry, thus by spanning the incident neutron energy E_i and keeping fixed the final energy E_f selected by the analyzer. The spectrometer analyzer is made by a ~1 m^2 surface composed by 612 PG crystals and built along the perpendicular of the beam axis, at the sample position (side view in fig. 2.4). This particular configuration of the analyzer enable the reflection of the neutron scattered by the sample, over an extremely wide solid angle (2.5 Steradian), with a fixed final energy of 4.5 meV. These scattered neutrons are thus focused by the analyzer reflection and recorded by a single ^{3}He counter, equipped with a Boron screen to suppress the elastic scattering. The incident energy of the neutrons is defined by a set of double-focusing monochromators: Cu(220), Cu(331), Si(311), Si(111) that enable to scan a wide range of energy from 4 to 600 meV. To each monochromator corresponds a specific energy range (slightly overlapping to favor the merging of the E_i scans) and a correlated energy resolution ΔE (see table below).

IN1-LAGRANGE monochromators

Crystal	E_i range	ΔE
Cu(220)	26-500 meV	2-3 % E_i
Cu(331)	67-500 meV	1.5-2 % E_i
Si(111)	4-20 meV	0.8 meV
Si(311)	16.5-60 meV	0.8 meV

This instrumental configuration can be considered an alternative to the triple axis configuration presented above for the spectrometer IN8 (fig. 2.3), where the analyzer is kept fixed in the scattering energy and very large in size. The second "axis" of the spectrometer is thus fixed here (no $\vec{Q}$ dependence information) and the INS spectra is collected by sweeping step by step the incident energy E_i.

2.2.3 Inelastic Xrays Scattering

When the scattering probe is a photon, the interaction potential assumes a different form. In the case of X-rays, in the weak relativistic limit, the photon-sample electrons interaction is well described by the Thomson interaction Hamiltonian:

$$H = \frac{1}{2} r_0 \sum_j \vec{A}^2(\vec{r}_j, t), \tag{2.39}$$

where $r_0 = \frac{e^2}{m_e c^2}$ is the classical electronic radius and $\vec{A}$ is the vector potential for the electromagnetic field of the jth electron. We now want to follow a path similar to the one outlined for neutron scattering in section 2.2.2. By expressing the vector potential $\vec{A}(\vec{r}_j, t)$ in plane wave expansion, the double differential cross section in 2.2.1 can be written, with explicit transition rate between the initial (i) and final (f) states λ, λ' (from Fermi Gold Rule), as:

$$\left(\frac{\partial^2 \sigma}{\partial \Omega \partial E}\right) = r_0 |\vec{\epsilon}_i \cdot \vec{\epsilon}_f|^2 \frac{k_f}{k_i} \left\{ \sum_{\lambda,\lambda'} p_\lambda \left| \left\langle \lambda' \left| \sum_j e^{i\vec{Q}\cdot\vec{r}_j} \right| \lambda \right\rangle \right|^2 \delta(E_\lambda - E_{\lambda'} + \hbar\omega) \right\}, \tag{2.40}$$

where the first term $r_0 |\vec{\epsilon}_i \cdot \vec{\epsilon}_f|^2$ is a scale factor from Thomson one electron scattering, p_λ is the thermal population of the initial state and the squared matrix element can be rewritten as a thermal average. The term within the curl brackets has the same the structure of the scattering function $S(\vec{Q}, \omega)$ defined for neutrons in section 2.2.2. Thus, for the description of the scattering experiment we now focus on this quantity. In adiabatic approximation we can focus only on the nuclear coordinates, assuming that the electronic part of the system wavefunction is unperturbed. In this approximation the summation over the j electrons is brought to atomic k coordinates $\sum_j e^{i\vec{Q}\cdot\vec{r}_j(t)} = \sum_k f_k(\vec{Q}) e^{i\vec{Q}\cdot\vec{R}_k(t)}$ expliciting the atomic form factor $f_k(\vec{Q})$ and the positions time-dependence. This last sum represents the charge density operator $\rho(\vec{Q}, t)$. After all these manipulations, the scattering function can be expressed as the integral thermal average of the charge density operator:

$$S(\vec{Q}, \omega) = \frac{1}{2\pi\hbar} \sum_{k,k'} \overline{f_k f_{k'}} \int_{-\infty}^{\infty} \langle e^{-i\vec{Q}\cdot\vec{R}_k(0)} e^{i\vec{Q}\cdot\vec{R}_{k'}(t)} \rangle e^{-i\omega t} dt. \tag{2.41}$$

This form permits to rewrite the scattering function in analogy to what is done for neutron scattering, thus introducing the coherent and incoherent contributions, accounting for the interference and single particle correlation terms, respectively. Indeed, for $k = k'$ then $\overline{f_k f_{k'}} = \overline{f^2}$, while if $k \neq k'$ then $\overline{f_k f_{k'}} = \overline{f}^2$. Substituting into the scattering function:

$$\begin{aligned} S(\vec{Q},\omega) =& S_{coh}(\vec{Q},\omega) + S_{incoh}(\vec{Q},\omega) = \\ & \frac{1}{2\pi\hbar}\sum_{k,k'}\overline{f}^2\int_{-\infty}^{\infty}\langle e^{-i\vec{Q}\cdot\vec{R}_k(0)}e^{i\vec{Q}\cdot\vec{R}_{k'}(t)}\rangle e^{-i\omega t}dt+ \\ & \frac{1}{2\pi\hbar}\sum_{k}\overline{f^2}\int_{-\infty}^{\infty}\langle e^{-i\vec{Q}\cdot\vec{R}_k(0)}e^{i\vec{Q}\cdot\vec{R}_{k}(t)}\rangle e^{-i\omega t}dt. \end{aligned} \tag{2.42}$$

Introducing a small displacement $\vec{u}_k(t)$ for each k atoms, we define the same operators $U = -i\vec{Q}\cdot u_k(0)$ and $V = i\vec{Q}\cdot u_{k'}(t)$ of equation 2.2.2 and we derive the one-phonon scattering function from the first order Taylor expansion of the thermal averaged exponential $\exp(\langle UV\rangle)$. The coherent one phonon X-rays scattering function thus becomes:

$$\begin{aligned} S(\vec{Q},\omega) \propto & \sum_{s,\vec{q}}\frac{1}{\omega_s(\vec{q})}|F^s_{1-ph}(\vec{Q})|^2 \\ & [(n_s(\vec{q})+1)\delta(\omega-\omega_s(\vec{q}))\delta(\vec{Q}-(\vec{\tau}+\vec{q})) + n_s(\vec{q})\delta(\omega+\omega_s(\vec{q}))\delta(\vec{Q}-(\vec{\tau}-\vec{q}))], \end{aligned} \tag{2.43}$$

with the structure factor $F^s_{1-ph}(Q)$ defined as:

$$F^s_{1-ph}(\vec{Q}) = \sum_k \frac{f_k(\vec{Q})}{\sqrt{2M_k}}e^{-2W_k(\vec{Q})}(\vec{Q}\cdot\vec{e}^s(\vec{q}))e^{i\vec{Q}\cdot\vec{r}_k}, \tag{2.44}$$

where we note the explicit dependence on the phonon modes energies $\omega_s(\vec{q})$ (eigenvalue) and polarization $e^s(\vec{q})$ (eigenvectors), which can be directly probed in the scattering experiment.

We finally note that, differently from a neutron scattering experiment, here the energy of the excited phonon modes are much smaller than the incident photon energy ($\hbar\omega \ll E_i$), thus the exchanged momentum Q and incident photon momentum k_i ratio depends only on the scattering angle θ (in fig. 2.2). Thus, there are no kinematic restriction on the energy transfer depending on the Q values. Moreover, the IXS cross section is mainly composed by the coherent scattering function extracted above, with the incoherent scattering that contributes at higher energies and, in the moderate low energy phonon regime, can be neglected. Finally, elements contribute differenlty to the IXS and INS cross sections. This is due to the intrinsic difference between the X-rays form factor and the neutron scattering length, which feature distinct dependence on the momentum transfer Q and on the scattering system electron number Z. A more detailed analysis of the differences and similarities between INS and IXS is reported below, as a subsection of this chapter.

ID28

The Inelastic X-ray scattering measurements shown in section 4 were collected at the European Syncrothron Radiation Facility (ESRF) on the beamline ID28. ID28 is a triple axis spectrometer dedicated to the study of phonon dispersions in condensed matter in a wide range of transferred momentum $\vec{Q}$ and exchanged energy

$\hbar\omega$, even for samples of very small dimensions. Measurements can also be performed in a variety of sample environments, such as high-vacuum, cryogenic temperatures, high-pressure, etc. This beamline is a one-of-a-kind because, thanks to its unique capabilities in terms of lineshape and resolution, enables the characterization of optical and acoustic phonons of molecular crystals. The beamline layout is shown in figure 2.5. The spectrometer features an almost exact backscattering Si monochromator

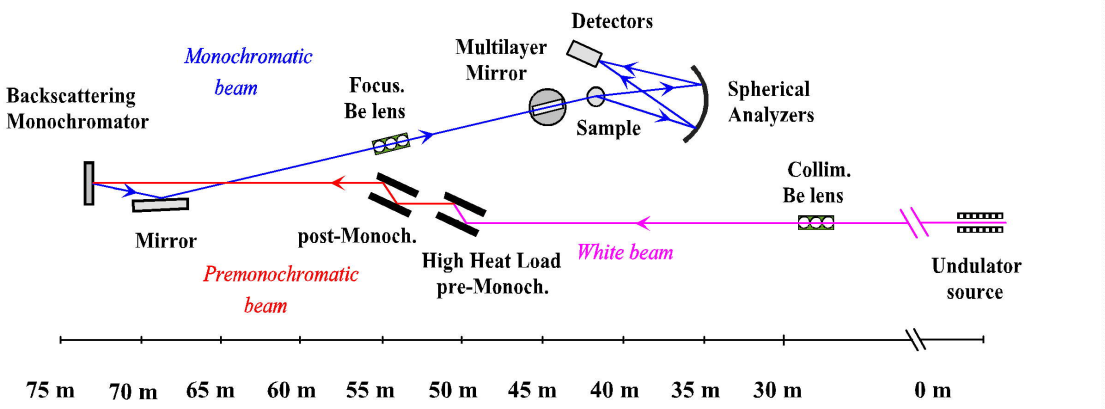

Figure 2.5: Schematic representation of the ID28 spectrometer layout. The picture is reproduced from the ESRF website

(89.98°) that exploit different Si(n,n,n) reflection orders. Each of these reflections selects an initial energy E_i and a lineshape width ΔE (resolution), for a X-rays flux that decrease by increasing the reflection order n (see table below).

ID28 monochromators

n order	E_i (keV) range	ΔE (meV)	flux (photons/s)
Si(777)	13.84	5.3	10.5×10^{10}
Si(888)	15.817	4.4	9×10^{10}
Si(999)	17.794	2.2	2.7×10^{10}
Si(111111)	21.747	0.83	6.6×10^{9}
Si(121212)	23.725	0.73	5.8×10^{9}
Si(131313)	25.704	0.5	1.47×10^{9}

After the monochromation, the beam is focused on the sample, positioned on a rotating goniometer with rotational, tilting and translational degrees of freedom, back into the experimental cabin. Here lays the second "axis" of the spectrometer, a 7 meters arm, equipped with nine analyzer, each of them constituted by 1200 single crystals bent in a spherical shape, for focusing the beam on the detectors over an angular acceptance of 40 mrad^2. The nine analyzers are placed in the horizontal scattering plane, with an angular displacement of 0.75°, and select nine different momentum transfer $\vec{Q}$ in the range 1-80 nm^{-1} with a momentum resolutions of 0.03 nm^{-1}. The individual Si detectors constitute the third "axis" of the spectrometer and select the final scattering energy E_f. They are integrated on a monolithic Si chip, together with their preamplifier and the Peltier cooling modulus (for electronic noise reduction). The length of the spectrometer arms is justified by the backscattering geometry and the need to offset the incoming white beam with respect to the monochromated and focused one E_i.

INS and IXS, differences and similarities

Since in this thesis both INS and IXS techniques are used, it is worth mentioning some of the main differences between the two probes. In particular, we will focus on the aspects that makes X-rays favorable with respect to neutrons for the investigation of phonon dispersions in molecular crystals. The first aspect relates to the cross section that for X-rays is highly coherent, while in neutron scattering some elements like ^{1}H, abundantly present in molecular complexes, display an highly incoherent cross section that causes the blurring of the experimental phonon dispersions due to incoherent scattering. Conversely in IXS, the incoherent scattering involves energies way higher than the typical phonon energies of molecular magnets we are interested in. Thus, it is not necessary to, e.g., deuterate the crystals employed. Together with the absence of incoherent scattering, multiple scattering events can also be neglected, making IXS a basically background free technique. Thus, with respect to INS the data reduction procedure results smoother. Conversely to INS, IXS do not suffer of strong dynamical limitation within the (Q,E) space and the order of magnitude difference between the incident and the exchanged energies leads to the decoupling of energy and momentum transfer (which depends only on the scattering angle) and causes the resolution of the experiment to be independent from the energy. Moreover, the almost absence of X-ray magnetic cross section makes this probe favorable for the study of phonon dispersions and polarization vectors, since the magnetic excitations within the energy range of interest are naturally removed. For INS instead, where the magnetic cross section is comparatble at low Q to the nuclear one, the subtraction must be done manually by measuring a diamagnetic analogue of the studied crystal.

However, the two techniques features also some similarities, such as the coupling strength, which is comparable between X-ray-electron and neutron-nucleus. Finally, the easier focusing of the X-ray beam and its intrinsic higher flux makes IXS best suited for the study of crystals of small dimensions in reasonable times, with respect to INS that, in absence of large crystals, requires long counting times.

Chapter 3

Extensive broadband NMR study of Vanadium-based molecular qudits

In this chapter we focus on the characterization of Vanadium-based molecular qubits. By exploiting the broadband NMR technique, we access a comprehensive description of the coupled electro-nuclear spin Hamiltonian and of the spin coherence times of these systems. By further combining nuclear and electronic resonance techniques, we further increase the extent and the accuracy of the description of this complexes, achieving complementary and non redundant results. Moreover, we demonstrate that targeted radio-frequency (rf) and microwave (mw) pulses can be exploited to implement monochromatic coherent manipulations of the electronic and nuclear states of these systems. Finally, the ability to manipulate nuclear state with rf pulses is pushed further by implementing the elementary encoding operations of a Quantum Error Correction algorithm, under the guide of realistic simulations. This capability demonstrates that these complexes are promising units for quantum information processes applications.

3.1 Vanadium-based qudits

Molecular complexes embedding a single transition metal ion have been intensively studied in the last decade for quantum information processing applications. Indeed, the chemical ability to tailor the ligands environment and thus to engineer the quantum properties of the system makes these complexes an ideal test bed to discern the different contribution to relaxation and decoherence. Among plenty of possibilities, Vanadium and Oxidovanadium(IV) based complexes are emerging as promising candidates, because of an innate robust quantum coherence. [5, 6, 35, 67] Moreover, these Vanadium-based systems feature a crucial advantage. The Vanadium nuclear spin $I = \frac{7}{2}$ can in fact be exploit to expand the available computational space within a single quantum object. Indeed, the hyperfine coupling between the nuclear spin degrees of freedom and the electronic spin doublet generates a multilevel structure which is called Qudit, i.e. a quantum digit featuring more than two levels. [42, 51] Encoding information on this multilevel structure expands the dimensions of the computational Hilbert space from a two-dimensional qubit to a

d-dimensional ($d > 2$) qudit.
In this frame, resonant techniques that exploit electromagnetic pulses (as NMR and EPR, respectively in sect. 2.1.1 and 2.1.2) play a crucial role, since they allow both the characterization and the coherent manipulation of these multilevel structures. [55, 100] In particular, in the following, we demonstrate why broadband NMR is an ideal technique for coherently manipulating the nuclear states of prototypical molecular qudits and how this technique can be used to characterize them. [4, 12]

3.2 NMR investigation of the [VO(TPP)] molecular qudit

The first prototypical Vanadium-based molecular qudit studied here is Vanadyl tetraphenylporphyrinate [VO(TPP)]. The complex is composed by a single Vanadium ion bound to an oxygen to form a Vanadyl group which is inserted at the center of a porphyrine ring. The molecule crystallizes as a square pyramid with a tetragonal $I4$ space group. In the crystal cell, the porphyrine group lies in the crystallographic ab-plane, with the O-V bond developing along the c-axis (see fig. 3.1). [4, 14] Moreover, the square pyramid basis matches the crystallographic ab-plane, while the pyramid height correspond to the crystallographic c-axis.

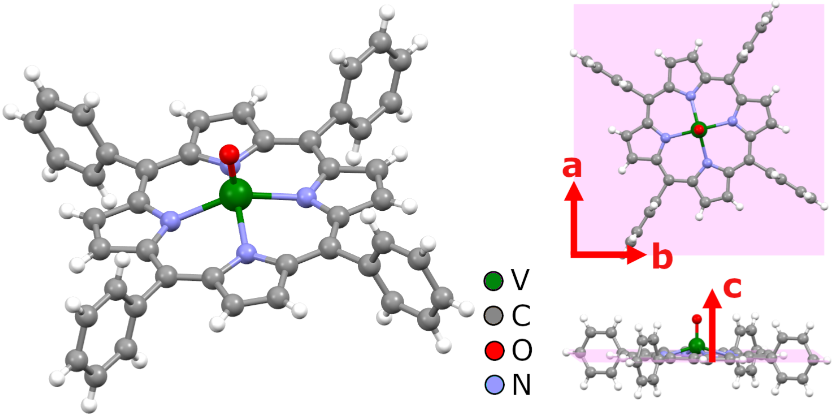

Figure 3.1: [VO(TPP)] molecular structure. The principal orthogonal symmetry directions of the molecular crystal are shown independently: the porphyrin lying in the ab plane and the oxidovanadium bond direction along the c axis

The NMR spectra of ^{51}V nuclei are measured by the home-built broadband spectrometer "HyReSpect" described in section 2.1.1 and in Ref.[11]. The data were collected at $T = 1.4$ K, in order to suppress as much as possible decoherence effects induced by temperature, on a single crystal of [VO(TPP)] diluted at 2% into its isostructural diamagnetic analogue [TiO(TPP)]. Dilution represents the most efficient way to suppress the dipolar inter-molecular interactions as a source of decoherence. However, dilution must also be tuned in order to permit the detection of the NMR signal from the targeted nuclei. The dilution percentage used for [VO(TPP)] measurements therefore represents a good trade-off between these two factors. [100] The single diluted crystal is placed on a custom 3D printed plastic sample-holder and hold in place by vacuum grease. This sample holder permits to easily orient the crystal in order to apply the external static field along specific symmetry directions. The first step of the analysis was the characterization of the model spin Hamiltonian parameters by an extensive broadband NMR study as a function of the applied field. We measured ^{51}V spectra by collecting Hanh-echoes over a wide frequency range at various applied static fields in the range $B_0 = 0.05 - 0.3$ T. The pulse sequence used is the unconventional $\frac{2\pi}{3} - \tau - \frac{2\pi}{3}$ sequence which provides an optimized resonance signal,[100, 110] with pulses duration of $T_{pulse} = 0.202$ μs and delay $\tau \approx 6$ μs. The discrete frequency steps can be thickened in data post-processing by merging the overlapping frequency domains of spin-echoes fast Fourier transform for subsequent frequency shifted steps. [111]

In Figure 3.2 we show two examples of ^{51}V spectra, measured by applying the static field along the two nonequivalent and orthogonal symmetry directions of the [VO(TPP)] molecule, the porphyrin plane ab and the oxidovanadium bond direction c.

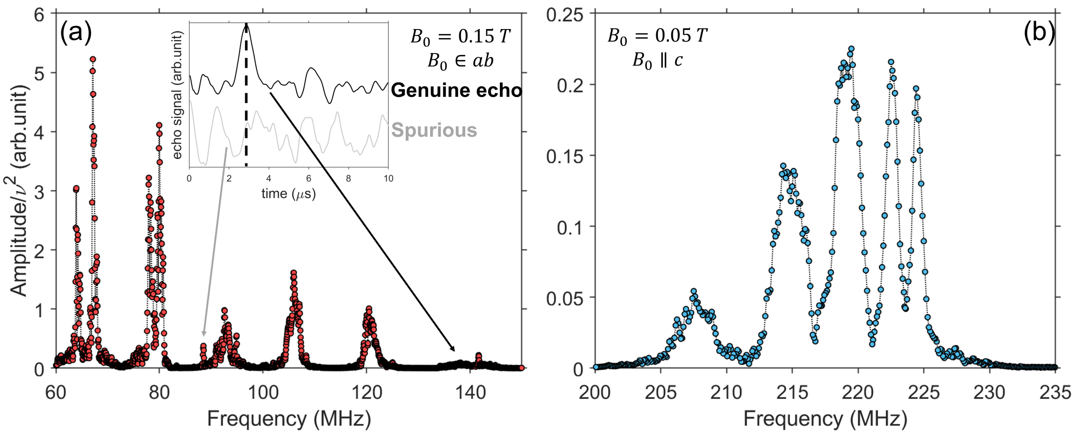

Figure 3.2: Spectra collected at different applied field B_0 along the molecule symmetry directions: the ab plane (a), and the c axis (b). In inset, a spurious peak is identified from the absence of any time-domain spin-echo signals. Indeed black line shows the echo signal in quadrature for a real nuclear excitation in correspondence of τ (dashed line), whereas a spurious appears as the persistent gray oscillations. Reproduced from Ref. [4] with permission from the Royal Society of Chemistry.

The [VO(TPP)] molecule can be described by a simple coupled electro-nuclear spin Hamiltonian composed as follows:

$$H_0 = \hat{\mathbf{I}} \cdot \mathbf{A} \cdot \hat{\mathbf{S}} + p\hat{I}_z^2 + \mu_B \hat{\mathbf{S}} \cdot \mathbf{g}_S \cdot \mathbf{B}_0 + \mu_N g_N \hat{\mathbf{I}} \cdot \mathbf{B}_0. \tag{3.1}$$

The first term in eq. 3.2 accounts for the Hyperfine coupling between the electronic $\hat{S}$ and the nuclear $\hat{I}$ Vanadium spins, while the second one expresses a small axial nuclear quadrupolar contribution (see sect. 1.3). Finally, the last two terms represent the nuclear and electronic Zeeman interactions. As seen in section 1.3, the parameters of the spin Hamiltonian determine the field evolution of the nuclear resonances. Therefore, by comparing the measured field dependence of the spectra peaks with the simulated spectra, we can fit the spin Hamiltonian parameter. By considering the crystallographic axes as reference frame $abc = xyz$, we assume the Hamiltonian tensors to be diagonal, axial and collinear. Moreover, this choice of axes combined with the crystal shape simplify the definition of the direction of the applied fields $\vec{B}_0$, $\vec{B}_1$, because the xy plane matches the square pyramid basis while the z axis coincides with the vertex.

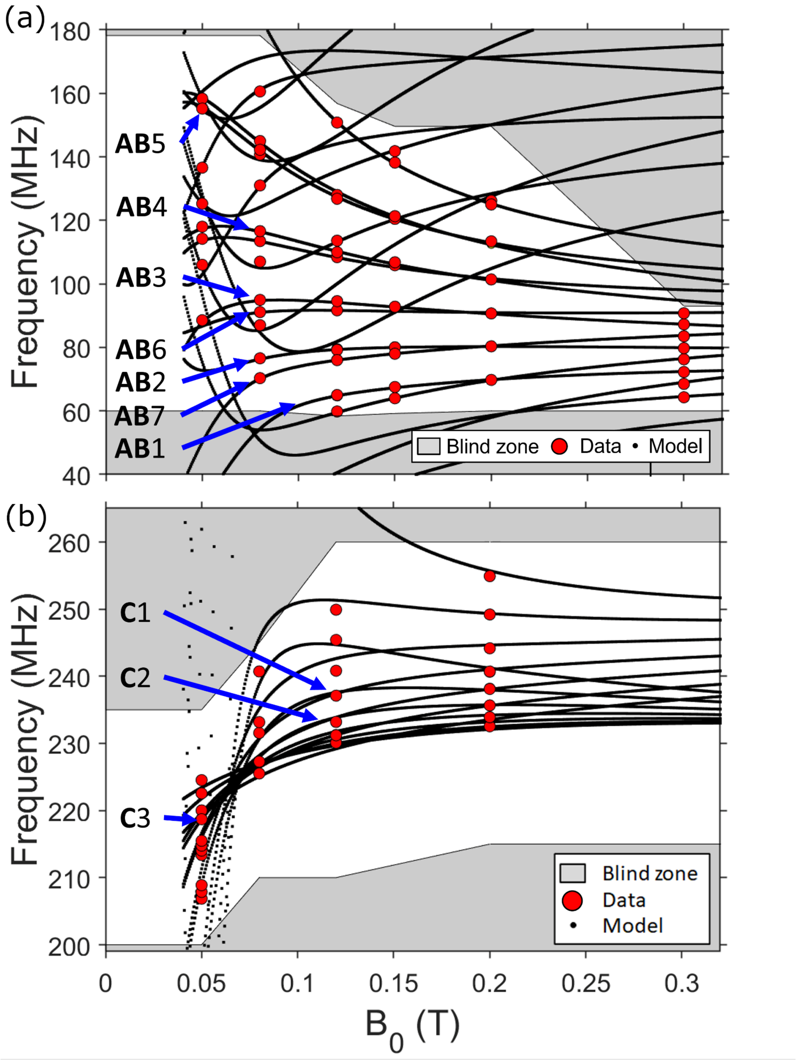

Figure 3.3: Red dots correspond to the measured transition frequencies in the broadband NMR spectra of ^{51}V. Black lines represent the calculated evolution of the transition frequencies as a function of the field B_0 applied (a) in the *ab*-plane, and (b) along *c*-axis. With capital letters **AB#** and **C#** we label the $\Delta m_I = \pm 1$ transitions for each direction. Shaded areas were not experimentally explored. Reproduced from Ref. [4] with permission from the Royal Society of Chemistry.

The best agreement between the calculations and the experimental spectra is found with an axial Hyperfine tensor and a small axial quadrupolar coupling (see table 3.1). [4] The electronic spectroscopic splitting tensor $\mathbf{g}_s$ is kept fixed to values obtained from a previous EPR study [14], since that technique feature an higher sensitivity on the determination of the electronic g-values. Finally, the nuclear g-factor is fixed to the constant isotropic value for the ^{51}V nucleus $\mu_N g_N = -11.213$ MHzT^{-1}. [112] The best fit parameter of [VO(TPP)] spin Hamiltonian are listed in table 3.1.
The agreement achieved between the experimental resonance frequencies and the model Hamiltonian curves is excellent for both the orthogonal field directions (plane *ab* and *c* axis), as shown in figure 3.3. By diagonalizing the spin Hamiltonian 3.2

[VO(TPP)] spin Hamiltonian

	$\mathbf{A}$ (MHz)	$\mathbf{p}$ (MHz)	$\mathbf{g}_S$ (MHz)
x	-170 ± 1	0	1.9865
y	-170 ± 1	0	1.9865
z	-480 ± 1	-0.35 ± 0.07	1.963

Table 3.1: Best fit parameter of the [VO(TPP)] spin Hamiltonian 3.2. [4]

with the obtained parameters we can access the eigenvalues of the system and plot its energy levels diagram as a function of the applied field (fig. 3.4).
The calculated energy levels are labeled as $|m_S, m_I\rangle$, thus with the component of the electronic S and nuclear I spins parallel to the applied static field B_0. This attribution is accurate above $B_0 = 0.25$ T, where $g_{S,x}\mu_B B_0 > |A_z|$ with the field applied along the x axis of the molecule frame. In this regime, the system eigenstates are factorized for more than 98%.

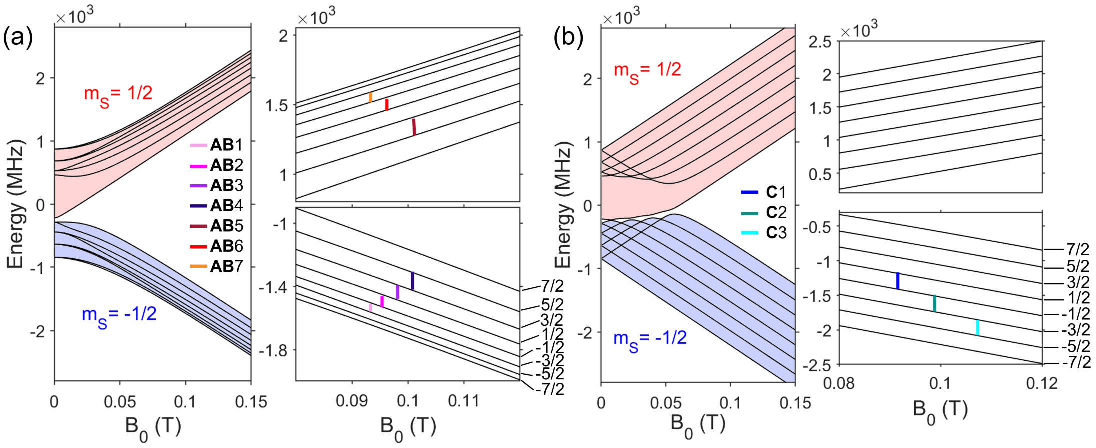

Figure 3.4: Energy levels as a function of the applied field from the diagonalization of the spin Hamiltonian with static field B_0 applied (a) in plane ab and (b) along c-axis. The red and blue shades highlight the $m_S = \pm 1/2$ multiplets, respectively. On the left of each plot, two insets show a zoom into the nuclear level splitting of the lower and upper multiplets, with the levels marked by the nuclear spin components m$_I$ along the field. Vertical marks highlight the nuclear transitions identified in the spectra of figure 3.2. Reproduced from Ref. [4] with permission from the Royal Society of Chemistry.

For the purpose of exploiting the nuclear states of this system as the multi-levels of a qudit, they must fulfill two fundamental requirements. Firstly, the nuclear spin dynamics must be conditioned by the electronic spin state, which means that the energies of the nuclear transitions belonging to an electronic spin state are different from the energies of the same nuclear transitions of the other electronic spin multiplet. As a consequence of this, any manipulation of the nuclear state is conditioned by the electronic state. The second requirement concerns the addressability of individual nuclear transitions. Indeed, any quantum operation on the nuclear spin states can be expressed as a combination of transitions between single pairs of nuclear consecutive levels m_I. To ensure this, the difference between subsequent nuclear gaps $\delta_{m_I} = (E_{m_I+1} - E_{m_I}) - (E_{m_I} - E_{m_I-1})$ must be bigger then the *rf* irra-

diation bandwidth used for the nuclear manipulation. Indeed, this feature enables one to address single nuclear transitions, without perturbing nearby states.
The [VO(TPP)] complex fulfills both the requirements reported above. In particular, the pseudo quadrupolar coupling described in section 1.3.4 plays a key role, since the differences in the transitions energies are mostly imputable to this effect. Indeed, the differences 2ζ between the transition energies obtained by diagonalizing the effective Hamiltonian of section 1.3.4 (composed by the defined pseudo-Zeeman and pseudo-quadrupolar contributions), match those calculated by diagonalizing the real spin Hamiltonian of the system $\delta(m_I)$ (see fig. 3.5). It is therefore demonstrated that this pseudo-contribution is particularly effective in systems with strong Hyperfine couplings.

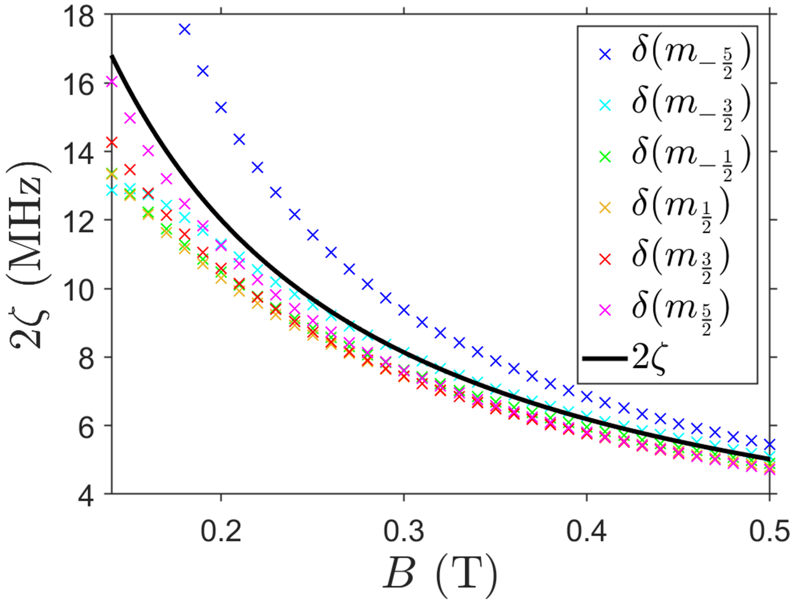

Figure 3.5: Difference in subsequent nuclear transitions energies $\delta(m_I) = (E_{m_I+1} - E_{m_I}) - (E_{m_I} - E_{m_I-1})$ in the $m_S = 1/2$ multiplet (crosses), as a function of the applied field $B\hat{\mathbf{x}}$. These values are in sound agreement with what expected from the diagonalization of the pseudo-quadrupolar Hamiltonian (black line). Reproduced from Ref. [4] with permission from the Royal Society of Chemistry.

The dephasing rates of the nuclear spin $1/T_2^{m_I,m_I'}$ are also investigated by means of the $\frac{2\pi}{3} - \tau - \frac{2\pi}{3}$ Hahn pulse sequence with increasing τ, as a function of the applied static field B_0 along molecule c-axis and ab-plane. The echo intensity decays following a single exponential law as a function of τ, for all the measured transitions (fig. 3.6). The extracted time constant $T_2^{m_I,m_I'}$ is the spin phase memory time of the system, corresponding to the lifetime of the induced states superposition. The values obtained for [VO(TPP)] are reported in figure 3.7 as a function of B_0 and show an increment from 10 μs to 60 μs with increasing field. The results are remarkable, since [VO(TPP)] T_2 values are among the highest in this category of complexes. Moreover, the phase memory times result much longer than the time expected for implementing elementary operations on the qudit system. Thus, these requisites make this complex very promising for Quantum Information Processing (QIP) applications.

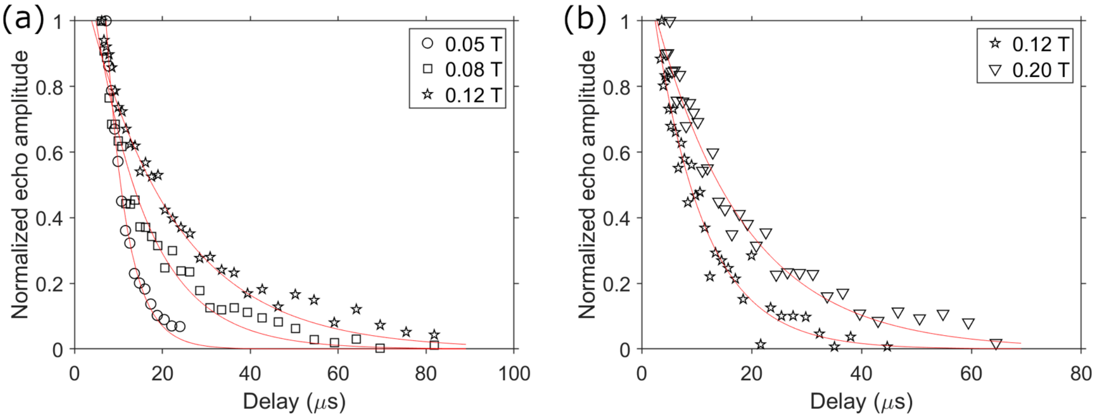

Figure 3.6: Echo intensity decay as a function of the delay between the Hahn echo exciting and refocusing pulses. The experimental data for a selected nuclear transition ((a) **AB**2, (b) **C**1) are plotted together with the relaxation rate T_2 single exponential fit for different applied fields. Reproduced from Ref. [4] with permission from the Royal Society of Chemistry.

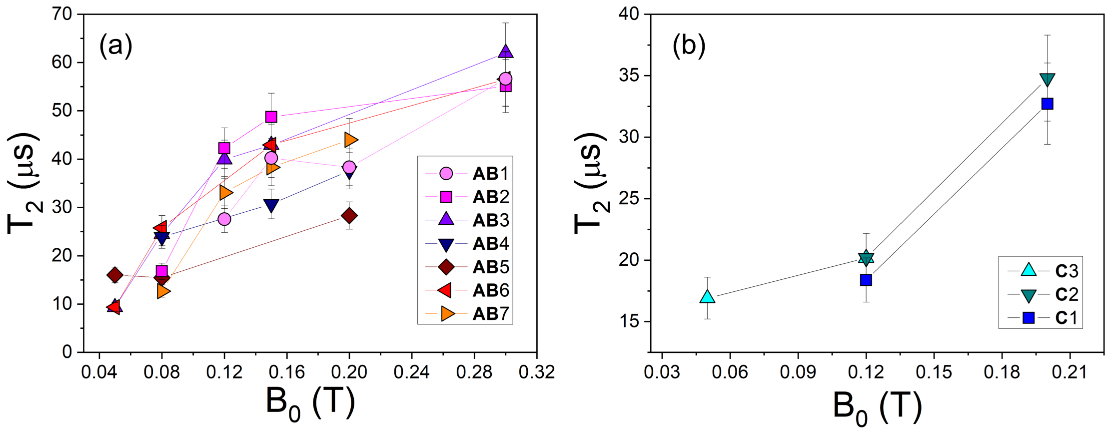

Figure 3.7: Nuclear phase memory time for different nuclear transitions, measured with a refocusing Hahn-echo sequence, as a function of the applied field B_0 (a) in the *ab*-plane and (b) along *c*-axis. Reproduced from Ref. [4] with permission from the Royal Society of Chemistry.

In a diluted sample the dipolar coupling between electronic spins and the interaction of the nuclei with surrounding electron spins are both strongly suppressed. Therefore, the nuclear spin decoherence is governed by the interaction with nearby magnetic nuclei mediated by the virtual excitation of the electronic spins. In our [VO(TPP)] molecule, this mechanism dominates over the direct nucleus-nucleus mechanism as reported for other similar compounds. [45] The electro-nuclear mixing of the system wave functions promotes this relaxation mechanism. Thus, the increment of the measured phase memory times with the applied field, is justified by an increase in the factorization of the electronic and nuclear components of the wave-function. Moreover, the increment in the electronic polarization by increasing B_0 suppresses the electronic spin fluctuations and further reduce their interaction with the probed nuclei. [113, 114]
Nuclear spin state populations can be manipulated by means of rf pulses. Indeed,

nutation experiments in which selective nuclear transitions are induced in the system have already been reported for similar molecular systems. [45] We successfully realized monochromatic Rabi nutation experiments on the [VO(TPP)] nuclear states, by selectively inducing some of the transitions highlighted above (see fig. 3.8).

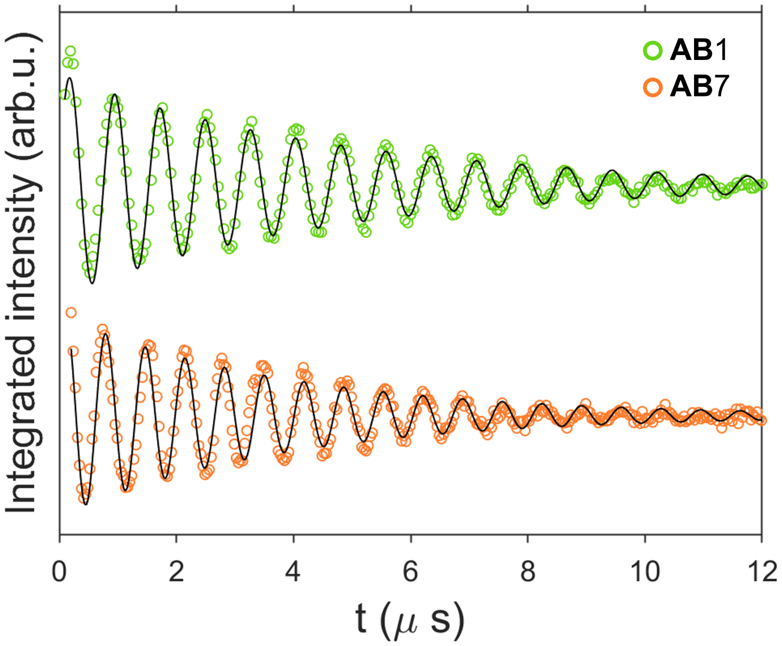

Figure 3.8: Nuclear Rabi oscillations over a wide time interval, for transitions **AB**1 and **AB**7, corresponding to the transition $m_I = -3/2 \rightarrow -1/2$ for both the lower and higher-energy electronic multiplets $m_S = \pm 1/2$, respectively. Reproduced from Ref. [4] with permission from the Royal Society of Chemistry.

The oscillations are induced with a first rf pulse resonant with a well define transition and of increasing length, followed by a standard Hahn-echo refocusing pulse. These oscillations, of frequency ω_R, can be fitted by a sinusoidal function damped exponentially $f(t) \propto e^{-\lambda t}\sin(\omega_R t)$. The pulse intensity B_1 is crucial since, as shown in figure 3.9, it is directly correlated to the Rabi frequency ω_R and to the oscillations decay time.

The Rabi frequencies ω_R are indeed observed to increase linearly with the intensity of the manipulating rf-pulse, as expected for nutations induced by coupling with a resonant field. The damping dependence on B_1 amplitude suggests that the key role in this relaxation phenomena is played by the disomogeneities of the rf exciting field at the sample, that enhance the spin-spin decoherence. The disomogeneities of B_1 depend on several non-reproducible aspects such as the the probing coil geometry, the power injected, the system-probe temperature and other experimental conditions that prevent an accurate determination. Despite this effect, for low-power selective pulses, the measured damping rate of the transient population results much lower than the time required to implement single π rotation of the spin state $\lambda^{-1} \approx 0.3-1$ μs. This means that the nuclear states of this molecular qudit can be manipulated several times before significant coherence losses.

As already stressed, it is fundamental for these transitions to satisfy the criterion of monochromaticity, that define the absence of nearby nuclear states perturbations.

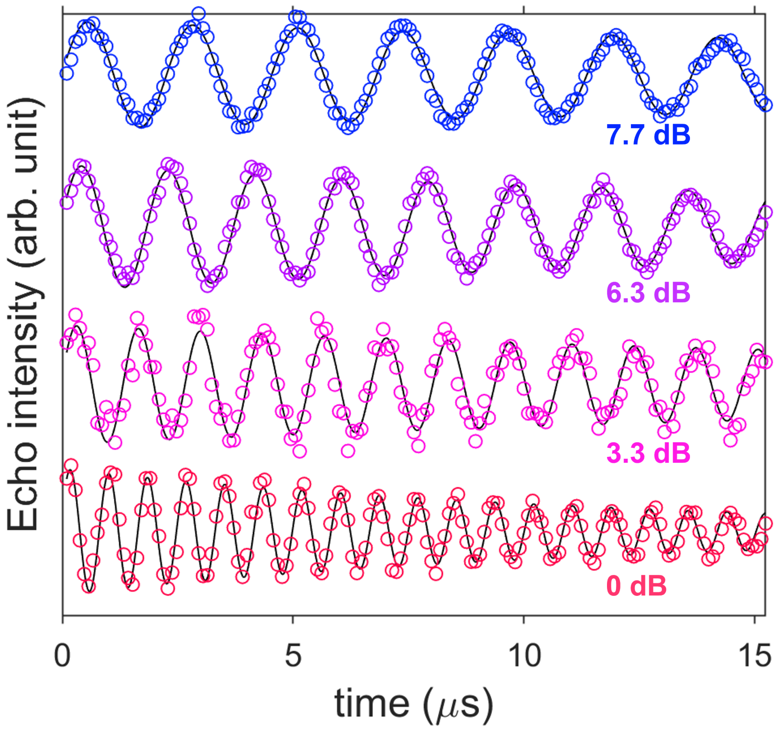

Figure 3.9: Rabi oscillations as a function of pulse B_1 attenuation, on the transition labeled **AB**1 between the states $m_I = -3/2 \rightarrow -1/2$ of the lowest electronic multiplet $m_S = 1/2$. The rf power is defined with an increasing attenuation from a reference value (0 dB). Reproduced from Ref. [4] with permission from the Royal Society of Chemistry.

Here, numerical simulation can help in the double-check of this feature for the systems at hand. Indeed, from the extensive NMR characterization we obtained the parameters of the spin Hamiltonian H_0 and the relaxation times of each specific nuclear transition. Therefore, we have all the ingredients to set up a realistic simulation of the evolution of the system under an external electromagnetic perturbation. For an open quantum system it is convenient to describe its incoherent dynamics with a master equation approach, starting from the equation of motion for the spin system density matrix $\hat{\rho}_S(t)$. As demonstrated in section 1.4, the spin dynamics of molecular nanomagnets slightly coupled to the environment can be treated with the *Linblad* master equation, which derives from a generalization of the *Liouville-von Neumann* equation for open quantum systems. In the case of this Vanadyl complex subject to a resonant ($|m_I\rangle \rightarrow |m'_I\rangle$) time dependent linear rf rectangular pulse $H_1(t)$, the *Linblad* equation can be written as:

$$\begin{aligned}\frac{d\rho}{dt} =& -i[H_0 + H_1(t), \rho] + \\ & \sum_{m_I, m'_I} \gamma_{m_I} \delta_{m_I, m'_I} [\, |m_I\rangle\langle m_I|\rho|m_I\rangle\langle m_I| - (|m_I\rangle\langle m_I|\rho + \rho|m_I\rangle\langle m_I|)/2\,], \end{aligned} \tag{3.2}$$

where the pulse is defined in interaction picture by an Heaviside function shaping the pulse and the amplitude B_1 of the linearly polarized exciting field.

We focus on the first three labeled nuclear transitions of the system, respectively **AB**1, **AB**2, **AB**3, with an applied static field of $B_0 = 0.3$ T within the ab-plane of the molecule and a perpendicular pulse B_1. These conditions, as can be seen from figure 3.3, are chosen because represent a good trade-off between the spectral separation of resonances and the electro-nuclear mixing of the wavefunctions (both field dependent). In this conditions the states can be labeled with the I_x, S_x eigenvalues, which are still good quantum numbers. Then, we simulate the effect of a $B_1 \approx 5$ G rectangular pulse resonant with the chosen transitions, with the system initialized in the targeted starting state $|m_I, m_S\rangle$. The simulated B_1 intensity is chosen in order to roughly match the oscillation frequency observed experimentally in figure 3.9 for the most attenuated power. [4, 100] The effects of the excitation can be clearly seen in the colormap of figure 3.10, where the population evolution, of all the nuclear states of the same $|m_S\rangle$ multiplet, is shown as a function of time under the effect of the B_1 pulse. It is evident that the only significant evolution is between the states resonant with the induced excitation and the population leakage to nearby nuclear state is negligible in the time scale of the simulation, which correspond to several π rotations of the nuclear state.

However, this theoretical picture does not match exactly the experimental one, since at the temperature of $T = 1.4$ K all the nuclear states $|m_I\rangle$ of both the electronic multiplets $|m_S = \pm 1/2\rangle$ are populated. We have therefore evaluated the effect of the same resonant pulse on the system with thermally populated states (not initialized on the target state as before) and the results reported in figure 3.11 are in strong agreement with those shown in figure 3.10. Therefore, also in the experimental conditions, the nuclear states of the system can be manipulated independently and with negligible effect on the surrounding states. These simulations confirmed the ability to induce coherent monochromatic oscillations of nuclear states population by means of properly tuned rf pulses.

It is worth mentioning that a condition in which only the lowest energy electronic multiplet $m_S = 1/2$ is populated can be reached also experimentally (see sect. 1.2), at temperature lower than $T < 100$ mK or by exploiting cooling algorithms, see [83].

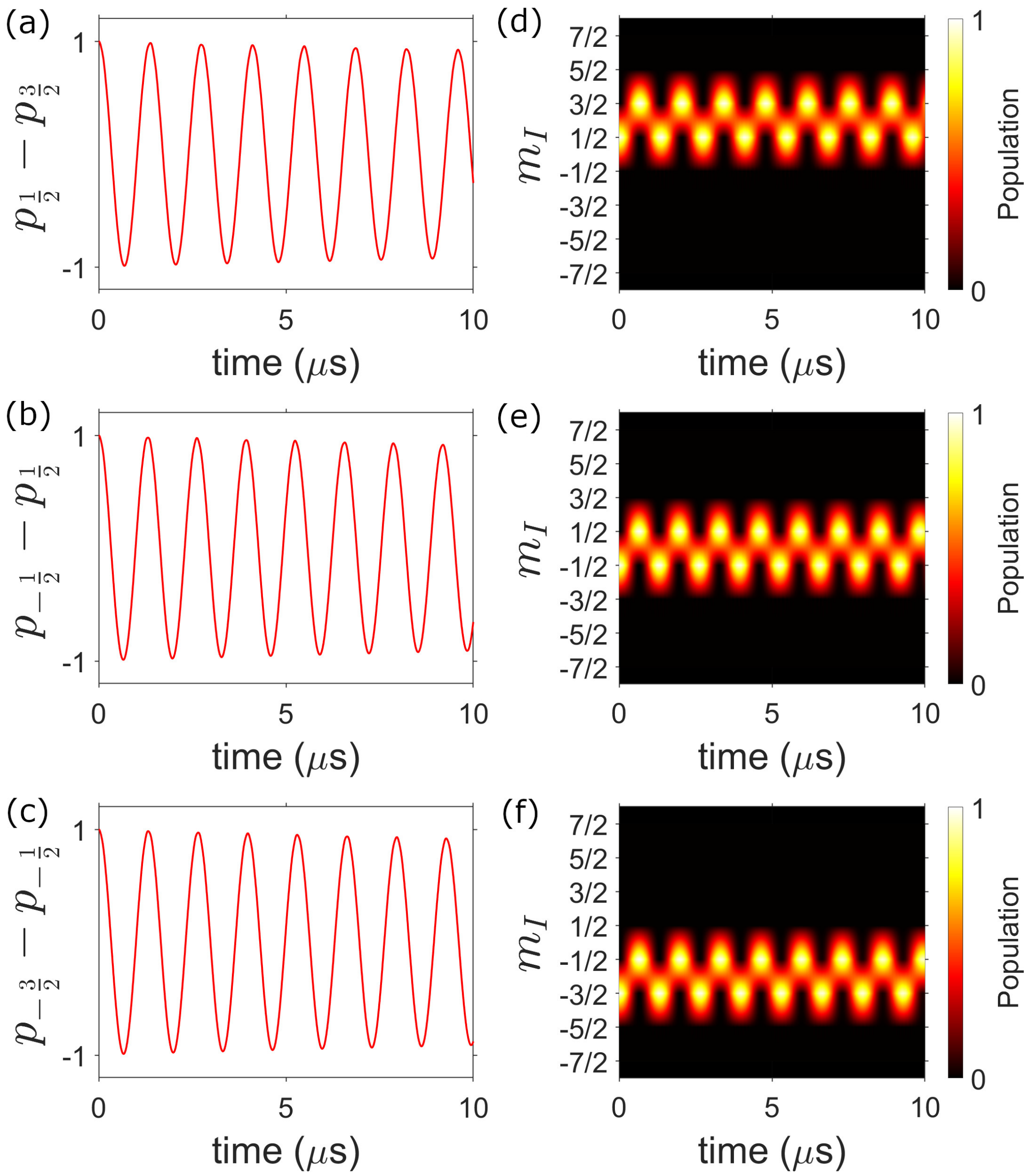

Figure 3.10: Simulated effect of a rf pulse resonant with a nuclear transition that increase the m_I value by $\Delta m_I = +1$, when the system is initialized in $m_I = 1/2, -1/2, -3/2$ (a,d; b,e; c,f respectively). On the left (a-c) the difference between target level population as a function of time. On the right (d-f) the colormap represents the population evolution with time for all the nuclear states. The pulse is applied along the molecule $\hat{x}$ axis with intensity $B_1 = 5$ G. The targeted transitions are: (a,d) $m_I = 1/2 \rightarrow 3/2$, (b,e) $m_I = -1/2 \rightarrow 1/2$, (c,f) $m_I = -3/2 \rightarrow -1/2$, with $\Delta m_S = 0$. The focus here is on the $m_S = 1/2$ spin multiplet, which is the only one populated because of the states initialization. Reproduced from Ref. [4] with permission from the Royal Society of Chemistry.

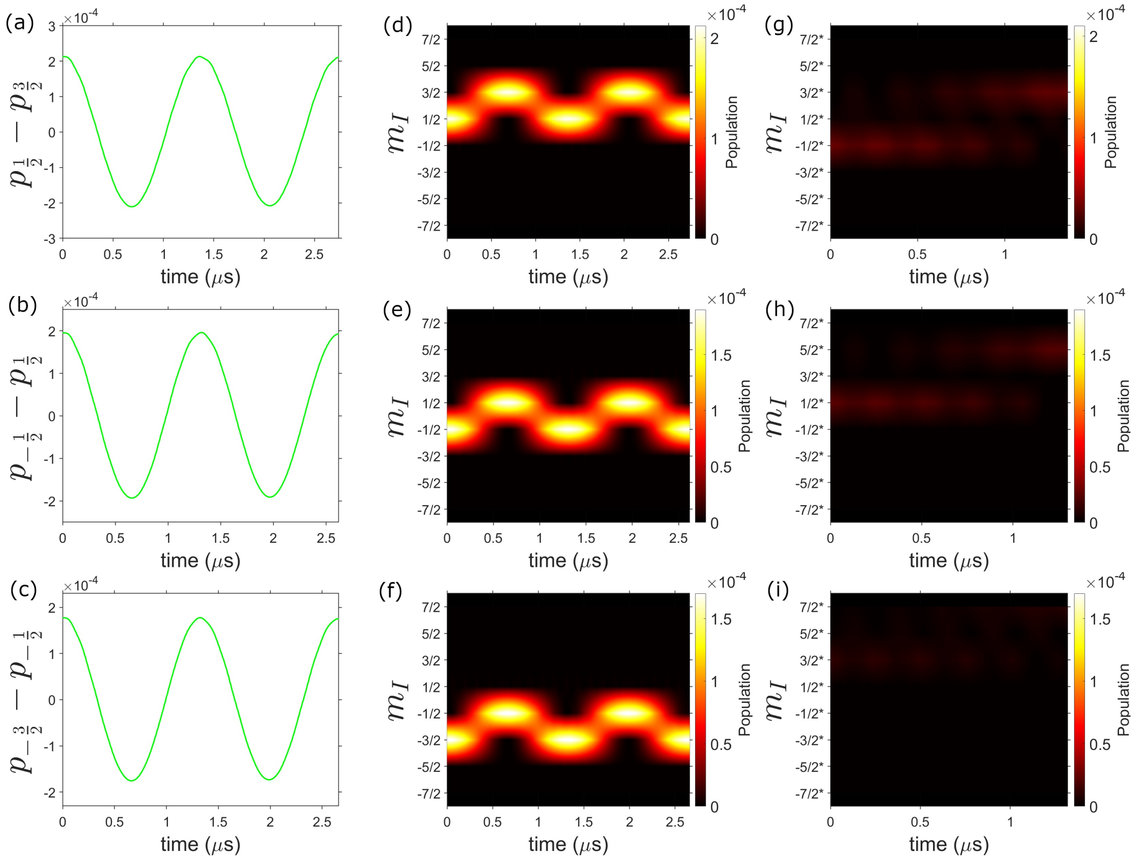

Figure 3.11: Simulated effect of a rf pulse resonant with a nuclear transition $\Delta m_I = +1$, on the thermally populated system. On the left (a-c) the difference between the target levels populations as a function of time. On the right (d-i) the colormap represents the population evolution over time for all the nuclear states of both the electronic spin multiplets $m_S = \pm 1/2$. The pulse is applied along the molecule $\hat{x}$ axis with intensity $B_1 = 5$ G. The targeted transitions are: (a-d) $m_I = 1/2 \rightarrow 3/2$, (b-e) $m_I = -1/2 \rightarrow 1/2$, (c-f) $m_I = -3/2 \rightarrow -1/2$, with $\Delta m_S = 0$. Reproduced from Ref. [4] with permission from the Royal Society of Chemistry.

3.3 Comprehensive study of an Organometallic spin Qudit with Radiofrequency and Microwave techniques

The combination of different resonance techniques can give fundamental and non redundant information on molecular systems. Indeed, by combining broadband nuclear magnetic resonance (NMR) and electron paramagnetic resonance (EPR) we achieved an extensive picture of the spin Hamiltonian and relaxation dynamics of an organometallic [V(Cp)$_2$Cl$_2$] complex (Cp = cyclopentadienyl). With these two resonance techniques we were also able to induce selective manipulations on both the electronic and nuclear spin degrees of freedom. This approach is thus of fundamental interest for studying coupled electro-nuclear qudits and for the development of tailored experimental setups embedding the ability to manipulate both electronic and nuclear spins over a wide frequency regime.
Metallorganic molecular qubits constitute a class of systems still not widely explored.

However, recently, a Ti-based organometallic molecule was reported to display interesting coherence properties.[115] Because of the great results obtained with this class of compounds in single molecule magnets science,[15] due to their prominent axial structure and bonding strength of the central ion, it is therefore interesting to study the behavior that these systems can display also as molecular qubits.
The complex investigated hereinafter, [V(Cp)$_2$Cl$_2$] (fig. 3.12), was synthesized by our collaborators at the University of Florence and at the Laboratoire National des Champs Magnétiques Intenses (LNCMI) in Grenoble (see the List of Collaborators). It display a bent-metallocene structure in which a central Vanadium atom is coordinated with two ligand-ring Cp (cyclopentadienyl). Two additional Chlorides coordinating ligands are bound to the metallic center in the plane perpendicular to the axial direction. The metallocene double-decker environment of the Vanadium is bent from the perfect axiality to a 132° angle. In order to reduce the effects of dipolar couplings in the electronic relaxation, for the spectroscopic characterization with resonant techniques, the molecule has been crystallized in an isostructural diamagnetic [Ti(Cp)$_2$Cl$_2$] analogue.

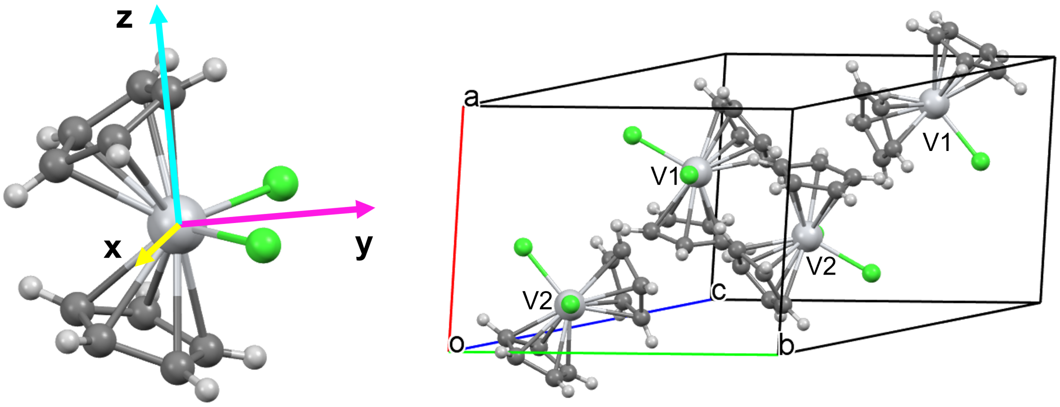

Figure 3.12: On the left, the [V(Cp)$_2$Cl$_2$] bent-metallocene structure. The molecular reference frame is shown, with the y-axis bisecting the Cl-V-Cl angle, the z-axis perpendicular to the Cl-V-Cl plane (axial direction) and the x-axis unequivocally defined. On the right the crystallographic unit cell with the two inequivalent molecules labeled as V1 and V2. Reprinted with permission from Ref. [12]. Copyright 2021 American Chemical Society.

The diluted crystals (for three different crystalline dispersion 10% (**3a**), 1% (**3b**), 0.1%(**3c**)) crystallizes in a triclinic P$\bar{1}$ space group and possesses two crystallographically inequivalent molecules in the unit cell. The comparison between different concentrations of diamagnetic dilution permits to interpret the electronic dipolar contribution to the electronic relaxation dynamics.
The crystal (fig. 3.13) grows in a block shape, exposing the crystallographic planes (111) (growth direction), (010) and (10$\bar{1}$). These crystal directions are used as a guideline for the orientation of the crystal in the experiments and thus, for the sake of simplicity, are labeled referring to their length. Therefore, when the static field in the NMR spectra of figure 3.16 is applied along the "longer" crystal edge (**L**), corresponding to the crystal direction [010], the field is labelled B_L. The same stand for the "shorter" edge (**S**) and the one which length is in between the two above

(**M**) (see fig. 3.13). However, because of the crystallographic inequivalence, each of the previously defined directions comprises two different configurations of the field with respect to the two molecules (fig. 3.14).

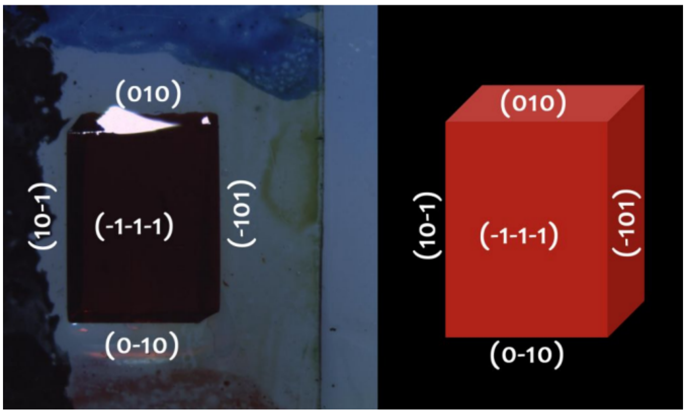

Figure 3.13: Picture of the crystal collected from microscopy (left) and a sketch of the crystal shape (right). The two are compared to show the edge length hierarchy and the relative indexing of crystal faces with the corresponding crystallographic planes. Reprinted with permission from Ref. [12]. Copyright 2021 American Chemical Society.

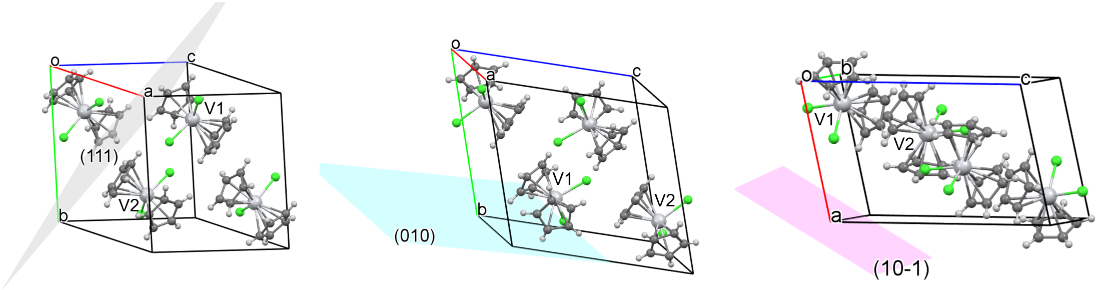

Figure 3.14: The crystallographic planes (111), (010) and (10-1), that correspond to the crystal faces, are highlighted in the unit cell. This sketch assist in the visualization of the applied field directions with respect to the molecular reference frame. Reprinted with permission from Ref. [12]. Copyright 2021 American Chemical Society.

To determine the spin Hamiltonian parameter of this systems a hybrid NMR-EPR approach was used for the first time. Indeed, the two techniques (see sect. 2.1.2 and 2.1.1) features different resolution and sensibility to each of the spin Hamiltonian terms. The starting point is the electro-nuclear spin Hamiltonian, written as:

$$H_0 = \mu_B \hat{\mathbf{S}} \cdot \mathbf{g}_S \cdot \mathbf{B}_0 + \hat{\mathbf{I}} \cdot \mathbf{A} \cdot \hat{\mathbf{S}} + \mu_N g_N \hat{\mathbf{I}} \cdot \mathbf{B}_0 + \hat{\mathbf{I}} \cdot \mathbf{P} \cdot \hat{\mathbf{I}}. \tag{3.3}$$

Here, the first two terms correspond to the electronic Zeeman term and to the Hyperfine coupling between the electronic and the nuclear spins. The other two terms constitute the fine-structure Hamiltonian of section 1.3 and correspond to the nuclear quadrupolar and the nuclear Zeeman couplings.

Continuous wave (CW) X-band and Q-band EPR spectra (9.405 GHz and 33.7 GHz respectively) were measured by our collaborators at the University of Florence and at the Laboratoire National des Champs Magnétiques Intenses (LNCMI) in Grenoble, (see the List of Collaborators) on the diluted powders (shown in fig. 3.15-(a,b) for sample **3c**). The spectra clearly show the eight spectral lines induced by the Hyperfine coupling with the ^{51}V nuclear spin, corresponding to the eight electronic transitions $m_S = \pm 1/2$ at fixed nuclear components $\Delta m_I = 0$.

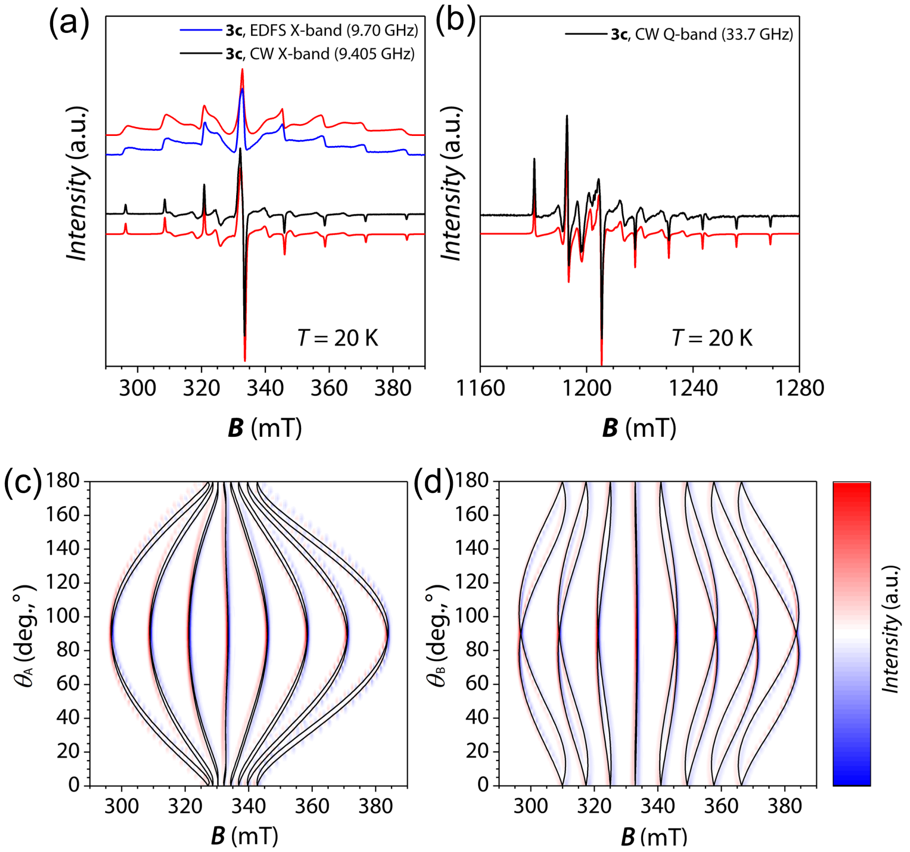

Figure 3.15: (a) Continuous Wave ($\nu = 9.405$ GHz, black) and Echo Detected Field Sweep ($\nu = 9.70$ GHz, blue) X-band EPR powder spectra of sample **3c** measured at $T = 20$ K. The spectra are both simulated (red) using the Hamiltonian parameter of table 3.2. EDFS is translated in B for better comparison. (b) CW-EPR Q band spectrum ($\nu = 33.7$ GHz, black). (c,d) 2D colormap (blue negative, red positive) of **3c** single crystal X-band EPR spectra as a function of θ_A and θ_B rotations. Black lines correspond to the simulated spectra for the two inequivalent molecules. It is evident the overlap of the two spectra along the reference frame axis ($\theta_{A,B} = 0°, 90°$) within the EPR resolution. Reprinted with permission from Ref. [12]. Copyright 2021 American Chemical Society.

The X and Q band EPR spectra are fitted only with the first two components of the spin Hamiltonian 3.3, i.e. the electronic Zeeman and the Hyperfine couplings, refining the spectroscopic **g** and Hyperfine **A** tensors. This because it was not possible to deduce the small nuclear interaction terms from the experimental resolution of this technique. To reproduce the data the two tensors are considered rhombic and collinear. The final values are shown in table 3.2 after the subsequent NMR refinements. Interestingly, it was not necessary for simulating the experiments results to assume different parameters for the two molecules in the unit cell. This proves that the two molecules differs only in the orientations within the crystal, which are averaged out by measuring powder samples.

The single crystal EPR investigation enables the determination of the relative molecules orientations. Starting with the external field applied along the (111) crystal face, the sample has been rotated step by step inside the cavity and the field dispersion of the resonances has been recorded in the angluar range $\theta = 0°$ to $\theta = 180°$ (fig. 3.15). The rotational axes were the edge between (111) and (010) planes (θ_A) and the edge between (111) and ($\bar{1}01$) planes (θ_B). The rotational axes defined above correspond with the molecular frame defined in figure 3.12, with θ_A corresponding to the rotation from x to z and θ_B corresponding to the rotation from y to z. For both the rotational axis, at 0° and 90° the spectra of the two molecules overlap in a single eight-line Hyperfine structure. This confirms that, within the experimental resolution of CW-EPR, their magnetic tensors appear to share the same orientation with respect to the applied field (see fig. 3.12). As we will see in the following, this aspect will be refined by the NMR analysis which features a finer sensitivity on the hyperfine components and enables to observe a slight misalignment of the magnetic tensors, not appreciable in CW-EPR.

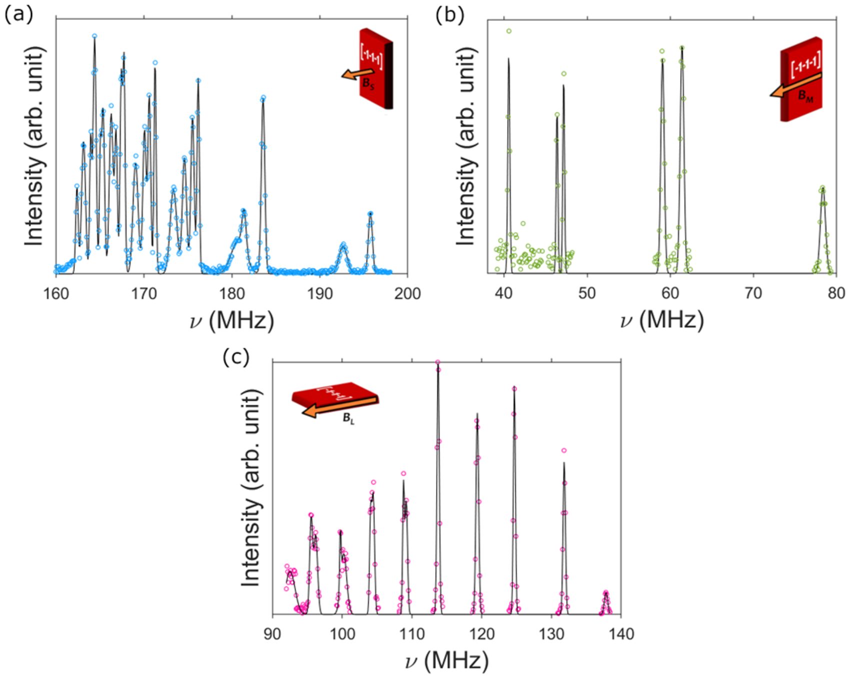

Figure 3.16: Broadband NMR spectra measured at $T = 4$ K at fixed applied static field $B_0 = 0.2$ T, for the field directions $\mathbf{B}_S$, $\mathbf{B}_M$, $\mathbf{B}_L$ schematized in inset with respect to the crystal faces. In black, the Gaussian spectral lines fitting. Reprinted with permission from Ref. [12]. Copyright 2021 American Chemical Society.

For investigating the nuclear fine-structure components of the spin Hamiltonian 3.3, ^{51}V ($I = 7/2$, $\gamma/2\pi = 11.21$ MHz) broadband NMR spectra were measured at T=4 K in the field range B_0=0 to 0.4 T, exploiting the "HyReSpect" spectrometer [11] at the University of Parma. The [V(Cp)$_2$Cl$_2$] single crystal **3b** was installed on a specifically printed sample holder, in order to apply the static magnetic field as much as possible along the crystal faces labeled as L, M and S. The field orientation was subsequently further refined as a fitting parameter of the spectra. Figure 3.16 shows an example of spectra collected in each of the field configurations ($\mathbf{B}_S$, $\mathbf{B}_M$ and $\mathbf{B}_L$). Despite the resonance overcrowding (14 nuclear transitions multiplied for the two molecules), thanks to the fine experimental resolution, all the transitions are distinguishable and can be fitted by attributing a Gaussian line-shape to each resonant frequency. The evolution of the NMR peak frequencies as a function of the applied field has been fitted with the model spin Hamiltonian in order to refine the parameter obtained by CW-EPR and to evaluate also the nuclear quadrupolar and Hyperfine contributions. Only the electronic spectroscopic **g** tensor was kept fixed from the EPR analysis, which is more sensitive to its determination. The fitting of the spectral components at different applied field is shown in figure 3.17.

The achieved agreement between the data and the modeled electro-nuclear spin Hamiltonian is excellent even when considering both the molecules in the unit cell (red and black lines). All the spin Hamiltonian parameters obtained from this double technique refining approach are shown in table 3.2 below.

[V(Cp$_2$)Cl$_2$] spin Hamiltonian

	A (MHz)	**p** (MHz)	$\mathbf{g}_S$ (MHz)
x	-55 ± 2	0.09 ± 0.01	$2.0010 \pm 5 \times 10^{-4}$
y	-216 ± 2	$0.09 \pm 0.01)$	$1.9834 \pm 5 \times 10^{-4}$
z	-315 ± 2	-0.18 ± 0.01	$1.9721 \pm 5 \times 10^{-4}$

Table 3.2: Best fit parameter of the [V(Cp)$_2$Cl$_2$] spin Hamiltonian 3.3. [12]

Both the spectroscopic **g** and Hyperfine **A** tensors show a rhombic symmetry, while a modeled nuclear quadrupolar contribution, axial along the Cp-V-Cp double-decker axis, was essential for the reproduction of NMR spectra. Apart from the nuclear fine structure components of 3.3, broadband NMR also enables an accurate refinement of the Hyperfine tensor values and absolute sign. The latter is in fact not accessible in CW-EPR.

By diagonalizing the spin Hamiltonian 3.3, we calculate the system energy levels for the three external field configurations, shown in figure 3.18. While the electronic multiplets splitting is not widely affected by the orientation of the field, the nuclear multi-level structure is strongly modified. Indeed, the remarkable differences in the hyperfine components causes the overall nuclear splitting to vary significantly between the three configurations. Moreover, rather than the small nuclear quadrupolar coupling, it is the hyperfine terms transverse to the applied field responsible for the second-order pseudo-quadrupolar effect that play a key role here in the intra-multiplet gaps anisotropy. The calculated energy levels fulfill the requirements for a promising qudit candidate. Indeed, the nuclear dynamics is conditioned by the electronic spin state, since the two m_S multiplets are well distinguished in energy. Moreover, the anisotropy in the nuclear transitions excitation energies is sufficient to enable their selective excitation with state of the art resonators.

The energy levels of the two inequivalent molecules are identical, with the exception of small differences due to the direction of the applied field in the reference frame of the two molecules. These small differences are however sufficient to distinguish the excitation spectral frequencies of each molecule, in most of the applied field

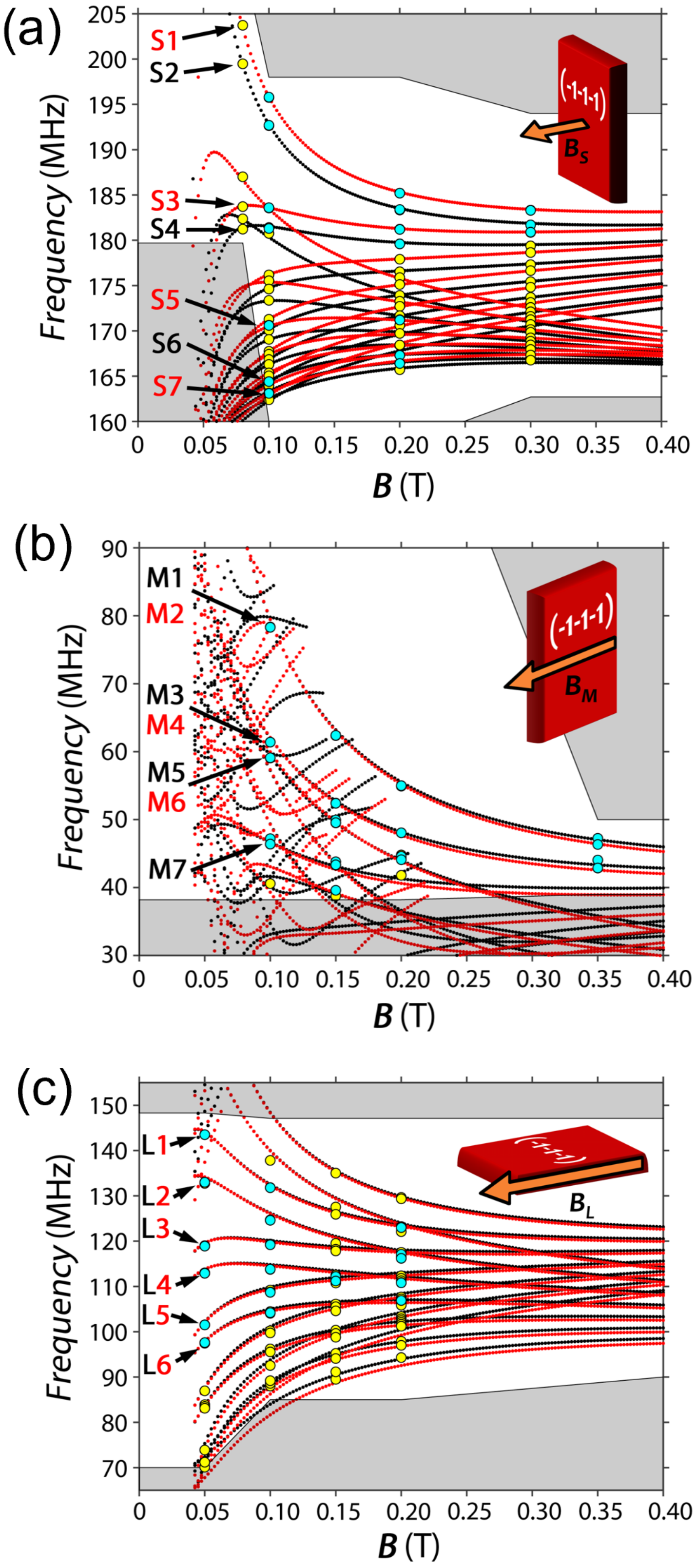

Figure 3.17: The measured NMR frequencies for a single crystal of **3b** (yellow and cyan dots) are compared with the spin Hamiltonian fitting model (black and red dots for each molecule, respectively). The applied field directions $\mathbf{B}_S$, $\mathbf{B}_M$, $\mathbf{B}_L$ are schematized in inset. Cyan experimental points label the transitions whose ${}^nT_2$ was measured. Shaded areas were not explored experimentally. Reprinted with permission from Ref. [12]. Copyright 2021 American Chemical Society.

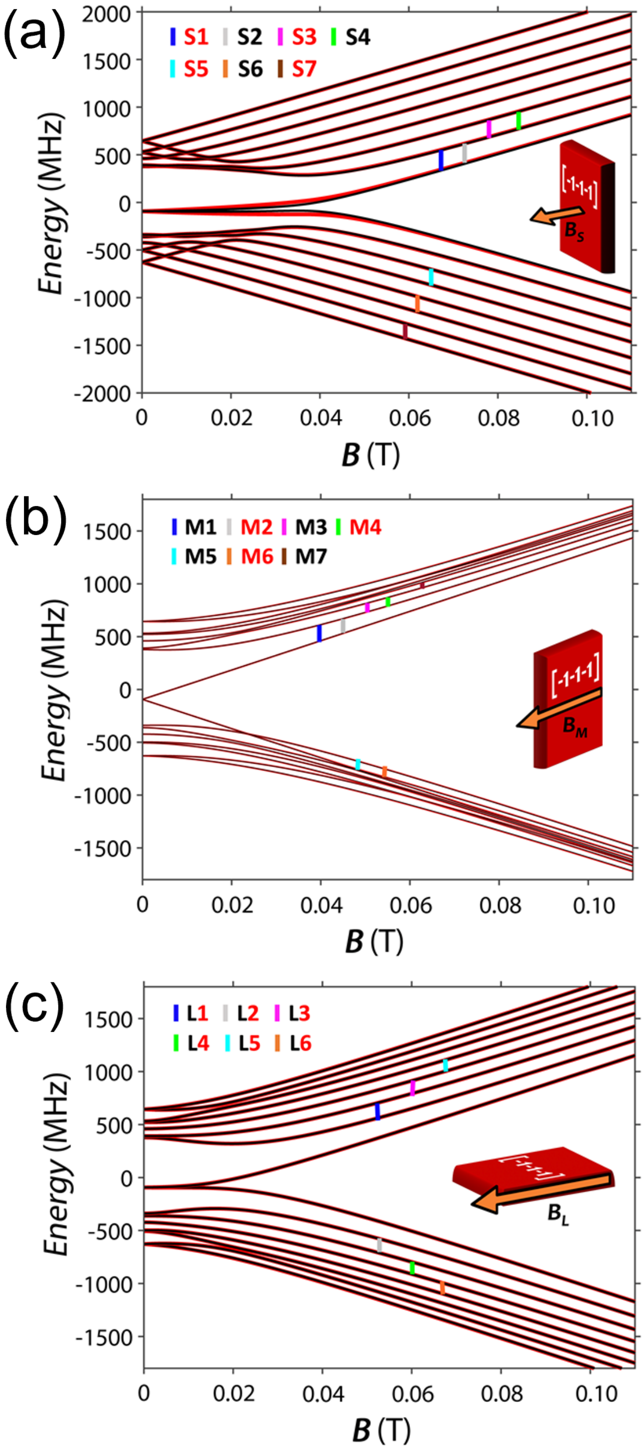

Figure 3.18: Calculated energy levels for the experimental field configurations $\mathbf{B}_S$, $\mathbf{B}_M$, $\mathbf{B}_L$ with respect to the crystal faces. Black and red lines relates to the two inequivalent molecules. For the nuclear transitions labeled by vertical colored lines it was also measured the nuclear phase memory time ${}^{n}T_2$ (fig. 3.19). Reprinted with permission from Ref. [12]. Copyright 2021 American Chemical Society.

conditions explored experimentally (see fig. 3.17).

The multitechnique approach exploited here has proven to be also essential in the study of the relaxation and coherence times of the electro-nuclear coupled system. An echo detected field sweep (EDFS) experiment performed by our collaborator at the University of Turin (see the List of Collaborators) with the pulsed EPR technique in the X band (fig. 3.15-(a)) confirms the presence of electronic coherence also at temperatures above 20 K. The electronic spin-lattice relaxation time ${}^{e}T_1$ was measured as a function of temperature on powders, with an inversion-recovery sequence. The applied field was fixed at 0.334 T in order to match the higher intensity transition in the spectra, corresponding to $\Delta m_S = \pm 1$ and $\Delta m_I = 0$ from $m_I = -1/2$. The recovery rates at fixed temperature were fitted with a stretched single exponential saturation model $I = I_0 + C_1 \exp(-(\tau/{}^{e}T_1)^{\beta})$. The extracted relaxation times ${}^{e}T_1$ are shown in figure 3.19. We observe a maximum and then flat relaxation rates below 10 K, with values increasing with dilution. At higher temperatures the relaxation time decreases abruptly and becomes independent from the dilution percentage. This anomalous temperature dependence of ${}^{e}T_1$ has been modeled by the sum of a direct and a Raman-like contributions to relaxation, dominating at lower and higher temperature, respectively:

$$ {}^{e}T_1^{-1} = aT + bT^n. \tag{3.4} $$

The evident difference with respect to other Vanadium based molecular system that display spin coherence approaching room temperature,[5, 6] can be linked to an unexpectedly efficient Raman-like path for relaxation, whose exponent approach $n = 5$ in the phenomenological model used here. The dilution-dependent differences are instead related to the enhanced dipolar interaction. A finer model for relaxation in the high temperature regime can be setup by making explicit the coupling of the spin with local vibrational modes:[116]

$$ T_1^{-1} = cT + d\frac{\exp(\hbar\omega/kT)}{(\exp(\hbar\omega/kT) - 1)^2}. \tag{3.5} $$

This more detailed model indeed refined the fit in figure 3.19 and suggests that a potential important role in the abrupt decrease of the relaxation time at 30-40 K is played by an optical phonon with energy $\hbar\omega \approx 14$ meV, together with low energy phonons ($\hbar\omega \approx 2-6$ meV) commonly involved in these processes. Spaces for a finer and in-depth analysis of the relaxation processes were left to a future dedicated work.

Electronic quantum coherence ${}^{e}T_m$ as a function of temperature was also investigated by our collaborators at the University of Turin (see the List of Collaborators) by pulsed X-band EPR on the same spectral line (0.334 T), with a Hahn-echo decay experiment. The echo decays were fitted with a stretched exponential decay $I = I_0 + C_2 \exp[-(2\tau/{}^{e}T_m)^{\beta}]$ and the extrapolated coherence times are shown in figure 3.19-(a). The rates are temperature independent below 40 K and in the order of magnitude of the μs (2.3 μs for the higher dilution). Thus, the low temperature coherence times are comparable with other parents compounds. [6, 35] The concentration dependence also below 1% suggests that in this temperature range the relaxation is still due to the electronic spin-spin interaction, that dominates over the less effective electron-nuclear interaction, despite the abundance of spin active nuclei (^{1}H). At higher temperature the spin coherence time ${}^{e}T_m$ shares with the spin lattice ${}^{e}T_1$ a similar abrupt drop. Even if ${}^{e}T_m$ is not limited by ${}^{e}T_1$ in this temperature range, it is clear that the two phenomena are correlated. A possible explanation is that the faster spin-lattice relaxation ${}^{e}T_1$ causes faster pronounced electronic fluctuations that directly impact the spin coherence ${}^{e}T_m$. Thus, in the definition of the electronic coherence time $1/{}^{e}T_m = 1/{}^{e}T_2 + 1/2{}^{e}T_1$ the spin-lattice ${}^{e}T_1$ cannot be neglected, even if the spin-spin relaxation ${}^{e}T_2$ is still the dominant contribution.

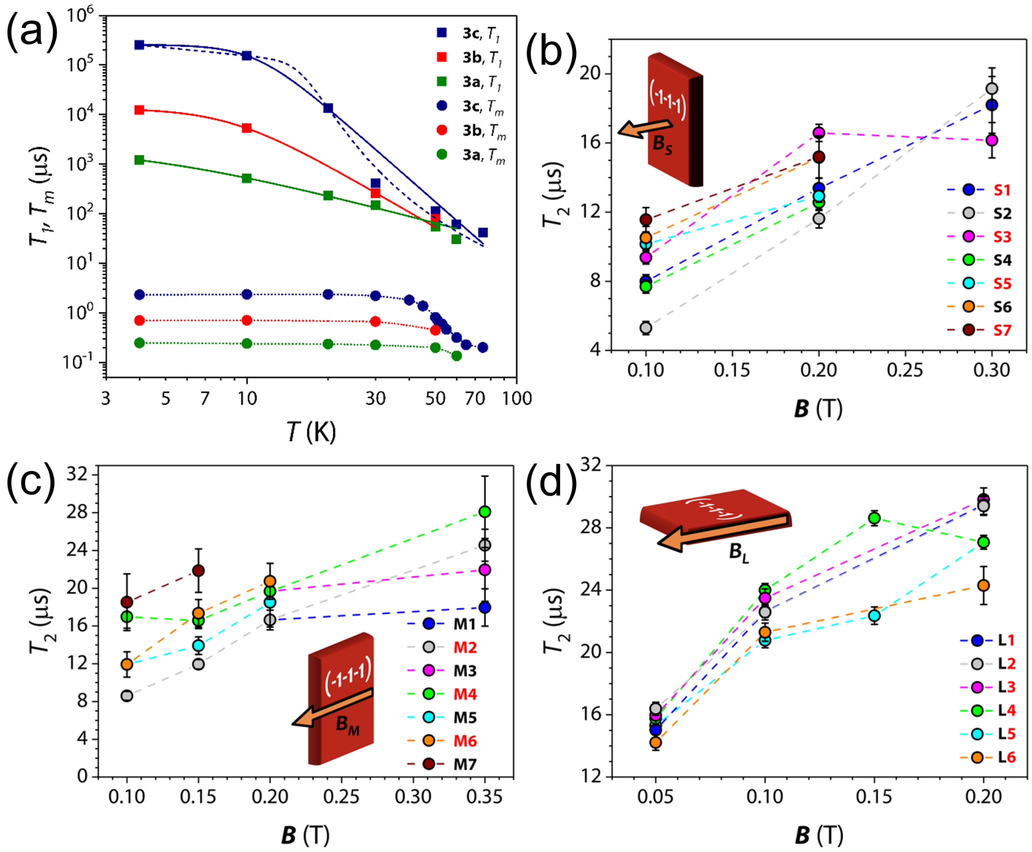

Figure 3.19: (a) Temperature evolution of the electronic spin-lattice ${}^{e}T_1$ and spin coherence ${}^{e}T_m$ relaxation times, for each dilution percentage of [V(Cp)$_2$ Cl$_2$]. Solid and dashed lines represent respectively the models 3.4 and 3.5 fitting results. (b,c,d) Nuclear phase memory time ${}^{n}T_2$ measured on dilution **3b** for the transitions labeled in figure 3.18 at $T = 4$ K as a function of the applied field, for $\mathbf{B}_S$, $\mathbf{B}_M$, $\mathbf{B}_L$ configuration, respectively (sketch in inset). Reprinted with permission from Ref. [12]. Copyright 2021 American Chemical Society.

Nuclear phase memory times were also investigated for a single crystal of sample **3b** (1 % dilution). The measurements have been performed at the University of Parma on the "HyReSpect" [11] broadband NMR spectrometer (see 2.1.1). Hahn-echo decays were measured as a function of the applied field, for all the transitions labeled in the energy levels scheme of figure 3.18. The echo decays as a function of the delay τ between the exciting and refocusing $2\pi/3$ rf-pulses, was modeled with a single exponential $M(\tau) = M_0 \exp(-2\tau/{}^{n}T_2)$ (fig. 3.20). The extracted phase memory times ${}^{n}T_2 \approx 20 - 30$ μs are competitive with respect to parent compounds as the [VO(TPP)] reported in section 3.2 and in Ref.[4].

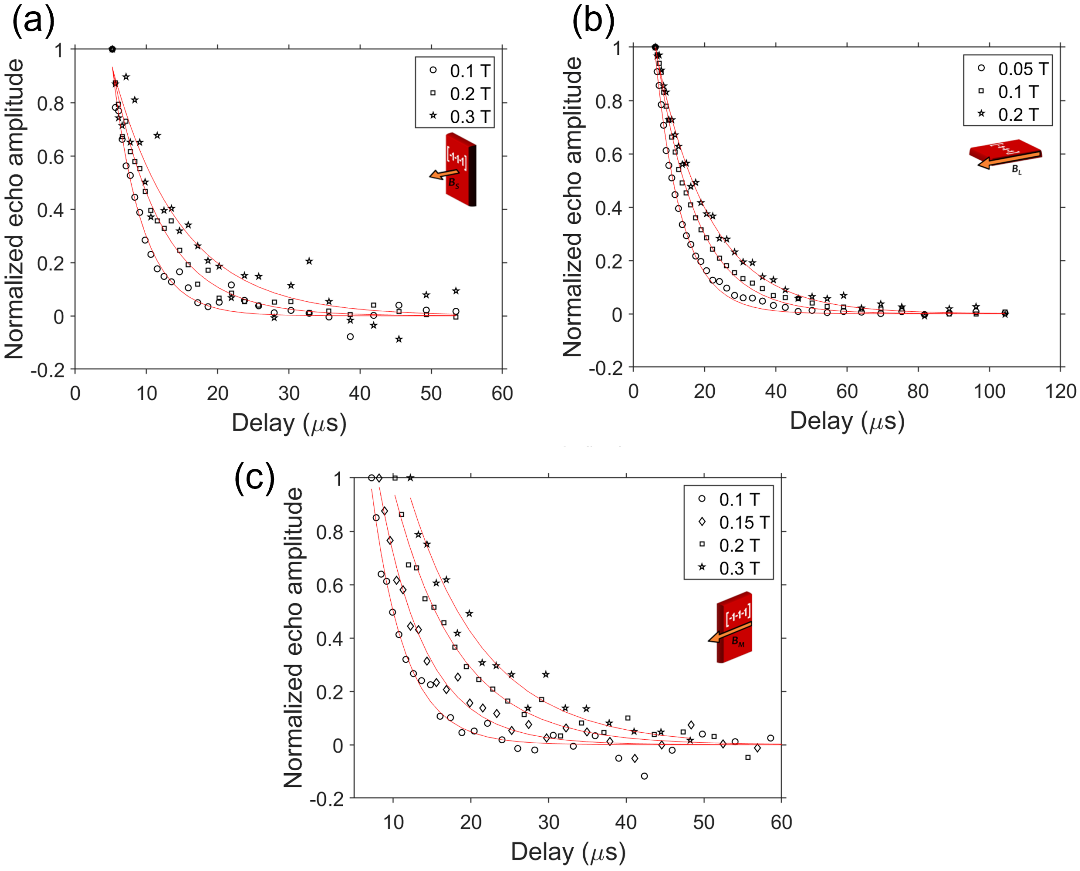

Figure 3.20: Transverse magnetization decay from NMR echo relaxation experiments, as a function of the delay τ between exciting and refocusing pulses, at $T = 4$ K and fixed static field B_0, along $\mathbf{B}_S$ (a), $\mathbf{B}_L$ (b), $\mathbf{B}_M$ (c) for transitions **S1**, **L2**, **M2**. Lines shows the single exponential decay fitting. Reprinted with permission from Ref. [12]. Copyright 2021 American Chemical Society.

The nuclear coherence increases with the applied field, because of the simultaneous reduction of the electro-nuclear mixing of the wave functions and increment of the electronic polarization. Indeed, the dominant phenomenon that times the nuclear decoherence is the indirect dipolar interaction with nearby nuclear and electronic spins. The latter is severely reduced by dilution in diamagnetic analogues (titanium(IV) in this case).

Considering the above results for the electronic and nuclear spin coherence times, this systems can be unequivocally considered a promising coupled qubit-qudit system. The further step to confirm this claim and prove that the coherence times allows arbitrary and selective manipulations of the electronic and nuclear multilevel structure, is to realize experimentally electronic and nuclear spin nutation experiments. Low temperature electronic Rabi oscillations were realized on crystal powders at X-band frequency by our collaborators at the University of Turin (see the List of Collaborators). The system is targeted by a first resonant pulse of variable length $\theta(t)$ that excites the chosen transition, followed by the canonical $\pi - \tau - \pi/2$ Hahn-echo refocusing sequence to stimulate the spin-echo. The Rabi frequency ${}^{e}\omega_R$ (fig. 3.21) scales linearly with the manipulation pulse amplitude. To further support the selectivity of the excitation, the calculated frequency domain spectra (fig. 3.21-(b)) are basically monochromatic, showing only the genuine Rabi ${}^e\omega_R$ contribution and a small contamination in correspondence of the proton (^{1}H) nuclear Larmor frequency e^{ω}_H, which are inevitably coupled with ^{51}V.

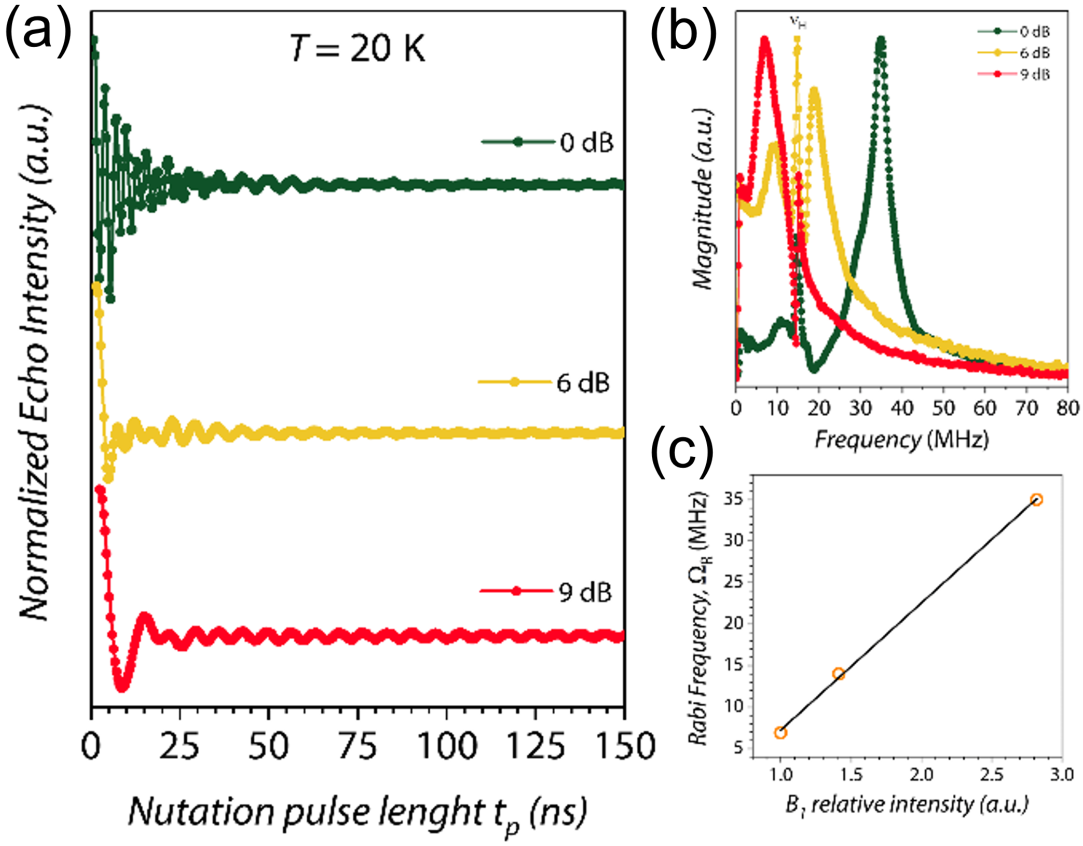

Figure 3.21: (a) Electronic Rabi nutation experiments (EPR X-band) on **3c** at $T = 20$ K at different excitation powers. (b) Frequency domain picture to highlight the monochromaticity of the oscillations. (c) Linear dependence of Rabi frequency ($\Omega_R = \omega_R/2\pi$) on the exciting microwave pulse amplitude B_1. Reprinted with permission from Ref. [12]. Copyright 2021 American Chemical Society.

Nuclear coherent manipulations were also realized at the University of Parma for various field directions with respect to the **3b** single crystal (see fig. 3.22). A first rf exciting pulse of variable length $\theta(t)$ resonant with a specific nuclear transition and with a narrow bandwidth is used to selectively induce the transition of interest. Then, the stimulated spin excitation is refocused by a subsequent π pulse for the detection of the echo intensity. The induced Rabi oscillations are damped by a factor λ that combines the effects originating from the system nuclear coherence times and the inomogeneities of the manipulating rf-field. The latter generally dominates over the long phase memory times of these systems. The oscillations are thus modeled with an exponentially damped oscillator function $I \propto \exp(-\lambda t)\sin({}^n\omega_R t)$. For all the field directions and pulse powers probed, the damping rate is considerably longer than the time required to induce a single inversion (π pulse) of the nuclear spin system. Combining this results with the fact that the damping is mainly due to the experimental inomogeneities of the manipulating field, we can firmly conclude that several manipulations of the nuclear spin state are possible before significant coherence losses.

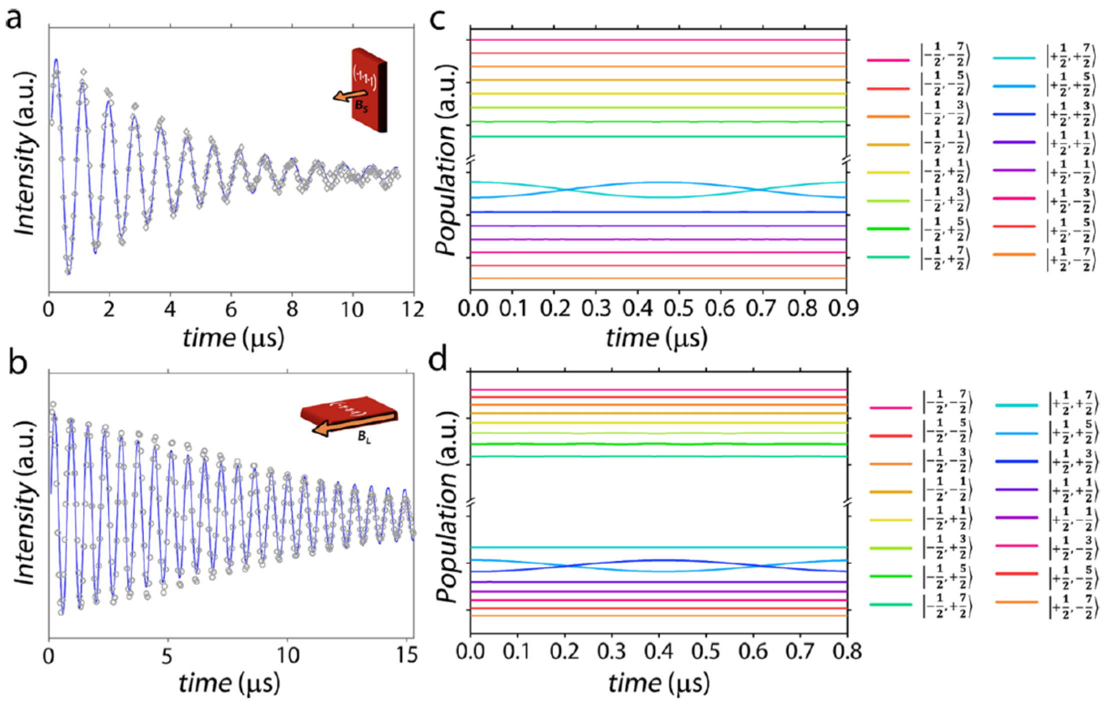

Figure 3.22: (a,b) Nuclear Rabi nutation experiments on transitions **S1** and **L1**, respectively, at $T = 4$ K and fixed field $B_S = B_L = 0.1$ T, on a single crystal of **3b**. Differences in the oscillations damping rates λ_S, λ_L are attributed to the inhomogeneities of the applied field with respect to crystal rather than to ${}^nT_2$, which is comparable for the two transitions. (c,d) Nuclear states population changes induced by the Rabi sequence for transitions **S1** and **L1** simulated by numerically solving the Lindblad master equation for a single π rotation of the nuclear spin system. All the states are labeled by the nuclear spin component m_I (accurate at more than 99 % because of state factorization at this field). The only levels that undergoes significant population changes are the targeted ones. Reprinted with permission from Ref. [12]. Copyright 2021 American Chemical Society.

The capability of selectively address the $\Delta m_I = \pm 1$ nuclear transitions, thus to induce monochromatic Rabi oscillations, was also confirmed by simulating the time evolution of the system targeted by a resonant rf perturbation. By implementing the measured spin Hamiltonian parameters of table 3.2 and the decoherence times into the Lindblad master equation 3.2 (sect. 1.4) for the time evolution of the system density matrix ρ, this simulation can realistically depict the system evolution. In figure 3.22-(c,d) we show the simulated evolution of the nuclear states populations when the molecule is addressed by a rf-pulse B_1 resonant with a single nuclear transition. The pulse amplitude is chosen in order to minimize the excitation bandwidth, within the realistic capabilities of our broadband NMR experimental setup. [11] It is evident that only the targeted levels undergoes a change in their populations, while the other nuclear states are practically unperturbed. Therefore, for both the field configurations studied, the gate fidelity for a π rotation is calculated to be around 99.99%.

In the perspective of efficiently implementing complex quantum algorithms on this nuclear multi-level structure, it was also demonstrated that subsequent nuclear states can be manipulated by a trivial sequence of pulses, without affecting the other nuclear states involved (see fig. 3.23). Thus, this organometallic [V(Cp)$_2$Cl$_2$] coupled electronic qubit-nuclear qudit shows promising properties for the applications in QIP, featuring the possibility to manipulate coherently and independently both the electronic and nuclear degrees of freedom, by coupling with external electromagnetic pulses.

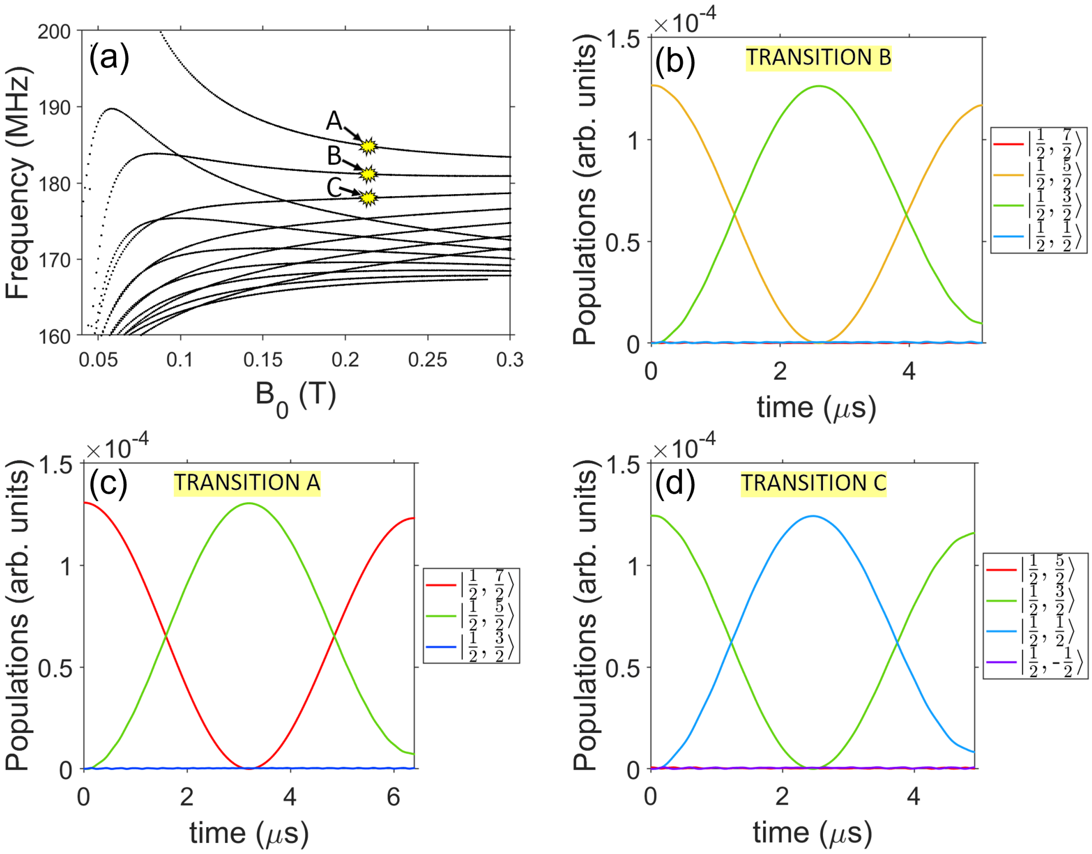

Figure 3.23: (a) Calculated spectral frequency of three subsequent transitions A, B and C, belonging to the same electronic multiplet. The static field is applied along $\mathbf{B}_S$. (b,c,d) Simulated coherent Rabi oscillations, corresponding to the transitions A: $m_I = 7/2 \rightarrow 5/2$ (b), B: $m_I = 5/2 \rightarrow 3/2$ (c) and C: $m_I = 3/2 \rightarrow 1/2$ (d). The leakage to the other nuclear states is negligible. The optimal excitation conditions for monochromatic oscillations are found to be: $B_0 = 0.22$ T and $B_1 = 2$ G. The resulting inversion (π-pulse) is still much shorter than the phase memory time ${}^nT_2$ corresponding to this transitions. Reprinted with permission from Ref. [12]. Copyright 2021 American Chemical Society.

3.4 Encoding a QEC algorithm on the [VO(TPP)] molecular qudit

In section 3.2, we introduced a prototypical molecular qudit and we demonstrate that it is promising for application in Quantum information processing. The step further is the investigation of the feasibility of a real qudit-based quantum algorithms. The enlarged Hilbert space of molecular qudits are particularly suited for the implementation of quantum error corrections codes at the single molecule level.[47, 88, 117]
As a test bed for the Vanadium-based molecular qudit [VO(TPP)] we thus chose to simulate the implementation of the encoding operations of the quantum error correction protocol proposed in Ref. [88]. The encoding consists in a replacement of the canonical definition of the basis quantum states, where the logical units $|0_L\rangle$ and $|1_L\rangle$ are represented by individual spin components m_I (e.g. $|0_L\rangle = |1/2\rangle$ and $|1_L\rangle = |-1/2\rangle$). Instead, the new error protected logical units $|0_L\rangle$ and $|1_L\rangle$ are defined by a non-trivial superposition of nuclear m_I states:

$$\begin{aligned}|0_L\rangle &\rightarrow \frac{|-3/2\rangle + \sqrt{3}|1/2\rangle}{2}\\ |1_L\rangle &\rightarrow \frac{\sqrt{3}|-1/2\rangle + |3/2\rangle}{2}.\end{aligned} \tag{3.6}$$

This "code word" composition of the logical units enables the correction of the error induced by pure dephasing effects of the spin system, by also exploiting the coupling of the nuclear states with the electronic ancilla. [88] We thus focus on the $m_I = -3/2, -1/2, 1/2, 3/2$ nuclear levels of the lowest electronic multiplet $m_S = -1/2$. The transitions between these levels have been already labeled as **AB**1, **AB**2, **AB**3, and characterized by Hahn-echo measurements in energy and phase memory time in section 3.2. We simulate the evolution of [VO(TPP)] when targeted with the sequence of pulses needed to encode the states in eq.3.6. We numerically solve the Lindblad equation 3.2 for the system density matrix, starting from the sound Hamiltonian 3.2 derived experimentally. For the sake of simplicity, given that the nuclear spin dephasing rates measured in 3.7 are very close to each other at fixed value of the applied field, we assume an average constant dephasing rate in the Lindblad equation terms that models the dephasing mechanisms.
Thus, starting from a generic superposition of the $m_I = -1/2, 1/2$ states, we shape consequently the pulse sequence in order to push the system into the error protected basis 3.6. This correspond to the transformation:

$$\alpha|1/2\rangle + \beta|-1/2\rangle \rightarrow \alpha\frac{|-3/2\rangle + \sqrt{3}|1/2\rangle}{2} + \beta\frac{\sqrt{3}|-1/2\rangle + |3/2\rangle}{2}. \tag{3.7}$$

This transformation can be deconstructed in a sequence of single transitions between subsequent states. The scheme is shown in figure 3.24-(a) and features a first π-pulse between the central states $m_I = \pm 1/2$, followed by two simultaneous $\pi/3$ pulses between the couples $\pm 1/2$ and $\pm 3/2$; finally a second π-pulse between the two central levels $m_I = \pm 1/2$ closes the sequence.
The simulation of this encoding is reported in figure 3.24-(b) with static field B_0 applied along $\hat{\mathbf{x}}$. The intensity of the static field is a crucial parameter of the simulation. Indeed, it must be set as the best trade-off between an optimal spectral

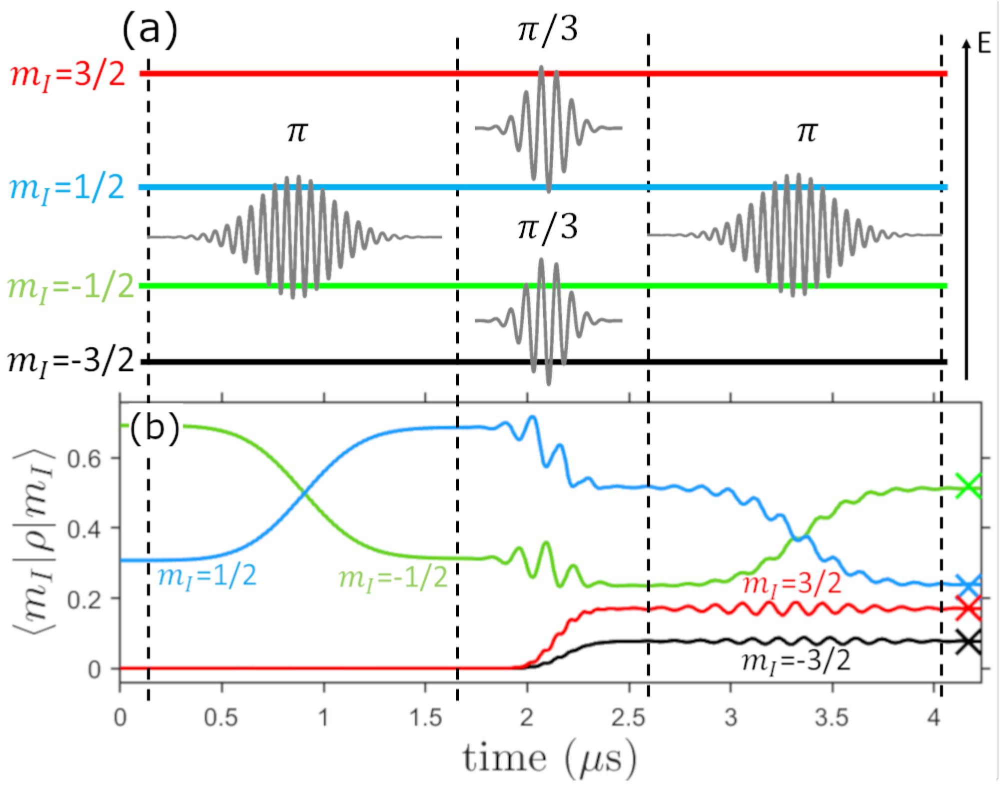

Figure 3.24: (a) Encoding sequence sketch for the four labeled nuclear spin states $m_I = -3/2, -1/2, 1/2, 3/2$ (colored horizontal lines), ordered by energy. Each rf-pulse in the sequence is labeled by the angular rotation induced on the nuclear system. (b) Step by step time evolution of the diagonal elements of the system density matrix ρ (colored lines) when targeted by the pulse sequence in (a) with a pulse amplitude of $B_1 = 1$ mT. The system is initialized in the generic $0.83|-1/2\rangle + 0.55i|1/2\rangle$ state superposition and brought into the encoded state 3.6 in an overall manipulation time of 4 μs. The final state is in sound agreement with the squared expectation values (crosses), with the secondary oscillations induced by the rf manipulations that do not affect significantly the encoding. Reproduced from Ref. [4] with permission from the Royal Society of Chemistry.

separation of the transitions (achieved at high field) and a considerable entanglement of the electronic and nuclear spins (reduced in high field), that enables fast manipulations. The transitions, instead, are implemented by narrow (in frequency domain) Gaussian-shaped rf pulses of intensity $B_1 = 1$ mT, that excite selectively each transition (compatible with the excitation bandwidth of the broadband spectrometer used for the characterization [100, 11]). The time evolution of the nuclear state populations is represented in 3.24 by the diagonal elements of the system density matrix $\langle m_I|\rho|m_I\rangle$ as a function of time. The encoded superposition of the [VO(TPP)] nuclear states after the simulated pulse sequence coincides almost exactly with the exact one (crosses in fig. 3.24). This evidence further prove the suitability of this complex for encoding quantum error correction algorithms.

The natural next step is the experimental realization of the transitions required to implement the algorithm above. We thus perform Rabi coherent manipulations for each of the nuclear $\Delta m_I = \pm 1$ transitions involved in 3.24, i.e. $|-3/2\rangle \rightarrow |-1/2\rangle$ (**AB**1), $|-1/2\rangle \rightarrow |1/2\rangle$ **AB**2, $|1/2\rangle \rightarrow |3/2\rangle$ **AB**3.

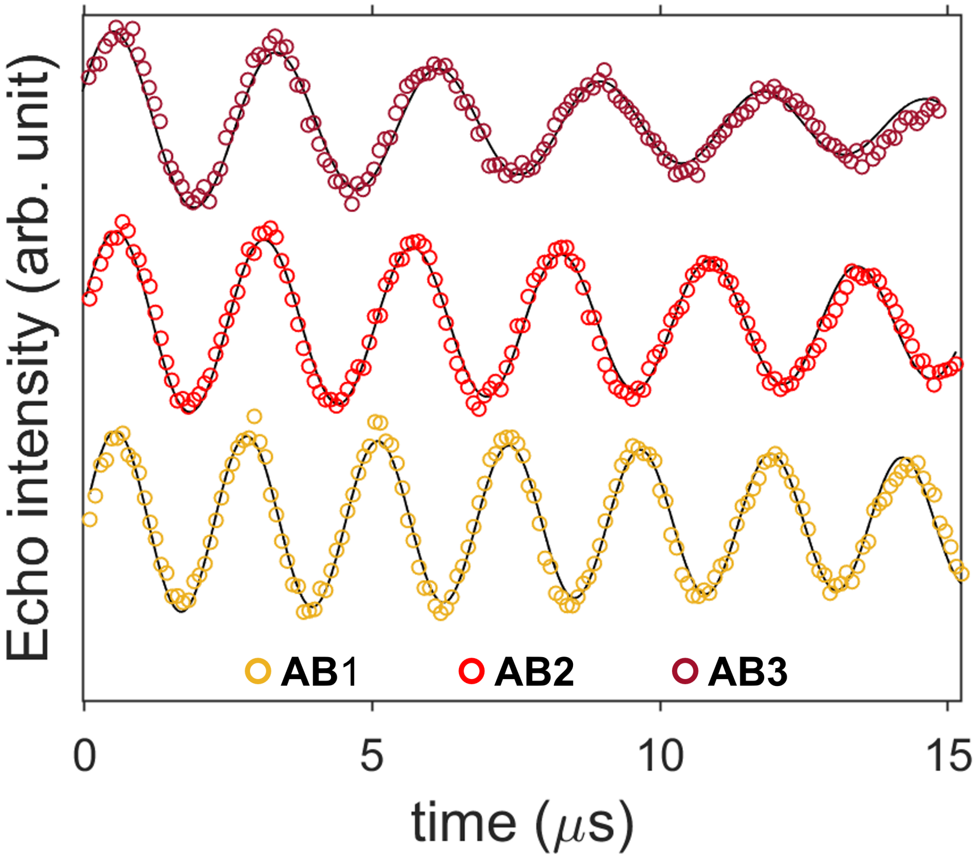

Figure 3.25: Rabi nutation experiment at the fixed static field $B_0 = 0.3$ mT along the system $\hat{\mathbf{x}}$-axis induced by 7.7 dB attenuated linearly polarized rf-pulses B_1 along $\hat{\mathbf{z}}$. The targeted nuclear states are the one involved in the encoding sequence 3.6. Reproduced from Ref. [4] with permission from the Royal Society of Chemistry.

All these selective manipulations were implemented by means of the "HyReSpect" home-built broadband NMR spectrometer, [11] described in section 2.1.1, for calibrated exciting bandwidths. The results, shown in figure 3.25, are promising since for each transition the average duration of a π inversion pulse results remarkably shorter than the coherence loss induced by spin-spin relaxation T_2 and disomogeneities in the rf-pulse.

3.5 Conclusions

Broadband NMR is an election technique for the characterization and manipulation of molecular qudits. It permits to access the spin Hamiltonian parameters, the coupling with the electronic ancilla and the coherence times of two prototypical molecular qudits [VO(TPP)] (3.2) and [VCp$_2$Cl$_2$] (3.3). These two Vanadium based molecular complexes were demonstrated to be promising quantum systems, featuring a electronic qubit ($S = 1/2$) coupled with a nuclear qudit ($I = 7/2$). The multilevel structure of the systems was demonstrated in both cases to be addressable with rf pulses in order to induce selective transitions. Moreover, the coherence times of the states superposition measured with Hahn-echo decay experiments is remarkable and comparable with what reported for similar molecular complexes.[45] By combining all these properties we demonstrated that this class of molecules is suitable for the efficient implementation of quantum algorithms. In particular, the encoding of a quantum error correction algorithm on the [VO(TPP)] complex was successfully simulated and the nuclear transitions involved in the encoding were also individually realized and detected experimentally by targeted rf-manipulations. The step further towards the actual implementation of the QEC encoding on the [VO(TPP)] complex will require the design of a dedicated multifrequency resonant probe that allows fast rf switching (to implement the transitions depicted in figs. 3.24 and 3.25), maintaining a high sensitivity.

Chapter 4

Unveiling phonons in a prototypical molecular qubit by IXS

In order to push further the performances of molecular qubits toward their use in quantum devices, it is fundamental to reach a thorough understanding of their relaxation dynamics and decoherence.
In this work we exploited for the first time high-resolution Inelastic X-rays Scattering (IXS) together with cutting-edge *ab initio* calculations to study phonon dispersions in the prototypical molecular qudit [VO(TPP)] [4, 14] (see sect. 3.2 for its characterization with broadband NMR). With this synergetic experimental and theoretical approach, we validated the *ab initio* phonon calculations by comparing the measured spectra with the simulated scattering cross section. IXS data permit to investigate phonon dispersions over a wide section of the reciprocal space and to unravel the existence of extremely low energy optical phonons. Finally, we determined the critical role of those extremely low energy modes in the spin relaxation, by calculating their spin-phonon coupling constants. Identifying the vibrations which mostly contributes to relaxation indeed provides a viable option for synthetically improving the performances of molecular magnets. This new and powerful synergistic approach gave us an unprecedented insights on the spin dynamics of the [VO(TPP)] molecule, paving the way for the application of this technique to the characterization of phonons in MNMs.

4.1 State of art

Reaching a profound understanding of Molecular qubits relaxation dynamics and decoherence mechanisms is an aspect of paramount importance in order to unleash the potentialities of these systems for quantum information applications and computation. The coherence times of these systems must be long and temperature resilient in order to implement quantum algorithms.[70] A key role in determining those coherence times and their temperature dependence is played by the interaction of molecular spin with inter- and intra-molecular vibrations.[29, 86]
Recently, Inelastic Neutron Scattering experiments (INS) and *ab initio* spin dynamics simulation have been used for the investigation of phonons in molecular qubits

and single-molecule magnets. For instance, phonons have been recently investigated in the VO-based compound [VO(acac)$_2$] with the 4-dimensional inelastic neutron scattering technique. [30, 118]. This study unraveled the presence low energy optical phonons, involved in anti-crossing with the acoustic branches, causing a mutual spin-phonon coupling strength transfer. [29, 30] This picture was in clear contrast with the canonical treatment of phonons with the Debye model, in which acoustic phonons are predict to be well separated in energy from the optical modes, being also the main players in the spin relaxation of MNMs.

An experimental technique allowing us to access both phonons energies and polarization vectors is fundamental in order to construct a sound model of phonon-induced relaxation mechanisms. Indeed, only with such a solid starting point it is possible to determine the role of specific phonon branches in different relaxation processes. [28]. In fact, before the recent INS experiments on phonons, we only had information on phonon energy spectra at the Γ point obtained with Raman, IR or THZ spectroscopies, which can only be interpreted in the context of a Debye-like picture, which is violated in our molecular complexes. However, INS technique poses strong limitations (better detailed in the following section) in terms, e.g., of samples dimensions and chemical compositions. The purpose of this work is then to exploit for the first time inelastic X-rays scattering for a molecular qubit, to experimentally investigate the energies and the polarization vectors of phonons in a prototypical molecular qubit [VO(TPP)]. At the same time the implementation of *ab initio* state-of-art spin dynamic simulations enables to understand the critical role of different phonon branches in the relaxation dynamics.

The [VO(TPP)] complex is chosen not only as archetypes of the new generation of molecular qubits with promising performances (long coherence times even at high temperatures), [4] but also because, among the family of vanadium-based systems, it is considered to be one of the most robust to high energy irradiation. The experimental observation of ultra-low energy optical modes makes this system an ideal test-bed to study the role of these non-Debye modes in the spin dynamics.

4.2 Inelastic X-ray scattering experiment

The experimental study of phonon dispersion and polarization vectors on a molecular crystal is realized for the first time by exploiting high-resolution Inelastic X-ray Scattering (IXS). The advantages of this technique with respect to the complementary Inelastic Neutron Scattering (INS) are several. First of all, modern high-resolution IXS spectrometers as ID28 [119] at the European Synchrotron Radiation Facility (ESRF) allows to measure acoustics and optical phonons also for very small samples (order of 1 mm^3), while the small dimensions of molecular crystals still represent an hurdle even for modern high-flux neutron spectrometer, typically preventing the use of INS for studying phonon dispersion. Moreover, another downside of neutrons is represented by the large incoherent cross section of light elements, like ^1H, which are abundant in MNMs, causing the blurring of the phonons coherent scattering signal and thus of phonon dispersions. This drawback can be overcome by substituting the elements with large incoherent cross section with chemical analogues, such as deuterium in place of Hydrogen. However, deuteration has significant effects on the INS signal only if high percentage can be obtained, which, in the case of MNMs, it is very difficult. On the contrary, the large energy transfer involved in the X-ray incoherent scattering processes ($\sim eV$) is order of magnitude larger than the energy scale of interest when measuring phonons in MNMs ($\sim meV$), thus it does not contribute to the measured cross section. This, combined with the nearly absence of multiple scattering processes, makes IXS basically a background-free technique in the meV range. Furthermore, the employment of hard X-rays with high incident energies ($\sim keV$), several order of magnitude larger than the energy scale of MMNs molecular and lattice vibrations, causes the spectral resolution to be independent from the energy and momentum transfer of the scattering event. This is an important feature for the characterization of optical phonons. Indeed, in precedent studies performed with INS, acoustic modes dispersions were successfully observed, while the energy-dependent resolution was not sufficient to resolve optical modes with energies above 10-12 meV. [30] The energy and momentum transfer also result to be completely decoupled.

All the listed IXS advantages and ID28 [119] unique capabilities allowed us to succeed at measuring for the first time acoustic and optical phononic excitation in a molecular crystal of a prototypical qubit. A [VO(TPP)] single crystal (crystallografic cell in fig 4.1) of dimensions $1 \times 1 \times 0.5$ mm^3 was synthesized by our collaborators at the University of Florence (see the List of Collaborators). The crystal was oriented by means of diffuse scattering on the ID28 beamline side station. We focused on the $(h0l)$ scattering plane, and in particular on Bragg reflections 006 and 600, which offered the best compromise in terms of intensity of the inelastic signal and suppression of the elastic one. With this choice of Brillouin zone (BZ) we could explore the $\Gamma - K_z$, $\Gamma - K_x$ and $\Gamma - N$ path of the [VO(TPP)] reciprocal space, corresponding to directions $(00l)$, $(h00)$ and $(h0h)$ respectively, in longitudinal and transverse configuration.

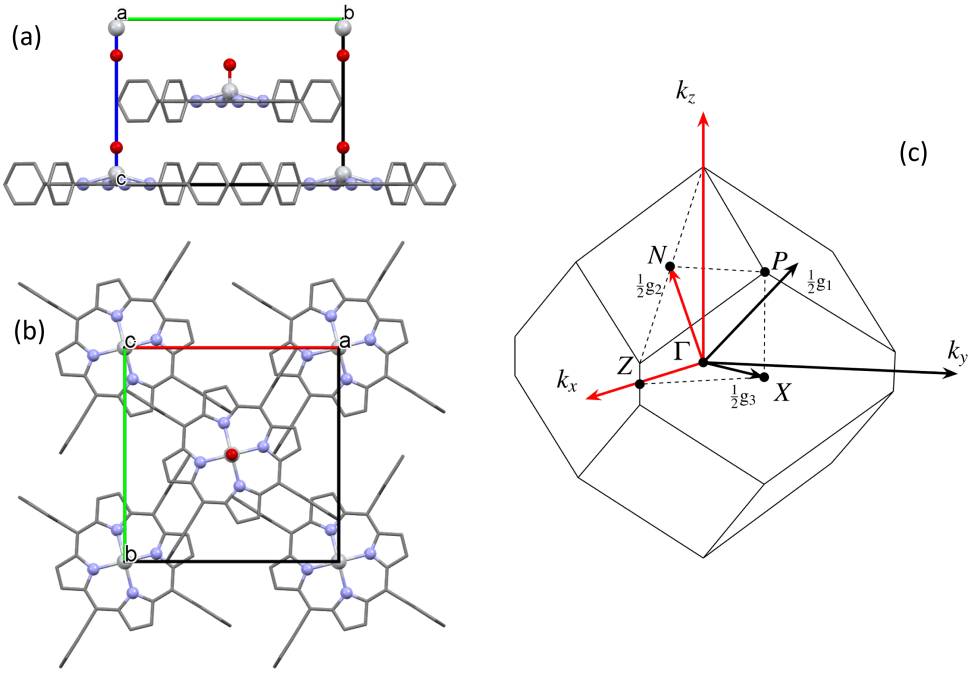

Figure 4.1: (a-b) view of the [VO(TPP)] crystal structure along the a and c axis respectively. (c) Brillouin zone picture, in which the symmetry direction probed in our experiment are highlighted (red arrows).

IXS measurement were collected at 300 K, with the sample glued on a standard sample holder. The ID28 spectrometer was used in backscattering configuration, exploiting two different reflections of the Si monochromators: the Si(9 9 9), which selects an incoming energy $E = 17.794$ KeV and features a resolution of $\delta E = 3.0$ meV, and the Si(12 12 12), whose selected energy is $E = 23.725$ KeV with a resolution $\delta E = 1.5$ meV. We refer to this two configurations as Low and High-resolution configurations. By exploiting the triple-axis geometry of the spectrometer in low-resolution configuration we performed an exploration scan of the phonon modes. The principal symmetry directions in the reciprocal space $\Gamma - N$, $\Gamma - K_x$ and $\Gamma - K_z$ (see the first Brillouin Zone of the crystal in fig. 4.1) were sampled spanning the energy from -25 meV to 25 meV at constant scattering vector Q values. In figure 4.2 examples of low resolution spectra are shown, for longitudinal and transverse scans at different points in the reciprocal space, for all the explored symmetry directions[1].

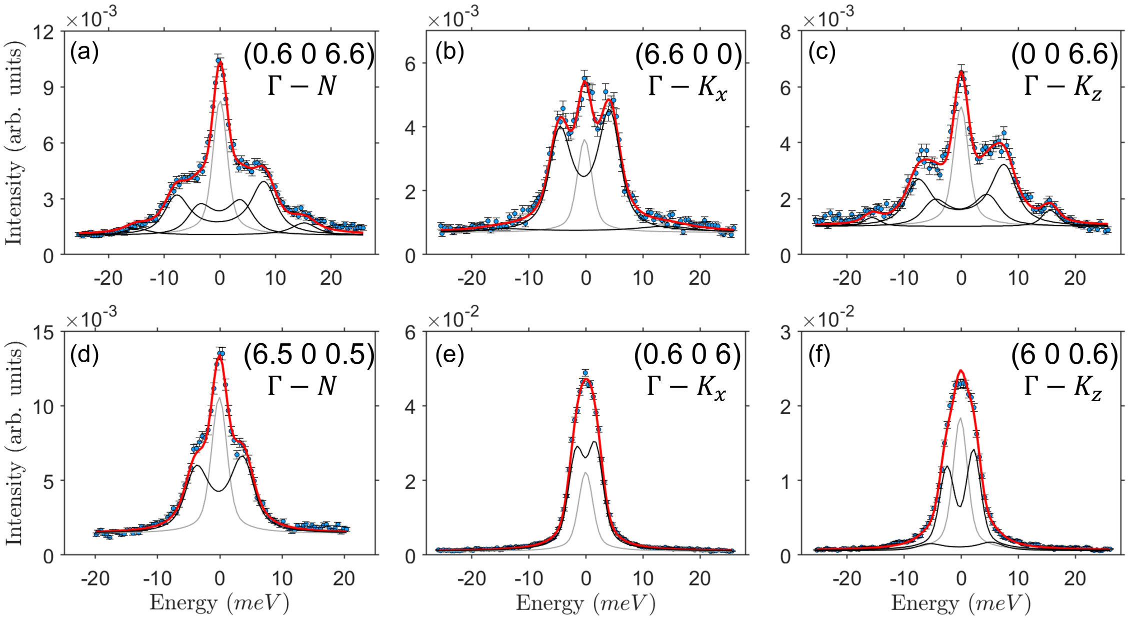

Figure 4.2: Longitudinal (**a**, **b**, **c**) and transverse (**d**, **e**, **f**) IXS scans along the directions $\Gamma - N$, $\Gamma - K_x$ and $\Gamma - K_z$, collected in low-resolution configuration.

From these scans is already evident the presence of low energy phonons, together with higher energy optical ones at around 8 and 15 meV (fig. 4.2-(a-c)). To better investigate low-energy phonon modes, we measured the direction in which these excitations are expected with the high-resolution configuration of the spectrometer (see fig. 4.3).

High resolution measurements indeed confirmed the ultra-low energy of [VO(TPP)] optical phonons (≤ 2 meV) in most of the probed BZ directions. The surprisingly-low energy of these modes is the lower ever measured in a molecular crystal.

The ID28 beamline has a set of nine analyzers, each of them corresponding to a detector in the detector desk. This feature enables the simultaneous collection of phonon spectra for nine different Q values. This is an important resource, since it

---

[1] It worth noticing that the definition of longitudinal and transverse scans along a diagonal reciprocal space direction as $\Gamma - N$ is essentially meaningless. The reason for which it is done is simply a notation convention to uniform the language.

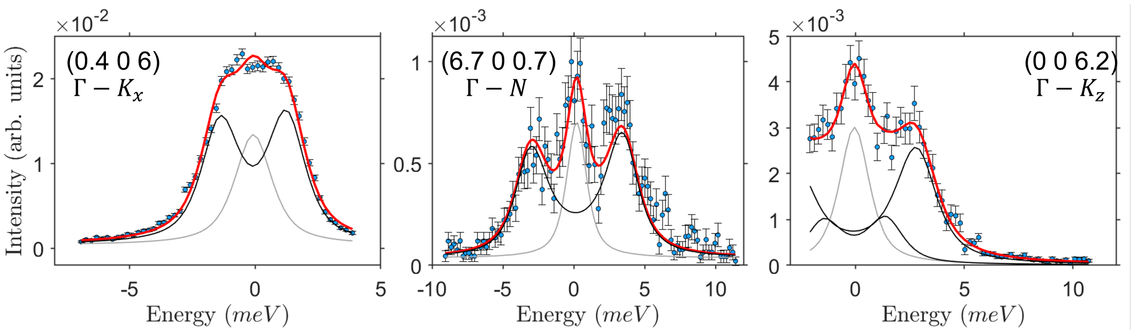

Figure 4.3: Longitudinal (**a**) and transverse (**c**) IXS scans along the directions $\Gamma - K_x$, $\Gamma - N$, and $\Gamma - K_z$, collected in high-resolution configuration, to resolve the low energy phonons contribution close to the elastic line.

allowed us to detect a secondary set of excitations, very close to the probed symmetry directions and with slightly different $|\vec{q}|$. Combining the two set of data we increase severely the sampling of the BZ.

4.2.1 Results

The measured spectra have been fitted using the beamline software @fit28, by including an elastic line centered at zero exchanged energy and a reasonable number of inelastic peaks, depending on the excitation clearly visible in each scan. The spectral function used was a damped harmonic oscillator (DHO) $f_{dho} = I_0(c\delta E)^2/(E^2 + c\delta E)$, reproducing the lineshape of the instrument, with a FWHM corresponding to the measurement resolution ($\delta E = 3$ meV or $\delta E = 1.5$). The energies of the resulting phonon excitations as a function of the BZ sampling represent the phonon dispersions along the probed symmetry directions. Therefore, they can be directly compared with those obtained with periodic density functional theory (DFT) calculations. However, not every phonon branch has the same IXS cross-section. The experimental data must therefore be compared with the simulated IXS cross section $\frac{\partial^2 \sigma}{\partial E \partial \Omega}$. The scattering intensity of each phonon branch can be simulated starting from calculated phonon eigenvalues and eigenvectors, as described in section 2.2.3. These DFT calculations on [VO(TPP)] phonons were realized by our collaborators from the Trinity College Dublin and from the University of Florence (see the List of Collaborators).

The most visible excitations in the measured spectra are thus expected to be the one with the stronger scattering cross section. The comparison between data and DFT calculations is done by superimposing the phonon energies extracted from the data fitting to the 2D color map of the simulated cross section in the energy/phonon wavevector plane. The result is shown in figure 4.4 for longitudinal and transverse modes along the three sampled symmetry directions $\Gamma - N$, $\Gamma - K_x$ and $\Gamma - K_z$. The agreement is excellent and the majority of the optical or acoustics phonons with a significant cross section are detected experimentally. From figure 4.4 the presence of the extremely low energy optical phonons observed in high-resolution configuration is also confirmed by DFT results. These modes are persistent in the whole BZ and characterized by a remarkable scattering intensity.

A complete description of phonon modes is fundamental for calculating the spin-

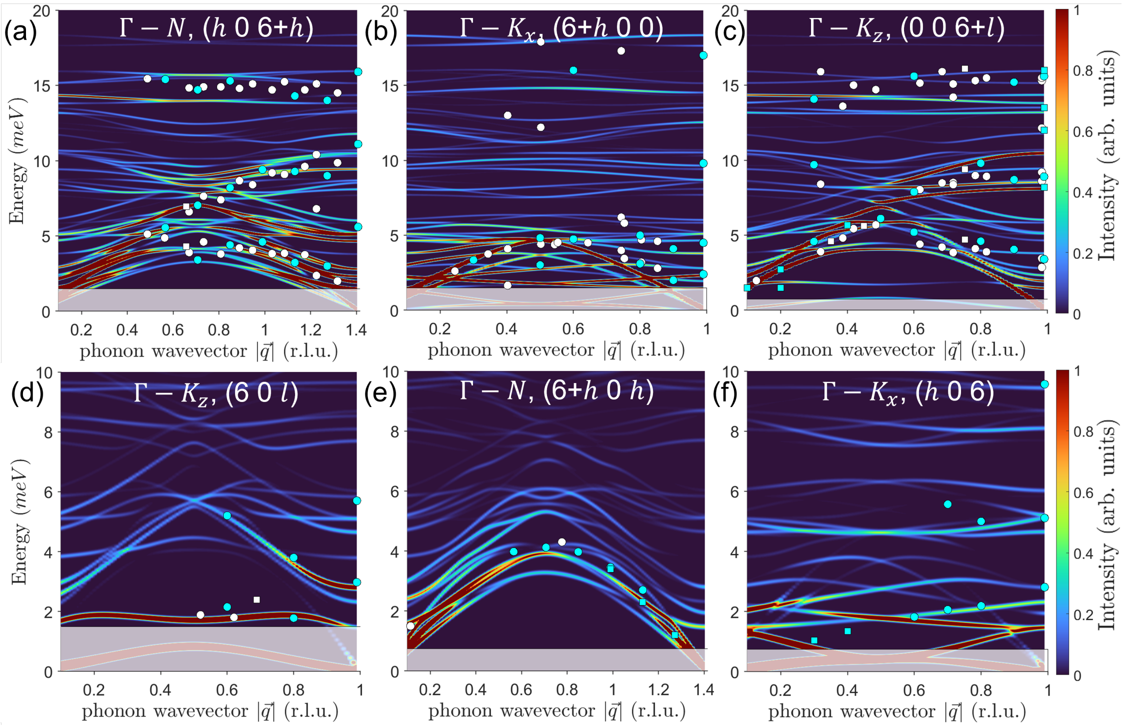

Figure 4.4: The 2D colormap shows the inelastic cross-section calculated starting from phonon energies and polarisazion vectors extracted from ab initio calculations, along the three sampled symmetry directions in the recirpocal space in both longitudinal and transverse configuration: (a,e) $\Gamma - N$, (b,f) $\Gamma - K_x$, (c,d) $\Gamma - K_z$. The line-width associated to each phonon modes is chosen small enough to enable the distinction of the contribution arising from any branch. Cyan dots and squares ($\delta E = 3$ / 1.5 meV respectively) represent the excitation energies extracted from the spectra in figures 4.2 and 4.3. White dots/squares represent the energies extracted from the inspection of secondary analyzers. Shaded areas highlight the regions non accessible experimentally due to the dominant elastic contribution.

phonon coupling coefficients. Therefore, the validation of DFT calculations must be supported by the analysis of both phonon energies $\omega_j(\mathbf{q})$ and polarization vectors $\sigma_j^d(\mathbf{q})$. Both these quantities, as seen in section 2.2.3, contribute to the inelastic scattering cross section. Thus, a comparison between the experimental spectra and the IXS cross section simulated with the DFT calculated $\omega_j(\mathbf{q})$ and $\sigma_j^d(\mathbf{q})$ gives a direct feedback on the accuracy of calculations. In order to put to the test the polarization vector of each phonon mode obtained with DFT, the most effective approach is to implement a convolution of the cross section of each mode with the experimental resolution and directly compare it with the experimental spectra as a function of the energy. The comparison is shown in figure 4.5 for some representative $\mathbf{Q}$ values and is excellent for the whole energy range for both low and high-resolution configurations. This test further confirms the reliability of the calculated phonon model. A typical small rescaling of $\sim 10\%$ is applied [30] to account for van der Waals interaction and temperature effects. Moreover, small discrepancies in the low energy regime excitation intensity are mainly due to the Bose factor $n_j(\mathbf{q}) = (exp(\beta\omega_j(\mathbf{q})) - 1)^{-1}$ which exponentially depends on the exact phonon energy and thus enhance small differences.

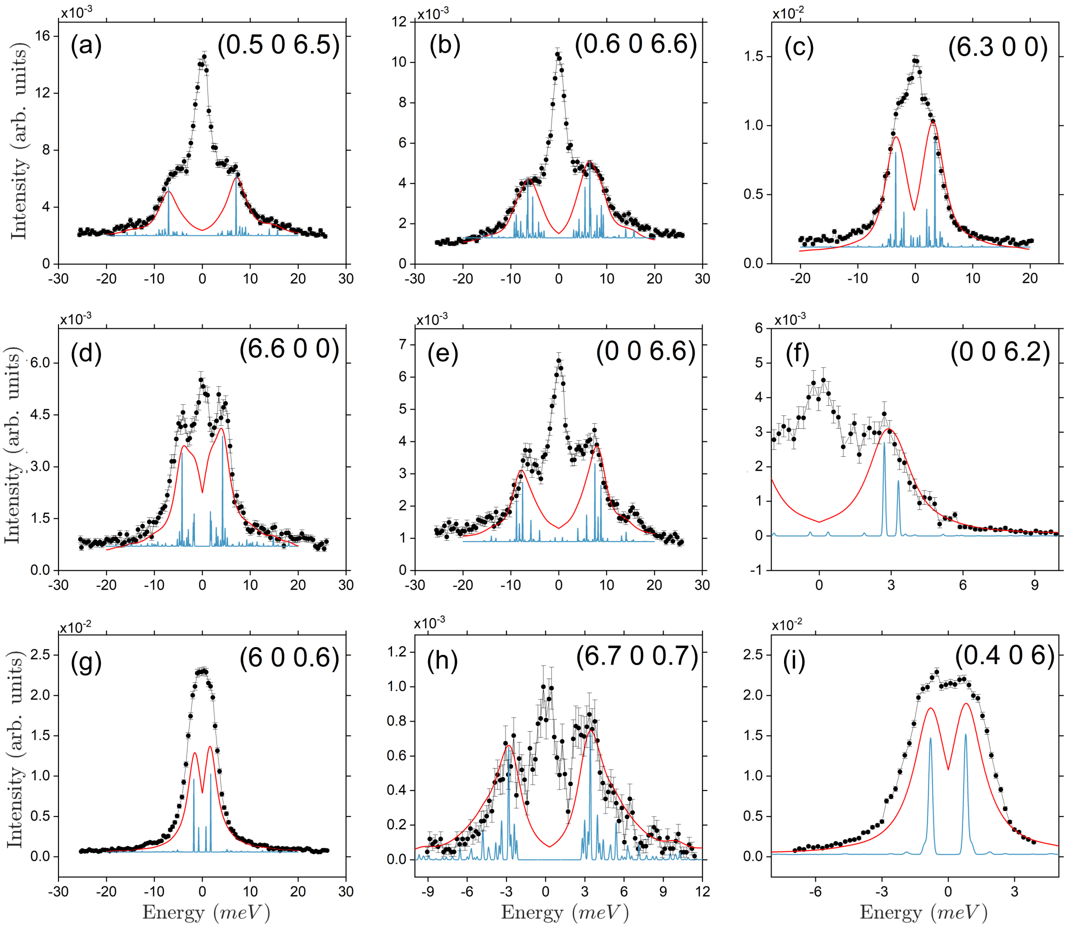

Figure 4.5: Experimental IXS spectra (black dots) are compared with the simulated cross-sections (red line). The latter are convoluted with the experimental resolution ((a-e,g): $\delta E = 3$ meV; (f,h,i): $\delta E = 1.5$ meV). A representative spectra is shown for each probed symmetry direction. Blue lines represent the inelastic cross-section, calculated with a line-width that enables to discriminate the contribution of each phonon mode. The elastic line is omitted for clarity.

4.3 The critical role of ultra-low energy vibrations

This extensive experimental IXS characterization of the [VO(TPP)] phonon dispersions enabled the validation of the *ab initio* phonon calculations. From this validated results it has been possible to move a step further and simulate also the system spin relaxation. The *ab initio* calculation of spin-phonon coupling parameters requires to simulate the effect of phonons on the parameters of the system spin Hamiltonian. As in section 3.2, the spin Hamiltonian for [VO(TPP)] is written as $H_0 = \hat{\mathbf{I}} \cdot \mathbf{A} \cdot \hat{\mathbf{S}} + p\hat{I}_z^2 + \mu_B \hat{\mathbf{S}} \cdot \mathbf{g}_S \cdot \mathbf{B}_0 + \mu_N g_N \hat{\mathbf{I}} \cdot \mathbf{B}_0$ and the parameters are derived both experimentally in [4] and confirmed by DFT calculations.
The modulations induced on the Hyperfine $\mathbf{A}$ and spectroscopic splitting $\mathbf{g}$ tensors are calculated from the first and second partial-derivative of those tensors with respect to the phonon wavevector for each phonon branch, $\mathbf{V}_\alpha = (\partial \mathbf{A}/\partial q_\alpha)$ and $\mathbf{V}_{\alpha\beta} = (\partial^2 \mathbf{A}/\partial q_\alpha \partial q_\beta)$, respectively. Even for a modern computational hardware, this huge calculation is very demanding in terms of time and computational resources. This hurdle is overcome, by our collaborators from Dublin Trinity College and from Florence University (see the List of Collaborators), exploiting a trained neural network to interpolate *ab initio* results and compute the differentiation efficiently. [120] The calculated spin-phonon coupling coefficients, represented by the modulus $|\mathbf{V}_\alpha|$, are shown in figure 4.6 together with the calculated phonon density of state.

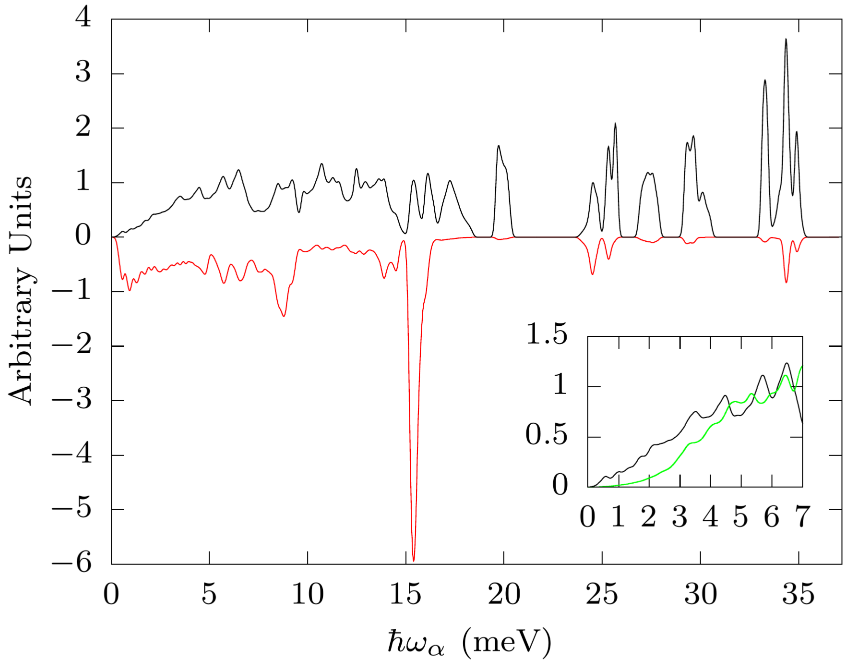

Figure 4.6: Phonon density of state (black line) and modulus $|\mathbf{V}_\alpha|$ of the spin-phonon coupling coefficient (red line, negative axis) computed *ab initio*, as a function of energy. In inset the comparison between the low energy pDOS of [VO(TPP)] (black) and the parent molecular qubit [VO(acac)$_2$] (green). [13]

Two important conclusions can be extracted here: the first is that the extremely low energy optical modes possess a remarkable coupling with the spin and thus are ex-

pected to play a key role in spin relaxation processes. Secondly, from the calculated low energy phonon density of states (pDOS), we observe a complete deviation from the Debye model. Indeed, the [VO(TPP)] pDOS grows linearly with the phonons energy below 5 meV, while a $\sim \omega^2$ behavior would be expected for the canonical representation of the Debye model, in which optical and acoustics phonons are well separated in energy. This second point is further supported in the inset of figure 4.6 in which the low energy pDOS profile of [VO(TPP)] is compared to the one of the parent compound [VO(acac)$_2$], recently studied by 4D-INS [30] which does not feature optical phonons at energy lower than $\sim$ 6 meV at Γ-point. [13]
It has been demonstrated that, for molecular systems, the spin lifetime at temperature higher than $\sim$ 10 K is strongly influenced by the coupling with phonons. [13] In molecular qubits like [VO(TPP)] relaxation dynamics is mostly triggered by non-resonant two-phonon Raman processes. [116] The spin relaxation induced by these phonon absorption and re-emission phenomena can be simulated by including, in the secular Redfield equation, the spin-phonon coupling coefficients $|V_\alpha|$ and $|V_{\alpha\beta}|$. At moderate applied field (0.3 T) the leading term for the relaxation are the modulation of the hyperfine **A** and spectroscopic splitting **g** tensors. The latter contribution is here neglected in the calculation without loss of generality, since the contribution of the two to the spin-phonon coupling is analogous and follows a similar trend for the considered fields. The extrapolated spin lattice relaxation time T_1 as a function of temperature is compared in figure 4.7 with the data measured in [14] by X-band EPR with an inversion and recovery experiment (see sect. 2.1.2). The agreement is remarkable above $\sim$ 10 K and both the simulation and the experiment display a T^{-2} dependence, typical of phonon-induced Raman relaxation processes.

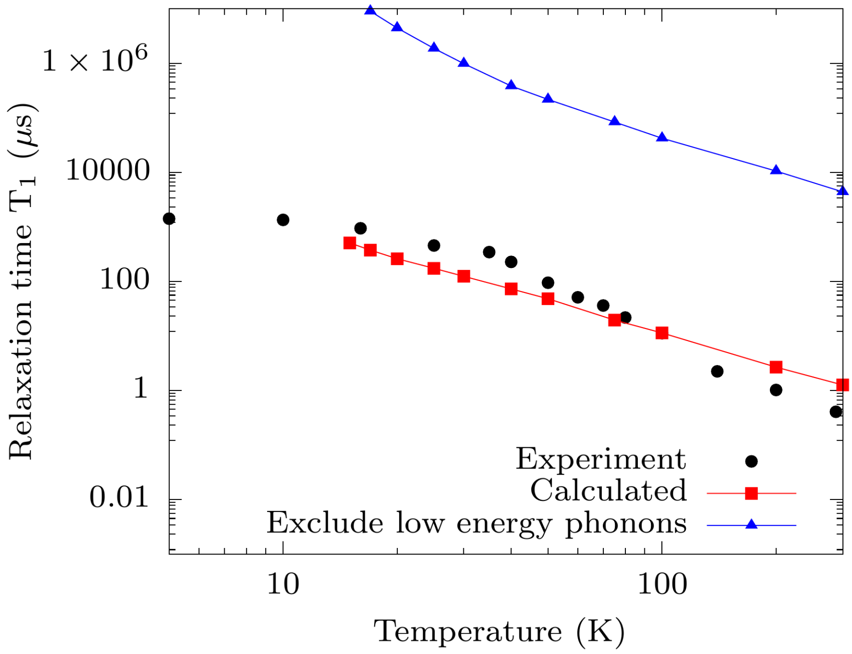

Figure 4.7: Calculated spin relaxation time T$_1$ for [VO(TPP)] (red squares) compared to the T$_1$ measured in [14] with pulsed X-band EPR (black dots). These data are then compared to the simulated T$_1$ after the removal of phonons with energy lower then 6 meV (blue triangles).

We note that the low temperature experimental T_1 deviates from the trend visible at higher temperature. This can be related to the effect of spin-spin dipolar interaction, which is only partially removed by dilution at %2 in the isostructural [TiO(TPP)] diamagnetic analogue. The Raman-like trend in the spin lattice relaxation rates down to low temperatures supports the leading role of the ultra-low energy optical modes which are demonstrated to be strongly coupled with the molecular spin (fig. 4.6). Indeed, by removing low-lying phonons ($\hbar\omega < 6$ meV) strongly coupled with the spin, the simulated T_1 increases by two order of magnitude in the whole probed temperature range (fig. 4.7). This test further stress the paramount importance of low-energy optical phonons in suppressing spin lifetime.
The vibrations associated with low energy optical phonons ($\sim 2meV$) correspond, at the molecular site, to distortion of the molecular structure. In this particular case it has been observed that the vibrations involved cause distortion of the phenyl groups of the molecule, and the bending of the porphirin planar ring (see fig. 4.8). Being able to associate the critically coupled phonon modes with a specific molecular distortion represents an effective approach for improving the spin lifetime performances by chemically tailoring the molecule structure and thus the vibrational spectra.

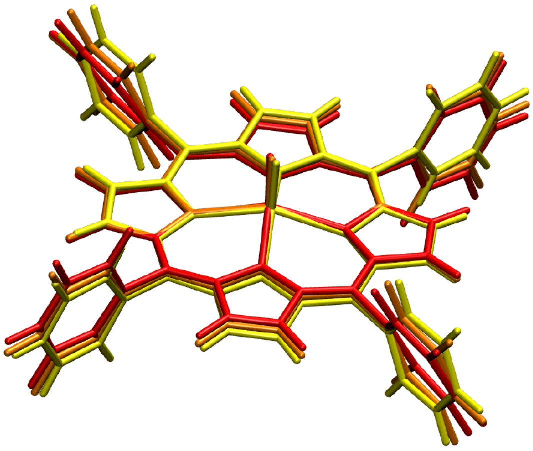

Figure 4.8: Sketch of the distortion of the molecular structure, from the equilibrium structure (yellow) to an extensively distorted one (red). These distortions consist in a bending of the porphirin planar ring and a twist of the phenyl groups, and are associated with the lowest energy optical mode at Γ-point.

It is worth mentioning that even though the experiments are typically performed on single molecular crystals, the application of these molecules in quantum devices requires the exploitation of single molecules. Thus, the investigation of single molecule vibrations is also an important piece of information, when compared with the single crystal results. The persistence of the low energy intra-molecular distortions in [VO(TPP)] was confirmed by gas phase calculations on a single molecule. It was also verified that by removing the phenyl groups from the molecule, the lowest energy optical phonons are shifted up to 6.5 meV. Therefore, the strategy of chemically engineering the molecule by removing the phenyl rings as in Vanadyl porphirin can potentially improve the relaxation times by removing low energy vibrations critically coupled with the spin.

4.4 Conclusions

In this work we developed a synergistic approach that combines high-resolution inelastic X-rays scattering with cutting-edge *ab initio* simulations of spin dynamics for the study of phonons in molecular qubits. This method gave an unprecedented insight on the vibrations of the prototypical molecular qubit [VO(TPP)], enabling to access the coupling of these vibrations with the spin and their role in spin-relaxation processes. This approach also permits to elaborate strategies for incrementing the spin relaxation time in prototypical qubits, in order to improve their performances for application in quantum information processing. The novelty of exploiting IXS for this characterization is of fundamental interest in the field of molecular magnets science and this work can pave the way for a systematic application of this technique. Indeed, IXS overcomes some of the most critical downsides of inelastic neutron scattering, expanding the class of materials that can be studied.
The molecular complex [VO(TOPP)] was chosen in order to benchmark this new approach on a well known and characterized promising system, which is also among the most radiation-robust Vanadyl-based complexes. All these aspects allowed us to realize a complete experimental characterization of its vibrational spectra, highlighting the presence of ultra-low energy optical phonons, never observed before in a molecular complex. Thus, by validating the ab initio model by means of the experimental data, we determined also the critical role of these low energy non-Debye optical phonons in triggering the relaxation of the spin, together with their intra-molecular origin. This accurate picture provides an important feedback for the synthesis of new molecular qubits.

Chapter 5

Effect of chemical and structural modifications on the phonon induced magnetization dynamics of Dysprosium-based Single-Molecule Magnets

Single-Molecule Magnets (SMMs) are promising candidates for a further nano-miniaturization of data storage devices. This because SMMs possess a bi-stable ground state and display slow relaxation of the magnetization. [1, 19] Mononuclear Dy-based SMMs are actually the best performing complexes for this application. In particular, for Dysprosocenium compounds, a record breaking blocking temperature above liquid nitrogen have been reported. [2, 15] The high anisotropy barriers is not the only player governing the blocking temperature of these systems. Indeed, the interaction of spins with phonons and molecular vibrations critically hampers the slow magnetization dynamics. [30, 86] Therefore, it is of fundamental interest to understand the interplay of different phonon-induced relaxation mechanisms and the way in which chemical composition and physical stimuli affects phonon dispersions.

In this chapter we report both these approaches. In section 5.1 we compare the phonon density of states (pDOS) measured with Inelastic neutron scattering with *ab initio* calculation for new dysprosocenium SMMs with different ligands and solid-state counter-ions. In section 5.2 instead, we characterize phonons in a prototype Dy-based SMM as a function of the applied pressure. The results achieved in these two work gave us new insights about the effect of different molecular vibrations on the relaxation mechanisms and contribute in highlighting the key ingredients of high-temperature magnetic bistability, for the development of the next generation of Single Molecule Magnets.

5.1 The effect of chemical composition on the pDOS of new Dy-based SMMS

In 2017 the Manchester group (see the List of Collaborators) synthesized the first SMM of the Dysprosocenium family [15], which constitutes a crucial breakthrough in terms of high temperature relaxation performances ($T_B = 56$ K). One year later, Guo *et al.* [2] discovered that a substitution of the Cp groups in the double-decker structure of the disprosocenium $[Dy(Cp^{ttt})_2][B(C_6F_5)_4]$ (**a**, where Cp^{ttt}=1,2,4-tri-tert-butylcyclopentadienyl) [15] induces a blocking temperature increment of dozens of K, breaking the thermal limit of liquid nitrogen ($T_B = 80$ K). Indeed, the introduction of Cp^{iPr5} and Cp^* in the metallocene dysprosium cation $[Cp^{iPr5}DyCp^*]$ (**b**, Cp^{iPr5} = penta-iso-propylcyclopentadienyl, Cp^* = pentamethylcyclopentadienyl) widens the ligand-Dy-ligand angle, and shortens the ligand-Dy distances, resulting in an increased axiality and strengthening of ligands. These structural modification induce a significant improvement of the SMM performances in this new family of compounds, dysprosocenium complexes. However, even though the reported energy barrier in **b** for the magnetization reversal $U_{eff} = 1541$ cm^{-1} is larger than the one measured for **a** [15] ($U_{eff} = 1277$ cm^{-1}), it is clear that the energy barrier is not the only factor contributing to the difference in the blocking temperature. Indeed, in recent years, several Dy-based SMMs have been synthesized, displaying very different relaxation dynamics and blocking temperatures not competitive with the original Dysprosocenium, despite their energy barriers of the order of thousands of Kelvin degrees.[16, 18, 31] The magnetization relaxation of these systems is mainly governed by three relaxation mechanisms: the quantum tunneling of the magnetization (QTM), the non-resonant two phonon Raman processes and the direct Orbach process.[19, 24, 25] Each of this relaxation mechanisms dominates over a well defined temperature regime. In particular, the QTM processes govern the low temperature relaxation, while the Raman and Orbach processes, which are phonon-induced, play the key role at intermediate and high temperatures, respectively. In particular, the blocking temperature of these SMMs crucially depends on the Raman regime and its interplay with the higher energy Orbach processes.[17, 31]. Therefore, for instance, the blocking temperature increment going from complex **a** to complex **b** can be attributed to the substituent ring introduced in **b**, that displays only out-of-plane vibrations, less coupled with the Dy spin and thus less effective in inducing the relaxation dynamics. [2] It is then clear that the molecular and crystal structures of the compounds and the correlated phonon spectra are crucial aspects for the optimization of the relaxation dynamics. Thus, a systematic study in which small structural modifications are associated to the corresponding variation in the phonon spectra is of fundamental interest to deduce the key ingredients of magnetic bistability at high temperatures in SMMs.

In this chapter we present three SMMs complexes, synthesized by our collaborators at the University of Manchester (see the List of Collaborators), based on the benchmark Dysprosocenium $[Dy(Cp^{ttt})_2][B(C_6F_5)_4]$ (**a**, where Cp^{ttt}=$C_5H_2{}^tBu_3$-1,2,4) [15], but with slightly different ligands and solid-state counter-ions. In order to fully understand the mechanisms which determine the high blocking temperature in this SMMs class, the strategy we implement was a systematic comparison of the phonon density of states (pDOS) measured with inelastic neutron scattering for these slight modifications. The measured pDOS is also a fundamental for the validation of pe-

riodic DFT calculations of phonons, which are the starting point of the relaxation dynamics simulations of these systems. This approach can, in fact, solve the relaxation puzzle for the promising class of Dy-based SMMs, by understanding the correlations between the cystal and molecular structure, the phonon modes and the relaxation processes they trigger.
As a first step in the gradual structural modification of Dy-cenium, we focus on the B-based counterion of the complex **a**, where in first instance we replace the ^{1}H ions with the fluorine ones, resulting in the structure $[Dy(Cp^{ttt})_2][B(C_6H_5)_4]$ (**3**, see fig. 5.1).

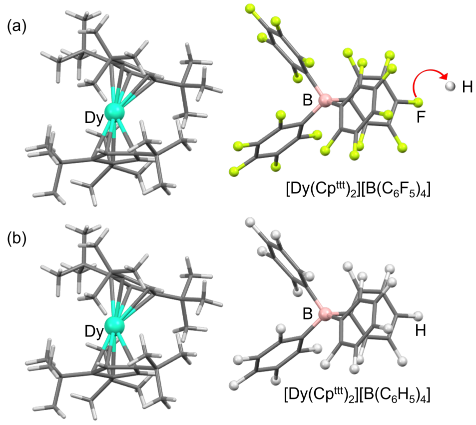

Figure 5.1: (a) Dysprosocenium **a** molecule and its counterion [15]. The arrow sketches the substitution made on the counterion for the synthesis of sample **3**. (b) Sample **3** structure $[Dy(Cp^{ttt})_2][B(C_6H_5)_4]$ with ^{1}H substituted with F in the counterion.

A second more radical modification involves a complete substitution of the counterion, which was replaced by an Aluminum based one: $[Dy(Cp^{ttt})_2][Al\{OC(CF_3)_3\}_4]$ (**2**, see fig. 5.2).

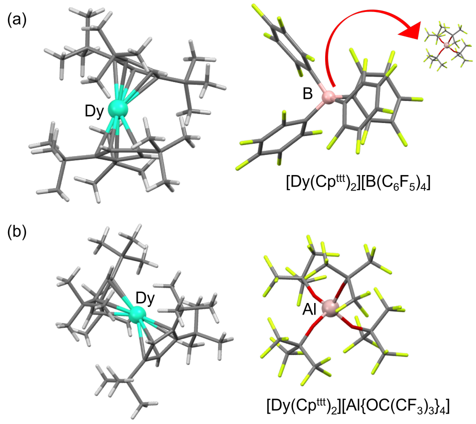

Figure 5.2: (a) Dysprosocenium **a** molecule and its counterion [15]. The arrow sketches the counterion substitution made for the synthesis of sample **2**. (b) Structure of sample **2** $[Dy(Cp^{ttt})_2][Al\{OC(CF_3)_3\}_4]$ with the Al-based counterion that substitute the Boron-based one of sample **a**

Finally, this counterion replacement was combined with the replacement of a carbon atom in the Cp^{ttt} ring with a P ion, leading to the structure $[Dy(Dtp)_2][Al\{OC(CF_3)_3\}_4]$ (**1**, where DTp = $\{P(C^tBuCMe)_2\}$, see fig. 5.3).

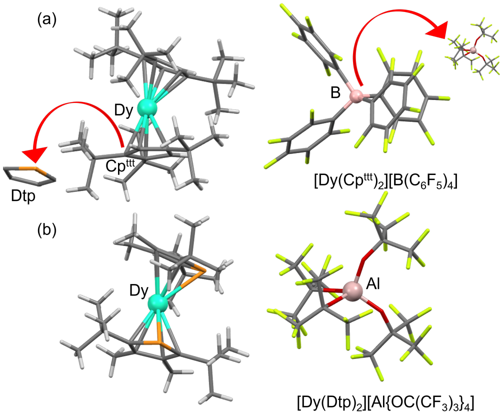

Figure 5.3: (a) Dysprosocenium **a** molecule and its counterion [15]. The arrow sketches the counterion and Cp-group substitution made for the synthesis of sample **1**. (b) Sample **1** structure $[Dy(Dtp)_2][Al\{OC(CF_3)_3\}_4]$ with counterion and Dysprosium ligands substitution.

In particular, the latter modification can be crucial to understand the relative importance of the counterion modifications with respect to the effect induced by variation of the metallocene group. The coupling of the Dy spin with the vibrations originating from these two groups indeed can provide different contributions and different magnitude to the overall magnetic relaxation.
The preliminary results, reported here in figure 5.4, for the temperature dependence of the magnetization relaxation rates τ^{-1} for **1**,[16] **2** and **3** were collected by our collaborators at the University of Manchester (see the List of Collaborators). The comparison of the relaxation rates for these three compounds display significant differences in both the low and intermediate temperature relaxation regimes. Conversely, the high temperature relaxation regime for **1**, **2** and **3** is almost superimposable. This outcome confirms that despite the structural modifications being small, the relaxation dynamics is strongly affected by the presence of different counterions and/or ligands around the Dy ion. In particular, the intermediate temperature regime is very different for the three compounds, with the relaxation rates varying of 1-2 orders of magnitudes. This suggests that these modifications can play a significant role in triggering non-resonant Raman-like relaxation processes.
Magnetometry data for **1** reveal an energy barrier for the reversal of the magnetization of U_{eff} = 1760 K, identical to the one measured for sample **a** in [15], and the presence of magnetic hysteresis up to 48 K. In figure 5.5, the temperature dependence of the magnetization relaxation rate τ^{-1} for **1** is compared with what previously measured for Dysprosocenium **a** in [15]. The relaxation rate was measured by out-of-phase ac susceptibility measurements with zero applied field.
Despite having exactly the same anisotropy barriers, the temperature dependence of the characteristic rates for the relaxation dynamics are different. Analogously to **a**, the relaxation rate τ^{-1} for sample **1** follows at high temperature ($T > 50$ K) an exponential Arrhenius law $\tau^{-1} = \tau_0^{-1}\exp(-U_{eff}/T)$ typical of Orbach-like

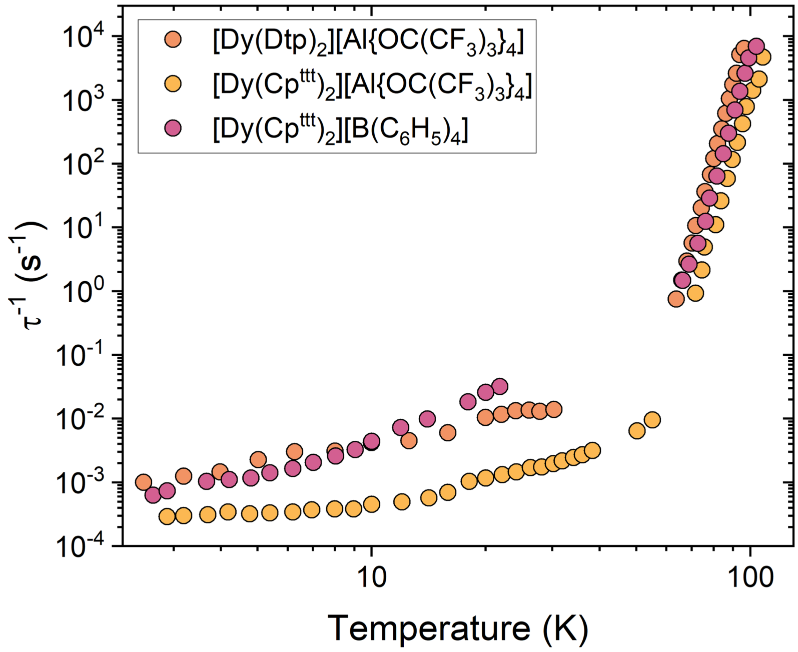

Figure 5.4: Magnetization relaxation rates for **1** (from [16]), **2** and **3** in the range T=2-110 K, from ac susceptibility (high-T) and dc decay experiments (low-T). These measurements were performed by Prof. Mills group at the University of Manchester (see List of Collaborators).

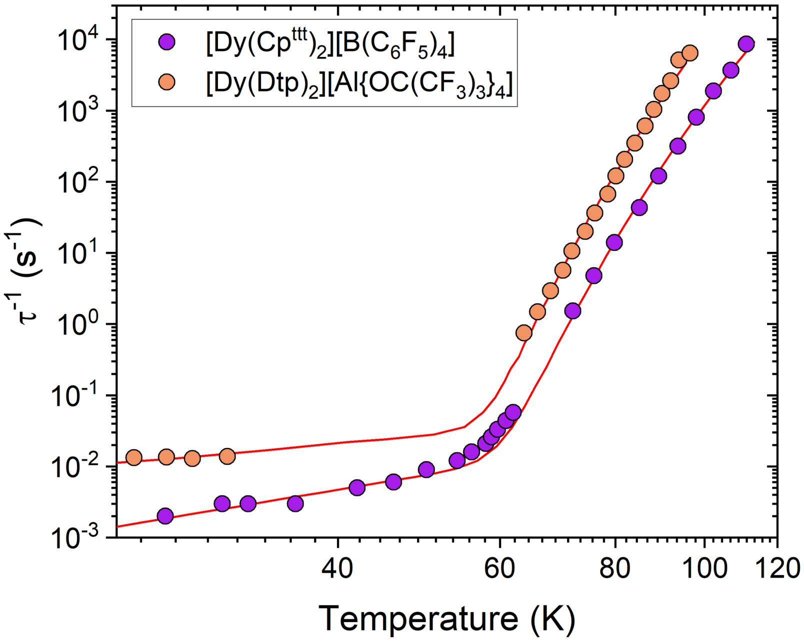

Figure 5.5: Magnetization relaxation rates for **1** (orange dots) and **a** (light purple dots) respectively (from [16] and [15]), extracted at high temperature from ac susceptibility measurements and at low temperature from dc decay experiments. Solid red lines represents a fit of the Orbach and Raman contributions. The fitting results of the two curves are respectively: $U_{eff}^{\mathbf{1}} = 1760$ K, $\tau_0^{\mathbf{1}} = 10^{-11.7}$ s, $C^{\mathbf{1}} = 10^{-3.5}$ $s^{-1}K^{-n}$, $n^{\mathbf{1}} = 1.1$; $U_{eff}^{\mathbf{a}} = 1760$ K, $\tau_0^{\mathbf{a}} = 1.98 \times 10^{-11}$ s, $C^{\mathbf{a}} = 1.66 \times 10^{-6}$ $s^{-1}K^{-n}$, $n^{\mathbf{a}} = 2.15$

relaxation processes, with and an extracted effective barrier $U_{eff} = 1760$ K. At lower temperature instead, relaxation in **1** results to be dominated by power law Raman-like mechanisms, with $\tau^{-1} = CT^n$ and a exponent $n = 1.1$, half of the one reported for **a**. Indeed, overall, **1** displays a relaxation 10 to 100 times faster with respect of **a**, with a 100 seconds blocking temperature of 23 K, compared to 56 K for **a**. Since at these temperatures the spin dynamics is confined to the lowest Kramers doublet, the relaxation is driven by the coupling with low energy dispersive phonons that trigger non-resonant Raman mechanisms. Therefore, the faster relaxation can be attributed to the differences in the low energy phonon spectra. Insights on the low-energy phonons spectra are then crucial to understand the processes governing the relaxation and to unravel the key ingredients to reach a high blocking temperature.[31] For samples **a**, **2** and **3** for example, simulations of the pDOS reveal two very peculiar trends in the low and high energy spectral regions. The high energy DOS, dominated by localized vibrational modes resonant with the crystal field gaps and promoter of Orbach relaxation over the effective energy barrier U_{eff}, display similar spectral features, especially above 100 meV. Conversely, the DOS of low-energy dispersive modes, triggering non-resonant Raman processes varies significantly (see fig. 5.6).

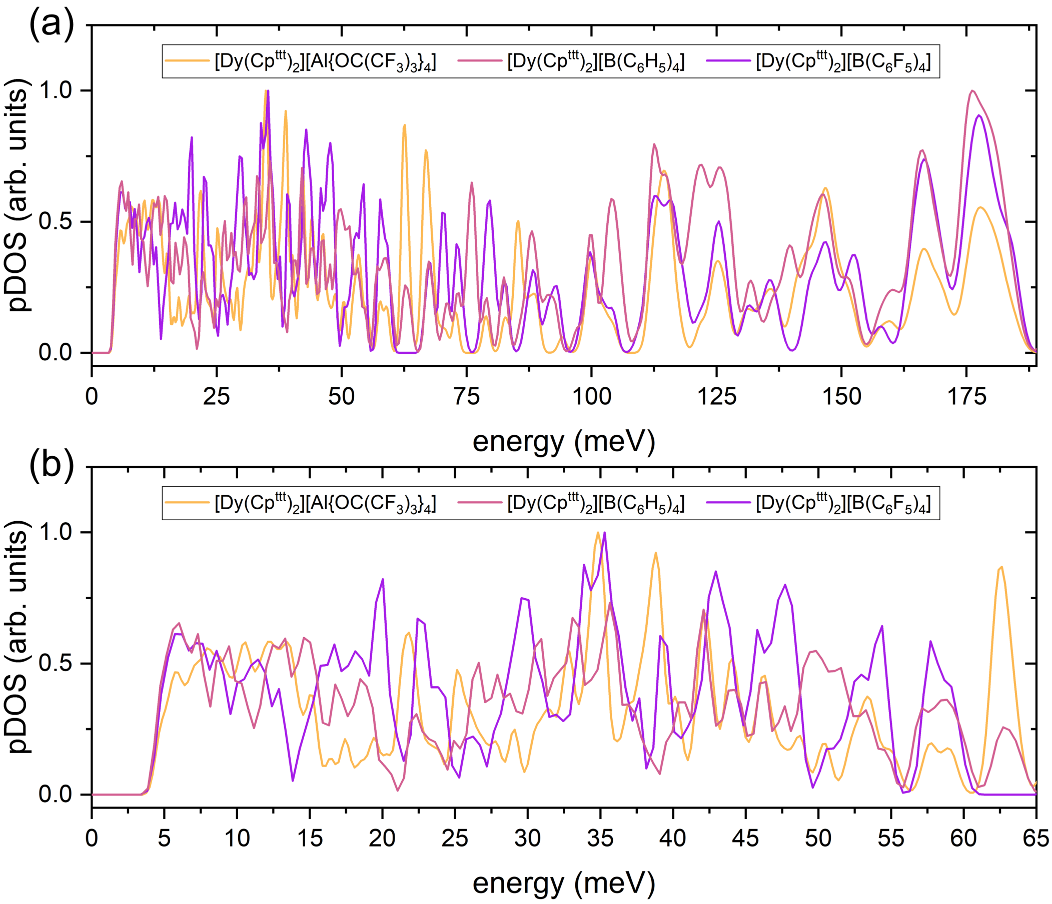

Figure 5.6: Comparison of the calculated pDOS for samples **a**, **2**, **3**. Panel (a) exhibits the whole calculated energy range, while panel (b) shows the restricted low-energy regime, highlighting the significant differences in the low energy spectra, compared to the less pronounced ones in the intermediate-energy spectra.

By comparing these *ab initio* pDOS calculations with those measured by INS reported in the following section, we can validate the DFT results to be used as the starting point for the calculation of the spin-phonon coupling coefficients and the simulation of the temperature dependence of the relaxation rate in figure 5.4.
It must be remarked that in this approach we are neglecting the effect of the quantum tunneling of the magnetization (QTM), which is temperature-independent and thus is not triggered by the interaction with phonons. The effect of QTM can be in fact quantified only by measuring the temperature and field dependence of the magnetization relaxation rates. However, this mechanism was demonstrated to be non dominant at low temperature in this compounds class, due to the strong axial ligands environment that suppress the efficiency of this relaxation process.[17]

5.1.1 Inelastic neutron scattering experiment

The inelastic neutron scattering (INS) experiment was performed at the institute Laue-Langevin (ILL) on the indirect geometry spectrometer IN1-Lagrange (LArge GRaphite ANalyser for Genuine Excitations), described in section 2.2.2.[109] This beamline, installed on the hot neutron source of the reactor, features a combination of wide energy-range and high resolution with an high neutron flux. For this reason, it is well suited for the study of molecular vibrations in complex systems, through the evaluation of the pDOS. In particular, a part from constant factors (see sect. 2.2.2), the measured scattering function corresponds to the neutron weighted pDOS of the studied systems (once the elastic and quasi elastic contribution are subtracted).
The experiment was performed at the temperature of 5 K on ≈ 2 g of powder for each of the sample under investigation (**1**,**2**,**3**). The energy transfer was chosen in order to cover the 0 to 200 meV range. To cover this low and intermediate energy range with a constant energy step, three monochromators were used, each of them featuring different resolutions:

- Si(1 1 1), available in a 4.5 to 20 meV range and featuring a 0.8 meV resolution;
- Si(3 1 1), available in a 16.5 to 35 meV range and featuring the same 0.8 meV resolution;
- Cu(220), in the wider range 26 to 200 meV and a proportional resolution of 2-3 % of the incident energy.

Each dataset was then normalized by the number of incident neutron, before merging them together in a single curve. Further refinements of the collected data require the subtraction of the empty sample holder signal and the spectral spike smoothing by comparison with a water spectra previously collected. Elastic and quasi-elastic scattering contributions are then subtracted by fitting the sum of a Gaussian curve centered at E=0 and a Lorentzian function centered at non-zero exchanged energy, keeping the width as a fitting parameter. The results of these data reduction procedure (performed with the software LAMP [121]) are shown in figure 5.7 for the three Dy complexes, compared with the data published by Chiesa *et al.* for the benchmark Dysprosocenium **a**.[17]
The measured pDOSs confirm what was expected from *ab initio* calculation. The high energy spectral components for the three samples feature analogous peaks, with

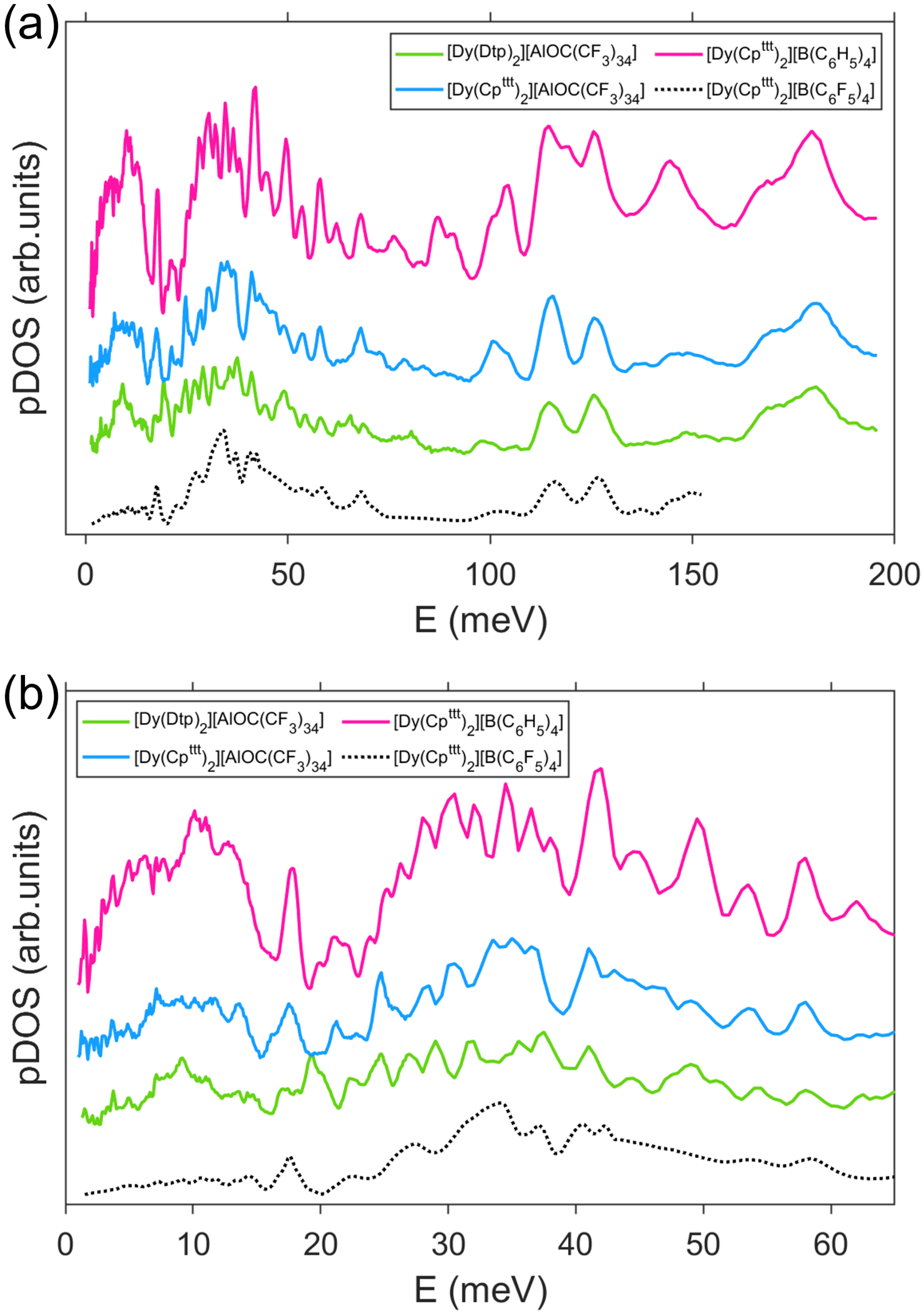

Figure 5.7: pDOS measured on IN1 for sample **1** (green line), **2** (light blue line) and **3** (magenta line), compared with the same measurement collected for the benchmark Dysprosocenium on the MERLIN spectrometer at ISIS (dotted black line).[17] The two panels (a) and (b) show the whole collected energy range and a close up of the low energy pDOS, respectively.

a comparable relative intensity. This trend is confirmed also by comparison with sample **a**. Conversely, at low energy the pDOSs display strong differences in both the energy of the modes and their intensity. The largest differences are found in the very low energy branches, from 0 to 30 meV, where the scattering intensity increase severly with respect to sample **a**, reaching the maximum in sample **3**. This sample in particular display an overall higher scattered intensity, which is justified by the higher number of ^{1}H in the counterion, yielding a relevant incoherent contribution.

5.1.2 Results

The preliminary conclusions outlined from the comparison between the experimental pDOS are in sound agreement with those drawn from the *ab initio* calculated ones. Both experimental data and DFT results in fact confirm that the main differences in the pDOS of the three compunds are in the low-energy range and thus can be directly linked to the different behaviour of the relaxation rates in figure 5.4 in the Raman temperature regime. To confirm these thesis, it is fundamental to develop a sound model for the phonon-induced relaxation of the magnetization. This can be done exploiting the DFT phonon results to determine the coupling of molecular and lattice vibration with the molecular spin. The comparison between the measured pDOSs with the calculated ones allows us also to validate the exploited DFT method. The periodic DFT calculations of the pDOSs reported in figure 5.6 have been performed by our collaborators at the University of Manchester (see the List of Collaborators) with the code VASP [122], exploiting the PBE exchange-correlation functional [123, 124] and D2 van deer Waals corrections.[125] Phonon density of states are computed using the finite displacement method as implemented in the PHONOPY package.[126, 127]
The comparison outcome is shown in figure 5.8 for sample **a**, **2**, **3** respectively.

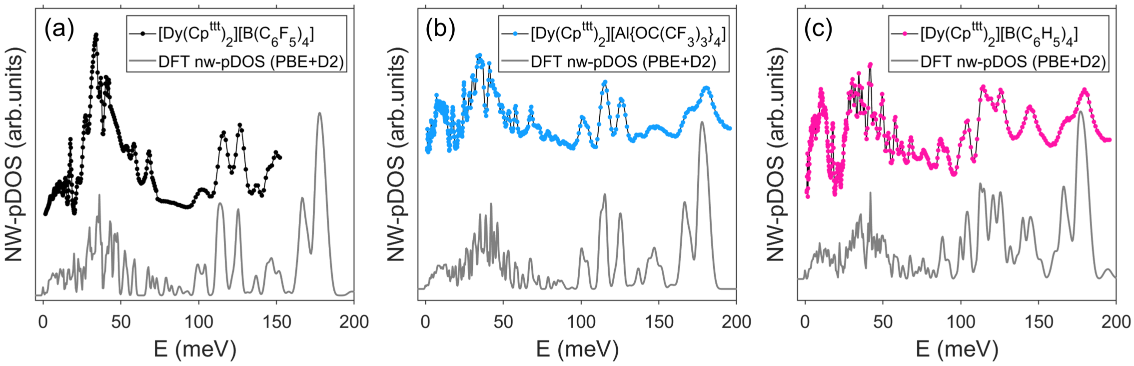

Figure 5.8: Comparison of the experimental phonon density of state (5 K) with the neutron weighted pDOS calculated *ab initio* for (a) sample **a**, (b) sample **2** and (c) sample **3**. The *ab initio* calculations were performed by our collaborators at the University of Manchester (see the List of Collaborators).

The agreement between the experimental data and the calculated pDOSs is excellent. The most relevant spectral features are indeed reproduced by the calculations. As a result of this successful comparison, the phonon model is assumed to be accurate and can be used for the development of a realistic model for the relaxation of these compounds. This work in particular is still ongoing, since the *ab initio* calculation of the spin phonon coupling coefficients and the simulation of the spin relaxation is very demanding in terms of computational time.

5.2 Measuring phonon modes of a Dy-based SMM in applied pressure

Chemical and structural modifications are not the only strategy that can be exploited in order to trigger variations in the phonon spectra of molecular nanomagnets. Indeed, by applying an external hydrostatic pressure, it is possible to induce gradual distortion of the crystal and molecular structure of these systems, and consequently to modify the phonon spectra. By investigating how phonons and thus the phonon-induced relaxation dynamics vary in SMMs as a function of the applied pressure, we can in principle disentangle the role played by specific lattice and molecular vibrations in the dominating relaxation mechanisms. In particular, this information can give fundamental insight in order to develop future synthetic strategies for improving the performances of SMMs.
To apply this innovative approach, we decided to characterize a mononuclear Dysprosium based SMMs $[Dy(H_2O)_5(HMPA)_2]I_3{\cdot}2HMPA$ (with HMPA = hexamethylphosphoramide, $[(CH_3)_2N]_3PO$), synthesized by our collaborators at the University of Glasgow (see the List of Collaborators). The synthesis of this system, together with magnetometry data have already been published in 2018 by A. Canaj *et al.* [18]. The compound presents an almost ideal pentagonal bipyramidal geometry, with a prominent axial crystal field promoted by the two HMPA ligands (see fig. 5.9), which form a $\sim 182°$ axial angle. The system shows magnetic hysteresis up

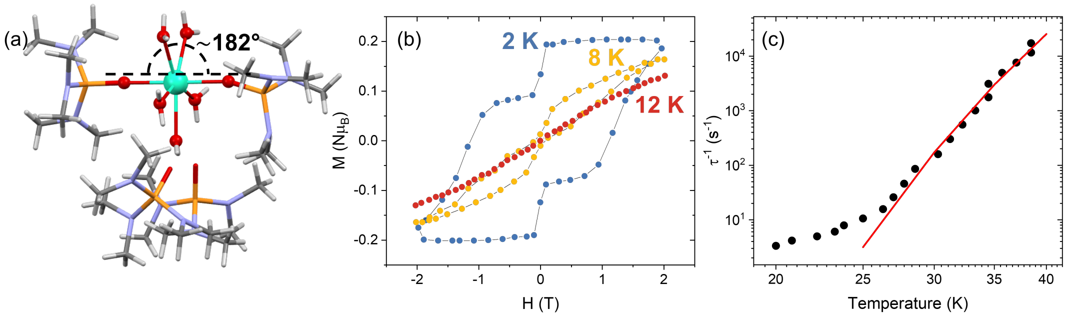

Figure 5.9: (a) Molecular structure of $[Dy(H_2O)_5(HMPA)_2]$ and its counterion $I_3{\cdot}2HMPA$ at ambient pressure. The Dy ion (seagreen) and the O (red) environment are highlighted for clarity. (b) Magnetization data from Ref.[18] as a function of the applied field showing hysteresis loops at different temperature in ambient pressure (Y-diluted sample). (c) Magnetization relaxation rates from Ref.[18] as a function of temperature (black dots), extracted from ac susceptibility measurements. The Orbach regime is highlighted by the Arrhenius fit (red line) for an energy barrier $U_{eff} = 600$ K and $\tau_0 = 1.2 \times 10^{-11}$ s, as reported in [18]

to T=9 K (10 K if the molecule is diluted into its Y diamagnetic analogue). The quantum tunneling mechanism is not suppressed completely by the axial symmetry;

therefore, at around zero applied field the hysteresis loop becomes narrower, as a signature of the activation of this relaxation process (see fig. 5.9). From ac susceptibility measurements a relaxation rate was also extracted and fitted with a single exponential Arrhenius curve above 30 K (fig. 5.9). This suggests that the dominant relaxation process above 30 K is an Orbach-like mechanisms with an energy barrier $U_{eff} = 600$ K, induced by the coupling of the spin with phonons with energy comparable with the crystal field gaps. At temperature below 30 K instead, we do expect the deviation from the Orbach trend to represent the insurgence of non-resonant two phonons Raman processes as the leading mechanisms of the relaxation dynamics (fig 5.9).[18]
When an hydrostatic pressure is applied to the system, crystallographic investigations of the molecule with X-ray diffraction have revealed a gradual tilting of the ligands axial angle, that in an applied pressure of 1.1 GPa becomes 190° degree (see fig. 5.10). This loss of axiality causes several differences in the magnetization curves measured under pressure. At an applied pressure of 1.1 GPa the magnetic hysteresis

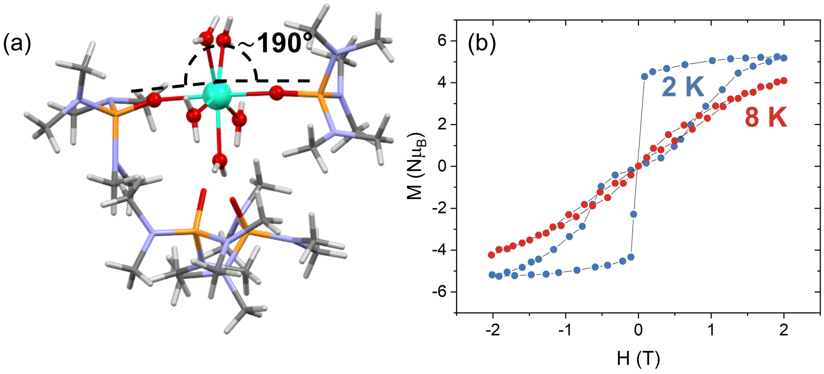

Figure 5.10: (a) Molecular structure of $[Dy(H_2O)_5(HMPA)_2]$ and its counterions $I_3 \cdot 2HMPA$ under an applied pressure of 1.1 GPa. Dysprosium ion (seagreen) and the Oxygen (red) environment are highlighted. (b) Magnetization data as a function of the applied field showing hysteresis loops at different temperature in an applied hydrostatic pressure of 1.1 GPa. These measurements were performed by our collaborators at the University of Glasgow (see the List of Collaborators)

loop is in fact completely closed in zero applied field, also at 2 K, due to the relaxation induced by the magnetization tunneling under the barrier. When the field is applied the hysteresis cycle opens, but with a reduced relative area if compared to the data in ambient pressure and equivalent temperature (see fig. 5.10).
In order to understand the modulations induced in the phonon spectrum by the applied pressure and the effects on the relaxation dynamics, we combine the magnetization measurements with under pressure INS experiments, that allows the measurements of phonon excitations as a function of the applied pressure. These results can then be compared with DFT calculations of the phonon modes. These DFT results, validated by comparison with the experimental data, will be exploited to simulate the system spin dynamic under different pressure regimes.

5.2.1 Inelastic neutron scattering experiment

The inelastic neutron scattering experiment under applied pressure was performed at the Institute Laue-Langevin (ILL) on the thermal neutron triple-axis spectrometer IN8 (more details on IN8 see sect. 2.2.2).[108] This high incident flux spectrometer is optimized for the characterization of lattice vibrations and magnetic excitations in the range from zero to ~100 meV, in sample of small volume and weak signals. Moreover, IN8 can be equipped with a high pressure Paris-Edimburg cell that can emulate the range of pressure applied previously for the magnetometry experiments (0 to 1.1 GPa). Due to the chemical incompatibility of the $[Dy(H_2O)_5(HMPA)_2]$ single crystal with the liquid vectors used to apply the hydrostatic pressure, we used lead filings as a vector to distribute uniformly the external pressure. The crystal has been placed inside the CuBe gasket of the Paris-Edimburg cell, the empty spaces have been closed with the lead filings and then pressed to a gapless pocket.
After the alignement of the single crystal sample, we investigated the phonon excitations at Γ-point in the reciprocal space for two different $\vec{Q}$ vector values: $\vec{Q}_1 = (0\ 3\ \ -12)$ and $\vec{Q}_2 = (0\ 8\ \ -16)$. The energy scans are collected by fixing the final wave vector k_f and varying the incident k_i, to keep constant the scattering $\vec{Q}$ value. We exploited two different monochromators, Si (111) and PG (002), featuring two different resolutions (0.88 meV and 3 meV, respectively). The low resolution configuration have been used for an exhaustive scan of the energy range $0 - 70$ meV with a final wavevector $k_f = 4.11\ \mathring{A}^{-1}$. Then the low energy range $0 - 34$ meV has been refined in the high resolution configuration with $k_f = 2.66\ \mathring{A}^{-1}$. In this case, the actual accessible energy was limited below 34 meV due to the presence of a spurious signal from an analyzer armonics for $k_i = 2k_f$.
The Γ-point energy scans shown in figure 5.11 were collected at the temperature of 77 K for two different applied pressures 0 GPa and 1 GPa. Each dataset has been normalized by the number of scattered neutrons at the pre-sample monitor. Then, the empty pressure cell signal, collected with the same CuBe gasket but without the crystal inside the lead filing, was subtracted, together with a quasi-elastic lorentian-shape signal at very low energies. These data are also compared with the inelastic double differential cross-section of the Dy-complex (see sec.2.2.2) simulated with the eigenvalues and eigenvectors of periodic DFT-calculated phonon modes. From the comparison it is evident that the major difference induced by the applied pressure lies in the low energy region, between 0 and 25 meV. In this range, phonon modes shift to higher energy by increasing the applied pressure (with a sizeable shift of the order of some meV) and change the scattered spectral intensity. Some changes in the phonon excitations are also observable at higher energies; however, non sizeable as the effects on the low energy phonons.
Data were also collected as a function of temperature (fig. 5.12). The different scans are normalized for the temperature dependent Bose Factor (sect. 2.2.2). This approach can be useful to determine the reliability of the spectral details, that are expected to gradually broaden by increasing the temperature. From the comparison of different scans we observe that most of the spectral features at low temperature survive at higher temperatures, but broaden significantly and lose intensity.
Various single crystals have been then milled into few grams of powder and placed in a thin Aluminum cylinder, that is screwed on the cryostat probe. By measuring powder samples we average out the $\vec{Q}$ dependence of the scattering intensity over a wide range of orientations. Thus, the scattering function can be described

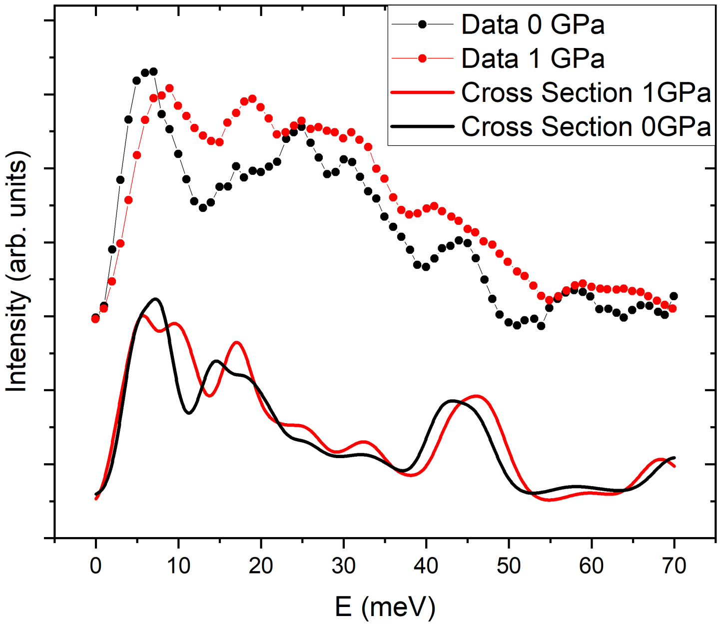

Figure 5.11: INS cross section measured at 77 K for two different applied pressure on a [Dy(H_2O)$_5$(HMPA)$_2$] single crystal (dots), at the Γ-point for $\vec{Q}_1 = (0\ 3\ -12)$. Here, the pressure cell+gasket blank signal is already subtracted from the scattered intensity. The solid line represent the INS cross section calculated starting from DFT-calculated eigenvalues and eigenvectors and convoluted with experimental resolution of 3 meV (low resolution configuration). The low-energy differences in the INS cross section induced by the applied pressure are evident and emerge considerably from the error bars.

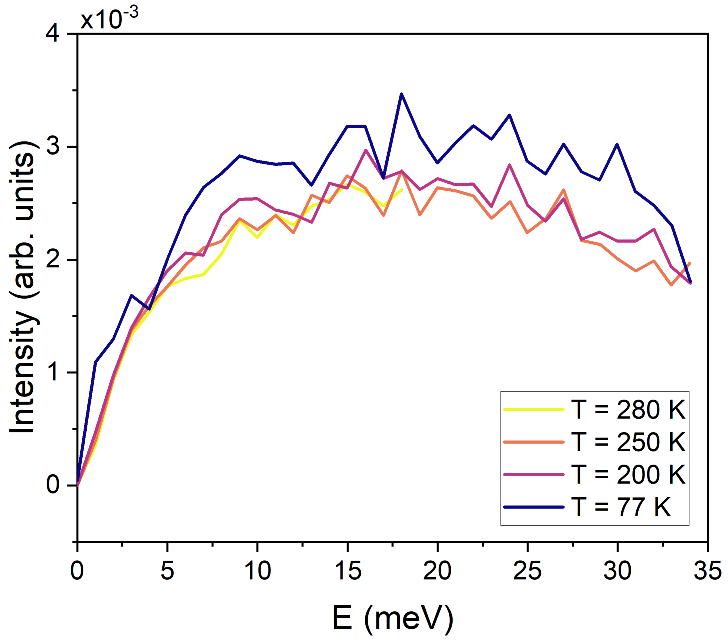

Figure 5.12: Temperature dependence of the high-resolution INS cross section measured at $\vec{Q}_1 = (0\ 3\ -12)$ in a [Dy(H_2O)$_5$(HMPA)$_2$] single crystal, for a constant applied pressure of 1 GPa.

in the so-called incoherent approximation (see sect. 2.2.2), where it results directly proportional to the neutron weighted phonon density of states (nw-pDOS). From the powder spectra measured at 77 K, we can therefore obtain the nw-pDOS of the sample. In figure 5.13 we compare the measured nw-pDOS for two different $|\vec{Q}|$ values. For both these values, the phonon density of states present the same spectral details, confirming that the observed excitations are purely phononics. The measured nw-pDOS can then be compared with the one calculated with periodic DFT.

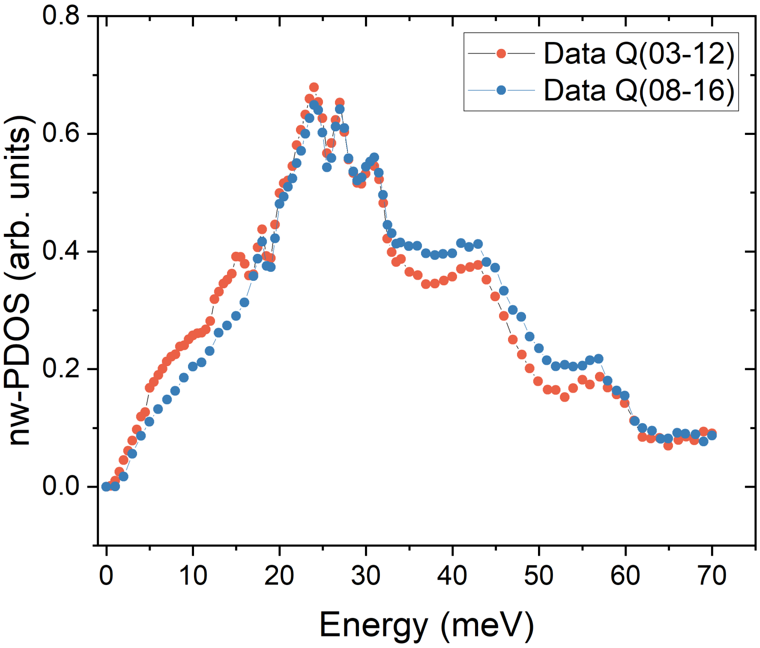

Figure 5.13: Phonon density of states from normalized inelastic neutron scattering experiment on [Dy(H_2O)$_5$(HMPA)$_2$] powders. The spectra was collected at 77 K for two $|\vec{Q}|$ values. The high and low resolution scans are merged in order to maximize the extent of the high resolution region.

5.2.2 Results

The pDOS as a function of the applied pressure can be calculated *ab initio* with periodic DFT. These calculations were performed by our collaborators at the University of Parma, P. Bonfà and I. J. Onuorah (see the List of Collaborators), using the QuantumESPRESSO package [128, 129, 130] which uses a plane wave basis set and pseudopotentials. The energy cutoff for the wavefunctions was set to 1225 eV while the reciprocal space integration was performed with a $2 \times 2 \times 1$ Monkhost-Pack [131] grid when considering the primitive unit cell. The ONCV norm conserving pseudopotentials [132] were used for all elements and the exchange and correlation contribution was described with the Perdew, Burke, and Ernzerhof (PBE) functional.[123]

The atomic positions were optimized until atomic forces were smaller than 2.57×10^{-4}

eVÅ^{-1} and total energy differences among optimization steps were smaller than 2 meV while the experimental lattice parameters were kept fixed during the relaxation. Phonon frequencies were obtained with the Phonopy package.[133] In this case a $2 \times 2 \times 1$ supercell is used to collect the inter-atomic force constants by performing 0.011 Å position displacements. The reciprocal space is sampled using only the Γ point in this latter case. The starting crystallographic cell has been adapted to each pressure condition and verified by comparison with X-ray diffraction data under the same conditions. The results for the simulated pDOS (fig. 5.14) confirms the conclusions derived from the experimental data, thus that the largest difference as a function of the applied pressure is observed for low energy phonon modes.

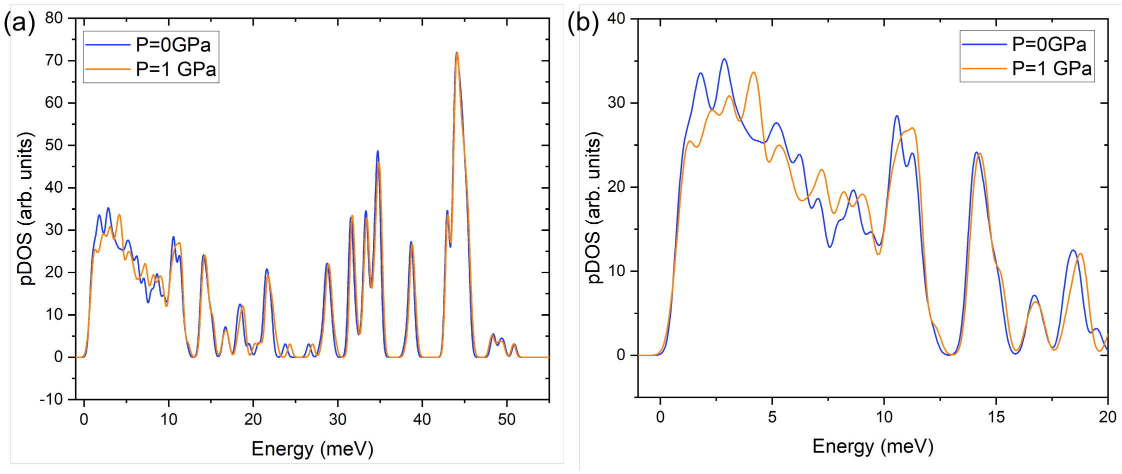

Figure 5.14: (a) Simulated pDOS at two different applied pressures (atmospheric and 1 GPa). The pDOS is convoluted with a sharp resolution σ in order to better evaluate the contribution of different phonon branches that would overlap with the experimental one. (b) Zoom to the lower energy regime, where the larger pressure-induced differences are observed.

In order to validate our DFT results, we have compared the nw-pDOS measured at atmospheric pressure with the one calculated ab initio (fig. 5.15). The spectral features are reproduced by the calculation in both the low and high energy regime. The only evident difference resides in the high-energy experimental background that results enhanced if compared to the simulated pDOS. This effect is not completely understood up to date, but can be attributed to a non negligible coherent contribution to the scattered intensity, not included in the incoherent approximation, and to multi-phonon contributions at high energy, excluded by focusing only on the first order phonon expansion for the scattering function (see sect. 2.2.2). Indeed, the sharp aspect of all the other spectral features permit to exclude *a priori* that this effect is related to the crystal phonon structure.
Once validated, the DFT-calcualted phonon modes will be used to simulate the relaxation dynamics and thus understand the effects of pressure-induced phonons modifications in promoting different relaxation mechanisms.

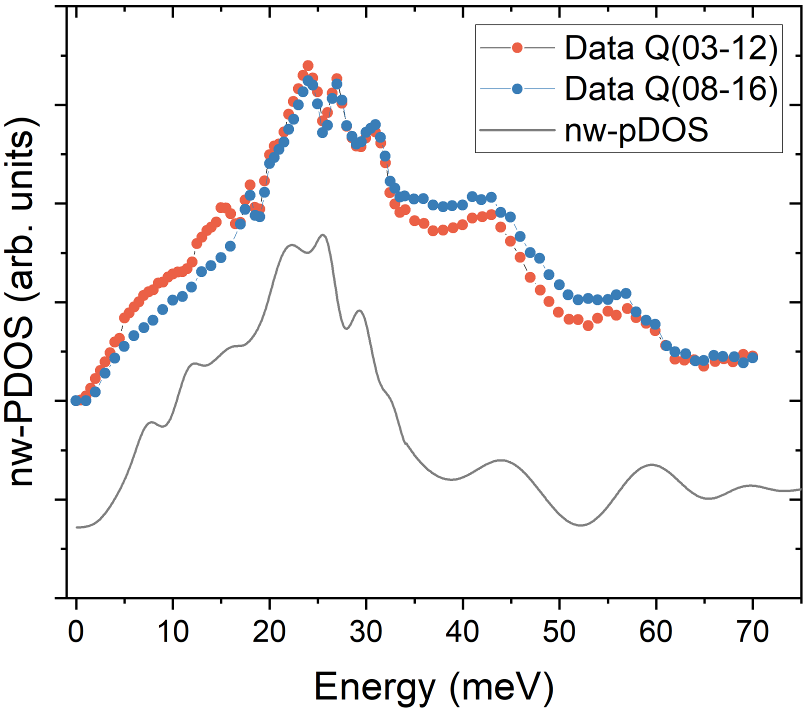

Figure 5.15: Comparison of the experimental nw-pDOS (dots) with the one obtained with periodic DFT (gray lines). The calculated pDOS is convoluted with the experimental resolution in the corresponding energy ranges.

5.3 Conclusions

In conclusion, these INS experiments allowed us to observe the effects of chemical or structural modifications of SMMs on the pDOS. In particular, the experimental data demonstrate that the low energy spectra feature the largest differences, in the energy range of the phonons responsible for Raman processes. These, in particular, are expected to play the crucial role in the relaxation dynamics of SMMs and in the determination of their blocking temperature. Moreover, the fruitful comparison of the INS nw-pDOS with the one calculated *ab initio* with periodic DFT enabled the validation of the calculations, which are the starting point for the simulations of the relaxation dynamics of SMMs.

For the Dy-based molecular magnets synthesized by the Manchester group a ”fully” *ab initio* approach for the calculation of the spin-phonon couplings and the resulting relaxation rates is ongoing. These results, will give us the opportunity to further test the effectiveness of the ”cost-effective” method developed for the relaxation study of the Dysprosocenium complex [17] and applied recently to other SMMs.[31] Moreover, this ”cost-effective” approach will be applied to the relaxation analysis of the Dy-based SMM synthesized by the Glasgow group and studied as a function of the applied pressure by INS (ongoing work). Both these ongoing simulations will give clear and fundamental indications on the relaxation dynamics of these SMMs, for the development of better performing systems, exhibiting higher blocking temperatures.

Chapter 6

Combined EPR-NMR study of the Supramolecular $\{Cr_7Ni\}$-Cu dynamics

The search for molecular qubits with increasingly long coherence times is still very active. A new approach to the problem could be to exploit hybrid supramolecular structures, in which a fast and efficient electronic spin-based molecular processor is connected with a robust nuclear spin-based molecular memory. Supramolecular architectures have been already synthesized in the last few years, linking together several electronic qubit units, within the same molecular structure. [75, 134, 135, 136] In particular, for $\{Cr_7Ni\}$ rings it was recently demonstrated the possibility to link together several units, enabling the processor scaling to several-qubit-architectures. [10]

In this section we will focus on the characterization of a hybrid system in which a $\{Cr_7Ni\}$ ring is linked to a copper $[Cu(hfac)_2]$ nuclear qudit in a $\{Cr_7Ni\}$-Cu^{II} assembly. The $\{Cr_7Ni\}$ ring features a total spin $S = 1/2$ ground state resulting from the AF interaction of the cluster ions (7 Cr^{3+} and 1 Ni^{2+}), while the single copper ion in the Cu-based qudit provides an electronic spin $S = 1/2$ coupled to the copper nuclear spin $I = 3/2$. This supramolecular unit is very promising, since it links an efficient qubit to a nuclear qudit providing a robust isolated memory which can also embed quantum error correction. [49] Storing the information in an error protected and isolated nuclear qudit during the idle periods of complex algorithms increases the reliability of quantum operations and releases the stringent requirements of qubits with long coherence times. Indeed, nuclear spins are much more isolated from the environment than electronic ones. Thus, nuclear spins are less affected by noise-induced decoherence processes. Moreover, as shown in Ref. [88] nuclei featuring a $I > 1$ spin can efficiently implement quantum error correction algorithms, further enhancing the information storing time by correcting the errors induced by pure dephasing processes. Conversely, the electronic total-spin of the $\{Cr_7Ni\}$ ring has been demonstrated to be a promising electronic spin-based processor with long phase memory times.[87] This molecular qubit can be easily manipulated, in very short times, by resonant microwave (mw) pulses. Short manipulation times allows the implementation of several single qubit operations before coherence losses.[75] Moreover, by coordination chemistry, more than one single units of the $\{Cr_7Ni\}$-Cu^{II} assembly can be linked together into promising scalable

platforms.[137]
The $\{Cr_7Ni\}$-Cu^{II} complexes under study were synthesized by our collaborators at the University of Manchester (see the List of Collaborators), where I spent three months of my PhD research activity for the pulsed EPR characterization of these supramolecular assemblies.

6.1 Electronic spin-lattice and spin-coherence times

A thorough characterization of the electronic spin relaxation times is done by exploiting a Q-band ($\nu = 33.426969$ GHz) pulsed EPR spectrometer (see sect. 2.1.2) equipped with a 3 K cryostat. This very-low temperature regime in fact allows the detection of the $\{Cr_7Ni\}$ ring signal that is strongly suppressed at higher temperatures. [32] Echo detected field sweep (EDFS) on a 0.2 mM diluted frozen solution of the investigated sample revealed two main spectral contributions, arising from the $\{Cr_7Ni\}$ ring and the Copper-based qudit $[Cu(hfac)_2]$ (see fig. 6.1).

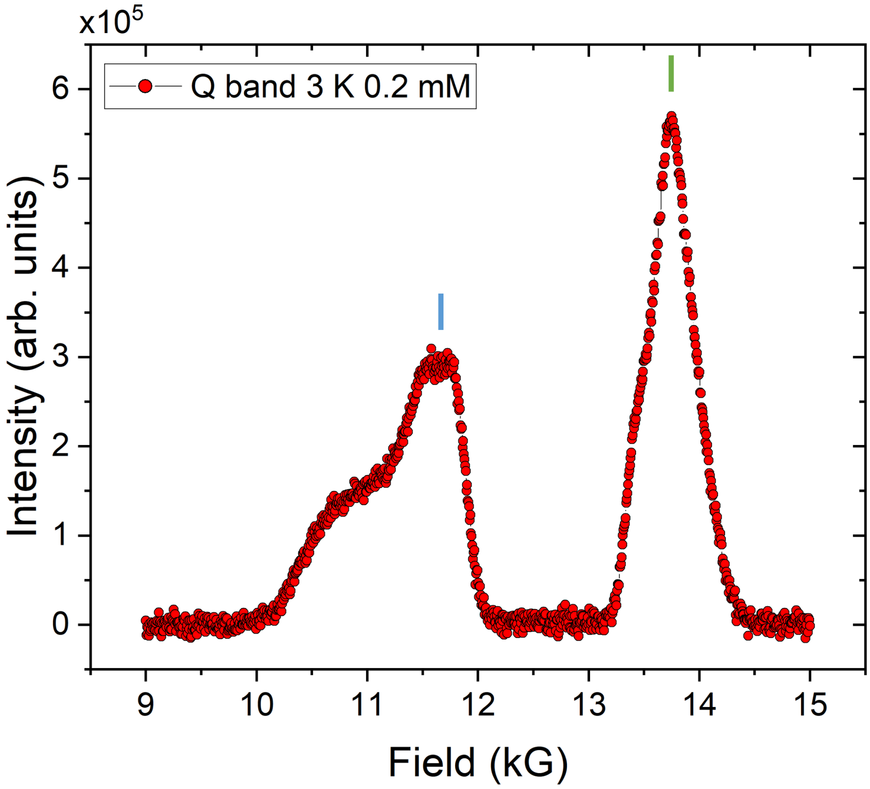

Figure 6.1: Q-band pulsed EPR EDFS at 3K on a 0.2 mM frozen solution of $\{Cr_7Ni\}[Cu(hfac)_2]$. The Hahn-echo refocusing sequence $\pi/2 - \tau - \pi$ used for the echo detection features a π-pulse of 120 ns. Light blue and green ticks mark the $\{Cr_7Ni\}$ and $[Cu(hfac)_2]$ in plane $g_{x,y}$ signals, respectively.

Here the two main peaks at $B_{Cu} \approx 11.745\ kG$ and $B_{ring} \approx 13.755\ kG$ correspond to the $g_{x,y}$ planar orientation, while the left shoulder of the Cu signal corresponds to the g_z direction showing the fourfold non-degenerate components of the Hyperfine coupling with its nuclear spin $I = 3/2$. These hyperfine components are however non distinguishable in the frozen solution spectra because of a lack of both resolution and signal intensity. Moreover, as expected from previous results reported in Ref. [49], the relative coupling J of the two electronic spin $S = 1/2$ from the Cu and the ring causes a splitting of each "in plane" spectral line. This splitting is visible for the more intense Cu and ring $g_{x,y}$ components, while for the low field g_z it causes a generalized broadening of the resonant signal that cannot be resolved in these experimental conditions. Electronic spin-lattice relaxation times ${}^eT_1$ have been also measured for all the spectral features at fixed field with a standard inversion-recovery sequence. The recovery paths are shown in figure 6.2, fitted with a double/triple exponentials saturation function $I(t) = \sum_i I_i(1 - \exp(-t/{}^eT_{1,i}))$, for the ring and Cu, respectively, in order to match the experimental data in such a wide time interval.

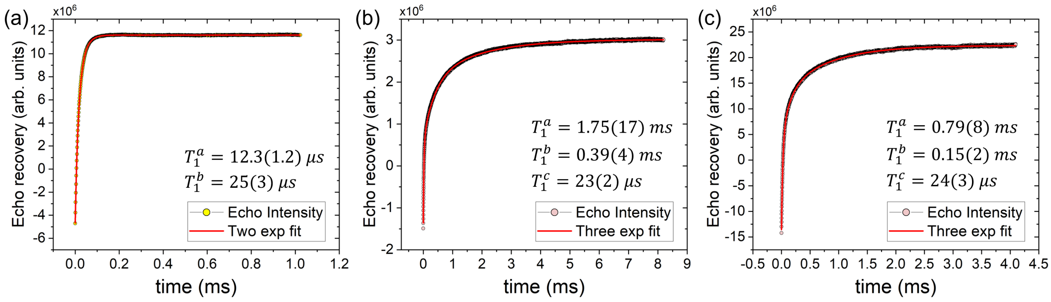

Figure 6.2: Electronic spin-lattice saturation recovery paths for a 0.2 mM frozen solution of $\{Cr_7Ni\}[Cu(hfac)_2]$ measured at 3K with Q-band EPR (dots). The three static fields shown correspond to: (a) the $g_{x,y}$ component of the ring $B_0 = 13.755$ kG, (b) the $g_{x,y}$ component of the Cu $B_0 = 11.745$ kG, and (c) one of the hyperfine lines along the g_z component of the Cu, at $B_0 = 10.862$ kG. The double or triple exponentials recovery rates are reported in the inset for each panel (red line).

The extracted spin-lattice ${}^eT_1$ corresponding to the fastest component of the recovery are higher then $10\mu s$ and thus promising for the envisaged applications, since these values confirm that the coupling of the two units within the supramolecular complex is not detrimental for the relaxation properties of the two systems. Indeed, for an isolated $\{Cr_7Ni\}$, the measured ${}^eT_1$ at 2.5 K is $\approx 50\mu$s, as reported in [39].

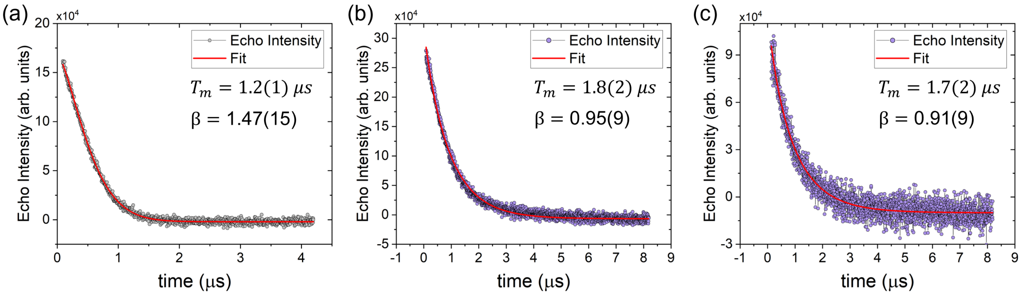

Figure 6.3: Electronic spin echo decays measured for a 0.2 mM frozen solution of $\{Cr_7Ni\}[Cu(hfac)_2]$, measured at 3K with Q-band EPR (dots). The three static fields shown correspond to: (a) the $g_{x,y}$ component of the ring $B_0 = 13.755$ kG, (b) the $g_{x,y}$ component of the Cu $B_0 = 11.745$ kG, and (c) one of the hyperfine lines along the g_z component of the Cu, at $B_0 = 10.862$ kG. The decays are fitted with a slightly stretched single exponential decay (parameters are shown in inset).

Electronic spin coherence times ${}^eT_m$ were measured for the same spectral features identified in figure 6.1 for both the ring and Cu electronic spins $S = 1/2$, by a Hahn-echo refocusing microwave-pulse (mw) sequence, as a function of increasing delay τ between the exciting and refocusing pulses. The echo intensity decays (fig. 6.3) are fitted by a slightly stretched single exponential law $M(\tau) = M_0(\exp(-2t/{}^eT_m)^\beta)$. At the working temperature of 3 K, the coherence times of the two electronic spins converge at remarkable values higher than 1 μs that, given the fast phonon-induced relaxation typical of AF ring complexes, [87, 138] is not detrimental in the perspective of implementing fast manipulations of the spins at lower temperatures.
The extracted spin coherence times are very similar for the $\{Cr_7Ni\}$ and the Cu electronic spins. This is due to the effective coupling between them inducing an averaging of the coherence times to the lowest value of the two. Indeed, by measuring the electronic spin coherence times of the $[Cu(hfac)_2]$ qudit hosted in the supramolecular structure in which it is coupled with the diamagnetic analogue of the AF ring, $\{Ti_7Ga\}$, we clearly observe that its spin coherence time is almost doubled (see fig. 6.5), since J coupling is removed. In figures 6.4 and 6.5 we show the X-band EDFS measured at 5.4 K on the partially diamagnetic $\{Ti_7Ga\}$-$[Cu(hfac)_2]$ together with the echo decay/saturation measurements. Here the spectra shows only the $[Cu(hfac)_2]$ signal, with a prominent planar component $g_{x,y}$ and a well resolved hyperfine splitting for the g_z one. The spin lattice ${}^eT_1$ and spin coherence ${}^eT_m$ times have been measured for all the spectral components. The saturation recovery curves are again fitted with a triple exponential function, while the echo decay is well represented by a slightly stretched single exponential model. Also the obtained spin-lattice relaxation times ${}^eT_1$ results more than doubled as a consequence of the absence of the J coupling in this partially-diamagnetic assembly.

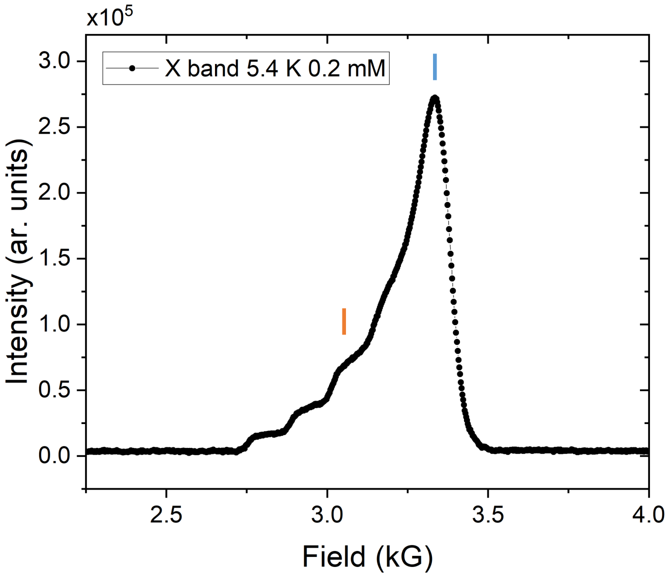

Figure 6.4: X-band pulsed EPR Echo Detected Field Sweep at 5.4K on a 0.2 mM frozen solution of $\{Ti_7Ga\}[Cu(hfac)_2]$. The π-pulse used for the detection, at fixed mw-power, was 32 ns long, calibrated on the highest spectral feature. Light blue and orange ticks mark the field at which the spin lattice and spin coherence times in figure 6.5 are measured and correspond to the in plane $g_{x,y}$ and one axial g_z $[Cu(hfac)_2]$ spectral components.

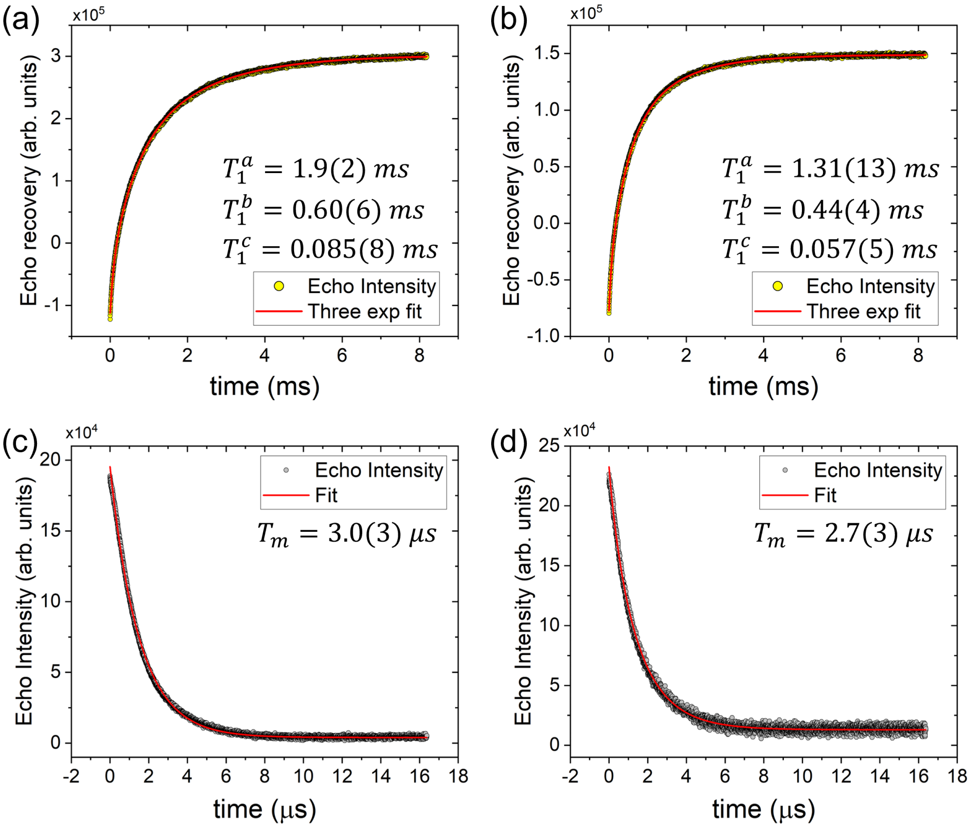

Figure 6.5: (a,b) X-band electronic saturation recovery data (dots) measured at 5.4 K on a 0.2 mM frozen solution of $\{Ti_7Ga\}[Cu(hfac)_2]$ with an inversion sequence for the two field (a) $B_0 = 3334$ G and (b) $B_0 = 3061$ G marked in figure 6.4. In inset the resulting triple exponential fit (red line) for spin-lattice rates. (c,d) X-band echo decay experiments for the same conditions above and at the same static fields. The spin coherence time extrapolated from the single exponential stretched fit (red line) are shown in inset.

6.2 Spin dynamics probed by ^{1}H-NMR

It was demonstrated in the last two decades that NMR techniques offers the possibility to investigate the details of the phonon-induced spin-lattice relaxation for electronic spins clusters.[138, 139, 140] Indeed, the thermal fluctuations of the electronic spin causes correlated variations in the local hyperfine field probed by the nuclei. Thus, by probing the nuclear spin-lattice relaxation rates $1/{}^nT_1$ of the abundant ^1H in the molecule, we can model the molecular magnetization decay and obtain some insights in the electronic spin-phonon coupling. This pulsed NMR investigation, complementary to the pulsed EPR analysis above, has been performed on the supramolecular $\{Cr_7Ni\}[Cu(hfac)_2]$ assembly by exploiting the broadband NMR spectrometer "HyReSpect" [11] (see sect. 2.1.1) at the University of Parma. Proton (^{1}H) nuclear spin-lattice relaxation times were measured in the temperature range $T = 5 - 50$ K for different static magnetic fields $B_0 = 0.33$, 0.75 and 1.5 T.

The technique used for measuring nuclear $^nT_1$ is not a simple inversion-recovery. Conversely, for measuring the recovery of the transverse nuclear magnetization we addressed the system with a saturating pulses train, followed by a standard Hahn-echo refocusing sequence $\pi/2 - \tau - \pi/2$. With this procedure we are confident that the nuclear absorption line is fully irradiated (maximum statistical temperature configuration).

The saturation recovery path follows a bi-exponential law $I(t) = I_1(1 - \exp(-t/^nT_{1,1})) + I_2(1 - \exp(-t/^nT_{1,2}))$, with a time scales difference of several order of magnitude; thus, the fastest relaxation we are interested in is easily distinguishable (fig. 6.6). The extracted spin-lattice relaxation rates $1/^nT_1$ for the fastest relaxing component are shown in figure 6.7 as a function of temperature for each applied field.

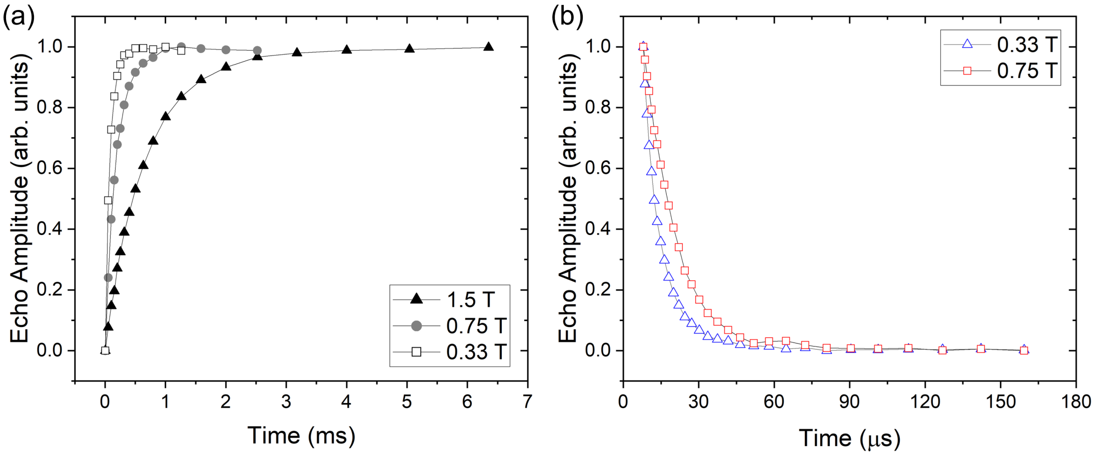

Figure 6.6: (a) Fastest ^{1}H-NMR normalized saturation recovery at 10 K for different applied static field B_0. (b) Normalized single exponential ^{1}H-NMR echo decay measured at 10 K for two applied fields.

The $1/^nT_1$ temperature dependence shows a peak at 11 K in 0.33 T applied field that, by increasing field, lowers in intensity, broadens and shifts at higher temperatures. A more detailed analysis of this relaxation dynamics is ongoing and the fitting of the data with a detailed theoretical framework, will give us information on the phonon coupling strength and, on the number of dominating relaxation rates/frequencies and on their temperature dependence.

In this analysis, an important effect that must be taken into account is the wipe out effect.[141] It consists in a gradual NMR signal loss at low temperature, due to an increment in the relaxation rates $^nT_2^{-1}$ of certain nuclei. The faster relaxation causes the signal to exit from the detectable window of our experimental setup (the so-called "dead-time", which is of the order of $\approx 10\ \mu s$). Thus, for simulating the spin-lattice relaxation rate we will retain only the ^1H nuclei with a transverse relaxation rate $^nT_2^{-1}$ smaller then the identified wipe out threshold. To evaluate this effect we measured the nuclear spin-spin relaxation rates $1/^nT_2$ over a wide temperature range, with a standard Hahn-echo refocusing sequence. The relaxation rates (fig. 6.6) are fitted with a slightly stretched mono-exponential function (with almost temperature-independend stretching parameter) and the values extracted are shown in figure 6.8. The extracted relaxation rates show a peak at 10 K in 0.33 T applied field that broadens, lowers in intensity, and shifts at higher temperatures by

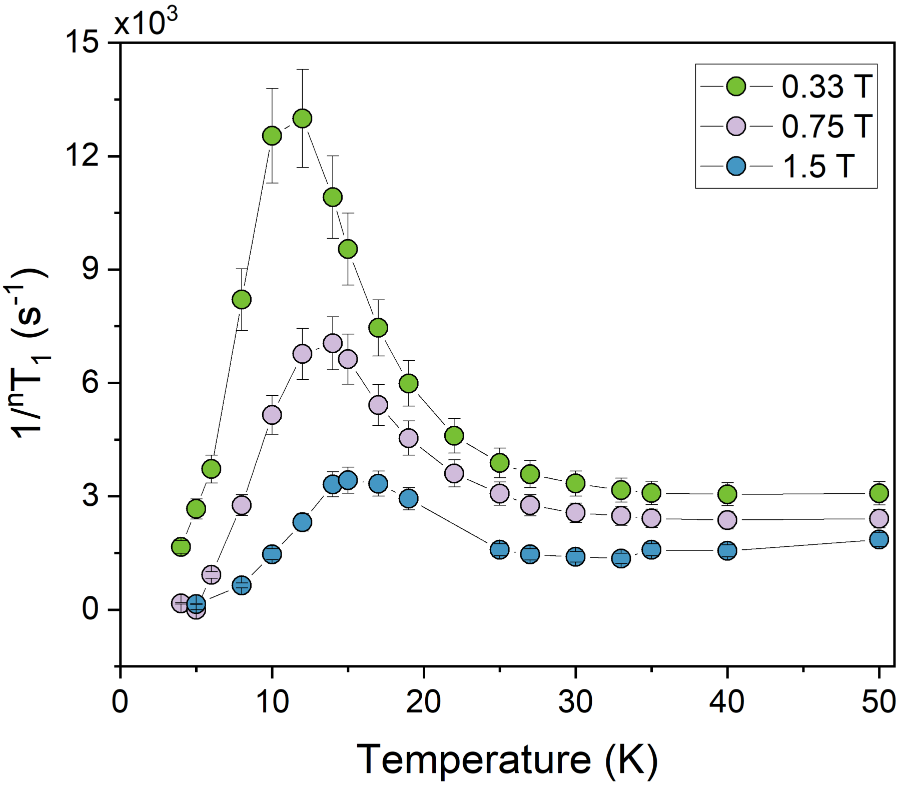

Figure 6.7: Proton nuclear spin-lattice relaxation rates $1/{}^{n}T_1$ extracted from fitting the saturation recovery curves in figure 6.6 as a function of the system temperature, at three different applied static field B_0.

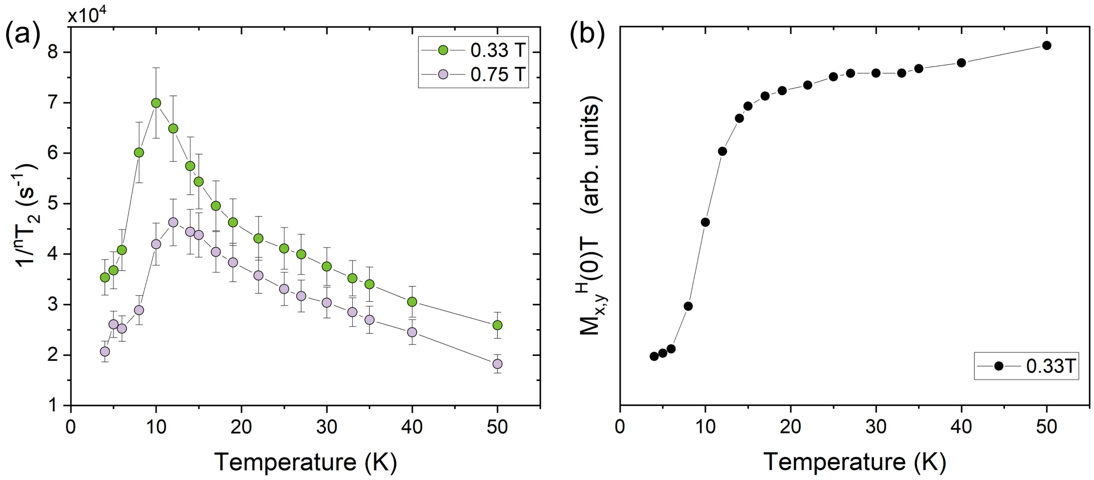

Figure 6.8: (a) Proton nuclear spin-spin relaxation rates $1/{}^{n}T_2$ at two static applied fields, extracted from fitting the echo amplitude decay with a stretched single exponential function at fixed stretching parameter β. (b) Transverse magnetization $M^{H}_{x,y}(0)T$ from the echo amplitude extrapolated at zero delay in the echo decays. Multiplied by the temperature, it gives a hint on the number of nuclei with a still measurable decoherence.

increasing the applied field. A visualization of the wipe out effect can be obtained by plotting the starting transverse magnetization values $M^H_{x,y}(0)$ extrapolated from the $\tau = 0$ point in the echo decay curves, multiplied by the measuring temperature (fig. 6.8). This quantity $M^H_{x,y}(0)T$ correspond to the number of resonating nuclei. In figure 6.8, at the applied field of 0.33 T, the number of resonating nuclei is saturated above 20 K, and decreases abruptly below 15 K, towards a low temperature (few Kelvin degrees) constant minimum value.

6.3 Electronic spin Manipulations

To better investigate the hyperfine splitting in the Cu g_z component, we milled several polycrystals (5 % diluted in the diamagnetic analogue $\{Ti_7Ga\}[Zn(hfac)_2]$) into fine powders and measured the echo detected field sweep in the Q-band EPR spectrometer (fig. 6.9). The signal to noise ratio is extremely high, thanks to a fine tuning of the resonant cavity, and consequently all the spectral features are well resolved. Indeed, in this configuration also the fourfold Hyperfine splitting of the g_z component is visible and enables the observation of the further splitting (five evident peaks are marked in fig. 6.9) induced by the J coupling.
Taking advantages of this fine tuning of the experimental setup, we performed a Rabi nutation experiment in order to demonstrate the ability to manipulate both the ring and Cu electronic spins coherently and independently from each other. The system was targeted by a manipulating pulse of variable length $\theta(t)$ followed by a Hahn-refocusing sequence $\pi/2 - \tau - \pi$. The Rabi oscillations for the $g_{x,y}$ components of the $\{Cr_7Ni\}$ ring and $[Cu(hfac)_2]$ are shown in figure 6.10 for different power attenuation.

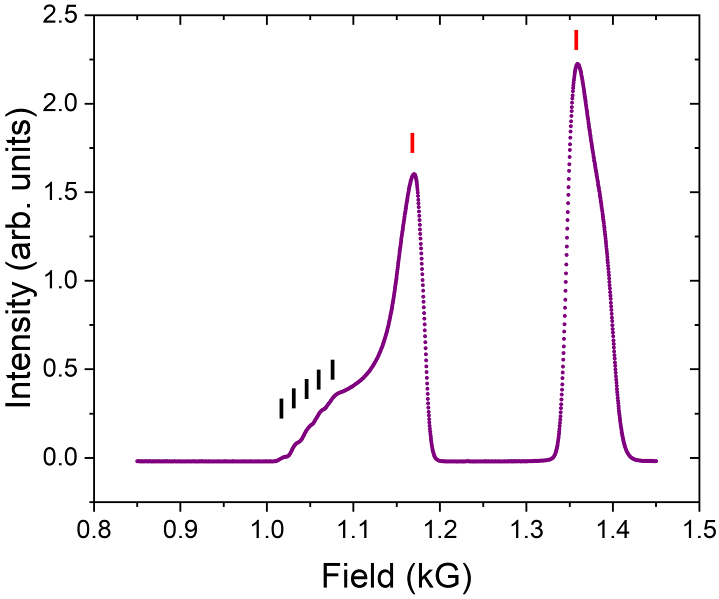

Figure 6.9: Q-band EPR-EDFS at 3K on a 5% diluted fine powder of $\{Cr_7Ni\}[Cu(hfac)_2]$. Red and black ticks mark the in plane $g_{x,y}$ and axial g_z ring and copper signal respectively.

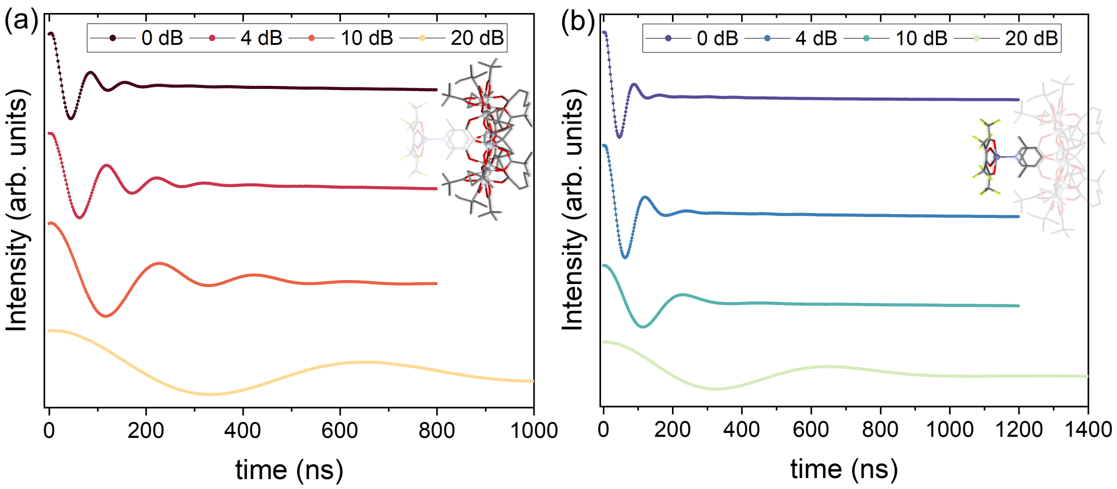

Figure 6.10: Rabi nutation experiments at 3 K on fine powder of {Cr_7Ni}-[Cu(hfac)$_2$]. The field was fixed to match respectively the two higher spectral components (a) B_{ring} = 13.597 kG and (b) B_{Cu} = 11.704 kG (as sketched in inset) corresponding to the $g_{x,y}$ plane. The pulse power-attenuation is varied to highlight the Rabi frequency ${}^{e}\omega_R$ and damping λ_R dependencies. For each pulse-power, the pulse length in the Rabi-sequence was modified in order to maintain the effectiveness of the $\pi/2 - \pi$ refocusing.

The obtained Rabi oscillations results coherent and monochromatic. Rabi frequency ${}^{e}\omega_R$ scales linearly with the pulse power attenuation, together with the oscillation damping, which is hampered in higher power configurations by the pulse inhomogeneities.

6.4 Conclusions

The electronic and nuclear spins relaxation dynamics of a {Cr_7Ni}[Cu(hfac)$_2$] complex has been thoroughly investigated by exploiting a combined pulsed EPR-NMR approach. The data analysis and the theoretical simulations on the relaxation dynamics are still ongoing. The theoretical model describing the system dynamics will be confirmed by fitting the relaxation rates for both the {Cr_7Ni} and the Cu electronic spins and Cu nuclear one. Interpreting these relaxation measurements will give fundamental insights for the determinations of the leading relaxation processes, such as their dependence on the temperature regime and the strength of spin-phonon coupling.[138, 139]
Putting together all this information, we will be able to deduct the key ingredients governing the system relaxation of this promising supramolecular assembly. Moreover, in view of the remarkable results achieved in the electronic spin manipulations through the Rabi nutations experiments on powder samples, studies on single crystals are ongoing. By exploiting a combined EPR-NMR approach, we expect to realize coherent manipulations of the qubit-qudit system, demonstrating the possibility to implement ordinary single qubit quantum algorithms and to realize efficiently the information swapping between the electronic spin processor and its nuclear memory. [49]

General Conclusions

In conclusion, in this thesis we have presented the results of different experimental characterizations of molecular nanomagnets. The spin Hamiltonian and the spin dynamics of these systems have been investigated by means of several different cutting-edge experimental techniques. We have demonstrated that broadband NMR is an election experimental tool for our studies, since it enabled a precise evaluation of the parameters of the electro-nuclear spin Hamiltonian of two V-based molecular qubits, together with their nuclear phase memory times (sect. 3). Proven that these systems possess the energy levels structure and the coherence prerequisites of an ideal qudit, by means of NMR rf-pulses we realized coherent manipulations of these electro-nuclear systems, inducing selectively the desired transitions between their nuclear states. In the case of the [VO(TPP)] complex, we also succeeded in simulating the encoding of a Quantum error correction algorithm and we addressed experimentally the same transitions involved in the encoding sequence, with really promising results, such as fast manipulations, negligible coherence losses and encoding reliability. By exploiting this technique and this, or similar complexes, we expect to succeed in realizing the firsts proof-of-principles experiments on the implementation of quantum error correction algorithms in molecular qudits. In particular, an interesting perspective-work would be the characterization of complexes from the class of Lanthanide-based monomers, dimers or trimers with the NMR experimental setup described above. [47, 44, 45] Indeed, also these systems represent ideal testbeds for the implementation of quantum algorithm on the expanded computational space that results from the coupling of different magnetic ions and of the electronic and nuclear spins within each ion.

The phonon-induced relaxation processes play a crucial role in the spin dynamics of molecular qudits such as the [VO(TPP)] molecule. The phonon dispersions of this complex were thoroughly investigated by exploiting, for the first time in a molecular crystal, inelastic X-ray scattering (sect. 4). The technique features several advantages with respect to the parent inelastic neutron scattering and the outstanding quality of the results achieved will pave the way for a systematic usage of this technique in parent compounds characterizations. In particular, in the [VO(TPP)] compound we observed extremely low-energy optical phonons and we validated the periodic DFT phonon calculations by comparing the measured IXS cross section with the simulated one. The validated phonon model was then used to simulate the spin relaxation of [VO(TPP)], identifying the crucial role of the low energy modes, which result to be critically coupled with the electronic spins. The results achieved in this study will be crucial for the development of new classes of molecular magnets with optimized coherence by tailoring of phonon modes.

In this thesis we also focused on the study of single molecule magnets with high energy barriers. In particular, our scientific effort was devoted to the determination of the key factors governing the phonon-induced relaxation processes. Focusing on Dy-based SMMs, we studied by inelastic neutron scattering the effects on the phonon density of states of chemical/structural substitutions in the molecule or of an external applied pressure (sect. 5). By exploiting INS, we accessed the phonon density of states and, in both systems, we demonstrated that the main differences are in the energy range of phonons involved in Raman relaxation processes. These relaxation processes are indeed the crucial ones for the determination of SMMs performances. The comparison of the experimental phonon density of states with the ones simulated with periodic DFT was exploited to validate the phonon models, to be used for simulating the spin dynamics of these complexes. This approach represent a valuable test-bed for the phonon model validation, that needs to be implemented systematically in future works.

Finally, we presented a combined EPR-NMR characterization of the spin dynamics of a supramolecular complex in which a $\{Cr_7Ni\}$ ring qubit is linked to a Cu-based nuclear qudit with long coherence times (sect. 6). By exploiting pulsed Q-band EPR we measured the electronic spin-lattice and spin-coherence relaxation times, and we realized coherent individual manipulations of both the ring and the Cu electronic spins. Moreover, with ^{1}H-NMR we accessed the proton nuclear spin-lattice and spin-spin rates. These results will be used to elaborate a model for the relaxation dynamics of the system.

To summarize, in this thesis we exploited several advanced experimental techniques which are essential in the study of MNMs and enabled to pinpoint the key ingredients for the optimization of their performances for applications in quantum technologies. The next step for this purpose is the realization of an experimental setup for multi-frequency addressing of these systems, capable of inducing several coherent transitions within the multilevel structure of these molecular qudits in short times. Such a platform would enable the implementation of both single and multi-qubit proof-of-principle quantum algorithms. At the same time, it is also pivotal to discuss and design the first single molecule experiments, which represents the final challenge for the implementation of molecular magnets in real quantum information processing devices.

Bibliography

[1] R. Sessoli, D. Gatteschi, A. Caneschi, M. A. Novak, Magnetic bistability in a metal-ion cluster. *Nature* **365**, 141–143 (1993).

[2] F.-S. Guo, B. M. Day, Y.-C. Chen, M.-L. Tong, A. Mansikkamäki, R. A. Layfield, Magnetic hysteresis up to 80 kelvin in a dysprosium metallocene single-molecule magnet. *Science* **362**, 1400-1403 (2018).

[3] F. K. Larsen, E. J. L. McInnes, H. E. Mkami, J. Overgaard, S. Piligkos, G. Rajaraman, E. Rentschler, A. A. Smith, G. M. Smith, V. Boote, M. Jennings, G. A. Timco, R. E. P. Winpenny, Synthesis and Characterization of Heterometallic Cr_7M Wheels. *Angew. Chem. Int. Ed* **42**, 101-105 (2003).

[4] S. Chicco, A. Chiesa, G. Allodi, E. Garlatti, M. Atzori, L. Sorace, R. D. Renzi, R. Sessoli, S. Carretta, Controlled coherent dynamics of [VO(TPP)], a prototype molecular nuclear qudit with an electronic ancilla. *Chem. Sci.* **12**, 12046 (2021).

[5] J. M. Zadrozny, J. Niklas, O. G. Poluektov, D. E. Freedman, Millisecond Coherence Time in a Tunable Molecular Electronic Spin Qubit. *ACS Cent. Sci.* **1**, 488-492 (2015).

[6] M. Atzori, E. Morra, L. Tesi, A. Albino, M. Chiesa, L. Sorace, R. Sessoli, Quantum Coherence Times Enhancement in Vanadium(IV)-based Potential Molecular Qubits: the Key Role of the Vanadyl Moiety. *J. Am. Chem. Soc.* **138**, 11234-11244 (2016).

[7] S. Thiele, F. Balestro, R. Ballou, S. Klyatskaya, M. Ruben, W. Wernsdorfer, Electrically driven nuclear spin resonance in single-molecule magnets. *Science* **344**, 1135-1138 (2014).

[8] K. S. Pedersen, A.-M. Ariciu, S. McAdams, H. Weihe, J. Bendix, F. Tuna, S. Piligkos, Toward Molecular 4f Single-Ion Magnet Qubits. *J. Am. Chem. Soc.* **138**, 5801-5804 (2016).

[9] G. Aromí, D. Aguilà, P. Gamez, F. Luis, O. Roubeau, Design of magnetic coordination complexes for quantum computing. *Chem. Soc. Rev.* **41**, 537-546 (2012).

[10] S. J. Lockyer, A. Chiesa, A. Brookfield, G. A. Timco, G. F. S. Whitehead, E. J. L. McInnes, S. Carretta, R. E. P. Winpenny, Five-Spin Supramolecule for Simulating Quantum Decoherence of Bell States. *J. Am. Chem. Soc.* **144**, 16086-16092 (2022).

[11] G. Allodi, A. Banderini, R. De Renzi, C. Vignali, HyReSpect: A broadband fast-averaging spectrometer for nuclear magnetic resonance of magnetic materials. *Rev. Sci. Instrum.* **76**, 083911 (2005).

[12] M. Atzori, E. Garlatti, G. Allodi, S. Chicco, A. Chiesa, A. Albino, R. De Renzi, E. Salvadori, M. Chiesa, S. Carretta, L. Sorace, Radiofrequency to Microwave Coherent Manipulation of an Organometallic Electronic Spin Qubit Coupled to a Nuclear Qudit. *Inorg. Chem.* **60**, 11273–11286 (2021).

[13] A. Lunghi, S. Sanvito, How do phonons relax molecular spins? *Sci. Adv* **5**, eaax7163 (2019).

[14] T. Yamabayashi, M. Atzori, L. Tesi, G. Cosquer, F. Santanni, M.-E. Boulon, E. Morra, S. Benci, R. Torre, M. Chiesa, L. Sorace, R. Sessoli, M. Yamashita, Scaling Up Electronic Spin Qubits into a Three-Dimensional Metal-Organic Framework. *J. Am. Chem. Soc.* **140**, 12090-12101 (2018).

[15] C. A. P. Goodwin, F. Ortu, D. Reta, N. F. Chilton, D. P. Mills, Molecular magnetic hysteresis at 60 kelvin in dysprosocenium. *Nature* **548**, 439-442 (2017).

[16] P. Evans, D. Reta, G. F. Whitehead, N. F. Chilton, D. P. Mills, Bis-Monophospholyl Dysprosium Cation Showing Magnetic Hysteresis at 48 K. *J. Am. Chem. Soc.* **141**, 19935-19940 (2019).

[17] A. Chiesa, F. Cugini, R. Hussain, E. Macaluso, G. Allodi, E. Garlatti, M. Giansiracusa, C. A. P. Goodwin, F. Ortu, D. Reta, J. M. Skelton, T. Guidi, P. Santini, M. Solzi, R. De Renzi, D. P. Mills, N. F. Chilton, S. Carretta, Understanding magnetic relaxation in single-ion magnets with high blocking temperature. *Phys. Rev. B* **101**, 174402 (2020).

[18] A. B. Canaj, M. K. Singh, C. Wilson, G. Rajaraman, M. Murrie, Chemical and in silico tuning of the magnetisation reversal barrier in pentagonal bipyramidal Dy(iii) single-ion magnets. *Chem. Commun.* **54**, 8273-8276 (2018).

[19] D. Gatteschi, R. Sessoli, J. Villain, *Molecular Nanomagnets* (Oxford University Press, 2006).

[20] A. Caneschi, D. Gatteschi, R. Sessoli, A. L. Barra, L. C. Brunel, M. Guillot, Alternating current susceptibility, high field magnetization, and millimeter band EPR evidence for a ground S = 10 state in $[Mn_{12}O_{12}(Ch_3COO)_{16}(H_2O)_4]_2CH_3COOH_4H_2O$. *J. Am. Chem. Soc.* **113**, 5873-5874 (1991).

[21] W. Wernsdorfer, T. Ohm, C. Sangregorio, R. Sessoli, D. Mailly, C. Paulsen, Observation of the Distribution of Molecular Spin States by Resonant Quantum Tunneling of the Magnetization. *Phys. Rev. Lett.* **82**, 3903–3906 (1999).

[22] S. Carretta, P. Santini, G. Amoretti, M. Affronte, A. Candini, A. Ghirri, I. S. Tidmarsh, R. H. Laye, R. Shaw, E. J. L. McInnes, High-Temperature Slow Relaxation of the Magnetization in Ni_{10} Magnetic Molecules. *Phys. Rev. Lett.* **97**, 207201 (2006).

[23] C. J. Milios, A. Vinslava, W. Wernsdorfer, S. Moggach, S. Parsons, S. P. Perlepes, G. Christou, E. K. Brechin, A Record Anisotropy Barrier for a Single-Molecule Magnet. *J. Am. Chem. Soc.* **129**, 2754-2755 (2007).

[24] R. . Orbach, B. Bleaney, Spin-lattice relaxation in rare-earth salts. *Proc. R. Soc. Lond. A* **264**, 458-484 (1961).

[25] K. N. Shrivastava, Theory of Spin–Lattice Relaxation. *phys. stat. sol. (b)* **117**, 437-458 (1983).

[26] N. Ishikawa, M. Sugita, T. Ishikawa, S.-y. Koshihara, Y. Kaizu, Lanthanide Double-Decker Complexes Functioning as Magnets at the Single-Molecular Level. *J. Am. Chem. Soc.* **125**, 8694-8695 (2003).

[27] M. Gregson, N. F. Chilton, A.-M. Ariciu, F. Tuna, I. F. Crowe, W. Lewis, A. J. Blake, D. Collison, E. J. L. McInnes, R. E. P. Winpenny, S. T. Liddle, A monometallic lanthanide bis(methanediide) single molecule magnet with a large energy barrier and complex spin relaxation behaviour. *Chem. Sci.* **7**, 155-165 (2016).

[28] L. Escalera-Moreno, J. J. Baldoví, A. Gaita-Ariño, E. Coronado, Spin states, vibrations and spin relaxation in molecular nanomagnets and spin qubits: a critical perspective. *Chem. Sci.* **9**, 3265-3275 (2018).

[29] A. Lunghi, F. Totti, R. Sessoli, S. Sanvito, The role of anharmonic phonons in under-barrier spin relaxation of single molecule magnets. *Nat. Commun.* **8**, 14620 (2017).

[30] E. Garlatti, L. Tesi, A. Lunghi, M. Atzori, D. J. Voneshen, P. Santini, S. Sanvito, T. Guidi, R. Sessoli, S. Carretta, Unveiling phonons in a molecular qubit with four-dimensional inelastic neutron scattering and density functional theory. *Nat. Commun* **11**, 1751 (2020).

[31] E. Garlatti, A. Chiesa, P. Bonfà, E. Macaluso, I. J. Onuorah, V. S. Parmar, Y.-S. Ding, Y.-Z. Zheng, M. J. Giansiracusa, D. Reta, E. Pavarini, T. Guidi, D. P. Mills, N. F. Chilton, R. E. P. Winpenny, P. Santini, S. Carretta, A Cost-Effective Semi-Ab Initio Approach to Model Relaxation in Rare-Earth Single-Molecule Magnets. *J. Phys. Chem. Lett.* **12**, 8826-8832 (2021).

[32] C. J. Wedge, G. A. Timco, E. T. Spielberg, R. E. George, F. Tuna, S. Rigby, E. J. L. McInnes, R. E. P. Winpenny, S. J. Blundell, A. Ardavan, Chemical Engineering of Molecular Qubits. *Phys. Rev. Lett.* **108**, 107204 (2012).

[33] M. Shiddiq, D. Komijani, Y. Duan, A. Gaita-Ariño, E. Coronado, S. Hill, Enhancing coherence in molecular spin qubits via atomic clock transitions. *Nature* **531**, 348-351 (2016).

[34] M. J. Graham, J. M. Zadrozny, M. Shiddiq, J. S. Anderson, M. S. Fataftah, S. Hill, D. E. Freedman, Influence of Electronic Spin and Spin–Orbit Coupling on Decoherence in Mononuclear Transition Metal Complexes. *J. Am. Chem. Soc.* **136**, 7623-7626 (2014).

[35] M. Atzori, L. Tesi, E. Morra, M. Chiesa, L. Sorace, R. Sessoli, Room-Temperature Quantum Coherence and Rabi Oscillations in Vanadyl Phthalocyanine: Toward Multifunctional Molecular Spin Qubits. *J. Am. Chem. Soc.* **138**, 2154-2157 (2016).

[36] F. Petiziol, A. Chiesa, S. Wimberger, P. Santini, S. Carretta, Counteracting dephasing in Molecular Nanomagnets by optimized qudit encodings. *npj Quantum Inf* p. 133 (2021).

[37] M. Atzori, L. Tesi, S. Benci, A. Lunghi, R. Righini, A. Taschin, R. Torre, L. Sorace, R. Sessoli, Spin Dynamics and Low Energy Vibrations: Insights from Vanadyl-Based Potential Molecular Qubits. *J. Am. Chem. Soc.* **139**, 4338-4341 (2017).

[38] J. van Slageren, R. Sessoli, D. Gatteschi, A. A. Smith, M. Helliwell, R. E. P. Winpenny, A. Cornia, A.-L. Barra, A. G. M. Jansen, E. Rentschler, G. A. Timco, Magnetic Anisotropy of the Antiferromagnetic Ring [$Cr_8F_8Piv_{16}$]. *Chem. Eur. J.* **8**, 277-285 (2002).

[39] A. Ardavan, O. Rival, J. J. L. Morton, S. J. Blundell, A. M. Tyryshkin, G. A. Timco, R. E. P. Winpenny, Will Spin-Relaxation Times in Molecular Magnets Permit Quantum Information Processing? *Phys. Rev. Lett.* **98**, 057201 (2007).

[40] F. Moro, D. Kaminski, F. Tuna, G. F. S. Whitehead, G. A. Timco, D. Collison, R. E. P. Winpenny, A. Ardavan, E. J. L. McInnes, Coherent electron spin manipulation in a dilute oriented ensemble of molecular nanomagnets: pulsed EPR on doped single crystals. *Chem. Commun.* **50**, 91-93 (2014).

[41] S. Bertaina, S. Gambarelli, T. Mitra, B. Tsukerblat, A. Müller, B. Barbara, Quantum oscillations in a molecular magnet. *Nature* **453**, 203-206 (2008).

[42] E. Moreno-Pineda, C. Godfrin, F. Balestro, W. Wernsdorfer, M. Ruben, Molecular spin qudits for quantum algorithms. *Chem. Soc. Rev.* **47**, 501-513 (2018).

[43] M. D. Jenkins, Y. Duan, B. Diosdado, J. J. García-Ripoll, A. Gaita-Ariño, C. Giménez-Saiz, P. J. Alonso, E. Coronado, F. Luis, Coherent manipulation of three-qubit states in a molecular single-ion magnet. *Phys. Rev. B* **95**, 064423 (2017).

[44] F. Luis, P. J. Alonso, O. Roubeau, V. Velasco, D. Zueco, D. Aguilà, J. I. Martínez, L. A. Barrios, G. Aromí, A dissymmetric [Gd_2] coordination molecular dimer hosting six addressable spin qubits. *Commun Chem* **3**, 176 (2020).

[45] R. Hussain, G. Allodi, A. Chiesa, E. Garlatti, D. Mitcov, A. Konstantatos, K. Pedersen, R. D. Renzi, S. Piligkos, S. Carretta, Coherent Manipulation of a Molecular Ln-Based Nuclear Qudit Coupled to an Electron Qubit. *J. Am. Chem. Soc.* **140**, 9814-9818 (2018).

[46] D. Aguilà, L. A. Barrios, V. Velasco, O. Roubeau, A. Repollés, P. J. Alonso, J. Sesé, S. J. Teat, F. Luis, G. Aromí, Heterodimetallic [LnLn'] Lanthanide Complexes: Toward a Chemical Design of Two-Qubit Molecular Spin Quantum Gates. *J. Am. Chem. Soc.* **136**, 14215-14222 (2014).

[47] E. Macaluso, M. Rubín, D. Aguilà, A. Chiesa, L. A. Barrios, J. I. Martínez, P. J. Alonso, O. Roubeau, F. Luis, G. Aromí, S. Carretta, A heterometallic [LnLn'Ln] lanthanide complex as a qubit with embedded quantum error correction. *Chem. Sci.* **11**, 10337-10343 (2020).

[48] J. Ferrando-Soria, E. Moreno Pineda, A. Chiesa, A. Fernandez, S. A. Magee, S. Carretta, P. Santini, I. J. Vitorica-Yrezabal, F. Tuna, G. A. Timco, E. J. McInnes, R. E. Winpenny, A modular design of molecular qubits to implement universal quantum gates. *Nat. Commun.* **7**, 11377 (2016).

[49] S. J. Lockyer, A. Chiesa, G. A. Timco, E. J. L. McInnes, T. S. Bennett, I. J. Vitorica-Yrezebal, S. Carretta, R. E. P. Winpenny, Targeting molecular quantum memory with embedded error correction. *Chem. Sci.* **12**, 9104-9113 (2021).

[50] S. Carretta, D. Zueco, A. Chiesa, A. Gómez-León, F. Luis, A perspective on scaling up quantum computation with molecular spins. *Appl. Phys. Lett.* **118**, 240501 (2021).

[51] A. Gaita-Ariño, F. Luis, S. Hill, C. Eugenio, Molecular spins for quantum computation. *Nature* **11**, 301–309 (2019).

[52] M. Mannini, F. Pineider, C. Danieli, F. Totti, L. Sorace, P. Sainctavit, M.-A. Arrio, E. Otero, L. Joly, J. C. Cezar, A. Cornia, R. Sessoli, Quantum tunnelling of the magnetization in a monolayer of oriented single-molecule magnets. *Nature* **468**, 417-421 (2010).

[53] V. Corradini, A. Ghirri, E. Garlatti, R. Biagi, V. De Renzi, U. del Pennino, V. Bellini, S. Carretta, P. Santini, G. Timco, R. E. P. Winpenny, M. Affronte, Magnetic Anisotropy of Cr_7Ni Spin Clusters on Surfaces. *Adv. Funct.* **22**, 3706-3713 (2012).

[54] I. Cimatti, L. Bondì, G. Serrano, L. Malavolti, B. Cortigiani, E. Velez-Fort, D. Betto, A. Ouerghi, N. B. Brookes, S. Loth, M. Mannini, F. Totti, R. Sessoli, Vanadyl phthalocyanines on graphene/SiC(0001): toward a hybrid architecture for molecular spin qubits. *Nanoscale Horiz.* **4**, 1202-1210 (2019).

[55] C. Bonizzoni, A. Ghirri, F. Santanni, M. Atzori, L. Sorace, R. Sessoli, M. Affronte, Storage and retrieval of microwave pulses with molecular spin ensembles. *npj Quantum Inf* **6**, 68 (2020).

[56] J. Preskill, Quantum Computing in the NISQ era and beyond. *Quantum* **2**, 79 (2018).

[57] F. Arute, *et al.*, Quantum supremacy using a programmable superconducting processor. *Nature* **574**, 505-510 (2019).

[58] A. W. Cross, L. S. Bishop, S. Sheldon, P. D. Nation, J. M. Gambetta, Validating quantum computers using randomized model circuits. *Phys. Rev. A* **100**, 032328 (2019).

[59] I. Bloch, Quantum coherence and entanglement with ultracold atoms in optical lattices. *Nature* **453**, 1016–1022 (2008).

[60] G. J. Milburn, Photons as qubits. *Phys. Scr.* **T137**, 014003 (2009).

[61] J. Clarke, F. Wilhelm, Superconducting quantum bits. *Nature* **453**, 1031–1042 (2008).

[62] I. Chiorescu, Y. Nakamura, C. J. P. M. Harmans, J. E. Mooij, Coherent Quantum Dynamics of a Superconducting Flux Qubit. *Science* **299** (2003).

[63] F. Jelezko, T. Gaebel, I. Popa, M. Domhan, A. Gruber, J. Wrachtrup, Observation of Coherent Oscillation of a Single Nuclear Spin and Realization of a Two-Qubit Conditional Quantum Gate. *Phys. Rev. Lett.* **93**, 130501 (2004).

[64] J. J. Pla, K. Y. Tan, J. P. Dehollain, W. H. Lim, J. J. L. Morton, D. N. Jamieson, A. S. Dzurak, A. Morello, A single-atom electron spin qubit in silicon. *Nature* **489**, 541–545 (2012).

[65] L. Childress, M. V. G. Dutt, J. M. Taylor, A. S. Zibrov, F. Jelezko, J. Wrachtrup, P. R. Hemmer, M. D. Lukin, Coherent Dynamics of Coupled Electron and Nuclear Spin Qubits in Diamond. *Science* **314**, 281-285 (2006).

[66] M. Sinha, T. J. Pearson, T. R. Reeder, H. K. Vivanco, D. E. Freedman, W. A. Phelan, T. M. McQueen, Introduction of spin centers in single crystals of $Ba_2CaWO_{6-\delta}$. *Phys. Rev. Materials* **3**, 125002 (2019).

[67] M. Atzori, R. Sessoli, The Second Quantum Revolution: Role and Challenges of Molecular Chemistry. *J. Am. Chem. Soc.* **141**, 11339-11352 (2019). PMID: 31287678.

[68] G. A. Timco, S. Carretta, F. Troiani, F. Tuna, R. J. Pritchard, C. A. Muryn, E. J. L. McInnes, A. Ghirri, A. Candini, P. Santini, G. Amoretti, M. Affronte, R. E. P. Winpenny, Engineering the coupling between molecular spin qubits by coordination chemistry. *Nature Nanotech* **4**, 173–178 (2009).

[69] C.-J. Yu, M. J. Graham, J. M. Zadrozny, J. Niklas, M. D. Krzyaniak, M. R. Wasielewski, O. G. Poluektov, D. E. Freedman, Long Coherence Times in Nuclear Spin-Free Vanadyl Qubits. *J. Am. Chem. Soc.* **138**, 14678-14685 (2016).

[70] D. P. DiVincenzo, The Physical Implementation of Quantum Computation. *Fortschr. Phys.* **48**, 771-783 (2000).

[71] A. P. M. Place, L. V. H. Rodgers, P. Mundada, B. M. Smitham, M. Fitzpatrick, Z. Leng, A. Premkumar, J. Bryon, A. Vrajitoarea, S. Sussman, G. Cheng, T. Madhavan, H. K. Babla, X. Hoang Le, Y. Gang, B. Jäck, A. Gyenis, N. Yao, R. J. Cava, N. P. de Leon, A. A. Houck, New material platform for superconducting transmon qubits with coherence times exceeding 0.3 milliseconds. *Nat. Commun.* **12** (2021).

[72] E. Garlatti, M. A. Albring, M. L. Baker, R. J. Docherty, H. Mutka, T. Guidi, V. Garcia Sakai, G. F. S. Whitehead, R. G. Pritchard, G. A. Timco, F. Tuna, G. Amoretti, S. Carretta, P. Santini, G. Lorusso, M. Affronte, E. J. L. McInnes, D. Collison, R. E. P. Winpenny, A Detailed Study of the Magnetism of Chiral

Cr7M Rings: An Investigation into Parametrization and Transferability of Parameters. *J. Am. Chem. Soc.* **136**, 9763-9772 (2014).

[73] K. Park, M. A. Novotny, N. S. Dalal, S. Hill, P. A. Rikvold, Effects of D-strain, g-strain, and dipolar interactions on EPR linewidths of the molecular magnets Fe_8 and Mn_{12}. *Phys. Rev. B* **65**, 014426 (2001).

[74] E. Garlatti, T. Guidi, S. Ansbro, P. Santini, G. Amoretti, J. Ollivier, H. Mutka, G. Timco, I. J. Vitorica-Yrezabal, G. F. S. Whitehead, R. E. P. Winpenny, S. Carretta, Portraying entanglement between molecular qubits with four-dimensional inelastic neutron scattering. *Nat. Commun.* p. 14543 (2017).

[75] A. Chiesa, G. F. S. Whitehead, S. Carretta, L. Carthy, G. A. Timco, S. J. Teat, G. Amoretti, E. Pavarini, R. E. P. Winpenny, P. Santini, Molecular nanomagnets with switchable coupling for quantum simulation. *Sci. Rep.* **4** (2014).

[76] J. Ferrando-Soria, S. A. Magee, A. Chiesa, S. Carretta, P. Santini, I. J. Vitorica-Yrezabal, F. Tuna, G. F. Whitehead, S. Sproules, K. M. Lancaster, A.-L. Barra, G. A. Timco, E. J. McInnes, R. E. Winpenny, Switchable Interaction in Molecular Double Qubits. *Chem* **1**, 727–752 (2016).

[77] D. Gatteschi, A. Cornia, M. Mannini, R. Sessoli, Organizing and Addressing Magnetic Molecules. *Inorganic Chemistry* **48**, 3408-3419 (2009).

[78] V. Corradini, R. Biagi, U. del Pennino, V. De Renzi, A. Gambardella, M. Affronte, C. A. Muryn, G. A. Timco, R. E. P. Winpenny, Isolated Heterometallic Cr7Ni Rings Grafted on Au(111) Surface. *Inorganic Chemistry* **46**, 4937-4943 (2007).

[79] J. S. Uber, M. Estrader, J. Garcia, P. Lloyd-Williams, A. Sadurní, D. Dengler, J. van Slageren, N. F. Chilton, O. Roubeau, S. J. Teat, J. Ribas-Arino, G. Aromí, Molecules Designed to Contain Two Weakly Coupled Spins with a Photoswitchable Spacer. *Chem. Eur. J.* **23**, 13648 (2017).

[80] M. V. Fedin, E. G. Bagryanskaya, H. Matsuoka, S. Yamauchi, S. L. Veber, K. Y. Maryunina, E. V. Tretyakov, V. I. Ovcharenko, R. Z. Sagdeev, W-Band Time-Resolved Electron Paramagnetic Resonance Study of Light-Induced Spin Dynamics in Copper–Nitroxide-Based Switchable Molecular Magnets. *J. Am. Chem. Soc.* **134**, 16319-16326 (2012). PMID: 22963168.

[81] M. D. Jenkins, D. Zueco, O. Roubeau, G. Aromí, J. Majer, F. Luis, A scalable architecture for quantum computation with molecular nanomagnets. *Dalton Trans.* **45**, 16682-16693 (2016).

[82] G. Wendin, Quantum information processing with superconducting circuits: a review. *Rep. Prog. Phys.* **80**, 106001 (2017).

[83] D. K. Park, G. Feng, R. Rahimi, S. Labruyère, T. Shibata, S. Nakazawa, K. Sato, T. Takui, R. Laflamme, Baugh, Hyperfine spin qubits in irradiated malonic acid: heat-bath algorithmic cooling. *J. Quantum Inf. Process* **14**, 2435 (2015).

[84] P. W. Shor, Scheme for reducing decoherence in quantum computer memory. *Phys. Rev. A* **52**, 2493 (1995).

[85] A. M. Steane, Error Correcting Codes in Quantum Theory. *Phys. Rev. Lett.* **77**, 793 (1996).

[86] L. Escalera-Moreno, N. Suaud, A. Gaita-Ariño, E. Coronado, Determining Key Local Vibrations in the Relaxation of Molecular Spin Qubits and Single-Molecule Magnets. *J. Phys. Chem. Lett.* **8**, 1695-1700 (2017).

[87] C. J. Wedge, G. A. Timco, E. T. Spielberg, R. E. George, F. Tuna, S. Rigby, E. J. L. McInnes, R. E. P. Winpenny, S. J. Blundell, A. Ardavan, Chemical Engineering of Molecular Qubits. *Phys. Rev. Lett.* **108**, 107204 (2012).

[88] A. Chiesa, E. Macaluso, F. Petiziol, S. Wimberger, P. Santini, S. Carretta, Molecular Nanomagnets as Qubits with Embedded Quantum-Error Correction. *J. Phys. Chem. Lett.* **11**, 8610 (2020).

[89] M. A. Nielsen, I. L. Chuang, *Quantum Computation and Quantum Information* (Cambridge University Press, 2010).

[90] A. Bienfait, J. J. Pla, Y. Kubo, M. Stern, X. Zhou, C. C. Lo, C. D. Weis, T. Schenkel, M. L. W. Thewalt, D. Vion, D. Esteve, B. Julsgaard, K. Mølmer, J. J. L. Morton, P. Bertet, Reaching the quantum limit of sensitivity in electron spin resonance. *Nat. Nanotechnol.* **11**, 253-257 (2016).

[91] S. L. Bayliss, D. W. Laorenza, P. J. Mintun, B. D. Kovos, D. E. Freedman, D. D. Awschalom, Optically addressable molecular spins for quantum information processing. *Science* **370**, 1309-1312 (2020).

[92] A. Abragam, B. Bleaney, *Electron paramagnetic resonance of transition ions* (Oxford University Press, 1970).

[93] G. Amoretti, *Formulazione Microscopica delle Interazioni Fondamentali nel Magnetismo* (dispense presentate al XXII corso del G.N.S.M., 1990).

[94] D. G. Tempel, A. Aspuru-Guzik, Relaxation and dephasing in open quantum systems time-dependent density functional theory: Properties of exact functionals from an exactly-solvable model system. *Chem. Phys.* **391**, 130-142 (2011). Open problems and new solutions in time dependent density functional theory.

[95] H. P. Breuer, F. Petruccione, *The theory of open quantum systems* (Oxford University Press, 2002).

[96] F. Bloch, Nuclear Induction. *Phys. Rev.* **70**, 460–474 (1946).

[97] F. Bloch, W. W. Hansen, M. Packard, The Nuclear Induction Experiment. *Phys. Rev.* **70**, 474–485 (1946).

[98] F. Bloch, W. W. Hansen, M. Packard, Nuclear Induction. *Phys. Rev.* **69**, 127–127 (1946).

[99] C. P. Slichter, *Principles of Magnetic Resonance* (Springer, 1996).

[100] S. Chicco, E. Garlatti, G. Allodi, A. Chiesa, M. Atzori, L. Sorace, R. De Renzi, R. Sessoli, S. Carretta, Coherent manipulation of molecular Qudits by broadband NMR. *Nuovo Cimento C* **45**, 163 (2022).

[101] A. Schweiger, G. Jeschke, *Principles of Pulse Electron Paramagnetic Resonance* (Oxford University Press, 2001).

[102] A. Abragam, B. Bleaney, *Electron Paramagnetic Resonance of Transition Ions* (Claredon Pres, Oxford, 1970).

[103] E. Garlatti, A. Chiesa, T. Guidi, G. Amoretti, P. Santini, S. Carretta, Unravelling the Spin Dynamics of Molecular Nanomagnets with Four-Dimensional Inelastic Neutron Scattering. *Eur. J. Inorg* **2019**, 1106-1118 (2019).

[104] G. L. Squires, *Introduction to the Theory of thermal neutron scattering* (Cambridge University Press, 1996).

[105] M. C. R. Merlin, *Light Scattering in Solids IX* (Springer, 2007).

[106] A. Q. R. Baron, Introduction to High-Resolution Inelastic X-Ray Scattering (2015).

[107] S. W. Lovesey, *Theory of Neutron Scattering from Condensed Matter* (Clarendon Press, Oxford, 1984).

[108] A. Hiess, M. Jiménez-Ruiz, P. Courtois, R. Currat, J. Kulda, F. Bermejo, ILL's renewed thermal three-axis spectrometer IN8: A review of its first three years on duty. *Physica B: Condens. Matter* **385-386**, 1077-1079 (2006).

[109] A. Ivanov, M. Jimenéz-Ruiz, J. Kulda, IN1-LAGRANGE – the new ILL instrument to explore vibration dynamics of complex materials. *J Phys Conf Ser* **554**, 012001 (2014).

[110] E. L. Hahn, Nuclear Induction Due to Free Larmor Precession. *Phys. Rev.* **77**, 297–298 (1950).

[111] W. G. Clark, M. E. Hanson, F. Lefloch, P. Ségransan, Magnetic resonance spectral reconstruction using frequency-shifted and summed Fourier transform processing. *Rev. Sci. Instrum.* **66**, 2453-2464 (1995).

[112] N. J. Stone, Table of Nuclear Magnetic Dipole and Electric Quadrupole Moments. *International Atomic Energy Agency* **45-11**, 11 (2014).

[113] S. Takahashi, R. Hanson, J. van Tol, M. S. Sherwin, D. D. Awschalom, Quenching Spin Decoherence in Diamond through Spin Bath Polarization. *Phys. Rev. Lett.* **101**, 047601 (2008).

[114] A. Ghirri, A. Chiesa, S. Carretta, F. Troiani, J. van Tol, S. Hill, I. Vitorica-Yrezabal, G. A. Timco, R. E. P. Winpenny, M. Affronte, Coherent Spin Dynamics in Molecular Cr8Zn Wheels. *J. Phys. Chem. Lett.* **6**, 5062-5066 (2015).

[115] L. C. de Camargo, M. Briganti, F. S. Santana, D. Stinghen, R. R. Ribeiro, G. G. Nunes, J. F. Soares, E. Salvadori, M. Chiesa, S. Benci, R. Torre, L. Sorace, F. Totti, R. Sessoli, Exploring the Organometallic Route to Molecular Spin Qubits: The [CpTi(cot)] Case. *Angew. Chem. Int. Ed* **60**, 2588-2593 (2021).

[116] A. Lunghi, S. Sanvito, The Limit of Spin Lifetime in Solid-State Electronic Spins. *J. Phys. Chem. Lett.* **11**, 6273-6278 (2020).

[117] A. Chiesa, F. Petiziol, E. Macaluso, S. Wimberger, P. Santini, S. Carretta, Embedded quantum-error correction and controlled-phase gate for molecular spin qubits. *AIP Adv* **11**, 025134 (2021).

[118] M. L. Baker, T. Guidi, S. Carretta, J. Ollivier, H. Mutka, H. U. Güdel, G. A. Timco, E. J. L. McInnes, G. Amoretti, R. E. P. Winpenny, P. Santini, Spin dynamics of molecular nanomagnets unravelled at atomic scale by four-dimensional inelastic neutron scattering. *Nature Phys* **8**, 906–911 (2012).

[119] Beamline description can be found at the website, `https://www.esrf.eu/home/UsersAndScience/Experiments/EMD/ID28.html`.

[120] A. Lunghi, Insights into the Spin-Lattice Dynamics of Organic Radicals Beyond Molecular Tumbling: A Combined Molecular Dynamics and Machine-Learning Approach. *Appl Magn Reson* **51**, 1343–1356 (2020).

[121] D. Richard, M. Ferrand, G. J. Kearley, Analysis and visualisation of neutron-scattering data. *J. Neutron Res* **4**, 33-39 (1996).

[122] G. Kresse, J. Furthmuller, Technische Universität Wien, Ph.D. thesis, Ph. D. Thesis (1993).

[123] J. P. Perdew, K. Burke, M. Ernzerhof, Generalized Gradient Approximation Made Simple. *Phys. Rev. Lett.* **77**, 3865–3868 (1996).

[124] J. P. Perdew, K. Burke, M. Ernzerhof, Generalized Gradient Approximation Made Simple [Phys. Rev. Lett. 77, 3865 (1996)]. *Phys. Rev. Lett.* **78**, 1396–1396 (1997).

[125] S. Grimme, Semiempirical GGA-type density functional constructed with a long-range dispersion correction. *J. Comput. Chem* **27**, 1787-1799 (2006).

[126] A. Togo, F. Oba, I. Tanaka, First-principles calculations of the ferroelastic transition between rutile-type and $CaCl_2$-type SiO_2 at high pressures. *Phys. Rev. B* **78**, 134106 (2008).

[127] J. M. Skelton, S. C. Parker, A. Togo, I. Tanaka, A. Walsh, Thermal physics of the lead chalcogenides PbS, PbSe, and PbTe from first principles. *Phys. Rev. B* **89**, 205203 (2014).

[128] P. Giannozzi, O. Baseggio, P. Bonfà, D. Brunato, R. Car, I. Carnimeo, C. Cavazzoni, S. de Gironcoli, P. Delugas, F. Ferrari Ruffino, A. Ferretti, N. Marzari, I. Timrov, A. Urru, S. Baroni, Quantum ESPRESSO toward the exascale. *J. Chem. Phys* **152**, 154105 (2020).

[129] P. Giannozzi, O. Andreussi, T. Brumme, O. Bunau, M. B. Nardelli, M. Calandra, R. Car, C. Cavazzoni, D. Ceresoli, M. Cococcioni, N. Colonna, I. Carnimeo, A. D. Corso, S. de Gironcoli, P. Delugas, R. A. DiStasio, A. Ferretti, A. Floris, G. Fratesi, G. Fugallo, R. Gebauer, U. Gerstmann, F. Giustino, T. Gorni, J. Jia, M. Kawamura, H.-Y. Ko, A. Kokalj, E. Küçükbenli, M. Lazzeri, M. Marsili, N. Marzari, F. Mauri, N. L. Nguyen, H.-V. Nguyen, A. O. de-la Roza, L. Paulatto, S. Poncé, D. Rocca, R. Sabatini, B. Santra, M. Schlipf, A. P. Seitsonen, A. Smogunov, I. Timrov, T. Thonhauser, P. Umari, N. Vast, X. Wu, S. Baroni, Advanced capabilities for materials modelling with Quantum ESPRESSO. *J. Phys. Condens* **29**, 465901 (2017).

[130] P. Giannozzi, S. Baroni, N. Bonini, M. Calandra, R. Car, C. Cavazzoni, D. Ceresoli, G. L. Chiarotti, M. Cococcioni, I. Dabo, A. D. Corso, S. de Gironcoli, S. Fabris, G. Fratesi, R. Gebauer, U. Gerstmann, C. Gougoussis, A. Kokalj, M. Lazzeri, L. Martin-Samos, N. Marzari, F. Mauri, R. Mazzarello, S. Paolini, A. Pasquarello, L. Paulatto, C. Sbraccia, S. Scandolo, G. Sclauzero, A. P. Seitsonen, A. Smogunov, P. Umari, R. M. Wentzcovitch, QUANTUM ESPRESSO: a modular and open-source software project for quantum simulations of materials. *J. Phys. Condens* **21**, 395502 (2009).

[131] H. J. Monkhorst, J. D. Pack, Special points for Brillouin-zone integrations. *Phys. Rev. B* **13**, 5188–5192 (1976).

[132] D. R. Hamann, Optimized norm-conserving Vanderbilt pseudopotentials. *Phys. Rev. B* **88**, 085117 (2013).

[133] A. Togo, I. Tanaka, First principles phonon calculations in materials science. *Scr. Mater.* **108**, 1-5 (2015).

[134] S. J. Lockyer, A. J. Fielding, G. F. S. Whitehead, G. A. Timco, R. E. P. Winpenny, E. J. L. McInnes, Close Encounters of the Weak Kind: Investigations of Electron–Electron Interactions between Dissimilar Spins in Hybrid Rotaxanes. *J. Am. Chem. Soc.* **141**, 14633-14642 (2019).

[135] J. Ferrando-Soria, S. Magee, A. Chiesa, S. Carretta, P. Santini, I. Vitorica-Yrezabal, F. Tuna, G. Whitehead, S. Sproules, K. Lancaster, A.-L. Barra, G. Timco, E. McInnes, R. Winpenny, Switchable Interaction in Molecular Double Qubits. *Chem* **1**, 727-752 (2016).

[136] J. Ferrando-Soria, E. Moreno Pineda, A. Chiesa, A. Fernandez, S. A. Magee, S. Carretta, P. Santini, I. J. Vitorica-Yrezabal, F. Tuna, G. A. Timco, E. J. McInnes, R. E. Winpenny, A modular design of molecular qubits to implement universal quantum gates. *Nat. Commun.* **7** (2016).

[137] G. F. S. Whitehead, B. Cross, L. Carthy, V. A. Milway, H. Rath, A. Fernandez, S. L. Heath, C. A. Muryn, R. G. Pritchard, S. J. Teat, G. A. Timco, R. E. P. Winpenny, Rings and threads as linkers in metal–organic frameworks and poly-rotaxanes. *Chem. Commun.* **49**, 7195-7197 (2013).

[138] E. Garlatti, S. Bordignon, S. Carretta, G. Allodi, G. Amoretti, R. De Renzi, A. Lascialfari, Y. Furukawa, G. A. Timco, R. Woolfson, R. E. P. Winpenny,

P. Santini, Relaxation dynamics in the frustrated Cr_9 antiferromagnetic ring probed by NMR. *Phys. Rev. B* **93**, 024424 (2016).

[139] P. Santini, S. Carretta, E. Liviotti, G. Amoretti, P. Carretta, M. Filibian, A. Lascialfari, E. Micotti, NMR as a Probe of the Relaxation of the Magnetization in Magnetic Molecules. *Phys. Rev. Lett.* **94**, 077203 (2005).

[140] E. Garlatti, S. Carretta, P. Santini, G. Amoretti, M. Mariani, A. Lascialfari, S. Sanna, K. Mason, J. Chang, P. Tasker, E. K. Brechin, Relaxation dynamics in a Fe_7 nanomagnet. *Phys. Rev. B* **87**, 054409 (2013).

[141] M. Belesi, A. Lascialfari, D. Procissi, Z. H. Jang, F. Borsa, Proton NMR wipeout effect due to slow fluctuations of the magnetization in single molecule magnets. *Phys. Rev. B* **72**, 014440 (2005).

List of Publications

Refereed publications

- S. Chicco, A. Chiesa, G. Allodi, E. Garlatti, M. Atzori, L. Sorace, R. de Renzi, R. Sessoli, S. Carretta, *"Controlled coherent dynamics of [VO(TPP)], a prototype molecular nuclear qudit with an electronic ancilla"*, Chemical Science, 12, 12046, **2021**.
- M. Atzori, E. Garlatti, G. Allodi, S. Chicco, A. Chiesa, A. Albino, R. de Renzi, E. Salvadori, M. Chiesa, S. Carretta and L. Sorace, *"Radiofrequency to microwave Coherent Manipulation of an Organometallic Electronic spin Qubit coupled to a Nuclear Qudit"*, Inorganic Chemistry, 60, 11273-11286, **2021**.
- L. Trombi, F. Cugini, R. Rosa, N. Sarzi Amadè, S. Chicco, M. Solzi, P. Veronesi, *"Rapid microwave synthesis of magnetocaloric Ni–Mn–Sn Heusler compounds"*, Scripta Materialia, 176, 63-66, 2020.
- F. Cugini, S. Chicco, F. Orlandi, G. Allodi, P. Bonfà, V. Vezzoni, O. Miroshkina, M. Gruner, L. Righi, S. Fabbrici, F. Albertini, R. De Renzi, M. Solzi, *"Effective decoupling of ferromagnetic sublattices by controlling magnetic interactions in Heusler compounds"*, Physical Review B, 105,174434 **2022**.
- P. Bonfà, S. Chicco, F. Cugini, S. Sharma, J. K. Dewhurst and G. Allodi, *"Magnetic phase diagram of the austenitic Mn-rich Ni-Mn-(In,Sn) Heusler alloys"*, Electronic Structure (IOP), 4, 024002, **2022**
- S. Chicco, E. Garlatti, G. Allodi, A. Chiesa, M. Atzori, L. Sorace, R. De Renzi, R. Sessoli and S. Carretta, *"Coherent manipulation of molecular Qudits by broadband NMR"*, Il Nuovo Cimento C, 45 (6). 1-4 **2022**.

Publications about to be published, after minor revision

- E. Garlatti, A. Albino, S. Chicco, V.H.A. Nguyen, F. Santanni, L. Paolasini, C. Mazzoli, R. Caciuffo, F. Totti, P. Santini, A. Lunghi, R. Sessoli and S. Carretta, *"The critical role of ultra-low energy vibrations in the relaxation dynamics of molecular qubits"*, Nature Communication, **2023**.

Acknowledgments

To conclude this thesis, I would like to sincerely thank all the scientist and collaborators that made it possible. First and foremost, I would like to thank my supervisor Prof. Stefano Carretta, for giving me the opportunity to start my research activity in this fantastic group, and for his extraordinary kindness. He introduced me, during my master degree, to the fascinating field of molecular magnetism and his enthusiasm has never ceased to inspire me. Every discussion we had or advice I received was priceless and I am extremely grateful for everything that he taught me. I would considered myself satisfied if I succeeded in learning even a tenth of his boundless knowledge. I am honored and proud to have had the opportunity to work with him and I also hope that these three years were only the beginning of a long run.

I will be forever thankful to Dr. Elena Garlatti, who co-supervised my PhD, for the extraordinary effort she put in helping me, with the kindness of a sister and an extraordinary competence. Without her support and supervision I would have been lost. I hope I have captured her passion for research and her expertise. Many special thanks to Prof. Giuseppe Allodi, who supervised me during the whole experimental NMR activity. During the time we spent together in the laboratory I tried my best to learn as much as possible from his immense experimental attitude and competence. I would also like to thank Dr. Alessandro Chiesa for the collaborations we had during these three years and for being so enthusiastic in teaching me. It is also important to me to thank my colleague Dr. Emilio Macaluso for the precious time spent discussing all the trivial questions I was not able to answer myself and I was ashamed to ask to my supervisors. All the people in the group have been, and always will be, an example for me, and I am immensely grateful to each of them.

I would like to thank our collaborators at the University of Manchester Prof. Richard Winpenny and Prof. Eric McInnes for giving me the opportunity to spend three months in their fantastic laboratories, welcoming me in their research group. I am very grateful to Dr. Selena F.J. Lockyer for her precious support during my stay in Manchester, it has been a great learning and working opportunity. I hope to collaborate again in the near future. I would also like to thank all the instrument scientists of the X-rays, neutrons and EPR facilities whose help and assistance was priceless: Dr. Luigi Paolasini, Dr. Claudio Mazzoli, Dr. Cai Yong, Prof. Tatiana Guidi, Dr. Andrea Piovano, Dr. Alexandre Ivanov, Dr. Monica Jimenez Ruiz, Mr. Adam Brookfield. Thanks to all of them I am very proud of the experimental results achieved in this thesis. Last but not the least, I would like to warmly thank my high school Physics teacher Gianni Melegari, who planted the seed many years ago and took care of it in the early stages. Finally I would like to thank all the collaborators cited at the beginning of this thesis.

Simone Chicco, January 2023

FUNDING PROJECTS

The work presented in this thesis has received funding from the European Union's Horizon 2020 Research and Innovation Programme, FET-OPEN project FATMOLS ("FAult Tolerant MOLecular Spin processor") under grant agreement No. 862893, including a three months stay at the University of Manchester for the research project: "Electron Spin Resonance measurements on molecular complexes for Quantum Information Processing". Other projects involved in this work were the European Project "Scaling Up quantum computation with MOlecular spins" (SUMO) of the call QuantERA, and the PRIN Project 2017CR5WCH Q-chiSS "Quantum detection of chiral induced spin selectivity at the molecular level" of the Italian Ministry of University and Research (MUR).